Lightning Surge Analysis of Transmission Lines Using Circuit Models Considering Electromagnetic Phenomena

by

Akifumi Yamanaka

A Thesis Submitted to Doshisha University, Kyoto, Japan

for the Degree of Doctor of Engineering

June 11, 2021

Abstract

A lightning strike to a transmission tower and resultant overvoltages are severe threats to the stable operation of electric power systems. The precise estimation of accidents and cost-effective countermeasures against lightning is indispensable. This thesis proposed a transmission tower and a line model to analyze lightning transients in power systems. Back-flashover (BFO) analyses of transmission lines were performed by the presented models. The BFO characteristics were clarified, and the effectiveness of transmission line surge arresters (TLSAs) for reducing lightning accidents was analyzed.

The presented tower and line model can consider the non-transverse electromagnetic (non-TEM) characteristics of lightning-struck transmission towers and lines. When lightning strikes tower top or overhead line, the electromagnetic field spherically expands from the lightning-struck point. The TEM-mode, which is assumed in existing transmission tower and line models, cannot fully explain this initially dynamic non-TEM characteristic and resultant insulator voltages. This thesis revealed the non-TEM characteristics by the finite difference time domain (FDTD) analysis. The non-TEM characteristics of the lightning-struck tower and line include 1) gradually rising characteristics of the tower surge impedance with time, 2) gradually rising self and mutual surge impedance of transmission line with time and the time delays in mutual couplings corresponding to the separation distances, and 3) significant wave attenuation along the tower. The presented tower and line model takes into account these characteristics. The insulator voltages computed by the presented model were thoroughly validated by referencing the FDTD-computed voltages and measured voltages at actual towers reported in the past. Existing transmission tower and line models could have underestimated the insulator voltages.

Practical BFO analyses in high voltage (HV) and extra-high voltage (EHV) transmission lines were performed using the presented models. The flashover (FO) model based on the leader progression method (LPM) was optimized for the HV line. The generalized FO model and the TLSA model represented by the nonlinear resistance were utilized for the BFO analyses. The analyses revealed that the BFO characteristics depend on the power frequency voltages: in case the negative lightning strikes, the BFO occurs preliminary at phases with the positive power frequency voltages, while there is a possibility of BFOs at phases with the negative voltages. The analyses also identified the significant dependence of the minimum lightning current causing a lightning failure on the power frequency voltages, and the dependence clearly explained the BFO characteristics observed in an actual HV transmission line reported in the past. The reduction of the lightning fault rate by installing TLSAs was further analyzed for HV and EHV transmission lines. The optimum arrangement of TLSAs for any transmission line can be determined based on the presented models and the methodologies.

The presented models can be implemented in any circuit simulator. The models and methodologies provide a high-speed and accurate estimation of the lightning performance of transmission lines.

Contents

List of Figures

List of Tables

List of Acronyms

AC	Alternating current
ATP	Alternative Transients Program
BFO	Back-flashover
CA	Circuit analysis
EGLA	Externally gaped line arrester
EHV	Extra-high voltage
EMT simulator	Electromagnetic transient simulator
EMTP	Electromagnetic Transients Program
FDTD method	Finite difference time domain method
FEM	Finite element method
FO	Flashover
GMD	Geometrical mean distance
HEM	Hybrid electromagnetic model
HV	High voltage
LEMP	Lightning electromagnetic pulse
LLS	Lightning location system
LPM	Leader progression method
MoM	Method of moments
NEA	Numerical electromagnetic analysis
OHGW	Overhead grounding wire
PEEC method	Partial element equivalent circuit method
PG	Pulse generator
SFFO	Shielding failure flashover
TEM	Transverse electromagnetic
TLSA	Transmission line surge arrester
UHV	Ultra-high voltage
VI	Voltage–current
VSTL	Virtual Serge Test Laboratory
V–t	Voltage–time
XTAP	eXpandable Transient Analysis Program
ZnO	Zinc oxide

List of Symbols

The symbols used in this thesis are listed. Some of them are used with a proper suffix for indicating specific values.

Admittance	Siemens [S]	Y
Angular frequency	Radians per second [rad/s]	ω
Electric capacitance	Farad [F]	C
Electric charge	Coulomb [C]	Q
Electric conductivity	Siemens per meter [S/m]	σ
Electric current	Ampere [A]	I, i, J
Electric field strength	Volt per meter [V/m]	E
Electric resistance (impedance)	Ohm [Ω]	R, Z
Electric resistivity	Ohm meter [Ωm]	ρ
Frequency	Hertz [Hz]	f
Imaginary number	$\sqrt{-1}$	j
Inductance	Henry [H]	L
Laplace operator		s
Length	Meter [m]	d, D, y (distance) r (radius) l, w, X (length) h (height)
Magnetic field	Ampere per meter [A/m]	H
Permeability	Henry per meter [H/m]	μ
Permittivity	Farad per meter [F/m]	ε
Potential difference, voltage, and electric potential	Voltage [V]	V, v
Propagation function		P, p
Steepness of current waveform	Ampere per second [A/s]	S
Time	Second [s]	T, t, τ
Transfer function		G
Velocity	Meter per second [m/s]	c_0, vel

1 Introduction

1.1 Lightning Related Accidents in Transmission Lines

A lightning strike to a transmission tower or line is one of the most severe threats to the stable and safe operation of electric power systems. The lightning strike causes temporary voltage drops, power outages, and damages to power transmission equipment such as transformers. Overvoltages generated by lightning strikes to the transmission systems should be estimated precisely, and cost-effective countermeasures should be prepared [1]–[3].

The lightning-related accidents in transmission lines can be categorized into three: 1) shielding failure and subsequent shielding failure flashover (SFFO), 2) back-flashover (BFO), and 3) mid-span BFO [3]. These events can cause power outages and initiate accidents in power plants, substations, or consumer equipment. Fig. 1.1 shows the concept of each phenomenon. The shielding failure occurs when the lightning directly strikes phase conductors and can result in the SFFO in case the voltage of an insulator exceeds the withstand voltage. Since the overhead grounding wires (OHGWs) fail to attract the lightning, they are called the "shielding failure." The BFO occurs due to a lightning strike to the tower top or OHGWs. The voltage of the transmission tower rises when lightning strikes the transmission tower top or the OHGWs. In case the voltage of an insulator exceeds the withstand voltage,

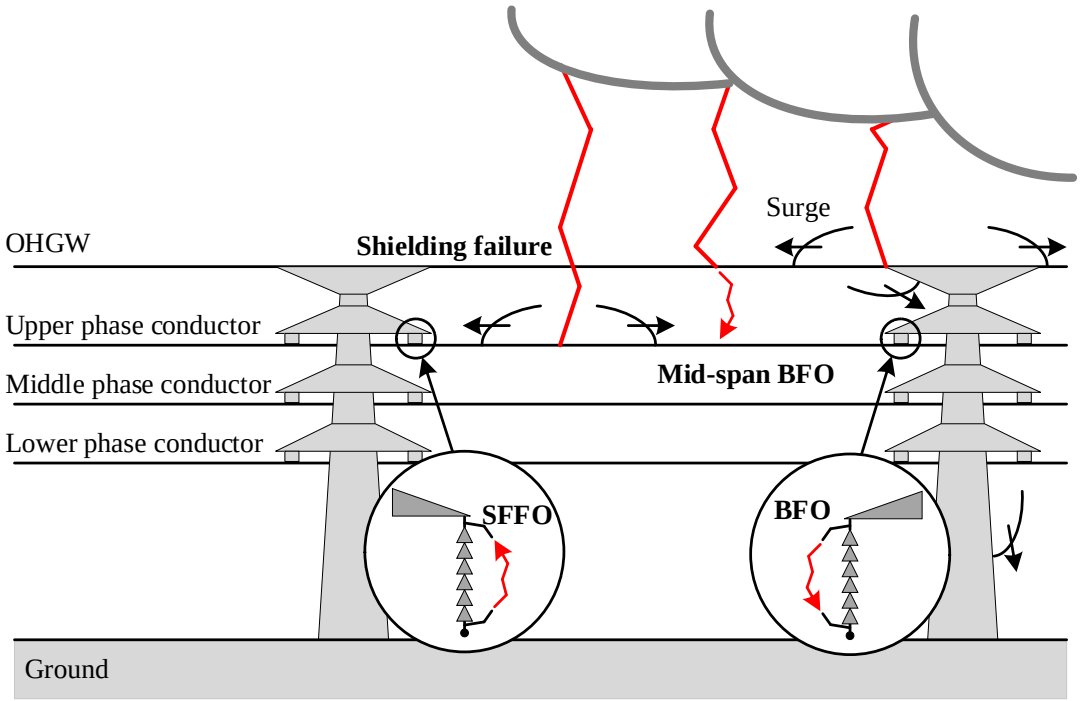

Fig. 1.1 Shielding failure and subsequent SFFO, BFO, and mid-span FO initiated by a lightning strike to a transmission tower or line.

the discharge occurs from the tower side to the phase conductors. Since the discharge occurs from the un-energized tower side under the normal power-system operation, this discharge is called the “back” flashover. The insulator voltages are determined by the characteristics of the transmission tower, line, grounding, lightning channel, and lightning current in the BFO case. The mid-span BFO occurs due to a lightning strike to the mid-span of the OHGWs. The mid-span BFO rarely occurs since the withstand voltage between the OHGW and phase conductor is higher than that of the arcing horns at nearby towers. SFFOs and BFOs can cause the line to ground fault.

The BFO occurs even in transmission lines with properly designed OHGWs because the lightning strikes to transmission tower top or OHGWs cannot be avoided. In other words, the BFO can occur in any overhead transmission system and threaten its stable operation. Therefore, the estimation and reduction of the BFOs have been one of the primary interests in power systems protection.

The transient characteristics of the transmission tower and line are one of the most critical aspects for discussing the BFOs. Aspects that characterize lightning transients in transmission lines include occurrence probability of lightning and characteristics such as the current waveforms and magnitude [4]–[11], shielding efficiency of OHGWs [12]–[15], discharge characteristics across insulators and arcing horns [16]–[21], corona discharge [22]–[24], tower footing characteristics [25]–[27], and surge response of a transmission tower and line itself [28]–[37]. Cost-effective countermeasures against SFFOs and BFOs are indispensable for reducing the probability of lightning-related accidents below the acceptable rate. The countermeasures include installation of appropriately designed OHGWs for reducing SFFOs, reduction of the tower footing resistance, extension of arcing-horn length, and installation of transmission line surge arresters (TLSAs) for BFOs [1]–[3], [38]. Above mentioned aspects should be speedily and accurately evaluated using analysis methods for preparing optimal countermeasures. The transmission tower and line characteristics are among the most critical aspects in estimating the occurrence of the BFOs because they preliminarily determine the insulator voltage that is responsible for the occurrence of BFOs.

1.2 Overview of Lightning Surge Analysis Methods

The lightning surge analysis method can be divided into two groups: 1) theoretical approaches based on the circuit or electromagnetic analysis using simplified models, and 2) numerical approaches based on the numerical circuit or electromagnetic analysis using complex models. Each analysis approach has its advantage and disadvantage. Considering the features of each analysis approach, the numerical circuit analysis has potential and advantages on the practical analysis for evaluating the lightning performance of transmission lines compared to other approaches.

The theoretical approaches are suitable for discussing the basic characteristics of the electrical component or the lightning event (e.g., [28], [29]). However, the approaches themselves usually have

limitations to perform practical analyses, such as the lightning surge analysis of the transmission lines considering several towers and the FO across arcing horns. Note that equivalent models of electrical components can be derived based on the theoretical approaches, and they can be utilized in numerical approaches. Furthermore, the theoretical approach can be utilized for checking the reliability of the numerical approaches.

The numerical approaches comprise numerical circuit and electromagnetic analyses. The circuit analysis by electromagnetic transient (EMT) simulators has long been used for lightning surge analysis of transmission lines. The representative simulators include Electromagnetic Transients Program (EMTP) [39], Alternative Transients Program (ATP) version of EMTP [40], PSCAD [41], eXpandable Transient Analysis Program (XTAP) [42], and others [43]–[45]. A transient phenomenon of transmission towers and lines, and other lightning-related phenomena such as BFOs, can be analyzed using EMT simulators with appropriate numerical models [46]–[49]. They require small computational resources and thus are suitable for analyzing lightning surges considering various conditions with iterative or statistical calculations. However, the circuit analysis method bases on a transverse electromagnetic (TEM) mode of wave propagation. An event with dynamic electromagnetic changes, such as a lightning strike to a transmission tower, cannot be accurately analyzed. Approximations have been applied to non-TEM characteristics, or these characteristics have been neglected in the conventional circuit models (e.g., [30], [31]).

Alternatively, numerical electromagnetic analysis (NEA) is suitable for analyzing the event with dynamic electromagnetic changes, such as the lightning strike to the transmission tower. The NEA method solves Maxwell's equations directly, and hence they do not require the TEM-mode assumption. The finite-difference time-domain (FDTD) method [50], method of moments (MoM) [51], finite element method (FEM) [52], partial-element equivalent-circuit (PEEC) method [53], and hybrid electromagnetic model (HEM) [54] have been employed for lightning surge analysis [55]–[59]. Especially, the FDTD method has been employed in practical lightning surge analyses owing to its simplicity, flexibility, and time-domain solution: analysis of grounding electrodes, lightning electromagnetic pulse (LEMP) propagation analysis, analysis of a lightning strike to telecommunication towers, overvoltage analysis on distribution systems, and wind power generators [60]–[75]. The method has also been applied to practical lightning surge analysis of transmission towers and lines considering imperfectly conducting ground, BFOs in a TLSA installed line, corona discharge, power frequency voltages, and substation entrances [76]–[80]. However, the method requires a massive amount of computational resources. Besides, its modeling process is rather sophisticated compared to circuit analysis methods.

Lightning surge analysis requires a large number of transient analyses taking various conditions into account. In addition, the statistical analysis considering the distributions of lightning parameters and others is sometimes performed (e.g., [47]). For the practical investigation of the lightning surges,

the circuit analysis that can incorporate the non-TEM characteristics of transmission towers and lines has the potential and advantages.

The above numerical circuit and electromagnetic analysis methods are validated if the experiment using actual objects or scale models or the observation of lightning events at actual objects [32]–[36], [81], [82] are available or can be performed. The experiment or observation using the actual objects takes enormous cost and time, and there is difficulty in controlling the experimental or observational conditions. The scale model experiment requires a lower cost than that using actual ones, but it is usually challenging to maintain the measurement accuracy of the very fast transient responses. Nevertheless, those invaluable results always provide insights for understanding lightning surge characteristics, and the numerical models should be carefully validated using them. The validated numerical models become further reliable, and they are employed for evaluating the lightning performance of transmission lines.

1.3 Objectives and Scope of the Thesis

The primary objective of this thesis was to reveal the non-TEM characteristics of the lightning-struck transmission tower and lines taking advantage of the FDTD method, and to propose the circuit models of a transmission tower and line considering the characteristics for evaluating the lightning performance of transmission lines. The FDTD method was adopted since it is one of the most validated NEA methods for lightning surge analysis by comparisons with actual measurements, in addition to its flexibility in three-dimensional time-domain modeling. Then, taking advantage of the circuit analysis method, lightning surge analyses were performed considering multiphase BFOs under various conditions, such as the simultaneous power frequency voltages and arrangements of TLSAs. The occurrence characteristics of BFOs were discussed and clarified for the sake of an optimal lightning protection scheme. Note that the lightning surge analysis was also performed by the existing circuit analysis models for practical discussions on systems under operation, which have been designed based on them.

The followings are the structure of this thesis. In Chapter 2, the non-TEM characteristics of the lightning-struck transmission tower and line are revealed using the FDTD method and the circuit analysis using tower and line models represented by lossless distributed-parameter lines. Existing transmission tower and line models are overviewed subsequently from the viewpoint of the inclusion of non-TEM characteristics. The experimental approaches on actual towers and small-scale models are deeply referenced during the discussion. Chapter 3 proposes TEM-delay transmission tower and line models representing the non-TEM characteristics in the circuit analysis method. They are validated based on the comparisons with the FDTD-computed insulator voltages and those measured at actual transmission towers reported in the past. In Chapter 4, BFO phenomena in a 77-kV transmission line are discussed with referencing observation results in the past. The characteristics of the BFO occurrences depending on the power frequency voltages are clarified. Chapter 4 further discusses the performances

of each circuit model, such as transmission tower and line models and FO models, and the effect of current waveforms on the BFO occurrence. In Chapter 5, the performance of TLSAs for high voltage (HV) and extra-high voltage (EHV) transmission lines is discussed based on the proposed circuit models. Chapter 6 concludes this thesis. Appendix A1 and A2 briefly describe the fundamentals of the FDTD method and the numerical circuit analysis method.

The presented models can be implemented in any EMT simulator. The BFO analysis performed based on the presented models reveals BFO characteristics of vertical double-circuit transmission towers and the effectiveness of TLSAs for reducing lightning accidents. The models and the analysis methodologies provide a high-speed and accurate estimation of the lightning performance of transmission lines.

References for Chapter 1

[1] CIGRE WG 33.01 (Lightning), "Guide to procedures for estimating the lightning performance of transmission lines," *CIGRE Technical Brochure*, no. 63, 1991.

[2] IEEE Standards Board, "IEEE guide for improving the lightning performance of transmission lines," *IEEE Std.*, no. 1243-1997, 1997 (reaffirmed in 2008).

[3] Subcommittee for transmission lines, lightning protection design committee, "Guide to lightning protection design for transmission lines," *CRIEPI Rep.*, no. T72, 2003.

[4] CIGRE WG C4.407 (Convenor: V. A. Rakov), "Lightning parameters for engineering applications," *CIGRE Technical Brochure*, no. 549, Jan. 2014.

[5] S.-E. Enno, J. Sugier, R. Alber, and M. Seltzer, "Lightning flash density in Europe based on 10 years of ATDnet data," *Atmospheric Research*, vol. 235, p. 104769-1–104769-14, May 2020.

[6] T. L. Koehler, "Cloud-to-ground lightning flash density and thunderstorm day distributions over the contiguous United States derived from NLDN measurements: 1993–2018," *Monthly Weather Review*, vol. 148, no. 1, pp. 313–332, Jan. 2020.

[7] M. Matsui, K. Michishita, and S. Yokoyama, "Cloud-to-ground lightning flash density and the number of lightning flashes hitting wind turbines in Japan," *Electr. Power Syst. Res.*, vol. 181, pp. 106066-1–106066-8, Apr. 2020.

[8] K. Berger, "Parameters of lightning flashes," *ELECTRA*, vol. 41, pp. 23–37, 1975.

[9] J. Takami, and S. Okabe, "Observational results of lightning current on transmission towers," *IEEE Trans. Power Del.*, vol. 22, no. 1, pp. 547–556, Jan. 2007.

[10] T. Miki, M. Saito, T. Shindo, and M. Ishii, "Current observation results of downward negative flashes at Tokyo Skytree from 2012 to 2018," *IEEE Trans. Electromagn. Compat.*, vol. 61, no. 3, pp. 663–673, Jun. 2019.

[11] F. H. Silveira, and S. Visacro, "Lightning parameters of a tropical region for engineering application: statistics of 51 flashes measured at Morro do Cachimbo and expressions for peak current distributions," *IEEE Trans. Electromagn. Compat.*, vol. 62, no. 4, pp. 1186–1191, Aug. 2020.

[12] H. R. Armstrong, and E. R. Whitehead, "Field and analytical studies of transmission line shielding," *IEEE Trans. Power App. Syst.*, vol. PAS-87, no. 1, pp. 270–281, Jan. 1968.

[13] S. Taniguchi, T. Tsuboi, S. Okabe, Y. Nagaraki, J. Takami, and H. Ota, "Improved method of calculating lightning stroke rate to large-sized transmission lines based on electric geometry model," *IEEE Trans. Dielectr. Electr. Insul.*, vol. 17, no. 1, pp. 53–62, Feb. 2010.

[14] F. A. M. Rizk, "Modeling of transmission line exposure to direct lightning strokes," *IEEE Trans. Power Del.*, vol. 5, no. 4, pp. 1983–1997, Oct. 1990.

[15] F. A. M. Rizk, "A simplified approach for assessment of exposure of EHV and UHV lines to direct lightning strikes," *IEEE Trans. Power Del.*, vol. 33, no. 5, pp. 2420–2427, Oct. 2018.

[16] T. Shindo, and T. Suzuki, "A new calculation method of breakdown voltage-time characteristics of long air gaps," *IEEE Trans. Power App. Syst.*, vol. PAS-104, no. 6, pp. 1556–1563, Jun. 1985.

[17] Y. Aoshima, and K. Miyake, "Flashover characteristics of air gaps for short tail waves," *Trans. IEE of Japan*, vol. 109-B, no. 3, pp. 135–142, Mar. 1989.

[18] A. Pigini, G. Rizzi, E. Garbagnati, A. Porrino, G. Baldo, and G. Pesavento, "Performance of large air gaps under lightning overvoltages: experimental study and analysis of accuracy predetermination methods," *IEEE Trans. Power Del.*, vol. 4, no. 2, pp. 1379–1392, Apr. 1989.

[19] H. Motoyama, "Experimental study and analysis of breakdown characteristics of long air gaps with short tail lightning impulse," *IEEE Trans. Power Del.*, vol. 11, no. 2, pp. 972–979, Apr. 1996.

[20] X. Wang, Z. Yu, and J. He, "Breakdown process experiments of 110- to 500-kV insulator strings under short tail lightning impulse," *IEEE Trans. Power Del.*, vol. 29, no. 5, pp. 2394–2401, Oct. 2014.

[21] T. Shindo, M. Miki, T. Miki, and M. Saito, "Effects of the external series impedance on concurrent flashover probability in a parallel gap configuration," *IEEJ Trans. Power and Energy*, vol. 138, no. 10, pp. 837–842, Oct. 2018.

[22] C. F. Wagner, and B. L. Lloyd, "Effects of corona on traveling waves," *AIEE Trans. Power App. Syst.*, vol. 74, no. 3, pp. 858–872, Jan. 1955.

[23] T. Noda, T. Ono, H. Matsubara, H. Motoyama, S. Sekioka, and A. Ametani, "Charge-voltage curves of surge corona on transmission lines: two measurement methods," *IEEE Trans. Power Del.*, vol. 18, no. 1, pp. 307–314, Jan. 2003.

[24] T. H. Thang, Y. Baba, N. Nagaoka, A. Ametani, J. Takami, S. Okabe, and V. A. Rakov, Vladimir A., "A simplified model of corona discharge on overhead wire for FDTD computations," *IEEE Trans. Electromagn. Compat.*, vol. 54, no. 3, pp. 585–593, Jun. 2012.

[25] L. Grcev, "Modeling of grounding electrodes under lightning currents," *IEEE Trans. Electromagn. Compat*., vol. 51, no. 3, pp. 559–571, Aug. 2009.

[26] S. Sekioka, "Frequency and current-dependent grounding resistance model for lightning surge analysis," *IEEE Trans. Electromagn. Compat.*, vol. 61, no. 2, pp. 419–425, Apr. 2019.

[27] CIGRE WG C4.33 (Convenor: S. Visacro), "Impact of soil-parameter frequency-dependence on the response of grounding electrode and on the lightning performance of electrical systems," *CIGRE Technical Brochure*, no 781, Oct. 2019.

[28] C. F. Wagner, and A. R. Hileman, "A new approach to the calculation of the lightning performance of transmission lines III—a simplified method: stroke to tower," *AIEE Trans. Power App. Syst.*, vol. 79, pp. 589–603, Oct. 1960.

[29] M. A. Sargent, and M. Darveniza, "Tower surge impedance," *IEEE Trans. Power App. Syst.*, vol. PAS-88, no. 5, pp. 680–687, May 1969.

[30] M. Ishii, T. Kawamura, T. Kouno, E. Ohsaki, K. Murotani, and T. Higuchi, "Multistory transmission tower model for lightning surge analysis," *IEEE Trans. Power Del.*, vol. 6, no. 3, pp. 1327–1335, Jul. 1991.

[31] T. Hara, and O. Yamamoto, "Modeling of a transmission tower for lightning-surge analysis," *IEE Proc.-Gener. Transm. Distrib.*, vol. 143, no. 3, pp. 283–289, May 1996.

[32] M. Kawai, "Studies of the surge response on a transmission line tower," *IEEE Trans. Power App. Syst.*, vol. 83, no. 1, pp. 30–34, Jan. 1964.

[33] W. A. Chisholm, Y. L. Chow, and K. D. Srivastava, "Lightning surge response of transmission towers," *IEEE Trans. Power App. Syst.*, vol. PAS-102, no. 9, pp. 3232–3242, Sep. 1983.

[34] T. Hara, O. Yamamoto, M. Hayashi, and C. Uenosono, "Empirical formulas of surge impedance for single and multiple vertical cylinder," *Trans. IEE of Japan*, vol. 110-B, no. 2, pp. 129–137, Feb. 1990.

[35] H. Motoyama, Y. Kinoshita, and K. Nonaka, "Experimental study on lightning surge response of 500-kV transmission tower with overhead lines," *IEEE Trans. Power Del.*, vol. 23, no. 4, pp. 2488–2495, Oct. 2008.

[36] H. Motoyama, Y. Kinoshita, K. Nonaka, and Y. Baba, "Experimental and analytical studies on lightning surge response of 500-kV transmission tower," *IEEE Trans. Power Del.*, vol. 24, no. 4, pp. 2232–2239, Oct. 2009.

[37] B. Salarieh, H. M. J. De Silva, A. M. Gole, A. Ametani, and B. Kordi, "An electromagnetic model for the calculation of tower surge impedance based on thin wire approximation," *IEEE Trans. Power Del.*, vol. 36, no. 2, pp. 1173–1182, Apr. 2021.

[38] Subcommittee for transmission lines, study committee on lightning risk, "Application guide for transmission line surge arresters," *CRIEPI Rep.*, no. H07, 2012.

[39] "Home | EMTP." https://www.emtp.com/ (accessed Apr. 03, 2021).

[40] "Home | EEUG." https://www.emtp.org/ (accessed May 23, 2021)

[41] "Home | PSCAD." https://www.pscad.com/ (accessed Apr. 03, 2021).

[42] "XTAP - The Smart Grid Simulator." https://www.xtap.org/ (accessed May 07, 2021).

[43] T. Noda, "Recent trend of electromagnetic transient programs for power system analysis," *IEEJ Trans. Power and Energy*, vol. 126, no. 11, pp. 1108–1111, Nov. 2006.

[44] T. Noda, "International and domestic development trends of electromagnetic transient analysis programs for power systems," *IEEJ Trans. Power and Energy*, vol. 131, no. 11, pp. 872–875, Nov. 2011.

[45] A. Ametani, "Electromagnetic Transients Program: history and future," *IEEJ Trans. Electr. Electro. Eng.*, vol. 16, no. 4, Sep. 2021 (advanced online publication version).

[46] A. Ametani, and T. Kawamura, "A method of a lightning surge analysis recommended in Japan using EMTP," *IEEE Trans. Power Del.*, vol. 20, no. 2, pp. 867–875, Apr. 2005.

[47] J. A. Martinez, and F. Castro-Aranda, "Lightning performance analysis of overhead transmission lines using the EMTP," *IEEE Trans. Power Del.*, vol. 20, no. 3, pp. 2200–2210, Jul. 2005.

[48] A. Ametani, N. Nagaoka, Y. Baba, T. Ohno, and K. Yamabuki, *Power System Transients: Theory and Applications, Second Edition*, CRC Press, FL, USA, 2017.

[49] J. A. Martinez, A. I. Ramirez, and M. Davila, "Overhead lines," *in Power system transients parameter determination*, edited by J. A. Martinez, CRC Press, FL, USA, 2010.

[50] K. S. Yee, "Numerical solution of initial boundary value problems involving Maxwell's equations in isotropic media," *IEEE Trans. Antennas Propag.*, vol. 14, no. 3, pp. 302–307, May 1966.

[51] R. F. Harrington, *Field Computation by Moment Methods*, MacMillan Co., New York, 1968.

[52] M. N. O. Sadiku, "A simple introduction to finite element analysis of electromagnetic problems," *IEEE Trans. Educ.*, vol. 32, no. 2, pp. 85–93, May 1989.

[53] A. E. Ruehli, "Equivalent circuit models for three-dimensional multiconductor systems," *IEEE Trans. Microw. Theory Tech.*, vol. 22, no. 3, pp. 216–221, Mar. 1974.

[54] S. Visacro, and A. Soares, "HEM: a model for simulation of lightning-related engineering problems," *IEEE Trans. Power Del.*, vol. 20, no. 2, pp. 1206–1208, Apr. 2005.

[55] CIGRE WG C4.37 (Convenor: Y. Baba), "Electromagnetic computation methods for lightning surge studies with emphasis on the FDTD method," *CIGRE Technical Brochure*, no. 785, Dec. 2019.

[56] e.g., M. Saito, T. Miki, T. Shindo, H. Motoyama, M. Ishii, T. Sonehara, H. Taguchi, A. Tajima, and A. Fujisawa, "Reproduction of electromagnetic field waveforms of subsequent return strokes hitting Tokyo Skytree over lossy ground," *IEEJ Trans. Power and Energy*, vol. 135, no. 7, pp. 472–478, 2015.

[57] e.g., P. C. Á. Mota, J. R. Camacho, and M. L. R. Chaves, "Analysis of tower surge impedance using the finite element method," *Electr. Power Syst. Res.*, vol. 152, pp. 184–193, Nov. 2017.

[58] e.g., P. Yutthagowith, A. Ametani, F. Rachidi, N. Nagaoka, and Y. Baba, "Application of a partial element equivalent circuit method to lightning surge analyses," *Electr. Power Syst. Res.*, vol. 94, pp. 30–37, Jan. 2013.

[59] e.g., F. H. Silveira, and S. Visacro, "Lightning performance of transmission lines: impact of current waveform and front-time on backflashover occurrence," *IEEE Trans. Power Del.*, vol. 34, no. 6, pp. 2145–2151, Dec. 2019.

[60] K. Tanabe, "A method for computational analysis of transient resistance for grounding systems based on the FD-TD method," *IEEJ Trans. Power and Energy*, vol. 120, no. 8–9, pp. 1119–1126, Aug. 2000.

[61] K. Tanabe, A. Asakawa, M. Sakae, M. Wada, and H. Sugimoto, "Verifying the computational method of transient performance with respect to grounding systems based on the FD-TD method," *IEEJ Trans. Power and Energy*, vol. 123, no. 3, pp. 358–367, Mar. 2003.

[62] A. Tatematsu, K. Yamazaki, K. Miyajima, and H. Motoyama, "A study on induced voltages on an aerial wire due to a current flowing through a grounding grid," *IEEJ Trans. Power and Energy*, vol. 129, no. 10, pp. 1245–1251, Oct. 2009.

[63] F. Zhang, H. Tanaka, Y. Baba, and N. Nagaoka, "Soil ionization effects on surge characteristics of grounding electrodes," *IEEJ Trans. Electr. Electro. Eng.*, vol. 14, no. 11, pp. 1609–1616, Jul. 2019.

[64] M. Aoki, Y. Baba, and V. A. Rakov, "FDTD simulation of LEMP propagation over lossy ground: Influence of distance, ground conductivity, and source parameters," *J. of Geophys. Res. Atmos.*, vol. 120, no. 16, pp. 8043–8051, Jul. 2015.

[65] A. Tatematsu, K. Yamazaki, and H. Matsumoto, "Lightning surge analysis of a microwave relay station using the FDTD method," *IEEE Trans Electromagn. Compat.*, vol. 57, no. 6, pp. 1616–1626, Dec. 2015.

[66] S. Araki, Y. Nasu, Y. Baba, V. A. Rakov, M. Saito, and T. Miki, "3-D finite difference time domain simulation of lightning strikes to the 634-m Tokyo Skytree," *Geophys. Res. Lett.*, vol. 45, no. 17, pp. 9267–9274, Aug. 2018.

[67] A. Yamanaka, N. Nagaoka, Y. Baba, M. Saito, and T. Miki, "Lightning strike to a tall-grounded object: part 2—LEMP calculation with a channel approximation," *IEEE Trans Electromagn. Compat.*, vol. 61, no. 3, pp. 736–744, Jun. 2019.

[68] W. Hou, M. Azadifar, M. Rubinstein, F. Rachidi, and Q. Zhang, "On the propagation of lightning-radiated electromagnetic fields across a mountain," *IEEE Trans. Electromagn. Compat.*, vol. 62, no. 5, pp. 2137–2147, Oct. 2020.

[69] A. Tatematsu, and T. Noda, "Three-dimensional FDTD calculation of lightning-induced voltages on a multiphase distribution line with the lightning arresters and an overhead shielding wire," *IEEE Trans. Electromagn. Compat.*, vol. 56, no. 1, pp. 159–167, Feb. 2014.

[70] T. H. Thang, Y. Baba, V. A. Rakov, and A. Piantini, "FDTD computation of lightning-induced voltages on multiconductor lines with surge arresters and pole transformers," *IEEE Trans. Electromagn. Compat.*, vol. 57, no. 3, pp. 442–447, Jun. 2015.

[71] T. H. Thang, Y. Baba, A. Piantini, and V. A. Rakov, "Lightning-induced voltages in the presence of nearby buildings: FDTD simulation versus small-scale experiment," *IEEE Trans. Electromagn. Compat.*, vol. 57, no. 6, pp. 1601–1607, Dec. 2015.

[72] M. Natsui, A. Ametani, J. Mahseredjian, S. Sekioka, and K. Yamamoto, "3-D FDTD analysis of lightning-induced voltages in distribution lines due to inclined lightning," *IEEE Trans. Electromagn. Compat.*, vol. 63, no. 1, pp. 189–197, Feb. 2021.

[73] M. Nagao, N. Nagaoka, Y. Baba, and A. Ametani, "FDTD analysis of the current distribution within the grounding system for a wind turbine generation tower struck by lightning," *IEEJ Trans. Power and Energy*, vol. 128, no. 11, pp. 1393–1400, Nov. 2008.

[74] K. Yamamoto, S. Yanagawa, K. Yamabuki, S. Sekioka, and S. Yokoyama, "Analytical surveys of transient and frequency-dependent grounding characteristics of a wind turbine generator system on the basis of field tests," *IEEE Trans. Power Del.*, vol. 25, no. 4, pp. 3035–3043, Oct. 2010.

[75] M. E. M. Rizk, F. Mahmood, M. Lehtonen, E. A. Badran, and M. H. Abdel-Rahman, "Investigation of lightning electromagnetic fields on underground cables in wind farms," *IEEE Trans. Electromagn. Compat*, vol. 58, no. 1, pp. 143–152, Feb. 2016.

[76] R. M. S. Oliveira and C. L. S. S. Sobrinho, "Computational environment for simulating lightning strokes in a power substation by finite-difference time-domain method," *IEEE Trans. Electromagn. Compat.*, vol. 51, no. 4, pp. 995–1000, Nov. 2009.

[77] J. Takami, T. Tsuboi, K. Yamamoto, S. Okabe, Y. Baba, and A. Ametani, "Lightning surge response of a double-circuit transmission tower with incoming lines to a substation through FDTD simulation," *IEEE Trans. Dielectr. Electr. Insul.*, vol. 21, no. 1, pp. 96–104, Feb. 2014.

[78] Y. Huangfu, S. Wang, and X. Tao, "Transient lightning impulse performance analysis for composite transmission line tower," *IEEE Trans. Electromagn. Compat.*, vol. 57, no. 5, pp. 1103–1111, Oct. 2015.

[79] A. Tatematsu, and T. Ueda, "FDTD-based lightning surge simulation of an HV air-insulated substation with back-flashover phenomena," *IEEE Trans. Electromagn. Compat.*, vol. 58, no. 5, pp. 1549–1560, Oct. 2016.

[80] T. H. Thang, Y. Baba, N. Itamoto, and V. A. Rakov, "FDTD simulation of back-flashover at the transmission-line tower struck by lightning considering ground-wire corona and operating voltages," *Electr. Power Syst. Res.*, vol. 159, pp. 17–23, Jun. 2018.

[81] T. Ueda, M. Yoda, and I. Miyachi, "Characteristics of lightning surges observed at 77 kV substations," *Trans. IEE of Japan*, vol. 116-B, no. 11, pp.1422–1428, Nov. 1996.

[82] H. Motoyama, K. Shinjo, Y. Matsumoto, and N. Itamoto, "Observation and analysis of multiphase back flashover on the Okushishiku Test Transmission Line caused by winter lightning," *IEEE Trans. Power Del*, vol. 13, no. 4, pp. 1391–1398, Oct. 1998.

2 Non-TEM Characteristics of Lightning-Struck Transmission Tower and Lines

The TEM-mode wave propagation assumed in the circuit analysis theory cannot fully explain an electromagnetic field generated by a lightning strike to a transmission tower top or overhead line. This is because the electromagnetic field generated by the lightning strike varies dynamically, but the TEM-mode wave propagation assumes a steady-state electromagnetic field, i.e., plane wave propagation. Thus, the dynamic non-TEM characteristics of the lightning-struck tower and line have to be revealed, and circuit models of transmission towers and lines should consider these characteristics. Fig. 2.1 illustrates a conceptual figure of TEM wave assumption and electromagnetic field generated by the lightning strike.

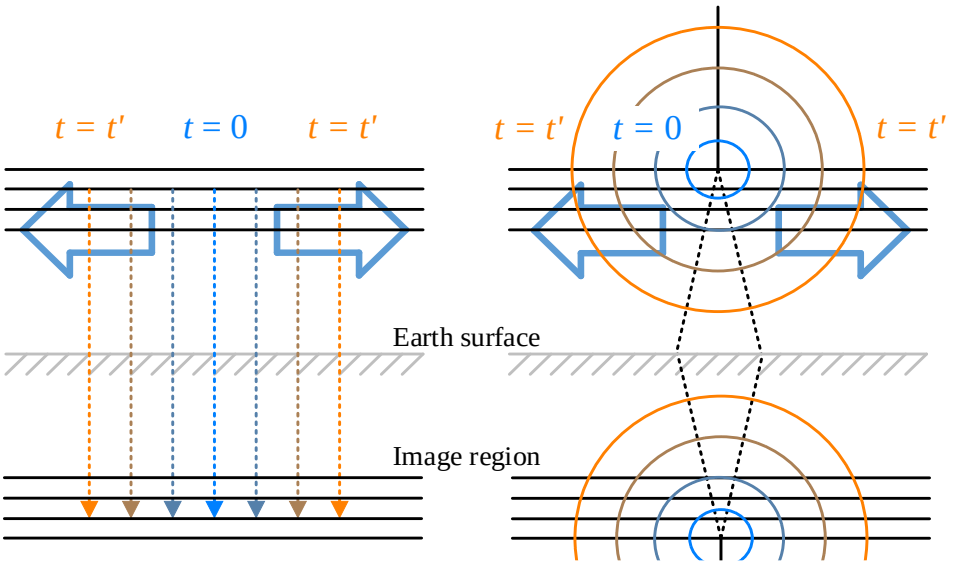

(a) TEM-mode assumption (b) non-TEM waves

Fig. 2.1 Conceptual figure of the TEM-mode assumption and the electromagnetic field generated by a lightning strike to the transmission tower and line (non-TEM waves).

The TEM-mode assumes the steady-state electromagnetic field about the vertical direction, as shown in Fig. 2.1 (a). Circuit parameters, such as capacitance and inductance per unit length and resultant surge impedance, are derived based on this assumption. Then, the transmission line is modeled by a distributed parameter line model [1]. The model can consider the wave propagation and the time delay about the horizontal direction along the line. However, the self and mutual surge impedances of an overhead line are almost constant in the TEM-mode transmission line model, except for the frequency-dependent characteristic due to the skin effect. Besides, the model neglects the time delay of mutual coupling among the transmission lines due to the non-plane electromagnetic field propagation.

The electromagnetic field generated due to a lightning strike to the transmission tower or line is initially different from that assumed in the TEM mode, and its modeling is indispensable for the lightning surge analysis. The electromagnetic field is radiated spherically from the lightning-struck point, as shown in Fig. 2.1 (b). As a result, both the transmission tower and line surge impedances can have a dynamic time dependence. Furthermore, the mutual coupling from one line to the others has a time delay corresponding to the separation distances. Due to the above reasons, the conventional circuit analysis model assuming the TEM-mode cannot precisely estimate the insulator voltages of a lightning-struck tower. The electromagnetic field distribution gradually converges to that assumed in the TEM mode. Thus, the modeling of the TEM-mode formation process is indispensable for accurately analyzing lightning transients in transmission towers and lines. Nevertheless, it should be noted that the TEM-mode assumption provides satisfactory solutions for fast transients, such as switching surges.

In this chapter, the non-TEM characteristics of the lightning-struck tower and line are discussed based on the FDTD analysis and the circuit analysis using basic TEM-mode models. The discussions reveal the differences between TEM and non-TEM characteristics and show the requirements of the circuit analysis models for precisely estimating insulator voltages of the lightning-struck towers. The latter half of this chapter thoroughly overviews existing transmission tower models from the viewpoint of the inclusion of the non-TEM characteristics.

2.1 Numerical Electromagnetic and Circuit Analysis for Clarifying Non-TEM Characteristics

2.1.1 FDTD analysis model for computing insulator voltages

FDTD analyses were performed for computing the voltages across the insulator strings considering non-TEM characteristics of a transmission tower and line. The FDTD method enables us to analyze the dynamic electromagnetic fields by directly solving Maxwell's equations numerically, though it requires massive computational resources. This section provides the FDTD analysis conditions and models.

The FDTD computations were carried out using Virtual Surge Test Laboratory (VSTL), developed by Central Research Institute Electric Power Industry, Japan [2]. The latest version was reported in [3]. Using VSTL, in [2], [4], a surge impedance of a single horizontal conductor was computed, and the computed result agreed with an experimental result. Besides, the analysis with VSTL reproduced a surge experiment using a 4-m vertical conductor system. Further, in [5], a small-scale experiment of a lightning strike to a transmission tower at a substation entrance was reproduced. For the actual scale experiment or measurement related to transmission systems, the accuracy of the VSTL was verified by a surge experiment of a 500-kV transmission tower in [6], [7], a measured lightning surge intruding a 77-kV air-insulation substation was reproduced in [8], and measured switching surges at an EHV substation was reproduced in [9].

The overall FDTD analysis space is shown in Fig. 2.2, and Table 2.1 summarizes the FDTD analysis conditions. A 500-kV vertical double-circuit transmission tower with a height of 76 m was located on a perfectly conducting plane. The perfectly conducting plane enables us to neglect the frequency dependence of the tower and line due to the earth-return impedance and the imperfect ground reflection at the tower foot. Under this ideal condition, we can clarify the non-TEM characteristic of the tower and line. The analysis space was 600 m × 600 m × 400 m in *x*-*y*-*z* directions and was enclosed by

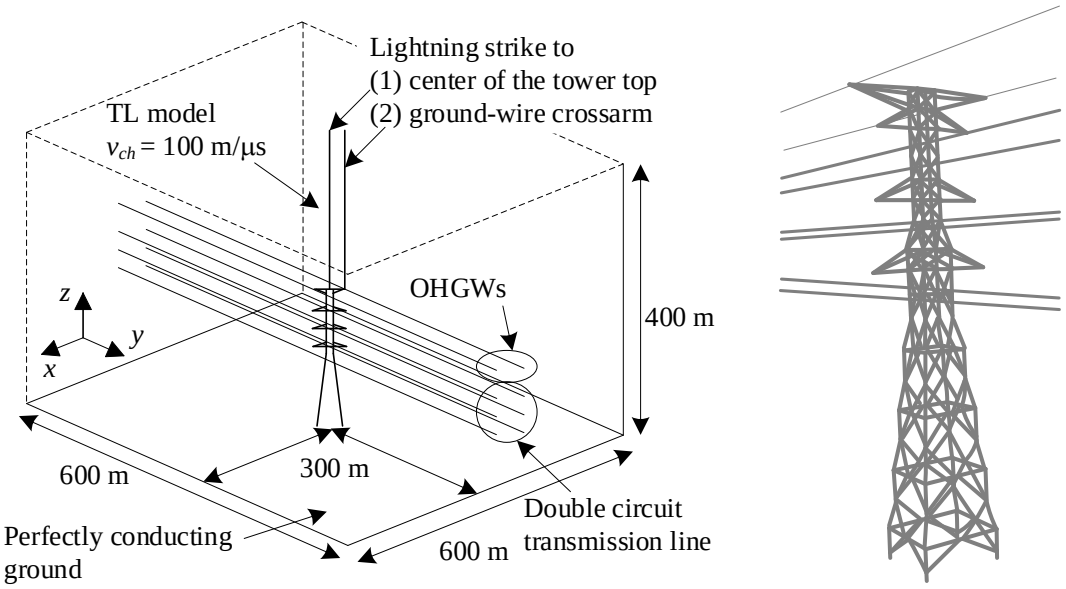

(a) FDTD analysis space (b) FDTD tower model

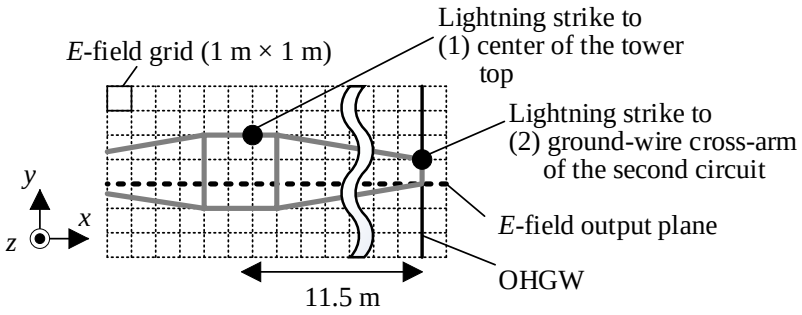

(c) Top view of the FDTD analysis space.

Fig. 2.2 FDTD analysis model of a lightning strike to a transmission tower top.

Table 2.1 FDTD analysis condition for calculating step-like current response.

Analysis space	600 m × 600 m × 400 m
Boundary condition (except for the bottom surface)	Liao's second-order absorbing boundary
Bottom surface	Perfectly conducting plane
Cell size	1 m × 1 m × 1 m
Time step	1.55 ns

Liao's second-order absorbing boundary [10] except for the bottom perfectly conducting ground plane. The space was uniformly divided into cubic cells of 1 m × 1 m × 1 m.

Modeling methods of the transmission tower and line models are described. Fig. 2.3 (a) shows the shape of the model transmission tower, and Fig. 2.2 (b) shows its FDTD analysis model. The cross-arms, main legs, and bracings were modeled in detail by thin wires using the staircase approximation method [11]. The thin wire is represented by forcing the electric field along line zero [4]. The 600-m long transmission line was attached to the absorbing boundaries, and thus they are interpreted as two semi-infinitely long lines seen from the tower. The OHGWs were grounded via the tower model. Fig. 2.3 (b) shows the arrangement of the OHGWs and phase conductors. The phase conductors were composed of four-bundled conductors with a separation of 0.5 m, and a single conductor modeled them since their radii were smaller than the cell size. The radius r_{eqp} of the single conductor was determined based on the geometrical mean distance (GMD). The radius of each OHGW and the equivalent radius of the phase conductors were implemented in the FDTD analysis using the thin wire representation method, which modifies the permittivity and permeability surrounding the wire [4]. The computation time step was set to 1.35 ns, which is 0.7 times the upper limit of the Courant stability condition, to avoid numerical instability due to the thin-wire approximation [12]. Note that the applicability of Liao's second-order absorbing boundary to the thin wire representation method in the presented case has been shown in [6].

The voltage across the insulator string was defined by the electric field between the phase conductor and the tip of the tower cross-arm. Each distance between the cross-arm and phase conductor was set to 4 m. No capacitor or resistor was connected across the insulator including its arcing horn, i.e.,

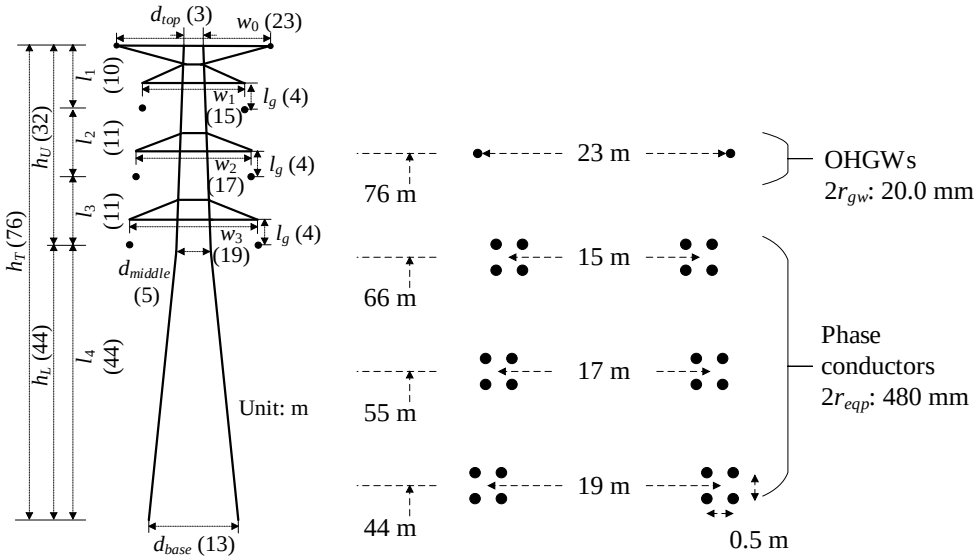

(a) Model tower (b) Model transmission line

Fig. 2.3 Configuration of the transmission tower and line for FDTD analysis.

its terminals were open-circuited. The voltage of the tower top and the phase conductor was evaluated as the gap voltage between the terminal and a horizontal voltage reference wire connected to the absorbing boundary. The current flowing into the OHGWs was defined by the magnetic field surrounding the wires. The current flowing into the tower was calculated by subtracting currents flowing into four OHGWs from the injected current.

The lightning channel was modeled by a transmission line model with a current propagation speed of 100 m/μs and implemented in the FDTD analysis by a phased-current-source array [13]. As shown in Fig. 2.2 (a) and (c), two lightning-struck point cases were analyzed: (1) lightning strike to the center of the tower top, and (2) lightning strike to the tip of the tower top cross-arm. The basic characteristics of the transmission tower and line are discussed based on the first case, a lightning strike to the center of the tower top. However, the lightning rarely strikes the center of the tower top but usually strikes the tip of the tower top cross-arms or OHGWs. The effect of the asymmetrical strike of the lightning on insulator voltages of the struck-side and the other side is discussed based on the second case, a lightning strike to the tip of the tower top cross-arm.

A step-like current having a time constant of 50 ns expressed by the following equation was injected into the tower top:

$$I_{in}(t)=\begin{cases}0 & (t<0)\\ 1-\exp(-t/50\ \mathrm{ns}) & (t\geq 0)\end{cases} \tag{2.1}$$

The step-like current can reveal the high-frequency characteristics of the tower and line, which are essential for lightning surge studies. At the same time, the step-like current does not cause numerical instabilities in the FDTD computation by reducing the current change rate *di/dt* at the wavefront compared to the ideal step-current. The current magnitude was normalized to 1 A because the analysis did not include any nonlinearity.

Note that in [6] and [7], a similar tower was studied using the FDTD method in a similar condition except for the perfectly conducting plane. This FDTD analysis reproduced a surge experiment performed for an actual 500-kV tower. In this chapter, the perfectly conducting plane was selected to obtain the pure characteristics of the lightning-struck transmission tower and line due to the TEM-mode formation. The frequency dependence of the tower and line due to the skin effect and the earth-return impedance are not considered.

2.1.2 Basic circuit analysis model for computing insulator voltages

TEM-assumed simple circuit models of a tower and line were employed for comparison with the FDTD analysis. The various models presented as of today, which will be overviewed in Section 2.2, were not utilized here because this chapter aimed to clarify the non-TEM characteristic of the transmission tower

and line struck by lightning. The discussions based on differences between the FDTD analysis results and those by the most basic circuit analysis model can reveal the non-TEM characteristics.

The transmission tower was represented by a lossless distributed-parameter line having a surge impedance Z_T of 202 Ω determined based on the modified Jordan's formula [14] considering the weighted-average equivalent radius. The modified Jordan's formula is provided by (2.14) shown in Section 2.2 and discussed there with other surge impedance formulae. The tower model was divided into four sections to obtain the voltage at the upper, middle, and lower cross-arm joints, as shown in Fig. 2.4. It should be noted that the cross-arms were not explicitly considered in this model.

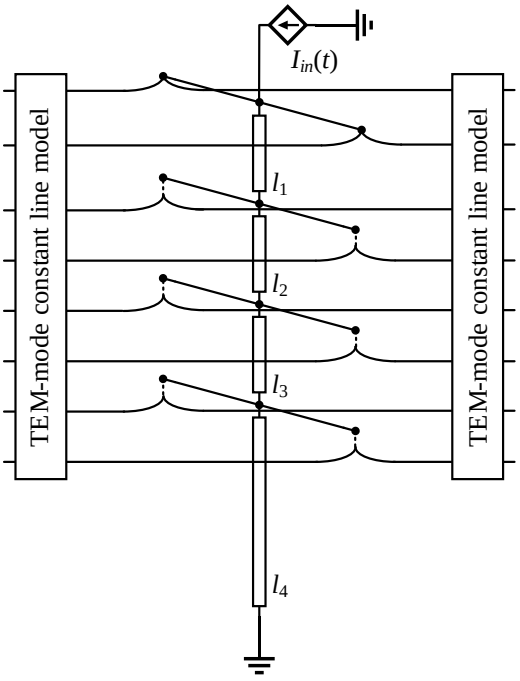

Fig. 2.4 Circuit model of a simple TEM-assumed transmission tower and line model.

The transmission line was represented by a lossless multiphase transmission line model. The self and mutual surge impedances of the line were given by the basic formula assuming infinitely long lossless lines above a perfectly conducting ground [1]. The four-bundled phase conductor was represented by a single-phase conductor using the GMD as was done in the FDTD analysis. The lossless line was selected following the assumption employed in the FDTD method.

The current, given in (1), was injected into the top of the tower by an ideal current source. The tower grounding impedance was set to 0 Ω since the perfectly conducting ground was assumed in this analysis. The wave propagation speed along the tower, vel_T, was set to the speed of light in free space, c_0. Table 2.2 summarizes the circuit parameters. The table shows the surge impedance of the transmission line seen from the tower: the combined surge impedance of the OHGWs Z_{gw} and the combined mutual surge impedance between the OHGWs and phase conductors, Z_{mU}, Z_{mM}, and Z_{mL}. These

impedances can be directly used for discussing the step-like current response of the lightning-struck tower and line. Table 2.3 shows the surge impedance matrix of the studied transmission line.

Table 2.2 Parameters of a transmission tower and line for circuit analysis method using the basic models.

Combined surge impedance of OHGWs, Z_{gw}	173 Ω
Combined mutual surge impedance between OHGWs and phase conductors, Z_{mU}, Z_{mM}, Z_{mL}	67.1 Ω 50.0 Ω 37.1 Ω
Tower surge impedance, Z_T	202 Ω
Tower footing impedance, Z_{gr}	0 Ω
Wave propagation speed, vel_T	300 m/μs

Table 2.3 Surge impedance of the studied transmission line in ohm.

	G1	G2	U1	M1	L1	U2	M2	L2
G1	577	114	155	109	79.1	114	91.1	69.4
G2	114	577	114	91.1	69.4	155	109	79.1
U1	155	114	349	144	96.3	131	110	83.2
M1	109	91.1	144	338	131	110	113	93.7
L1	79.1	69.4	96.3	131	324	83.2	93.7	93.3
U2	114	155	131	110	83.2	349	144	96.3
M2	91.1	109	110	113	93.7	144	338	131
L2	69.4	79.1	83.2	93.7	93.3	96.3	131	324

The combined surge impedance is derived by taking the following impedance as an example: the surge impedance of the OHGWs and the mutual surge impedance between the OHGWs and the upper phase conductor in the first circuit. The OHGWs voltages, V_{G1}, V_{G2}, and the upper-phase conductor voltage, V_{U1}, can be derived by each current I_{G1}, I_{G2}, I_{U1}, and the surge impedance $[Z_0]$ as:

$$\begin{pmatrix} V_{G1} \\ V_{G2} \\ V_{U1} \end{pmatrix} = \begin{bmatrix} Z_{011} & Z_{012} & Z_{013} \\ Z_{012} & Z_{011} & Z_{023} \\ Z_{013} & Z_{023} & Z_{033} \end{bmatrix} \begin{pmatrix} I_{G1} \\ I_{G2} \\ I_{U1} \end{pmatrix}, \qquad (V_{or}) = [Z_0](I_{or}). \tag{2.2}$$

Since the OHGWs are short-circuited by the transmission tower, the voltages V_{G1} and V_{G2} are identical, and hence the following relations can be derived:

$$\begin{pmatrix} V_{G1} \\ V_{G2} \\ V_{U1} \end{pmatrix} = \begin{bmatrix} 1 & 0 \\ 1 & 0 \\ 0 & 1 \end{bmatrix} \begin{pmatrix} V_{G12} \\ V_{U1} \end{pmatrix} = [K](V_{com}), \tag{2.3}$$

$$\begin{pmatrix} I_{G12} \\ I_{U1} \end{pmatrix} = (I_{com}) = \begin{bmatrix} 1 & 1 & 0 \\ 0 & 0 & 1 \end{bmatrix} \begin{pmatrix} I_{G1} \\ I_{G2} \\ I_{U1} \end{pmatrix} = [K]^T \begin{pmatrix} I_{G1} \\ I_{G2} \\ I_{U1} \end{pmatrix}, \tag{2.4}$$

where $[K]^T$ is the transpose of the matrix $[K]$. The surface impedance matrix is reduced and each impedance is combined by substituting (2.3) and (2.4) into (2.2).

$$\begin{aligned}(V_{com}) &= [K]^{-1}[Z_0]\left([K]^t\right)^{-1}(I_{com}) \\ &= [Z_{0com}](I_{com}),\end{aligned} \tag{2.5}$$

$$\text{where } [Z_{0com}] = \begin{bmatrix} \dfrac{Z_{011}+Z_{012}}{2} & \dfrac{Z_{013}+Z_{023}}{2} \\ \dfrac{Z_{013}+Z_{023}}{2} & Z_{033} \end{bmatrix}.$$

Finally, the combined surface impedance of the OHGWs and the combined mutual surface impedance between the OHGWs and the upper-phase conductor are derived by considering that there are parallel two OHGWs and vertical double-circuit transmission lines seen from the tower:

$$Z_{gw} = \frac{1}{2}\frac{Z_{011}+Z_{012}}{2}, \tag{2.6}$$

$$Z_{mU} = \frac{1}{2}\frac{Z_{012}+Z_{023}}{2}. \tag{2.7}$$

Other combined mutual surface impedances shown in Table 2.2 can be derived in the same manner and utilized for discussing the tower and line responses by a traveling wave theory based on the TEM mode.

2.1.3 Discussions on tower and line characteristics

A TEM and non-TEM characteristics

This section discusses transient characteristics of the lightning-struck transmission tower and line computed by the FDTD method and the TEM-assumed simple circuit analysis model. The discussed case is the lightning strike to the center of the tower top. The discussions in this section clarify the following non-TEM characteristics of the lightning-struck tower and line: 1) gradual rise of the tower surface impedance with time, 2) gradual rise of the self and mutual surface impedance of transmission line with time and time delay of mutual coupling among the lines corresponding to their separation distances, and 3) significant attenuation of traveling waves along the tower.

Following three significant differences between the waveforms computed by the FDTD method and the simple circuit model are observed from Fig. 2.5,

(i) Rise times of the voltages of the tower top and phase conductors and those across the insulator strings;
(ii) Initial undershoot and height-dependence of peaks of voltages across insulator strings;
(iii) Decay of the voltages and the ground wire current and increase of the tower top current after the arrival of ground reflection.

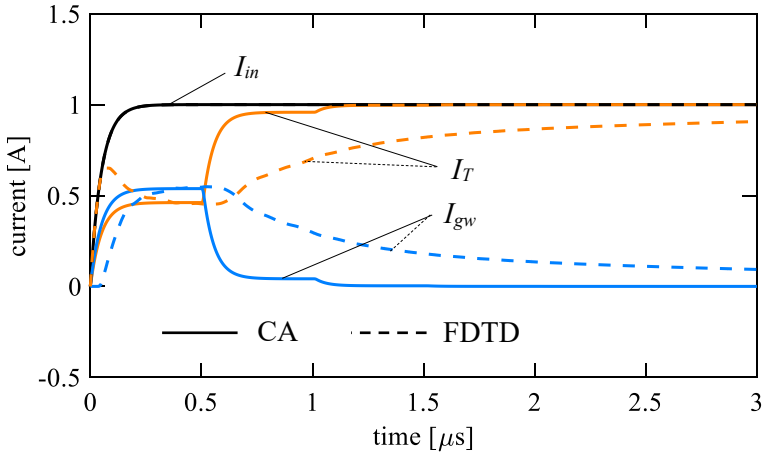

(a) Current

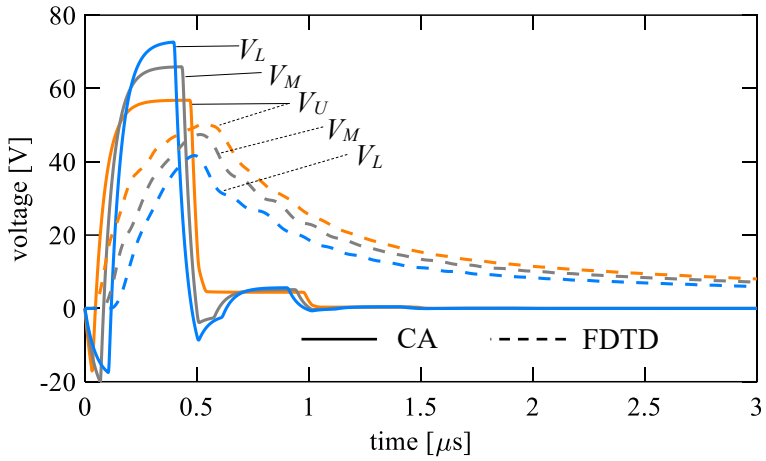

(b) Insulator voltage

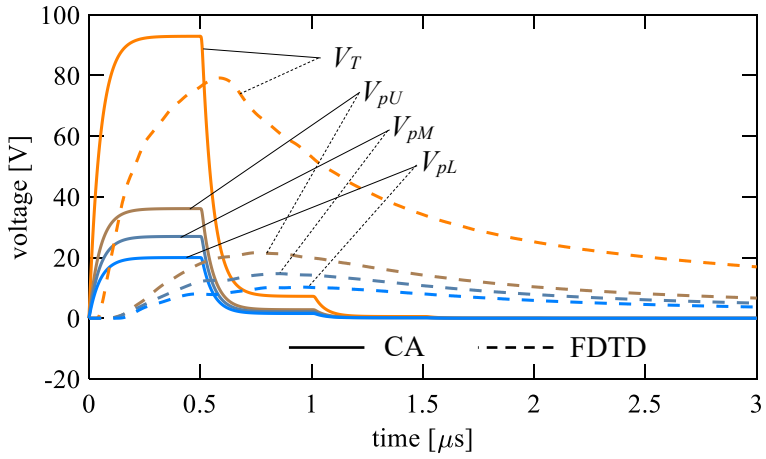

(c) Voltage of the tower top and phase conductors

Fig. 2.5 Step-like current responses of the 76-m high transmission tower computed with the FDTD method and a TEM-assumed simple circuit analysis (CA) model, in case the lightning strikes the center of the tower top.

The difference (i) shows that the surge impedance of the tower and lines struck by lightning has a gradually rising characteristic. The voltages shown in Fig. 2.5 (c) computed by the circuit analysis method have the same rise time as the injected current. The same rise time is observed because the distributed-parameter lines with the constant surge impedance represent the tower and lines in the TEM-mode assumption. The traveling wave theory based on the TEM-mode propagation provides the tower top voltage V_T until the arrival of ground reflections as

$$V_T(t) = \frac{Z_T Z_{gw}}{Z_T + Z_{gw}} I_{in}(t). \tag{2.8}$$

On the other hand, the voltages derived by the FDTD method have a longer rise time. The slowly-rising voltage characteristic can be explained by the spherical expansion of the electromagnetic field with time from the lightning attached point (center of the tower top in the present analysis case). The surge impedance of the tower and the self-surge impedance of the transmission lines do not converge to TEM-mode values at least until the reflections from the ground return to the tower top or each conductor. As shown in Fig. 2.5 (a), the surge impedance of the tower and the OHGWs seem to have almost the same time-dependence since the splitting ratio of the tower top and ground wire current, I_T and I_{gw}, is almost constant until the reflections from the ground arrive at the tower top (around 0.5 μs).

$$I_T(t) = \frac{1}{1 + Z_T / Z_{gw}} I_{in}(t), \tag{2.9}$$

$$I_{gw}(t) = \frac{1}{1 + Z_{gw} / Z_T} I_{in}(t). \tag{2.10}$$

The gradually rising tower surge impedance with time can be derived based on the electromagnetic field theory [15]–[19]. The theory and the derived surge impedance will be discussed in Section 2.2. The gradual rise of the tower surge impedance has been observed in surge experiments using actual towers [20]–[22] and scale models [23]. The gradual rise of horizontal conductor surge impedance has been shown in [24] based on a small-scale experiment. The transmission tower and line circuit models should consider the gradually rising characteristic of the tower surge impedance and the self-surge impedance of the transmission line.

The difference (ii) shows that the mutual coupling among transmission lines has gradually rising characteristics, and they are generated with time delays corresponding to their separation distances. Fig. 2.5 (b) shows that the voltage across the insulator strings at the upper phase is the lowest and is the highest in the lower phase ($V_U < V_M < V_L$, where V_U, V_M, and V_L are upper-, middle-, and lower-phase insulator voltages, respectively) in the circuit analysis. In contrast, in the FDTD analysis, the opposite order is obtained ($V_U > V_M > V_L$). The voltages computed by the circuit analysis also show an initial undershoot. In the circuit analysis, the voltages at each arm are the same ($V_{AU} = V_{AM} = V_{AL}$, where V_{AU}, V_{AM}, V_{AL} are voltages of upper-, middle-, lower-phase cross-arm, respectively) at which the voltages

attain their peaks. Besides, in the circuit analysis, the mutual surge impedance between the OHGWs and upper-phase conductor is the highest, and that between the OHGWs and lower-phase conductor is the lowest ($Z_{mU} > Z_{mM} > Z_{mL}$, where Z_{mU}, Z_{mM}, Z_{mL} are mutual-surge impedance between the OHGWs and upper-, middle-, lower-phase conductors, respectively) because of the TEM-mode assumption (see Table 2.2 for the specific impedances). The mutual couplings among lines are generated simultaneously. As a result, as shown in Fig. 2.5 (b), voltages across insulator strings have the initial undershoot and become the highest in the lower phase and the lowest in the upper phase. For instance, the traveling wave theory based on the TEM-mode propagation gives the upper-phase insulator voltage until the arrival of reflection from the ground as

$$\begin{aligned} V_U(t) &= V_{AU}(t) - V_{pU}(t) \\ &= Z_T I_T\left(t - l_1/c_0\right) - Z_{mU} I_{gw}(t), \end{aligned} \tag{2.11}$$

where l_1 denotes the length from the tower top to the upper phase cross-arm, note that the attenuation of the downward traveling voltage is not considered here. The initial undershoot seems not to affect the lightning surge analysis results as long as the voltages peaks are computed with sufficient accuracy. However, this anti-logical characteristic can significantly affect the analysis of an extremely high-speed phenomenon, such as the multiphase BFOs. In the FDTD-computed results, the mutual coupling between the OHGWs and phase conductors are initially lower than those derived in the TEM-mode assumption (see voltages of upper to lower phase conductors, V_{pU}, V_{pM}, and V_{pL}, in Fig. 2.5 (c)), and they are generated with time delays corresponding to the separation distances.

The height-dependent voltages across the insulator strings and the initially low mutual coupling characteristic have been reported in literature, from experimental results using an actual tower [20] and computational results by NEA methods including the MoM and the FDTD method [6], [25], [26]. The time delay in mutual coupling definitely occurs since the lines are spatially separated. The circuit analysis model of the transmission line should consider the gradually rising mutual surge impedances and the time delays corresponding to the separation distances of lines.

The difference (iii) shows the significant attenuation of the traveling waves along the transmission tower. In the FDTD analysis, the tower was put on a perfectly conducting plane to clarify the propagation characteristic of traveling waves along the tower. Following this assumption, the grounding impedance for the circuit analysis was set to zero. In the circuit analysis, the voltages, such as the tower top voltage, V_T, and voltages across insulator strings, V_U V_M, and V_L, quickly decay zero. The tower top current, I_T, is doubled quickly just after the arrival of the ground reflection owing to the zero-grounding impedance. For instance, the upper-phase insulator voltage after the arrival of the ground reflection and until reaching this reflection to the tower top is derived by the traveling wave theory based on the TEM-mode propagation as

$$\begin{aligned} V_U(t) &= V_{AU}(t) - V_{pU}(t) + V_{up}(t) \\ &= Z_T I_T(t - l_1/c_0) - Z_{mU} I_{gw}(t) + \exp\{-\alpha(2h - l_1)\}\theta_{gr} Z_T I_T(t - l_1/c_0 - (2h - l_1)/c_0) \\ &= Z_T I_T(t - l_1/c_0) - Z_{mU} I_{gw}(t) - Z_T I_T(t - l_1/c_0 - (2h - l_1)/c_0), \end{aligned} \quad (2.12)$$

where V_{up} is the upward traveling voltage along the tower, α is the attenuation constant and set zero in the present study, and θ_{gr} is the reflection coefficient at the tower base and –1 (the short-circuit condition can be applied to the tower base due to the zero-grounding impedance). However, in the FDTD analysis, the voltages gradually decay, and the tower top current gradually increases after the arrival of the ground reflection. In case the lightning current with a realistic wavefront, such as 1 μs and 2 μs or longer, is injected, the circuit analysis yields much lower voltages than those by the FDTD analysis due to the significant attenuation of traveling waves, as shown in Fig. 2.6.

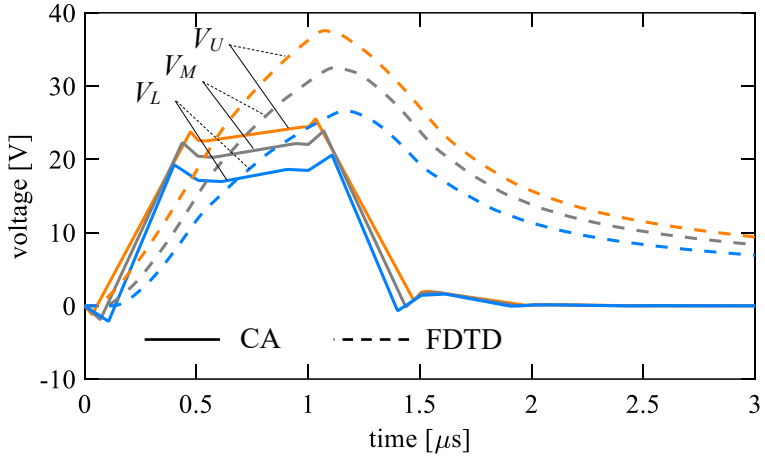

(a) 1-μs current responses

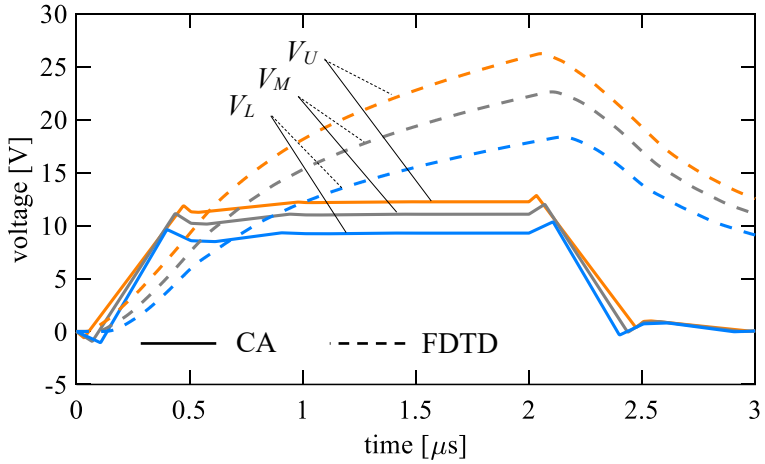

(b) 2-μs current responses

Fig. 2.6 1-μs and 2-μs linearly rising step-current responses of the 76-m high transmission tower insulator voltages computed with the FDTD method and a TEM-assumed simple circuit analysis (CA) model, in case the lightning strikes the center of the tower top.

These gradual decay of voltages and increase of currents were considered or interpreted to be caused by "apparently high grounding impedance," which was first identified in [27] by an experiment using a conical conductor. In this understanding, the reflection coefficient initially has a lower magnitude. However, the gradual decay of voltages is actually owing to the attenuation of (especially upward) traveling waves along a vertical object [28], [29]. From the theoretical viewpoint, therefore, the voltage decay should be represented by the wave attenuation characteristic as provided in (2.12), not by damping resistor-inductor parallel circuits [30], [31], by an inductive grounding impedance or controlled voltage sources for voltage adjustment [6], [25], [26], [32]. These representations adopted in existing tower models are overviewed in Section 2.2. The circuit analysis model should consider the significant attenuation characteristic along the transmission tower by the propagation characteristic.

Comparisons between the FDTD analysis results and those derived by circuit analysis using the basic TEM-mode model and discussions on them have revealed that a circuit model of a transmission tower and line should incorporate:

(i) The gradual rise of the tower surge impedance with time;
(ii) The gradual rise of the self and mutual surge impedances of transmission line with time, and the delay of the mutual couplings corresponding to the separation distances;
(iii) The significant wave attenuation along the transmission tower.

A circuit model of transmission towers and lines considering the above characteristics will be presented in the next chapter.

B Effect of lightning strike points

The effect of lightning strike points on the insulator voltages is discussed in this section. The insulator voltage of the lightning-struck side circuit becomes higher than those of the other side circuit due to the electromagnetic shielding by the tower and the further distances.

The FDTD analysis was performed considering a lightning strike to (a) the center of the tower top and (b) the ground-wire cross-arm of the second circuit. In these analyses, lightning currents having constant rising-time of 1 μs and 2 μs, which have been used in lightning protection designs, were injected. Fig. 2.2 illustrated the lightning strike point. The FDTD analysis computed the voltages across insulator strings at both sides of the line.

If lightning strikes the center of the tower top, insulator voltages on both sides are identical as expected (see Fig. 2.7 (a)). On the other hand, when lightning strikes the ground-wire cross-arm, higher voltages are generated across insulators located on the lightning struck-side (see Fig. 2.7 (b)). Table 2.4 summarizes the peak voltages of the insulators in case lightning strikes the ground-wire cross-arm of the second circuit. The maximum difference between the voltages of the struck side and the other side is 6.6%. This difference is not so significant but can affect the BFO phase. In [33], it has been shown that the 2% variation of the FO voltage can result in the BFOs in different phases. Note that the

magnitude of the voltage across the insulator when the rise time of the lightning is 2 μs is lower than that of 1 μs since the surge impedance of the transmission tower and line just after the lightning has time-dependent characteristics.

The voltage difference is further discussed by the electric field distribution. Fig. 2.8 shows the distribution of electric field strength in the *x*-*z* plane of the FDTD analysis space generated by the 1-μs rising current at a time of 0.16 μs after the current injection. If lightning strikes the center of the tower top (Fig. 2.8 (a)), the electric field propagates symmetrically. In contrast, when lightning strikes the ground-wire cross-arm of the second circuit (Fig. 2.8 (b)), the electric field is more intense on the struck-side, and the field is weakened on the other side due to the shielding effect by the tower body and farther distances. This difference in the spatial distribution of the electric field results in the difference in the insulator voltages shown in Fig. 2.7. The circuit analysis model of the tower with cross-arms, which can

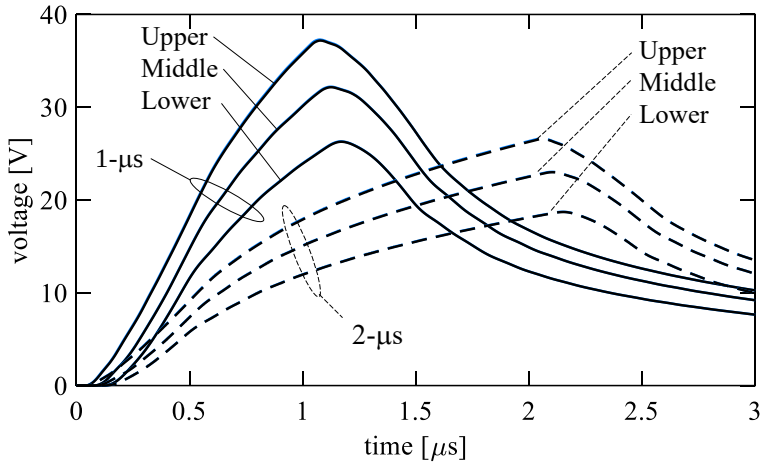

(a) A lightning strike to the center of the tower top
(voltages of strike side and the other side are overlapped).

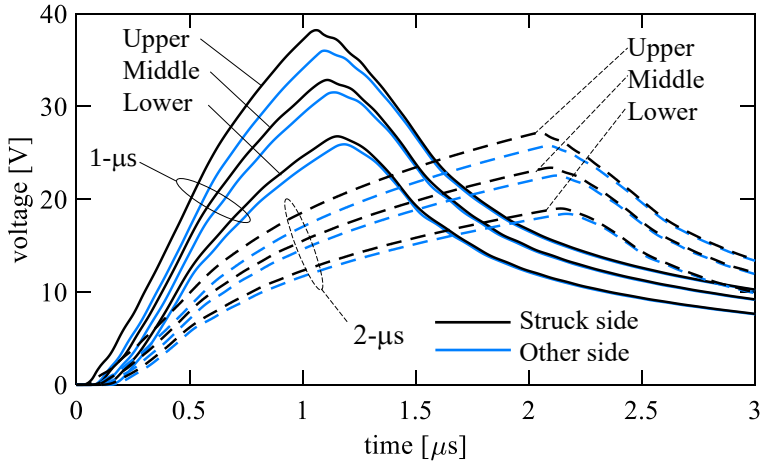

(b) A lightning strike to the tip of the ground-wire cross-arm.

Fig. 2.7 Insulator voltages generated by a lightning strike to the center of the tower top and the tip of the ground-wire cross-arm.

Table 2.4 Insulator voltages generated by a lightning strike to the ground-wire cross-arm of the second circuit with lightning currents having a rise time of 1 μs or 2 μs.

Rise time of current	Phase	Struck side [V]	Other side [V]	Difference, %
1 μs	Upper	37.7	35.2	6.6
	Middle	32.2	30.7	4.4
	Lower	26.3	25.4	3.6
2 μs	Upper	26.9	25.3	5.6
	Middle	23.0	22.1	3.9
	Lower	18.7	18.1	3.3

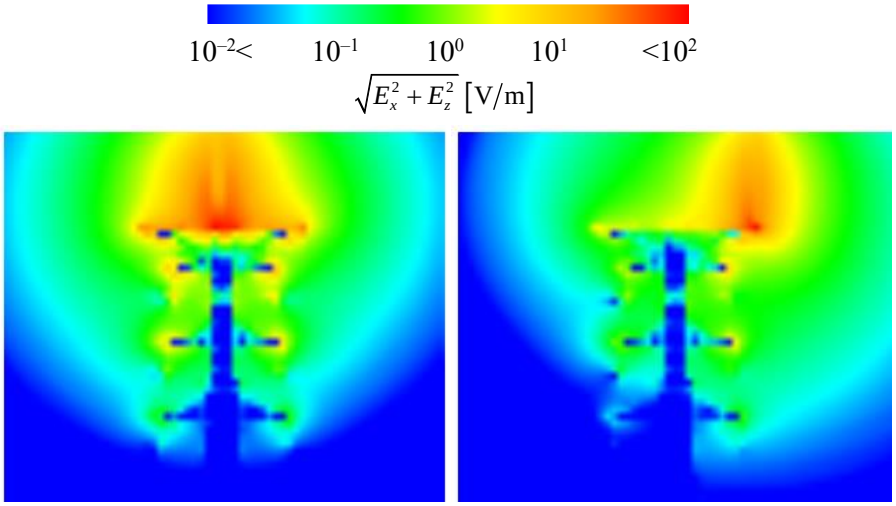

(a) Center of the tower top (b) Tip of ground-wire cross-arm

Fig. 2.8 FDTD-computed distribution of the electric field strength on an *x*-*z* plane around the tower at t = 0.16 μs generated by the 1-A peak current.

equivalently represent these asymmetrical insulator voltages initiated by the spatial distribution of the electric field, can further enhance the validity of the circuit analysis in discussing lightning surges.

2.1.4 Requirements for circuit analysis model

The differences between the TEM and non-TEM characteristics of the lightning-struck transmission tower and line have been discussed. The characteristics of the transmission tower and lines, which a new circuit analysis model of them should incorporate, are summarized as follows: 1) the tower surge impedance should have the gradually rising characteristic with time, 2) the self and mutual surge impedance of the transmission line should have the gradually rising characteristic with time, and the mutual coupling among the lines should have time delays corresponding to their separation distances, and 3) the traveling wave along the tower should attenuate significantly. A model considering the above three characteristics can represent the non-TEM characteristics, i.e., dynamic electromagnetic characteristics, and the resultant insulator voltages in the circuit analysis. In addition, the insulator

voltages on one side of the tower can be different from those on the other side depending on the lightning-struck point. A circuit model that can represent these voltage differences can further enhance the accuracy and usefulness of the circuit analysis method.

2.2 Overview of Existing Transmission Tower Models

This section overviews various kinds of transmission tower models presented as of today from the viewpoint of the inclusion of the non-TEM characteristics. Comparative studies of some of the models within the circuit analysis were performed in, e.g., [34], [35]. The transmission tower models can be categorized into six: 1) simplified models based on the surge impedances derived by the distributed-parameter line theory, electromagnetic field theory, or surge experimental results, 2) a multistory tower model, 3) a multi-section distributed line model, 4) models based on the numerical electromagnetic analysis, 5) frequency-dependent line models, and 6) non-uniform line models. Based on these models, insulator voltages of the lightning-struck transmission tower and line have been analyzed.

In this section, "tower models" are overviewed because the modeling of a transmission tower or a vertical conductor has been the primary interest of the research. The reason is that the per unit length parameters cannot be calculated for vertical conductors, while the TEM-mode assumption provides those for horizontal transmission lines. Nevertheless, the lightning-struck transmission lines can perform differently from those assumed in the TEM mode, as discussed in the previous section.

2.2.1 Simplified model

The simplified models include the lossless line model and the distortion-less model. The models are simple and can be easily implemented in EMT simulators. However, they neglect any non-TEM characteristic and resultant complicated insulator voltages of a lightning-struck tower.

Fig. 2.9 illustrates the simplified transmission tower model. In deriving the surge impedances for the simplified model, the transmission tower is usually approximated to be a cylinder with height h and radius r or a cone with height h and base radius r. The distortion-less model considers the loss of the traveling waves along the tower by introducing the attenuation constant. The surge impedance of these models is derived based on the distributed-parameter line theory [14], [36], electromagnetic field theory [15]–[19], or empirical formula derived based on surge experiments [23], as reviewed later. The typical surge impedance of a vertical double-circuit transmission tower ranges from 100 Ω to 300 Ω. The typical value of the attenuation constant in the distortion-less model ranges from 0.7 to 0.9. The wave propagation speed is set to the speed of light in free space, c_0, or around 70% and 80% of c_0.

Two types of surge impedances have been derived based on the distributed-parameter line theory. Here a vertical cylinder located above a perfectly conducting plane is discussed. The image vertical cylinder below the plane is estimated by the image theory, and the mutual inductance between the real and image cylinders is calculated by Neumann's formula. Based on the relation between the mutual

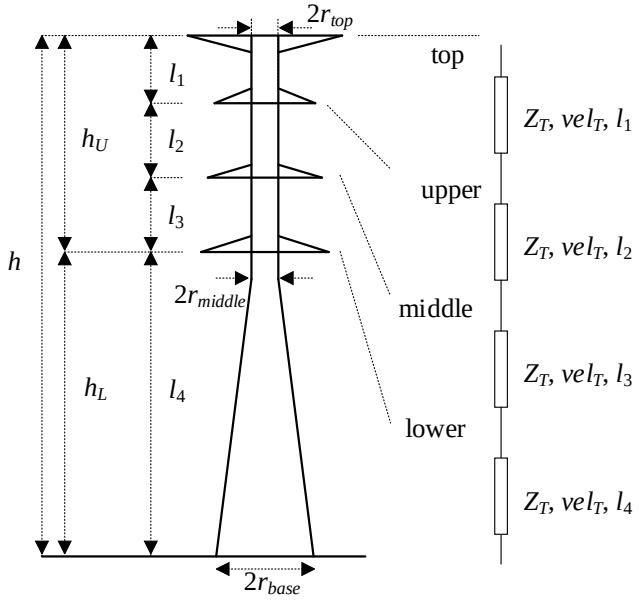

Fig. 2.9 Simplified transmission tower model.

inductance and speed of light in free space, the following surge impedances have been calculated:

$$Z_J = 60\left\{\ln\left(\frac{h}{r}\right)-1\right\} \tag{2.13}$$

$$Z_{MJ} = 60\left\{\ln\left(\frac{4h}{r}\right)-1\right\} \tag{2.14}$$

where $h >> r$ is assumed in these formulae. The equation (2.13) is mentioned as Jordan's formula [36] and (2.14) is mentioned as the modified Jordan's formula [14]. The equation (2.13) is derived by assuming the real and image current have the opposite direction, while (2.14) is derived by assuming they have the same direction. In [37], the frequency-dependent characteristic impedance has been presented based on the opposite direction currents by considering the earth return impedance using the complex penetration depth [38].

Several surge impedances for towers have been presented based on the electromagnetic field theory approach. In the electromagnetic field theory approach, step, ramp, or other current responses of the equivalent cylinder or cone are calculated theoretically in the time domain. Then the peak voltage observed at a round trip time, $t = 2h/c_0$, is mentioned as the surge impedance and implemented in the circuit analysis. Note that the surge impedance of the cylinder is time-dependent, but the surge impedance of the cone is time-independent because the spherical TEM-wave is generated in the cone case. Surge impedance formulae (2.15) and (2.16) are derived from the electromagnetic field theory based on the step- and ramp-current responses of a cylinder, respectively [16]:

$$Z_{Ws}(t) = 60\ln\left(\frac{\sqrt{2}c_0 t}{r}\right), \qquad Z_{Ws} = Z_{Ws}\left(\frac{2h}{c_0}\right) = 60\ln\left(\frac{2\sqrt{2}h}{r}\right), \tag{2.15}$$

$$Z_{Wr}(t) = 60\left\{\ln\left(\frac{\sqrt{2}c_0 t}{r}\right) - 1\right\}, Z_{Wr} = Z_{Wr}\left(\frac{2h}{c_0}\right) = 60\left\{\ln\left(\frac{2\sqrt{2}h}{r}\right) - 1\right\}. \tag{2.16}$$

Surge impedance formulae (2.17) and (2.18) are derived assuming the tower as a cone:

$$Z_S = 60\ln\left(\sqrt{2}\frac{\sqrt{h^2 + r^2}}{r}\right), \tag{2.17}$$

$$Z_C = 60\ln\left\{\cot\frac{1}{2}\arctan\left(\frac{r}{h}\right)\right\}. \tag{2.18}$$

A lightning strike to a conical conductor is assumed in (2.17) [17]. The surge impedance given by (2.18) is one-half of the impedance of a biconical antenna. This impedance is used because the lightning strike to the mid-span of the OHGWs and resultant surge intrusion into transmission towers can be interpreted as the current injection into an inverted cone [39]. A weighted-average equivalent radius, r_{eq}, of the transmission tower given by the following is sometimes utilized in the above-introduced formulae:

$$r_{eq} = \frac{r_{top}h_U + r_{middle}h + r_{base}h_L}{2h}. \tag{2.19}$$

The definitions of the above parameters are found in Fig. 2.9.

The following is the empirical formula of the surge impedance of cylinder derived in [23]:

$$Z_H = 60\left\{\ln\left(\frac{2\sqrt{2}h}{r}\right) - 2\right\}. \tag{2.20}$$

The empirical formula has been derived based on the step current responses of cylinders with various heights and radii. This formula can be interpreted as the modification of (2.16). Note that this empirical formula has been extended to the tower model by multi-section distributed lines introduced later.

Among the above surge impedance formulae, (2.18) has been recommended in the CIGRE guide for lightning protection [40]. The formulae (2.13) and (2.20) can reproduce various surge experimental results performed by cylinders with slight differences, while other equations generally provide higher impedances or voltages [41]. Note that considering the time-dependence of a vertical object, the surge impedance measured in experiments at a round-trip propagation time, $t = 2h/c_0$, can be smaller than the convergence value of an actual surge impedance. At the same time, the tower surge impedance depends on the definition of the tower voltage, though the insulator voltage can be defined uniquely [42].

2.2.2 Multistory transmission tower model

The multistory transmission tower model was developed based on the surge experiment performed by a 62.8-m high 500-kV transmission tower [30]. The model comprises constant lossless distributed-parameter lines and damping resistor-inductor parallel circuits, as shown in Fig. 2.10. The multistory tower model has been applied to transient analyses with TEM-mode-based transmission line models, namely, a constant line model or a frequency-dependent line model. The resistor-inductor damping circuits of the multistory model roughly represent the wave attenuation characteristics along the tower. The model does not consider the gradual rise of the tower surge impedance. In addition, the gradual rise of the self and mutual surge impedances a transmission line is not considered since the TEM-mode line model represents the transmission line. The model parameters, such as the tower surge impedance and resistor-inductor damping circuits, were determined to reproduce the measured insulator voltages by the multistory tower model connected with the transmission line model represented by Semlyen's frequency-dependent line [43]. In the experiment, a step-like current or current with 3 μs of wavefront was injected into the tower top via a coaxial cable.

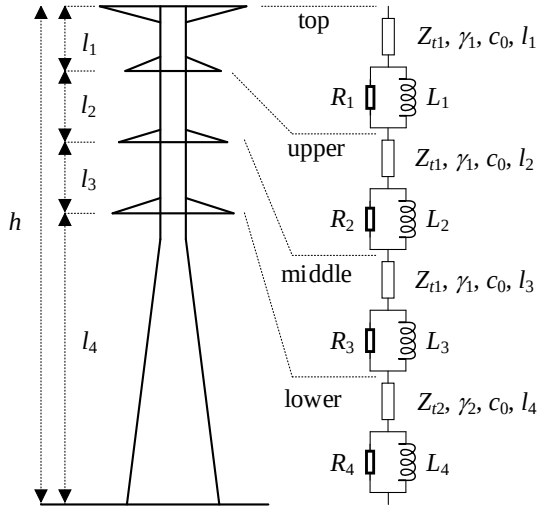

Fig. 2.10 Multistory transmission tower model.

Thanks to its ease of use and relatively high accuracy compared to the other models, the multistory tower model has become one of the most frequently and widely used transmission tower models for analyzing vertical double-circuit towers as of today. Japanese guidelines for calculating the lightning fault rate and performing the insulation design have adopted this model [44]–[46].

The parameters of the multistory tower model are determined as follows for reproducing the surge experiment performed using an actual 500-kV tower as mentioned above. The surge impedance Z_{T1} and Z_{T2} are set to 220 Ω and 150 Ω, respectively. The following formulae determine the resistance R_n and inductance L_n depending on the length of each section l_n:

$$R_{1-3} = R_{u1} \times l_{1-3},\ R_4 = R_{u2} \times l_4,$$
$$L_n = R_n \times \tau = R_n \times \frac{2h}{c_0}, \tag{2.21}$$

where

$$R_{u1} = -2 \times Z_{T1} \times \frac{\ln(\gamma_1)}{l_1 + l_2 + l_3},\ R_{u2} = -2 \times Z_{T2} \times \frac{\ln(\gamma_2)}{l_4}, \tag{2.22}$$
$$\gamma = \gamma_1 \times \gamma_2 = 0.8,\ \gamma_1 = \gamma_2 = \sqrt{0.8}.$$

Strictly speaking, the original parameters of the multistory tower model cannot be applied to other towers. Applying the model to the specific tower requires a trial-and-error determination of the parameters by referencing the tower's characteristics. For the 140-m high ultra-high voltage (UHV) tower model, the parameters have been tuned to $Z_{T1} = Z_{T2} = 120\ \Omega$, and the attenuation coefficient $\gamma = 0.7$ based on the surge experiment [20]. However, for other towers, the parameter for the 500-kV tower has been generally used without confirmation. Need for confirmation to analyze other towers than the referenced towers and insufficiency for analyzing an HV transmission tower have been pointed out [1], [45]. Recently, adjustment of the model parameters based on the NEA method has been proposed [31]. In this model, the surge impedance of the tower is computed by the conical approximation, and each inductance is determined to reproduce the FDTD-computed voltage peaks by a trial-and-error process. This adjusted model can reproduce the FDTD-computed voltages, but the basic feature regarding the inclusion of the non-TEM characteristics is the same as that of the original multistory tower model.

2.2.3 Multi-section distributed line model

The multi-section distributed line model of a transmission tower was developed based on the empirical formula of the surge impedance [23], [47]. The model reproduced a step-current response of an actual 500-kV transmission tower without overhead transmission lines. In this model, the transmission tower is represented by the main leg part model, bracing part model, and cross-arm part model, as shown in Fig. 2.11. The model parameters can be derived from the configuration of the tower. Hence, this model has been applied to several lightning surge analyses (but ignoring the basic assumption of the original model in some cases: applicable to vertical double-circuit transmission towers typically used in Japan). However, this model does not consider the non-TEM characteristics of the lightning-struck tower.

The following empirical formula provides the surge impedance of the main leg part model:

$$Z_{tk} = 60\left\{\ln\left(\frac{2\sqrt{2}h_k}{r_{ek}}\right) - 2\right\}\ (k = 1...4),$$
$$\text{where } r_{ek} = \begin{cases} 2^{1/8}\left(r_{tk}^{1/3} r_b'^{2/3}\right)^{1/4}\left(d_{tk}^{1/3} d_b'^{2/3}\right)^{3/4} & (k = 1, 2, 3) \\ 2^{1/8}\left(r_{tk}^{1/3} r_b^{2/3}\right)^{1/4}\left(d_{tk}^{1/3} d_b^{2/3}\right)^{3/4} & (k = 4). \end{cases} \tag{2.23}$$

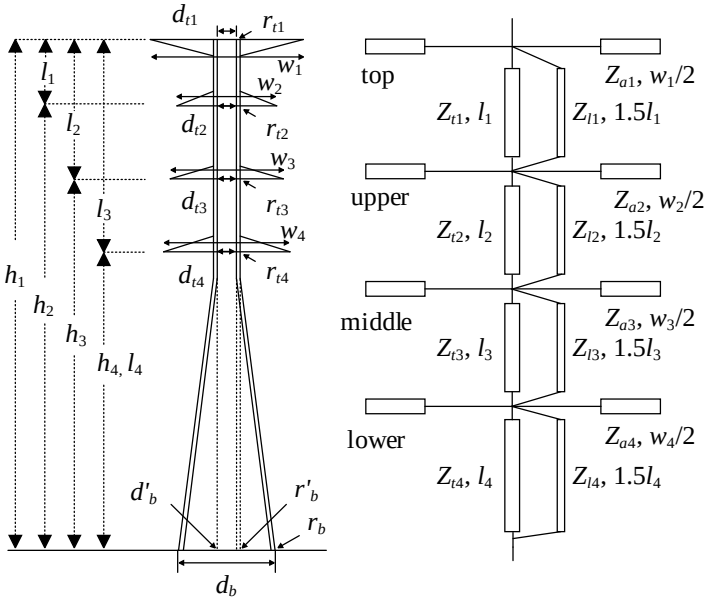

Fig. 2.11 Tower model by multi-section distributed lines.

The surge impedance formula (2.23) is an extension of (2.20), which is for the calculation of the cylinder surge impedance. The definitions of r_{tk}, r_b, r'_b, d_{tk}, d_b, and d'_b are provided in Fig. 2.11. The surge impedance of the bracing is given by

$$Z_{lk} = 9Z_{tk}. \tag{2.24}$$

The length of each bracing model is set 1.5 times longer than that of the corresponding main leg part to consider the effect of bracings. The authors noted that these formulae can be applied to standard vertical double-circuit transmission towers typically used in Japan. The surge impedance of the cross-arm part is given by

$$Z_{ak} = 60\ln\frac{2h_k}{r} \quad (k = 1...4), \tag{2.25}$$

where r_{ak} is one-fourth of the length of the junction of cross-arm and tower central part.

The model parameters of the multi-section distributed line model can be determined directly from the tower shape as shown by (2.23)–(2.25), not by referencing the experimental voltages. Besides, the multi-section distributed line model is the only model that can explicitly consider the presence of the tower cross-arms in widely used transmission tower models. Due to these reasons, the multi-section distributed line model has been applied to lightning surge analysis with towers having various shapes [48]–[50]. However, the model does not consider the non-TEM characteristic of the lightning-struck transmission tower since it is composed of the lossless constant distributed-parameter lines. The lower insulator voltages can be derived for lightning current with 1 μs or longer wavefront owing to the ignorance of the significant wave-attenuation characteristic. In addition, it should be noted that the

model is applicable to vertical double-circuit towers typically used in Japan because it is based on the experimental results for such towers.

2.2.4 Tower models based on the numerical electromagnetic analysis

Several tower models were proposed based on the numerical electromagnetic analysis results [6], [25], [26], [32]. In these models, the numerical electromagnetic analysis is performed for deriving voltages and currents at various points of the tower, and model parameters are determined to reproduce the numerical electromagnetic analysis results. The models partly consider the non-TEM characteristics of the lightning-struck tower and line, as mentioned later. However, the models have been rarely employed for practical lightning surge analysis because they require sophisticated modeling processes, such as the several times of numerical electromagnetic analysis, trial-and-error processes, and numerical convergence calculations. The models shown in Fig. 2.12 are briefly reviewed.

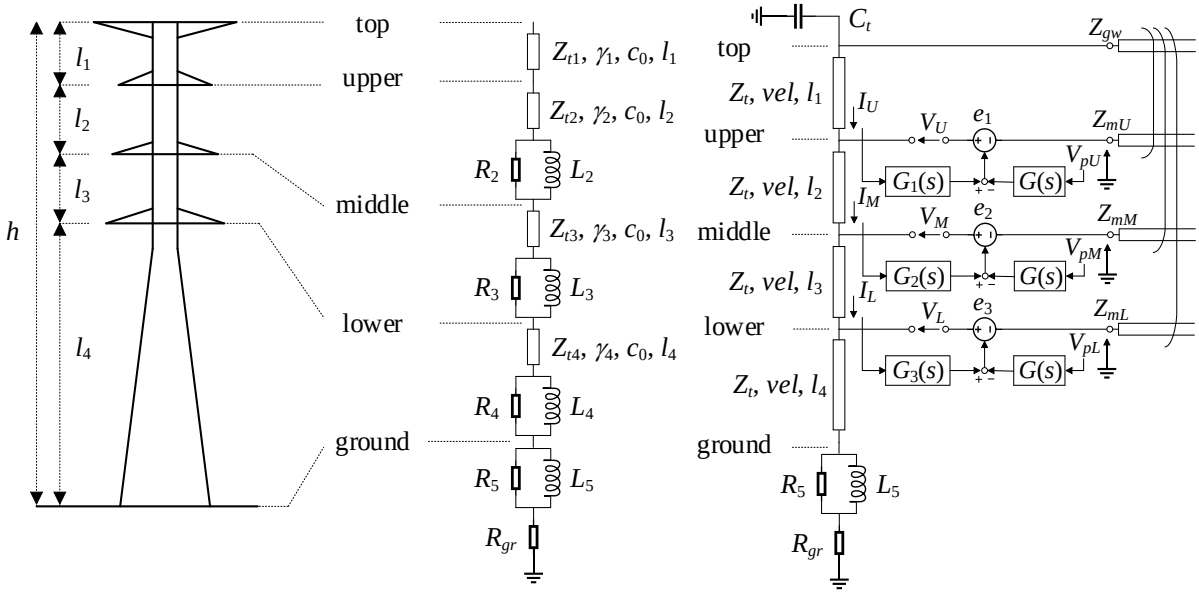

(a) Model tower (b) Modified multistory model (c) Model with controlled voltage sources

Fig. 2.12 Tower models based on the numerical electromagnetic analysis.

The modified multistory tower model [25], [26] shown in Fig. 2.12 is reviewed. This model approximately considers the wave attenuation characteristic along the tower and the initially lower mutual surge impedance between OHGWs and phase conductors. The modified model circuit is similar to the multistory tower model shown in Fig. 2.10. However, the modified model does not have the R_1L_1 parallel circuit between the tower top and upper-phase cross-arm. In addition, the model does have a tower footing model composed of an R_5L_5 parallel circuit and series-connected resistance R_{gr}.

In the modeling process, a step-current response of a transmission tower is calculated first with the MoM. The tower surge impedance Z_{t1} is determined based on the upper-phase insulator voltage and

mutual surge impedance between OHGWs and the upper-phase conductor. Then, the surge impedances Z_{t1}, Z_{t2}, and resistance R_2, R_3 are determined so that the model can reproduce the initially lower mutual coupling between OHGWs and phase conductors and resultant insulator voltages. The values of R_4, L_4, and R_5, L_5 are determined by a trial-and-error process for reproducing gradual decay of insulator voltages and initially high grounding impedance, respectively. It can be considered that these elements, R_4, L_4 and R_5, L_5, perform to approximately represent the significant wave attenuation along the tower. The inductance L_2 and L_3 are determined in the same manner as the multistory model (see (2.21)). As explained above, this model approximately represents the initially lower mutual surge impedances between the OHGWs and phase conductors and significant wave attenuation along the tower. The model was employed for the BFO analysis of a 500-kV transmission tower in [51].

The model with controlled voltage sources [6] shown in Fig. 2.12 (c) is reviewed. This model approximately considers the gradual rise of the tower surge impedance, initially low mutual surge impedances between the OHGWs and phase conductors, and the wave attenuation characteristic. The model requires the three cases of FDTD analysis and convergence calculation for determining circuit parameters, but the parameters can be derived systematically (no trial-and-error process is required).

The circuit parameters, except for the transfer functions, are determined based on the FDTD-computed voltages and current in the modeling process at first. The tower surge impedance Z_t, wave propagation speed *vel*, tower top capacitance C_t, and tower foot model composed of R_5L_5 parallel circuit and R_{gr}, are determined based on the step-like current response of the tower computed by the FDTD method. The FDTD analysis considers the imperfectly conducting soil and tower foundations. This computation of the step-like current response is the first case of the FDTD analysis. The tower surge impedance Z_t is derived based on the total surge impedance of OHGWs and the ratio of the FDTD-analyzed tower current and the OHGW current. The wave propagation speed of each tower section, *vel*, is determined based on the round-trip time of the traveling wave, tower height, and length of the tower top cross-arm. The tower top capacitance C_t is implemented for considering gradually rising tower surge impedance. The R_5L_5 parallel circuit is implemented for considering the initially high grounding impedance, as included in the modified multistory tower model. It can be considered that this *RL* parallel circuit performs to represent the significant wave attenuation along the tower approximately and at the same time the characteristics of the foundations.

The model parameters except for the transfer functions $G(s)$ and $G_k(s)$ have been determined by the above process. At this point, insulator voltages generated by 1-μs and 2-μs rising currents are calculated by the FDTD method (these are the second and third cases of the FDTD analysis) and circuit model without transfer functions. The model without the transfer functions roughly considers the gradually rising tower surge impedance and significant wave attenuation along the tower. However, the model cannot reproduce the FDTD-computed insulator voltages.

The transfer functions are introduced to reproduce the FDTD-computed insulator voltages. The transfer function, $G(s)$, is introduced at first. The input for this transfer function is each phase conductor voltage, V_{pU}, V_{pM}, and V_{pL}. The output suppresses the mutual coupling between the OHGWs and phase conductors:

$$G(s) = \frac{s\tau_g}{1 + s\tau_g}, \tag{2.26}$$

where s is the Laplace operator and τ_g is a time constant determined from the convergence characteristic of the tower current. At this point again, insulator voltages generated by 1-μs and 2-μs rising currents are calculated and compared with the FDTD-computed voltages. The circuit model at this stage is composed of lossless distributed line, lumped elements, and transfer function $G(s)$. This circuit roughly considers the gradually rising tower surge impedance by the tower top capacitance C_t, significant wave attenuation along the tower by the R_1L_1 parallel damping circuit, and gradually rising mutual coupling between OHGWs and phase conductors by the transfer function $G(s)$. However, the insulator voltages computed by this model still differ from those computed by the FDTD method. Therefore, the transfer functions $G_k(s)$ are finally introduced for eliminating the difference between the voltages computed by the circuit model and the FDTD method. The input for these transfer functions is the tower current at each cross-arm position, I_U, I_M, and I_L. The output adjusts the insulator voltages to reproduce the referenced voltages:

$$G_k(s) = \frac{\chi_k s^2}{(s+\alpha)(s+\beta_k)}. \tag{2.27}$$

In the determination of $G_k(s)$, numerical convergence calculations are performed.

The tower model with controlled voltage sources considers the non-TEM characteristics except for the time delays in mutual coupling among the transmission lines corresponding to their separation distances (strictly speaking, the model does not consider the gradual rise of self-surge impedances of transmission lines and the significant wave attenuation characteristic along the tower). The voltages computed by this model precisely reproduce those computed by the FDTD method. Despite such accuracy and the modeling process that uniquely determines the circuit parameters, the model has rarely been employed in practical lightning surge analysis. This is because it requires three cases of numerical electromagnetic analysis and a relatively sophisticated modeling process.

2.2.5 Frequency-dependent models and non-uniform line models

The frequency-dependent models were developed in [52]–[54], and the non-uniform models were developed in [55]–[60]. These models consider the gradual rise of the tower surge impedance with time and the wave propagation characteristic along the tower.

The frequency-dependent model of the tower presented in [52] was developed based on the results of the surge experiment performed by the 500-kV transmission tower, which was referenced in developing the multistory tower model. This model considers the significant attenuation characteristic of the traveling wave along the tower.

In the modeling, the step-current response of the tower top voltage is derived from the experimental results by using numerical Laplace transform. The tower surge impedance is determined as the constant value from the step-current response. The propagation characteristic along the tower is also determined based on the step current response considering the reflection of the traveling waves:

$$p(t) = 1 - \alpha_k \exp(-\beta_{k1} t) - (1 - \alpha_k) \exp(-\beta_{k2} t). \tag{2.28}$$

As described, this model requires reference voltages for deriving circuit parameters. This model was implemented into the ATP version of EMTP using Semlyen's frequency-dependent line model [43], and the wave attenuation characteristic along the tower is introduced in the circuit analysis. The model reproduced the voltages across insulators of the 500-kV tower. A tower model presented in this thesis represents a transmission tower using the frequency-dependent line since this representation is theoretically straightforward compared to the *RL* parallel circuit approach adopted in the multistory tower model and the models based on the numerical electromagnetic analysis introduced above.

The frequency-dependent non-uniform model in [53] is represented by the tower surge impedance Z_t and propagation constant $\alpha + j\beta$ given by

$$Z_t(s) = \frac{Z_d}{\left\{1 + \left(s\frac{4h}{c_0}\right)^m\right\}^n}, \alpha h = 10^{-k_1 + k_2 \ln|s|}, \beta = \frac{k_3 \omega h}{c_0}, \tag{2.29}$$

where s is the Laplace operator, and j is the imaginary number, $\sqrt{-1}$. The parameters Z_d, m, n, k_1, k_2, and k_3 are determined based on the step response of the tower: the model also requires reference voltages to determine circuit parameters. The model can be interfaced with EMT simulators by approximating (2.29) by rational functions. Though the model considers the gradual rise of the surge impedances and wave attenuation characteristics, it has not been applied to practical lightning surge analysis.

The frequency-dependent model presented in [54] is based on numerical electromagnetic analysis. The driving point admittance seen from the tower top is calculated by the MoM in the frequency domain at first. Then, the vector fitting technique [61] is applied to the admittance, and a rational function representing the tower is derived and interfaced with EMT simulators. Though the model considers the non-TEM characteristics of the tower as well as the tower footing characteristics, the insulator voltages cannot be evaluated.

Several non-uniform models presented in [55]–[60] are briefly reviewed. The model presented in [58] partly reproduced the measured insulator voltages of the transmission tower among the non-uniform models. The model presented in [55] comprises cascaded non-uniform lines whose surge impedance varies exponentially with distance. Transient responses can be derived by the numerical frequency transform, but the model cannot be interfaced with EMT simulators. In [56], the tower was represented with a lossless line whose surge impedances varying depending on the height. In [57], the tower was represented by a non-uniform line, including frequency-dependent loss. These models can be interfaced with EMT simulators. However, they cannot reproduce the order of the insulator voltages (voltage of upper-phase insulator is highest, and that of the lower-phase is lowest). The model presented in [58] adapted the non-uniform model presented in [55] to Bergeron's method [62]. Hence, this model can be interfaced with EMT simulators, and the model reproduced measured insulator voltages excepting the residual part. The models presented in [59] and [60] can consider the presence of the slanted part and cross-arms. The former reproduced the surge response of the scale model tower, and the latter reproduced the tower surge impedance without the overhead transmission lines.

2.3 Conclusions

The difference between the TEM and non-TEM characteristics of the lightning-struck transmission tower and line and resultant voltage characteristics have been discussed based on the FDTD analysis and circuit analysis based on the simplest tower and line models. The lightning-struck tower and line have the specific characteristics: 1) gradual rise of the tower surge impedance with time, 2) gradual rise of the self and mutual surge impedance of the transmission line with time and the time delays of mutual coupling among lines corresponding to their separation distances, and 3) significant wave attenuation characteristics along the tower. Besides, the insulator voltages of the lightning-strike side are up to 7% higher than those of the other side. The voltage difference is caused by the asymmetrical distributions of the electromagnetic field.

Several transmission tower models have been presented as of today. The models include simplified models with constant surge impedances, the multistory tower model, the multi-section distributed line model, the models based on electromagnetic analysis, the frequency-dependent models, and the non-uniform transmission line models. Some models partly consider the non-TEM characteristic of the lightning-struck tower. However, they require several times of numerical electromagnetic analyses, a trial-and-error process in parameter determination, and sophisticated modeling processes. The multistory tower model has long and widely been used owing to relatively high accuracy compared to the other models and simplicity (the model does not require the reference voltages to determine circuit parameters as long as using the fixed surge impedance). However, the model does not consider the non-TEM characteristics, and its applicability except for the referenced towers has not been confirmed.

Therefore, a new model, which can consider the non-TEM characteristics and can be quickly built from the tower and line configurations, will be presented in the next chapter.

References for Chapter 2

[1] A. Ametani, N. Nagaoka, Y. Baba, T. Ohno, and K. Yamabuki, *Power System Transients: Theory and Applications, Second Edition*. CRC Press, FL, USA, 2017.

[2] T. Noda, and S. Yokoyama, "Development of general surge analysis program based on the FDTD method," *Trans. IEE of Japan*, vol. 121-B, no. 5, pp. 625–632, May 2001.

[3] A. Tatematsu, "Overview of the three-dimensional FDTD-based surge simulation code VSTL REV" *in Proc. Asia-Pacific Int. Sym. on Electromagn. Compat.*, pp. 670–672, Shenzhen, China, May 2016.

[4] T. Noda, and S. Yokoyama, "Thin wire representation in finite difference time domain surge simulation," *IEEE Trans. Power Del.*, vol. 19, no. 3, pp. 840–847, Jul. 2002.

[5] J. Takami, T. Tsuboi, K. Yamamoto, S. Okabe, Y. Baba, and A. Ametani, "Lightning surge response of a double-circuit transmission tower with incoming lines to a substation through FDTD simulation," *IEEE Trans. Dielectr. Electr. Insul.*, vol. 21, no. 1, pp. 96–104, Feb. 2014.

[6] T. Noda, "A tower model for lightning overvoltage studies based on the result of an FDTD simulation," *Electr. Eng. Jpn.*, vol. 164, no. 1, pp. 8–20, Jan. 2008.

[7] T. Noda, "A numerical simulation of transient electromagnetic fields for obtaining the step response of a transmission tower using the FDTD method," *IEEE Trans. Power Del.*, vol. 23, no. 2, pp. 1262–1263, Apr. 2008.

[8] A. Tatematsu, and T. Ueda, "FDTD-based lightning surge simulation of an HV air-insulated substation with back-flashover phenomena," *IEEE Trans. Electromagn. Compat.*, vol. 58, no. 5, pp. 1549–1560, Oct. 2016.

[9] A. Tatematsu, S. Moriguchi, and T. Ueda, "Switching surge analysis of an EHV air-insulated substation using the 3-D FDTD method," *IEEE Trans. Power Del.*, vol. 33, no. 5, pp. 2324–2334, Oct. 2018.

[10] Z. P. Liao, H. L. Wong, B. P. Yang, and Y. F. Yuan, "A transmitting boundary for transient wave analysis," *Scientia Sinica,* vol. A27, no. 10, pp. 1063–1076, Oct. 1984.

[11] T. Noda, R. Yonezawa, S. Yokoyama, and Y. Takahashi, "Error in propagation velocity due to staircase approximation of an inclined thin wire in FDTD surge simulation," *IEEE Trans. Power Del.*, vol. 19, no. 4, pp. 1913–1918, Oct. 2004.

[12] Y. Taniguchi, Y. Baba, N. Nagaoka, and A. Ametani, "An improved thin wire representation for FDTD computations," *IEEE Trans. Antennas Propag.*, vol. 56, no. 10, pp. 3248–3252, Oct. 2008.

[13] Y. Baba, and V. A. Rakov, "On the transmission line model for lightning return stroke representation," *Geophys. Res. Lett.*, vol. 30, no. 24, 2294, pp. 13-1–13-4, Dec. 2003.

[14] A. De Conti, S. Visacro, A. Soares, Jr., M. A. O. Schroeder, "Revision, extension, and validation of Jordan's formula to calculate the surge impedance of vertical conductors," *IEEE Trans. Electromagn. Compat.*, vol. 48, no. 3, pp. 530–536, Aug. 2006.

[15] R. Lundholm, R. B. Finn, Jr., and W. S. Price, "Calculation of transmission line lightning voltages by field concepts," *AIEE Trans. Power App. Syst.*, vol. 77, pp. 1271–1283, Feb. 1958.

[16] C. F. Wagner, and A. R. Hileman, "A new approach to the calculation of the lightning performance of transmission lines III—a simplified method: stroke to tower," *AIEE Trans. Power App. Syst.*, vol. 79, pp. 589–603, Oct. 1960.

[17] M. A. Sargent, and M. Darveniza, "Tower surge impedance," *IEEE Trans. Power App. Syst.*, vol. PAS-88, no. 5, pp. 680–687, May 1969.

[18] H. Motoyama, and H. Matsubara, "Analytical and experimental study on surge response of transmission tower," *IEEE Trans. Power Del.*, vol. 15, no. 2, pp. 812–819, Apr. 2000.

[19] Y. Du, and Y. Ding, "Lightning surge propagation on a single conductor in free space," *IEEE Trans. Electromagn. Compat.*, vol. 59, no. 1, pp. 119-127, Feb. 2017.

[20] M. Kawai, "Studies of the surge response on a transmission line tower," *IEEE Trans. Power App. Syst.*, vol. PAS-83, no. 1, pp. 30–34, Jan. 1964.

[21] T. Yamada, A. Mochizuki, J. Sawada, E. Zaima, T. Kawamura, A. Ametani, M, Ishii, and S. Kato, "Experimental evaluation of a UHV tower model for lightning surge analysis," *IEEE Trans. Power Del.*, vol. 10, no. 1, pp. 393–402, Jan. 1995.

[22] H. Motoyama, Y. Kinoshita, K. Nonaka, and Y. Baba, "Experimental and analytical studies on lightning surge response of 500-kV transmission tower," *IEEE Trans. Power Del.*, vol. 24, no. 4, pp. 2232–2239, Oct. 2009.

[23] T. Hara, O. Yamamoto, M. Hayashi, and C. Uenosono, "Empirical formulas of surge impedance for single and multiple vertical cylinder," *Trans. IEE of Japan*, vol. 110-B, no. 2, pp. 129–137, Feb. 1990.

[24] J. Takami, T. Tsuboi, and S. Okabe, "Measured distortion of current waves and electrical potentials with propagation of a spherical wave in an electromagnetic field," *IEEE Trans. Electromagn. Compat.*, vol. 52, no. 3, pp. 753–756, Aug. 2010.

[25] Y. Baba, and M. Ishii, "Tower models for fast-front lightning currents," *Trans. IEE of Japan*, vol. 120-B, no. 1, pp. 18–23, Jan. 2000.

[26] Y. Baba, and M. Ishii, "Numerical electromagnetic field analysis on lightning surge response of tower with shield wire," *IEEE Trans. Power Del.*, vol. 15, no. 3, pp. 1010–1015, Jul. 2000.

[27] W. A. Chisholm, and W. Janischewskyj, "Lightning surge response of ground electrodes," *IEEE Trans. Power Del.*, vol. 4, no. 2, pp. 1329–1337, Apr. 1989.

[28] Y. Baba, and V. A. Rakov, "On the mechanism of attenuation of current waves propagating along a vertical perfectly conducting wire above ground: Application to lightning," *IEEE Trans. Electromagn. Compat.*, vol. 47, no. 3, pp. 521–532, Aug. 2005.

[29] Y. Baba, and V. A. Rakov, "On the interpretation of ground reflections observed in small-scale experiments simulating lightning strikes to towers," *IEEE Trans. Electromagn. Compat.*, vol. 47, no. 3, pp. 533–542, Aug. 2005.

[30] M. Ishii, T. Kawamura, T. Kouno, E. Ohsaki, K. Murotani, and T. Higuchi, "Multistory transmission tower model for lightning surge analysis," *IEEE Trans. Power Del.*, vol. 6, no. 3, pp. 1327–1335, Jul. 1991.

[31] M. Saito, M. Ishii, M. Miki, and K. Tsuge, "On the evaluation of the voltage rise on transmission line tower struck by lightning using electromagnetic and circuit-based analyses," *IEEE Trans. Power Del.*, vol. 36, no. 2, pp. 627–638, Apr. 2021.

[32] S. Hashimoto, Y. Baba, N. Nagaoka, A. Ametani, and N. Itamoto, "An equivalent circuit of a transmission line tower struck by lightning," *in Proc. Inter. Conf. on Lightning Protection,* Cagliari, Italy, no. 936, Sep. 2010.

[33] N. Itamoto, H. Kawamura, K. Shinjo, Y. Tanaka, and T. Noda, "Lightning fault rate calculation of transmission lines taking statistical variation of arching-horn flashovers into account," *IEEJ Trans. Power and Energy*, vol. 140, no. 2, pp. 126–133, Feb. 2020.

[34] J. A. Martinez, and F. Castro-Aranda, "Tower modeling for lightning analysis of overhead transmission lines," *in Proc., IEEE Power Engineering Society General Meeting, 2005*, vol. 2, pp. 121–1217. Jun. 2005.

[35] Z. G. Datsios, and P. N. Mikropoulos, "Effect of tower modelling on the minimum backflashover current of overhead transmission lines," *in Proc. 19th Int. Sym. on High Voltage Engineering*, no. 26, Pilsen, Czech Republic, Aug. 2015.

[36] C. A. Jordan, "Lightning computations for transmission lines with overhead ground wires, Part II," *General Electric Review*, vol. 37, no. 4, pp. 180–186, 1934.

[37] A. Ametani, Y. Kasai, J. Sawada, A. Mochizuki, and T. Yamada, "Frequency-dependent impedance of vertical conductors and a multiconductor tower model," *IEE Proc.-Gener. Transm. Distrib.*, vol. 141, no. 4, pp. 339–345, Jul. 1994.

[38] A. Deri, G. Tevan, A. Semlyen, and A. Castanheira, "The complex ground return plane a simplified model for homogeneous and multi-layer earth return," *IEEE Trans. Power App. and Syst.*, vol. PAS-100, no. 8, pp. 3686–3693, Aug. 1981.

[39] W. A. Chisholm, Y. L. Chow, and K. D. Srivastava, "Lightning surge response of transmission towers," *IEEE Trans. Power App. Syst.*, vol. PAS-102, no. 9, pp. 3232–3242, Sep. 1983.

[40] CIGRE WG 33.01 (Lightning), "Guide to procedures for estimating the lightning performance of transmission lines," *CIGRE Technical Brochure*, no. 63, Oct. 1991.

[41] A. Ametani, N. Triruttanapiruk, K. Yamamoto, Y. Baba, and F. Rachidi, "Impedance and admittance formulas for a multistair model of transmission towers," *IEEE Trans. Electromagn. Compat.*, vol. 62, no. 6, pp. 2491–2502, Dec. 2020.

[42] L. Grcev, and F. Rachidi, "On tower impedances for transient analysis," *IEEE Trans. Power Del.,* vol. 19, no. 3, pp. 1238–1244, Jul. 2005.

[43] A. Semlyen, and A. Dabuleanu, "Fast and accurate switching transient calculations on transmission lines with ground return using recursive convolutions," *IEEE Trans. Power App. Syst.*, vol. PAS-94, no. 2, pp. 561–571, Mar. 1975.

[44] Subcommittee for transmission lines, lightning protection design committee, "Guide to lightning protection design for transmission lines," *CRIEPI Rep.*, no. T72, 2003.

[45] A. Ametani, and T. Kawamura, "A method of a lightning surge analysis recommended in Japan using EMTP," *IEEE Trans. Power Del.*, vol. 20, no. 2, pp. 867–875, Apr. 2005.

[46] Subcommittee for power stations and substations, Study committee on lightning risk, "Guide to lightning protection design of power stations, substations and underground transmission lines (rev. 2011)," *CRIEPI Rep.*, no. H06, Sep. 2012.

[47] T. Hara, and O. Yamamoto, "Modeling of a transmission tower for lightning-surge analysis," *IEE Proc.-Gener. Transm. Distrib.*, vol. 143, no. 3, pp. 283–289, May 1996.

[48] Y. Yasuda, S. Shuhei, T. Hara, K. Ikeda, Y. Sonoi, and Y. Fukuoka, "Lightning surge analysis for 500-kV transmission lines using ground model with dynamic characteristics," *Trans. IEE of Japan*, vol. 123-B, no. 2, pp. 245–251, Feb. 2003.

[49] Y. Han, L. Li, H. Chen, and Y. Lu, "Influence of modeling methods on the calculated lightning surge overvoltages at a UHVDC converter station due to backflashover," *IEEE Trans. Power Del.*, vol. 27, no. 3, pp. 1090–1095, Jul. 2012.

[50] Y. Huangfu, S. Wang, and X. Tao, "Transient lightning impulse performance analysis for composite transmission line tower," *IEEE Trans. Electromagn., Compat.*, vol. 57, no. 5, pp. 1103–1111, Oct. 2015.

[51] T. Mozumi, Y. Baba, M. Ishii, N. Nagaoka, and A. Ametani, "Numerical electromagnetic field analysis of archorn voltages during a back-flashover on a 500-kV twin-circuit line," *IEEE Trans. Power Del.*, vol. 18, no. 1, pp. 207–213, Jan. 2003.

[52] N. Nagaoka, "A development of frequency-dependent tower model," *Trans. IEE of Japan*, vol. 111-B, no. 1, pp. 51–56, Jan. 1993.

[53] S. Kato, A. Mochizuki, and E. Zaima, "Transmission line models of tower in frequency domain," *Trans. IEE of Japan*, vol. 115-B, no. 5, pp. 524–531, 1995.

[54] A. R. J. de Araújo, C. M. de Seixas, B. Salarieh, S. Kurokawa, and B. Kordi, "Computation of lightning voltage surges on tall and conventional transmission towers," *Simpósio Brasileiro de Sistemas Elétricos - SBSE*, vol. 1, no. 1, art. no. 1, Aug. 2020.

[55] E. A. Oufi, A. S. Alfuhaid, and M. M. Saied, "Transient analysis of lossless single-phase nonuniform transmission lines," *IEEE Trans. Power Del.*, vol. 9, no. 3, pp. 1694–1700, Jul. 1994.

[56] M. E. Almeida, and M. T. C. de Barros, "Tower modelling for lightning surge analysis using Electro-Magnetic Transients Program," *IEE Proc.-Gener. Transm. Distrib.*, vol. 141, no. 6, pp. 637–639, Nov. 1994.

[57] M. T. C. de Barros, and M. E. Almeida, "Computation of electromagnetic transients on nonuniform transmission lines," *IEEE Trans. Power Del.*, vol. 11, no. 2, pp. 1082–1091, Apr. 1996.

[58] H. V. Nguyen, H.W. Dommel, and J. R. Marti, "Modeling of single-phase nonuniform transmission lines in electromagnetic transient simulations," *IEEE Trans. Power Del.*, vol. 12, no. 2, pp. 916–921, Apr. 1997.

[59] J. A. Gutierrez R., P. Moreno, J. L. Naredo, J. L. Bermudez, M. Paolone, C. A. Nucci, and F. Rachidi, "Nonuniform transmission tower model for lightning transient studies," *IEEE Trans. Power Del.*, vol. 19, no. 2, pp. 490–496, Apr. 2004.

[60] N. Harid, H. Griffiths, and A. Haddad, "A new frequency-dependent surge impedance calculation method for high-voltage towers," *IEEE Trans. Power Del.*, vol. 21, no. 3, pp. 1430–1437, Jul. 2006.

[61] B. Gustavsen, and A. Semlyen, "Rational approximation of frequency domain responses by vector fitting," *IEEE Trans. Power Del.*, vol. 14, no. 3, pp. 1052–1061, Jul. 1999.

[62] H. W. Dommel, "Digital computer solution of electromagnetic transients in single- and multiphase networks," *IEEE Trans. Power App. Syst.*, vol. PAS-88, no. 4, pp. 388–399, Apr. 1969.

3 TEM-delay Transmission Tower and Line Models

In this chapter, transmission tower and line models, which can approximately consider the non-TEM characteristics of the lightning-struck tower and line, are presented. The non-TEM characteristics include 1) the gradual rise of the tower surge impedance with time, 2) the gradual rise of the self and mutual surge impedance of the transmission line with time and the time delays of mutual coupling among lines corresponding to their separation distances, and 3) the significant wave attenuation characteristics along the tower, as discussed in Chapter 2. Some of the existing models have considered the above characteristics partly, but no model fully considers them. One of the reasons is that the existing models have been developed by focusing on the tower characteristics and representing them in the circuit analysis. Therefore, the presented models in this thesis include transmission tower and line models for fully considering the non-TEM characteristics.

The model named "TEM-delay" transmission tower and line model is presented in this chapter. The presented model can be derived from the configuration of the tower and line. The TEM-delay line model is presented firstly, and then the TEM-delay tower model is presented. The insulator voltages computed by the TEM-delay models are thoroughly validated by the FDTD computed voltages and voltages measured at actual towers reported in the past.

3.1 TEM-delay Transmission Line Model

3.1.1 Surge impedances

This section proposes the surge impedance of transmission lines considering the TEM-mode formation process. As discussed in Chapter 2, the electromagnetic field spreads gradually from the lightning struck point, and it takes time to form the TEM-mode coupling between the OHGWs and phase conductors. Besides, the self-surge impedance of each line increases gradually to its TEM-mode value owing to the same reason. In the presented model, simple first-order delay functions express the self and mutual surge impedances with specific time constants determined from the configuration. This section shows the impedance formulae. Section 3.1.2 will present an implementation method for EMT simulators considering the time delay in mutual couplings. The validity of the presented model will be shown in Section 3.1.3.

Here a multiphase overhead transmission line shown in Fig. 3.1 is discussed. The followings are assumed: the self-surge impedance Z_{0ii} of a horizontal conductor converges to its TEM mode value with a time constant given by the conductor height h_i divided by the speed of light in free space c_0 as follows:

$$Z_{0ii}(s) = 60\ln\left(\frac{2h_i}{r_i}\right)\times\frac{1}{1+\tau_{ii}s},\ \tau_{ii} = h_i/c_0 \tag{3.1}$$

where h_i, r_i, c_0, and s are the line height, line radius, the speed of light, and Laplace operator, respectively.

The mutual-surge impedance Z_{0ij} of horizontal conductors is assumed to converge to its TEM-mode value with a time constant given by the separation between conductors, d_{ij}, and that between real and image conductors, D_{ij}, with relevant weight:

$$Z_{0ij}(s) = 60\ln\left(\frac{D_{ij}}{d_{ij}}\right) \times \left(\begin{array}{c} \dfrac{d_{ij}}{D_{ij}+d_{ij}} \dfrac{1}{1+\tau_{ijd}s} \\ +\dfrac{D_{ij}}{D_{ij}+d_{ij}} \dfrac{1}{1+\tau_{ijD}s} \end{array} \right), \tag{3.2}$$

$$\tau_{ijd} = 2d_{ij}/c_0,\ \tau_{ijD} = 2D_{ij}/c_0,$$

where D_{ij} is the distance between the i^{th} real and j^{th} image conductors, and d_{ij} is the distance between the i^{th} and j^{th} real conductors, as shown in Fig. 3.1.

The first-order delay functions express the surge impedance because it can approximate the behavior that causes the gradual rise of transmission line voltages compared with the rise time of the injection current at the initial stage of the transient phenomenon. The validation will be shown in Section 3.1.3. The surge impedances given in (3.1) and (3.2) can also be directly introduced into the EMT simulators using the recursive convolution technique [1], [2]. The self-component is generated by the contribution of the current flowing through the real conductor. However, the mutual component is generated by the contributions from spatially separated real/image conductors. Hence, two first-order delay functions represent the mutual component, and their time constants are set to be longer for the same distance than that of the self-component.

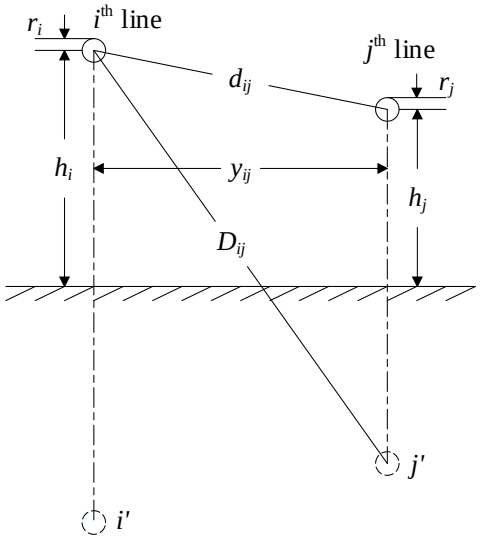

Fig. 3.1 Multiphase overhead transmission line.

Fig. 3.2 shows the combined surge impedance of the OHGW Z_{gw} and that between the OHGW and the upper phase conductor Z_{mU} for the 76-m high tower studied in Chapter 2. The surge impedances were computed by the lossless TEM-mode assumption and presented formulae (3.1) and (3.2). The time-dependence of the lightning-struck transmission line is realized by the first-order delay functions, which set the surge impedances smaller in the high-frequency region. The verification of the TEM-delay line model in the time domain will be shown in Section 3.1.3 by the transient response of the overhead transmission lines alone and in Section 3.3 by the insulator voltages of the lightning-struck transmission tower and line.

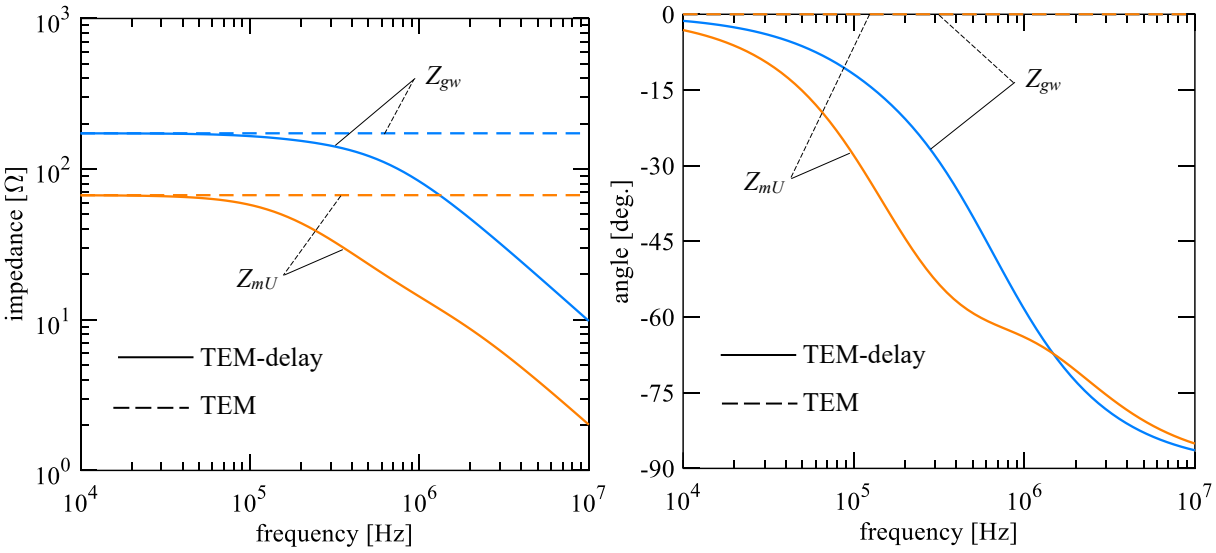

(a) Amplitude (b) Angle

Fig. 3.2 Amplitude and angle of the combined surge impedance of the OHGW and that between the OHGW and upper phase conductor in lossless TEM-mode and those computed by (3.1) and (3.2) for the 76-m high tower studied in Chapter 2.

3.1.2 Implementation method for circuit analysis

The implementation technique of the transmission line model considering the time delays of mutual coupling corresponding to the separation distances is presented. In the circuit analysis method, the numerical transmission line model is categorized into the modal-domain [1], [2], and phase-domain [3]–[6] models. The proposed model is implemented in the circuit analysis method using the phase-domain modeling for the following reasons. The self and mutual surge impedances of the proposed model are directly provided by the analytical formulae given in the phase domain; the physical distance between the conductors determines the time delays of the mutual couplings. The phase-domain modeling is more suitable than the modal-domain modeling for implementing the proposed TEM-delay transmission line model.

Let v_s, v_r, i_s, and i_r denote the voltage and current vectors at the sending and receiving ends of the N-phase transmission line, respectively. The Bergeron solution in the phase domain can be expressed in terms of the Thevenin equivalent in the time domain as follows:

$$\begin{aligned} v_s(t) &= Z_0(t) * i_s(t) + v_{p-s}(t) \\ v_r(t) &= Z_0(t) * i_r(t) + v_{p-r}(t) \end{aligned} \tag{3.3}$$

where $Z_0(t)$ is the impulse response of the characteristic impedance matrix, * denotes the matrix-vector convolution operation in the time domain. The voltages $v_{p-s}(t)$ and $v_{p-r}(t)$ provide the history and are obtained, respectively, as

$$\begin{aligned} v_{p-s}(t) &= P_0(t) * \left\{ 2v_r(t-\tau) - v_{p-r}(t-\tau) \right\} \\ v_{p-r}(t) &= P_0(t) * \left\{ 2v_s(t-\tau) - v_{p-s}(t-\tau) \right\} \end{aligned} \tag{3.4}$$

where $P_0(t)$ is the impulse response of the matrix obtained by removing the one-way propagation time delay τ of the line from the voltage propagation function matrix. The matrix $P_0(t)$ is a unit matrix in the present study because the attenuation and distortion of the traveling wave along the transmission line are not considered.

Delayed currents $i_{sdel}(t-t_d)$ and $i_{rdel}(t-t_d)$ are considered to express the time delay of the mutual coupling of lines corresponding to their separation distances due to the spatial propagation of the electromagnetic field. By considering the mutual coupling delay, the voltage at the sending end is derived as

$$\begin{aligned} & v_s(s) = \exp(-st_d) Z_0(s) i_s(s) \\ & \xrightarrow[\mathcal{L}]{\mathcal{L}^{-1}} \\ & v_s(t) = Z_0(t) * i_{sdel}(t-t_d) \end{aligned} \tag{3.5}$$

where $\mathcal{L}$ denotes the Laplace transformation, and the time delay term t_d corresponds to the line separation distance d_{ij}. The following equation provides the time delay t_d determined by the separation distance d_{ij} and the speed of light c_0 in free space:

$$t_d = \begin{bmatrix} t_{d11} & t_{d12} & \cdots & t_{d1N} \\ t_{d21} & \ddots & & \vdots \\ \vdots & & \ddots & \vdots \\ t_{dN1} & \cdots & \cdots & t_{dNN} \end{bmatrix} = \frac{1}{c_0} \begin{bmatrix} 0 & d_{12} & \cdots & d_{1N} \\ d_{21} & \ddots & & \vdots \\ \vdots & & \ddots & \vdots \\ d_{N1} & \cdots & \cdots & 0 \end{bmatrix}. \tag{3.6}$$

For instance, the i^{th} element of the voltage at the sending end is derived as

$$v_{si}(t) = \sum_{j}^{N} Z_{0ij}(t) * i_{sdelj}(t - t_{dij}). \tag{3.7}$$

The self and mutual surge impedances (3.1) and (3.2) of the presented model are provided by the analytical formulae expressed by the first-order delay functions. Upon applying the recursive convolution technique based on the trapezoidal rule, the surge impedance matrix $Z_0(t)$ in (3.3) is divided into the constant term Z_{00} and the time function term $Z_{01}(t)$. In the circuit analysis, the diagonal element of the constant term of the surge impedance matrix, Z'_{00}, is represented by the lumped constant resistance. The product between Z'_{00} and the self-components of the current $i_s(t)$ and $i_r(t)$, which do not include the time delay, is taken by this resistance. Controlled voltage sources $v_{z-s}(t)$ and $v_{z-r}(t)$ express (1): the product between the off-diagonal element of the constant term of the surge impedance matrix Z''_{00} and the delayed currents $i_{sdel}(t-t_d)$ and $i_{rdel}(t-t_d)$, and (2): the convolution between the time function term of the same matrix $Z_{01}(t)$ and the delayed currents as:

$$\begin{aligned} v_s(t) &= Z'_{00} i_s(t) + v_{h-s}(t),\ v_{h-s}(t) = v_{z-s}(t) + v_{p-s}(t) \\ v_r(t) &= Z'_{00} i_r(t) + v_{h-r}(t),\ v_{h-r}(t) = v_{z-r}(t) + v_{p-r}(t) \end{aligned} \tag{3.8}$$

where

$$\begin{aligned} v_{z-s}(t) &= Z''_{00} i_{sdel}(t-t_d) + Z_{01}(t) * i_{sdel}(t-t_d) \\ v_{z-r}(t) &= Z''_{00} i_{rdel}(t-t_d) + Z_{01}(t) * i_{rdel}(t-t_d) \end{aligned} \tag{3.9}$$

Note that, in (3.9), each element of the voltage source is calculated in the same way as (3.7). Each surge impedance matrix in (3.8) and (3.9), namely, the diagonal element of the constant term of the surge impedance matrix Z'_{00}, off-diagonal element of the same matrix Z''_{00}, and the time function term of the surge impedance matrix $Z_{01}(t)$, respectively, is provided as follows:

$$Z'_{00} = \begin{bmatrix} Z_{0011} & 0 & \cdots & 0 \\ 0 & \ddots & & \vdots \\ \vdots & & \ddots & \vdots \\ 0 & \cdots & \cdots & Z_{00NN} \end{bmatrix}, \tag{3.10}$$

$$Z''_{00} = \begin{bmatrix} 0 & Z_{0012} & \cdots & Z_{001N} \\ Z_{0021} & \ddots & & \vdots \\ \vdots & & \ddots & \vdots \\ Z_{00N1} & \cdots & \cdots & 0 \end{bmatrix}, \tag{3.11}$$

$$Z_{01}(t) = \begin{bmatrix} Z_{0111}(t) & Z_{0112}(t) & \cdots & Z_{011N}(t) \\ Z_{0121}(t) & \ddots & & \vdots \\ \vdots & & \ddots & \vdots \\ Z_{01N1}(t) & \cdots & \cdots & Z_{01NN}(t) \end{bmatrix}. \tag{3.12}$$

An equivalent circuit of the transmission line in the phase domain shown in Fig. 3.3 (a) is obtained from (3.3)–(3.9). This circuit considers the time delay of the mutual couplings and the time

dependence of the self and mutual surge impedances owing to the TEM-mode formation process by using the controlled voltage sources, $v_{z-s}(t)$ and $v_{z-r}(t)$, and the lumped resistance representing the diagonal element of the constant part of the characteristic impedance matrix, Z'_{00}. This equivalent circuit can be implemented into EMT simulators having a controlled voltage source model.

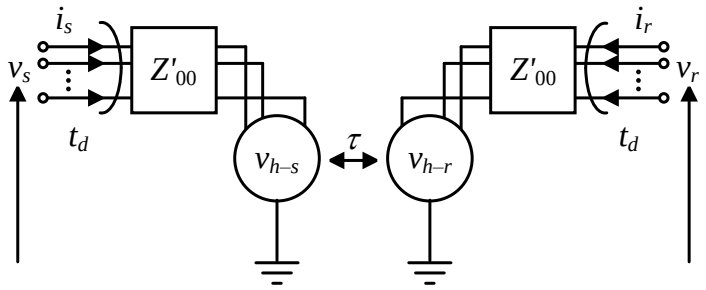

(a) Thevenin equivalent

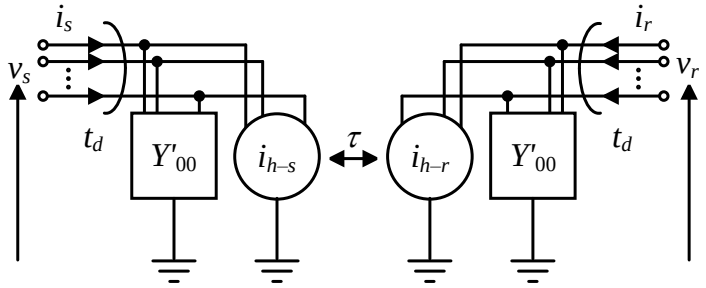

(b) Norton equivalent

Fig. 3.3 Equivalent circuit model of a transmission line in the phase domain considering time delay in mutual couplings: TEM-delay line model.

The equivalent circuit model is modified to the Norton equivalent form because the distributed parameter lines are simulated by equivalent conductance and current sources in the nodal-analysis-based circuit analysis in general. The equation (3.8) providing the Thevenin equivalent is modified to (3.13) and the equivalent circuit of the transmission line in the phase domain using the Norton equivalent, shown in Fig. 3.3 (b), is obtained.

$$\begin{aligned} i_s(t) &= Y'_{00}v_s(t) + i_{h-s}(t),\ i_{h-s}(t) = -Y'_{00}\left\{v_{z-s}(t) + v_{p-s}(t)\right\} \\ i_r(t) &= Y'_{00}v_r(t) + i_{h-r}(t),\ i_{h-r}(t) = -Y'_{00}\left\{v_{z-r}(t) + v_{p-r}(t)\right\} \end{aligned} \tag{3.13}$$

where Y'_{00} is the inverse of the diagonal element of the constant part of the characteristic impedance matrix Z'_{00}.

In case ATP [7] is used for the transient analysis, the presented TEM-delay transmission line model is implemented by the following method. The matrix Y'_{00} in (3.13) is modeled in the ATP

electrical circuit section. The current sources $i_{h-s}(t)$ and $i_{h-r}(t)$, which represent the self-components of the time-dependent term, all of the mutual components, and past histories of the other node, are modeled by MODELS-controlled current sources. MODELS is a programing language that can be interfaced with ATP [8].

3.1.3 Validation by FDTD computed voltages rises

As an example, the transient characteristic of a 500-kV vertical double-circuit transmission line was analyzed. The voltage rises computed by the presented line model were compared with those computed by the FDTD method. The comparisons show the validity of the presented TEM-delay model.

The FDTD analysis model is illustrated in Fig. 3.4 (a), and the transmission line configuration is shown in Fig. 3.4 (b). A transmission line consisting of two OHGWs and six-phase conductors was placed above a perfectly conducting ground. The FDTD modeling and analysis conditions were the same as those shown in Section 2.1.1, except that the transmission tower was removed and a 23-m long thin wire was inserted to connect the OHGWs in this case. The thin wire was installed to inject the symmetrical current into the OHGWs: the discussions on the voltage rise of the OHGWs and phase conductors become simplified.

The presented TEM-delay line model and the conventional TEM-mode line model were employed in the circuit analysis. The surge impedance is derived by equations (3.1) and (3.2) for the TEM-delay model. The surge impedance of the phase conductors was calculated using the GMD in the same manner as in the FDTD analysis. The transient response was computed using the method described in Section 3.1.2. The step-like current was injected into the OHGW.

The TEM-delay model can consider the initial TEM-mode formation characteristics, although the conventional TEM-mode model cannot. Fig. 3.5 shows the transient responses of the overhead transmission line calculated using the FDTD method and circuit analysis models, the TEM-mode model and the proposed model (TEM-delay). The calculation results by both circuit models and by the FDTD method all converge to almost the same voltages. However, in the results derived using the conventional TEM-mode model, the voltages of the OHGW, V_{gw}, and phase conductors, V_{pU}, V_{pM}, and V_{pL}, increase instantly with the same rise time as the injected current. In contrast, the voltages derived by the presented TEM-delay model show a gradual rising characteristic than the injected current and show a time delay of mutual couplings corresponding to the line separation distances. Thus, the TEM-delay model can approximately represent the TEM-mode formation process of the overhead transmission line struck by lightning. The model will be further validated for computing voltage across insulator strings of the lightning-struck transmission tower in Section 3.3.

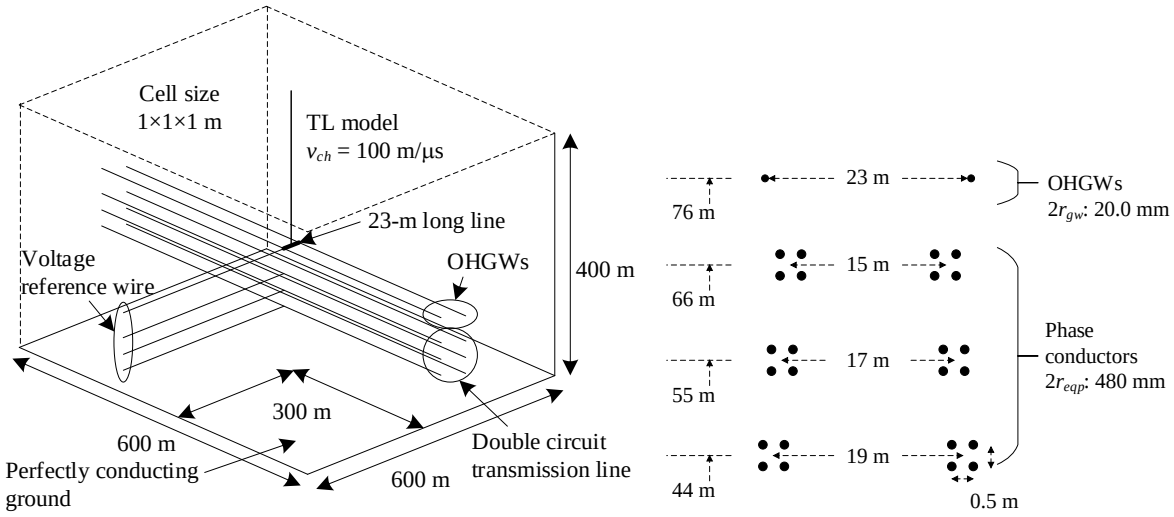

(a) FDTD analysis space (b) Transmission line configuration

Fig. 3.4 FDTD analysis model for validation of the TEM-delay line model.

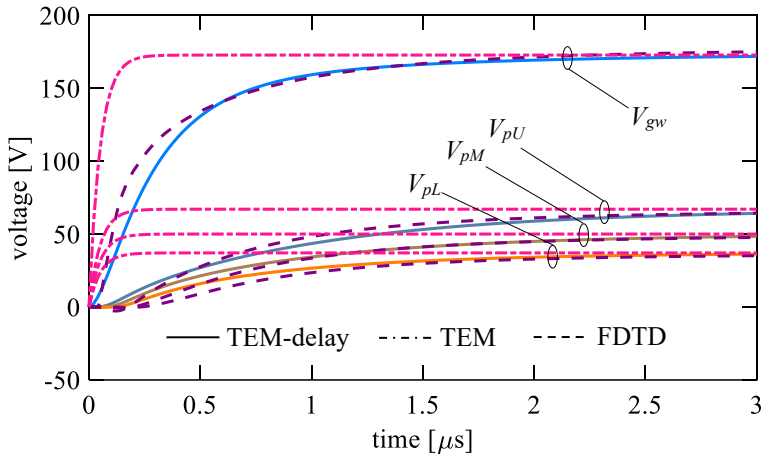

Fig. 3.5 Transient response of the transmission line computed by the FDTD method and circuit analysis using the TEM-mode and TEM-delay models.

3.2 TEM-delay Transmission Tower Model

3.2.1 Model parameters

Two types of TEM-delay transmission tower models shown in Fig. 3.6 are presented. The first model is the basic TEM-delay model represented by cascade-connected distributed-parameter lines with time-dependent surge impedance and the wave attenuation characteristic having no cross-arms. This model can represent the characteristics of the lightning-struck transmission tower, the gradual rise of the tower surge impedance and the significant attenuation of traveling waves along the tower, as revealed in Chapter 2. The second model is the extended model having cross-arms with mutual couplings among

them. This model can represent the asymmetrical voltage distribution due to the off-center lightning strike, in addition to the non-TEM characteristics. Therefore, the extended model can be utilized for an in-depth analysis of lightning surges considering lightning-struck points and BFO phases. Nevertheless, it should be noted that the basic model performs accurately enough for considering the non-TEM characteristic of the lightning-struck tower. Firstly, the formulation for the basic model is provided, and then modifications for the extended model are provided in this section.

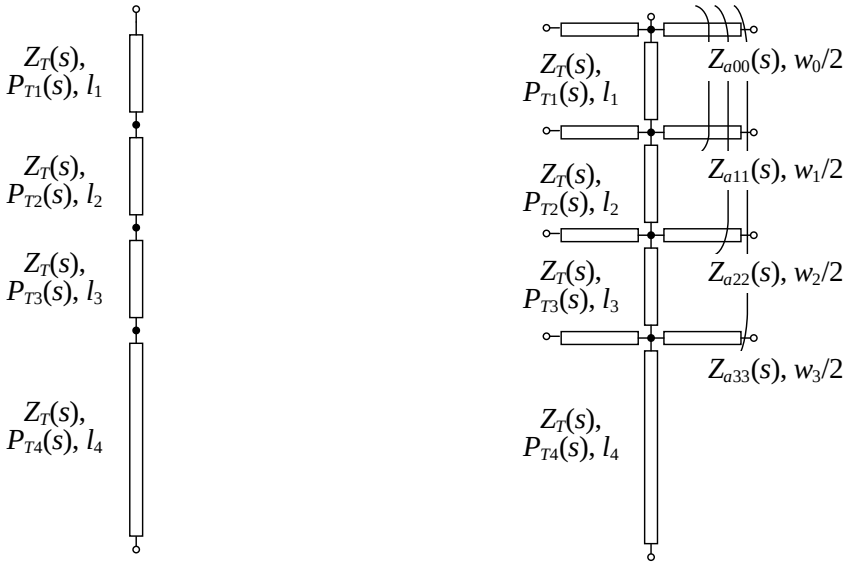

(a) Model without cross-arms (Basic TEM-delay model)

(b) Model with cross-arms (Extended TEM-delay model)

Fig. 3.6 TEM-delay transmission tower model.

A Basic TEM-delay transmission tower model

The surge impedance formula of the proposed tower model is discussed. The surge impedance of vertical cylinder or cone has been given based on the theoretical circuit or electromagnetic field theory [9]–[13] as overviewed in Section 2.2. According to the theory, the step-current response of a vertical cylinder rises logarithmically with time (e.g. (2.15)). Whereas in the presented model, the tower surge impedance is assumed to rise by the first-order decay with time. This expression is adopted because it can approximate the logarithmic increase in the time domain and can be directly interfaced with the circuit analysis method using the recursive convolution technique. As the convergence or steady-state value of surge impedance, the modified Jordan's formula [14] is employed. The constant impedance formula for vertical cone [15], [16] is not employed since the step-like current responses of vertical double-circuit transmission towers measured as of today [17]–[21] clearly show the time-dependence. The impedance formula for the presented model is given as follows:

$$
\begin{aligned}
&Z_T(s) = 60\left\{\ln\left(\frac{4h_T}{r_{eq}}\right) - 1\right\} \times \frac{1}{1+\tau_T s} \\
&\tau_T = \frac{h_T}{c_0},\ r_{eq} = \frac{r_{top}h_U + r_{middle}h_T + r_{base}h_L}{2h_T}, \\
&r_{top} = \frac{d_{top}}{\sqrt{\pi}},\ r_{middle} = \frac{d_{middle}}{\sqrt{\pi}},\ r_{base} = \frac{d_{base}}{\sqrt{\pi}},
\end{aligned}
\tag{3.14}
$$

where h_T, h_U, and h_L are total, upper, and lower tower height, d_{top}, d_{middle}, and d_{base} are top, middle, lower tower width, respectively. The definitions are also found in Fig. 2.3 and Fig. 3.15. The radii, r_{top}, r_{middle}, and r_{base} are obtained so that the circuital cross-section of the circuit model should have the same area as the square cross-section of the tower has. The radius r_{eq} is the weighted-equivalent radius of the whole tower.

Steady-state surge impedance is 202 Ω for the studied 76-m high tower in Section 2.1. If the step-current response of the tower is computed by (3.14), the maximum voltage that appears at the round-trip propagation time, $t = 2\tau_T$, is 175 V (= 202 × (1–e^{-2})). This surge impedance is higher than that reported in [20] because of the angle of the current injection wire [20], for instance. On the other hand, the impedance value is lower than that reported in [22], where the tower surge impedance was estimated using the surge impedance of OHGWs in the TEM mode. The rise time, 0.25 μs (= 76 m / 300 m/μs), is almost consistent with that of tower top voltage shown in Fig. 2.5 (c).

The step-response of the propagation function is given from the tower shape, and it is interfaced with circuit analysis using the recursive convolution technique. The current propagating upward along a vertical cylinder or cone is known to suffer significant attenuation due to the tangential electric field's boundary condition at the conductor's surface [23]. Along a vertical cylinder, both up-and down-ward propagating waves suffer attenuation since spherical TEM wave is not generated in either direction. Thus, the attenuation characteristic of both up-and down-ward traveling waves should be considered in the transmission tower model [24]. The step current response of each traveling wave is expressed as follows in the presented tower model:

$$
\begin{aligned}
&p_T(t) = 1 - \alpha_{Ta}\exp\left(-t/\beta_{Ta}\right) - \left(1-\alpha_{Ta}\right)\exp\left(-t/\beta_{Tb}\right), \\
&\text{where } \alpha_{Ta} = 0.8,\ \beta_{Ta} = 0.5h_U/c_0,\ \beta_{Tb} = 20h_L/c_0.
\end{aligned}
\tag{3.15}
$$

The parameters of the step current response are determined considering the gradual voltage decay discussed in Section 2.1.3. Section 3.2.2 and 3.3 will show that this circuit model can sufficiently reproduce step-like current responses of a transmission tower and insulator voltages derived by the FDTD analysis and experiments using actual towers.

The propagation characteristic along the whole tower provided by (3.15) is divided into four using an approximation method in the *s*-domain, such as the Padé approximation and the vector fitting technique [25], [26]. The division of the propagation characteristic is conducted because a transmission

tower should be represented by four cascaded distribute-parameter lines, as shown in Fig. 3.6, for deriving the voltages of each tower cross-arm. At first, the step current response given in (3.15) is transformed in s-domain, and its impulse response $P_T(s)$ is obtained by multiplying the propagation function by the Laplace operator, s (dividing the function $p_T(s)$ (= $\mathcal{L}\{p_T(t)\}$) by the step function, $1/s$):

$$\begin{aligned} P_T(s) &= \mathcal{L}\{p_T(t)\}s = 1 - \frac{\alpha_{Ta}s}{s+1/\beta_{Ta}} - \frac{(1-\alpha_{Ta})s}{s+1/\beta_{Tb}} \\ &= \frac{1+\{(1-\alpha_{Ta})\beta_{Ta} + \alpha_{Ta}\beta_{Tb}\}s}{(1+\beta_{Ta}s)(1+\beta_{Tb}s)}. \end{aligned} \tag{3.16}$$

Then the propagation function in each section is derived considering the section length, and each function is transformed into a rational function using approximation techniques.

$$\begin{aligned} P_{Tk}(s) &= \sqrt[\frac{h_T}{l_k}]{P_T(s)} \approx \frac{a_{k0} + a_{k1}s + a_{k2}s^2}{1 + b_{k1}s + b_{k2}s^2 + b_{k3}s^3} \\ &= \frac{\alpha_{Tk1}}{1+\beta_{Tk1}s} + \frac{\alpha_{Tk2}}{1+\beta_{Tk2}s} + \frac{\alpha_{Tk3}}{1+\beta_{Tk3}s}, \end{aligned} \tag{3.17}$$

where k denotes section number. The step current response of the propagation function in each section is readily derived. The response can be interfaced with the circuit analysis method using the recursive convolution technique. Fig. 3.7 shows propagation characteristics of the 76-m high tower studied in Chapter 2 in the frequency domain for each section and that along the whole tower, given by the original functions and their approximations using the vector fitting. Note that characteristics of sections one to three are almost overlapped, and the original and approximated curves are also almost overlapped. The

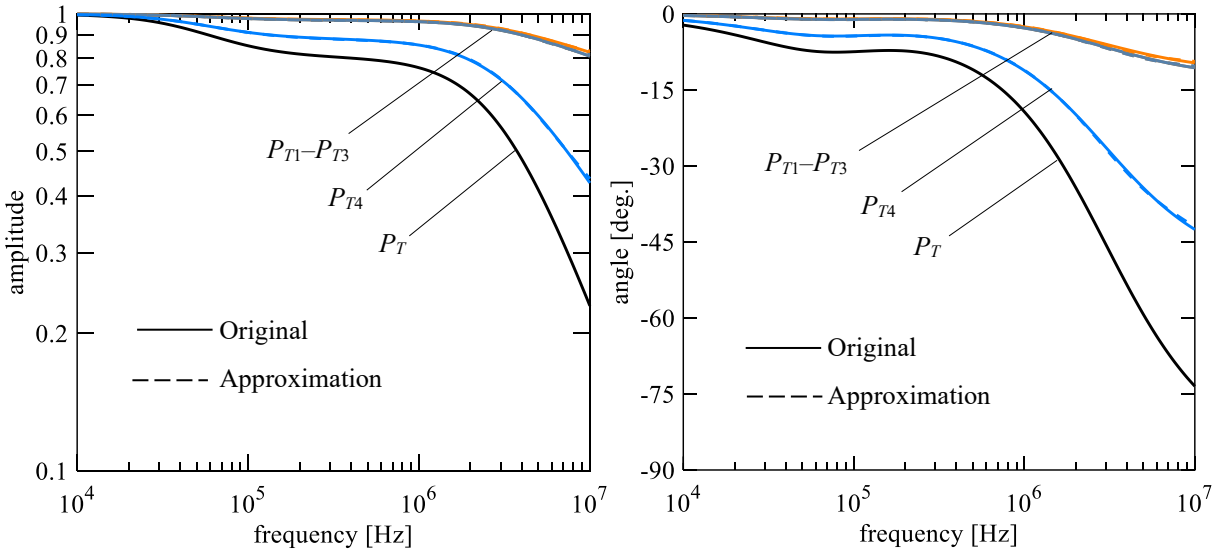

(a) Amplitude (b) Angle

Fig. 3.7 Propagation characteristic of the TEM-delay tower model in the frequency domain (the original and approximated curves are almost overlapped).

characteristic of the whole tower is divided into four considering the length of each section. The parameters for each section of the studied 76-m high tower in Chapter 2 are given in Table 3.1 as an example.

The presented TEM-delay tower model without cross-arms can be implemented into the circuit analysis method using a frequency-dependent parameter line model. For instance, the model is implemented in ATP using J. Marti's frequency-dependent line model.

Table 3.1 Parameters of wave propagation characteristic along the studied 76-m high transmission tower

	line#1	line#2	line#3	line#4
α_{Tk1}	0.0284	0.0312	0.0312	0.120
α_{Tk2}	0.118	0.129	0.129	0.443
α_{Tk3}	0.853	0.840	0.840	0.437
β_{Tk1}	2.67×10^{-6}	2.67×10^{-6}	2.67×10^{-6}	2.80×10^{-6}
β_{Tk2}	41.9×10^{-9}	42.2×10^{-9}	42.2×10^{-9}	49.9×10^{-9}
β_{Tk3}	2.22×10^{-9}	2.45×10^{-9}	2.45×10^{-9}	11.7×10^{-9}

B TEM-delay transmission tower model with cross-arms

The modeling procedure of the TEM-delay tower model with cross-arms is similar to that of the basic model. The tower surge impedance is determined by (3.14). The propagation characteristic is determined following (3.15), but the coefficient β_{Ta} is reduced from $0.5h_T/c_0$ to $0.1h_T/c_0$ because the cross-arms, which distort the wavefront of traveling waves, are considered. The cross-arms are modeled by the TEM-delay line model since they are interpreted as horizontal lines. The self and mutual surge impedance of the cross-arms are determined by (3.1) and (3.2), and time delays in mutual coupling are considered by the method described in Section 3.1.2. The cross-arms in each side of the tower are modeled independently by the TEM-delay line model considering the mutual coupling among cross-arms in each side (the mutual coupling from the lightning-struck side arms to those on the other side are not considered). In computing surge impedances of the cross-arms, their radii r_i are given by $(S_i/\pi)^{1/2}$, where S_i is the area of cross-section of each cross-arm at the junction to the tower. The characteristics and validity of the TEM-delay model with cross-arms are discussed in Section 3.3.3.

3.2.2 Validation by a surge experimental result

The TEM-delay tower model without cross-arms is validated by referencing the result of a surge experiment reported in [20]. Fig. 3.8 shows the shape of the transmission tower used in the surge experiment. The tower is an 89.5-m high transmission tower with 6.5-Ω footing resistance. The transient analysis was performed using the TEM-delay tower model and the multistory tower model shown in Fig. 3.9.

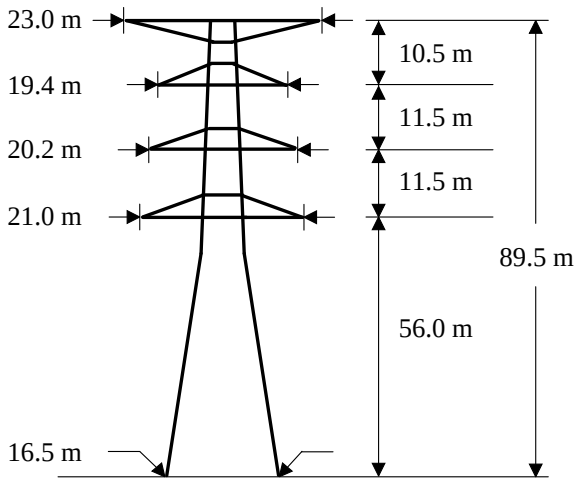

Fig. 3.8 An actual 500-kV transmission tower used for the experiment (adapted from [20]).

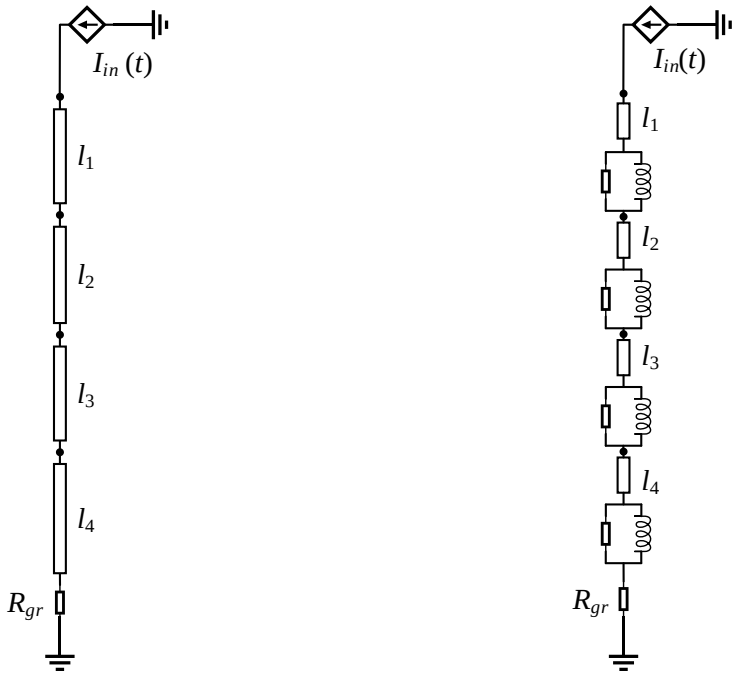

(a) TEM-delay model (b) Multistory model

Fig. 3.9 Circuit model for analyzing tower surge response.

The measured surge response of the transmission tower shows the gradually rising surge impedance and the significant wave attenuation along the tower. In the surge experiment, three types of current (step current, current with the rising time of 1 μs and 3 μs) shown in Fig. 3.10 (a) was injected by a pulse generator (PG) with internal resistance ranging from 150 Ω to 200 Ω, and tower top voltages shown in Fig. 3.11 (a) were measured. The current injection wire (a copper wire with a radius of

0.675 mm) was horizontally arranged via a 1000-Ω resistor or wave-shaping circuit having an internal impedance higher than 1000 Ω. A voltage reference wire was stretched between the test tower and the adjacent tower. Note that the ideal step current and the voltage response shown in Fig. 3.10 (a) and Fig. 3.11 (a) were derived using the numerical Laplace transform [20], [27]. The tower top voltage generated by the step current shows a gradual rise and a peak at approximately 0.6 μs. The voltages generated by the current with a longer rise time have smaller peaks observed subsequently. These measurement results show that the tower surge impedance has a slow rising characteristic with time, and the traveling waves attenuate significantly, as described in Chapter 2 and Section 3.2.

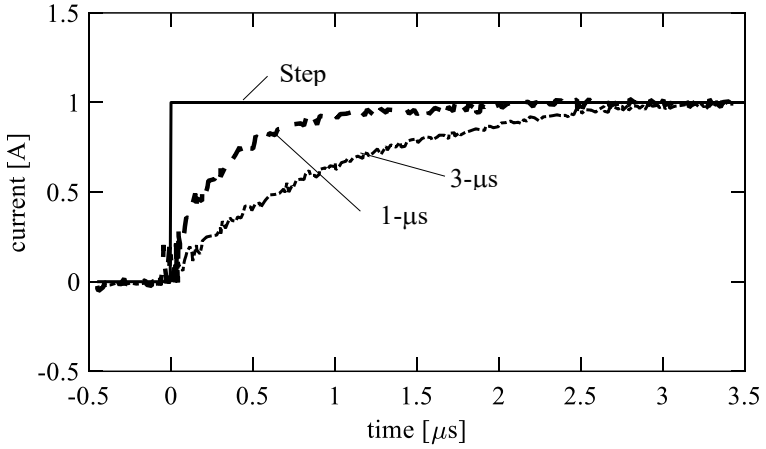

(a) Measured (adapted from [20])

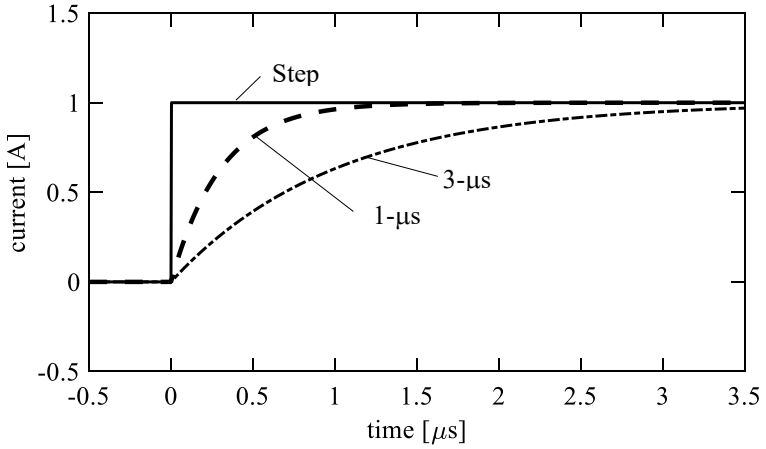

(b) Simulation

Fig. 3.10 Injection current for surge experiment and simulation.

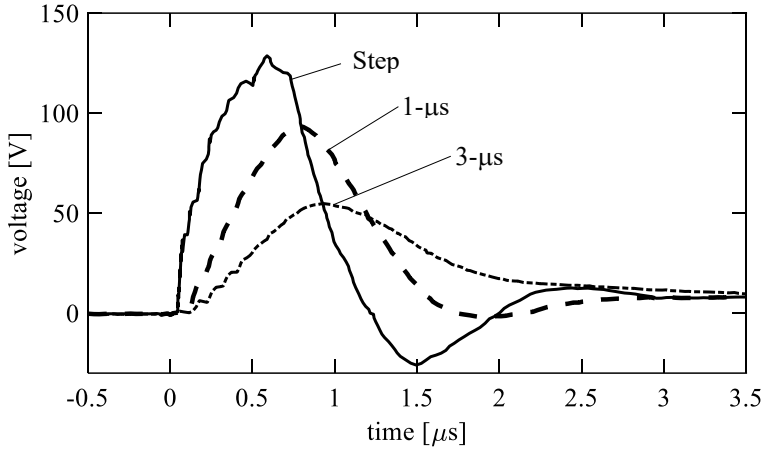

(a) Measured (adapted from [20])

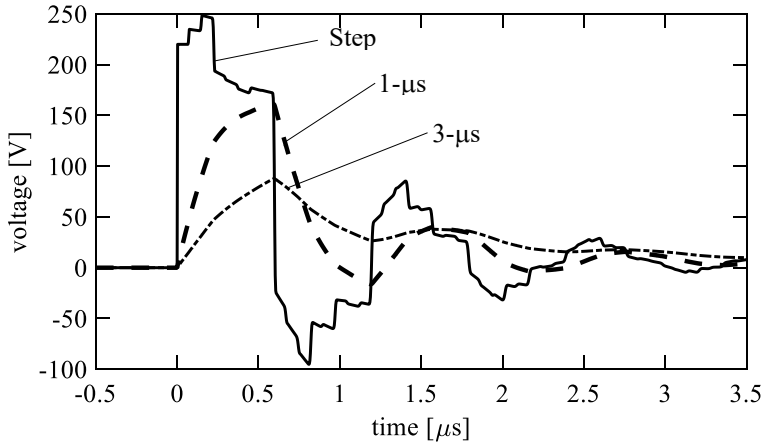

(b) Multistory tower model [a]

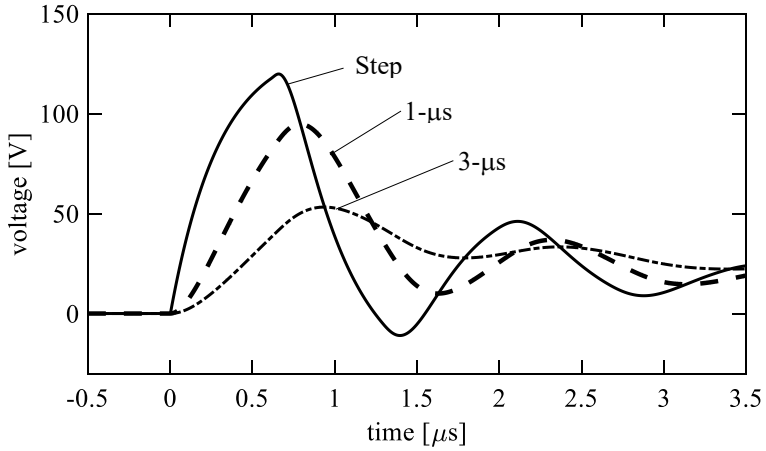

(c) TEM-delay tower model

Fig. 3.11 Surge response of a 500-kV transmission tower.

[a] The vertical axis range of (b) is different from that of (a) and (c)

The TEM-delay tower model can reproduce the observed tower surge response characteristics, while the multistory tower model cannot reproduce them. Fig. 3.10 (b) shows the current waveforms injected in the simulation, and Fig. 3.11 (b) and (c) show the circuit analysis results by the TEM-delay model and the multistory model, respectively. In the TEM-delay model case, both peak voltages and their occurrence time are reproduced with approximately a 10% difference or less. The TEM-delay model reproduces the TEM-mode formation characteristic of the transmission tower. On the other hand, in the multistory tower model case, the computed peak voltage is higher than the measured voltages. In addition, the model does not reproduce the delay of the voltage peak occurrence depending on the injected current in the measured waveform. The voltage peak dependence on the injected current is not reproduced because the multistory tower model does not consider the gradually rising characteristic of the surge impedance. Note that the surge impedance of the TEM-delay tower model was multiplied by 0.7 because the current was injected horizontally in the experiment [20], but the model has been developed based on the vertical lightning channel.

Although the TEM-delay tower model can reproduce the measured surge response of the tower, there is a deviation between the measured and the simulated waveform after the first peak. The voltages computed using the TEM-delay tower model show continuous oscillation due to the traveling wave reflection at the tower top and base compared with the measured voltages. In the experiment, the current injection wire was perpendicular to the tower and parallel to the ground [20]. In contrast, the TEM-delay model was derived assuming a lightning channel perpendicular to the ground. The difference between the measured and simulated results after their first peak voltage can be attributed to one or both of the following reasons: the traveling wave propagation characteristics in the tower might have changed, the potential of the voltage reference wire might have increased because of the electromagnetic field generated by the current injection wire. Nevertheless, the TEM-delay tower model can still express the non-TEM characteristic of the transmission tower.

3.3 Validation of the Insulator Voltages Computed by the TEM-delay Tower and Line Models

The insulator voltages computed by the TEM-delay transmission tower and line models are validated. For the validation, the followings are referenced: 1) surge experimental results performed using an actual 500-kV transmission tower in the past [22], 2) FDTD computed insulator voltages generated by a lightning strike to the center of the tower top, 3) those by a strike to the tip of the tower top cross-arm, and 4) insulator voltages measured using an actual UHV transmission tower in the past [19].

3.3.1 Surge experiment on an actual 500-kV transmission tower

The presented TEM-delay tower and line models are validated by the results of surge experiments performed at an actual 500-kV transmission tower in the past [22]. The TEM-delay model reproduces

the experimental results well. The conventional model has limitations in reproducing characteristics of the transient response of the transmission tower and line.

The surge experiment was performed using the 89.5-m high 500-kV tower shown in Fig. 3.8 [22]. In the experiment, the PG was used to inject surge current into the tower top, and the insulator voltages of the upper, middle, and lower phases were measured. The PG injected the current via an external resistor of 1000 Ω or a wave-shaping circuit with an internal impedance higher than 1000 Ω. It was shown in [22] that transient characteristics of the tower vary depending on the current injection angle, for instance. The transmission line had three OHGWs composed of one AC260 mm^2 conductor and two OPGW260 mm^2 conductors. The phase conductor was a four-bundled TACSR/AC810 mm^2 with a spacing of 50 cm. The other conditions were determined in accordance with [22].

The circuit analysis was performed using the TEM-delay transmission tower and line models as well as the existing tower and line models. The basic TEM-delay tower model that does not consider the presence of cross-arms was used in this analysis. The analysis was also performed using the conventional models: the multistory tower model [21] with J. Marti's frequency-dependent transmission line model [2]. The multistory tower model is one of the most widely and frequently used transmission tower models for towers taller than 30 m (e.g., [28]–[31]). For discussing the characteristics, the following three model sets were used:

1) Multistory tower model with J. Marti's frequency-dependent line model
2) TEM-delay tower model with J. Marti's frequency-dependent line model
3) TEM-delay tower and line model

Fig. 3.12 illustrates circuit analysis models. The earth resistivity for calculating the line constant for J. Marti's frequency-dependent line model was set to 200 Ωm [20]. A 6.5-Ω lumped constant resistance, R_{gr}, modeled the tower foot in both circuit models. Since the voltages generated by a horizontal current injection were measured, the surge impedance of the TEM-delay tower model was multiplied by 0.7 [20]. The step-like, 1-μs, and 3-μs rising currents with 1-A peak were injected by an ideal current source, respectively.

Measured insulator voltages show the non-TEM characteristics, as revealed in Chapter 2. Fig. 3.13 (a) shows the actual measurement results of the upper insulator voltages generated by the three types of injected currents. The insulator voltages gradually increase, and their rise time is longer than that of the injected current. The smaller peak voltages are generated as the rise time of the injected current increases. These characteristics indicate that the tower surge impedance itself has time dependence, and the mutual couplings between the OHGWs and the phase conductors are formed gradually. The insulator voltage does not drop to zero instantly after the peak due to the traveling wave attenuation characteristics along the tower.

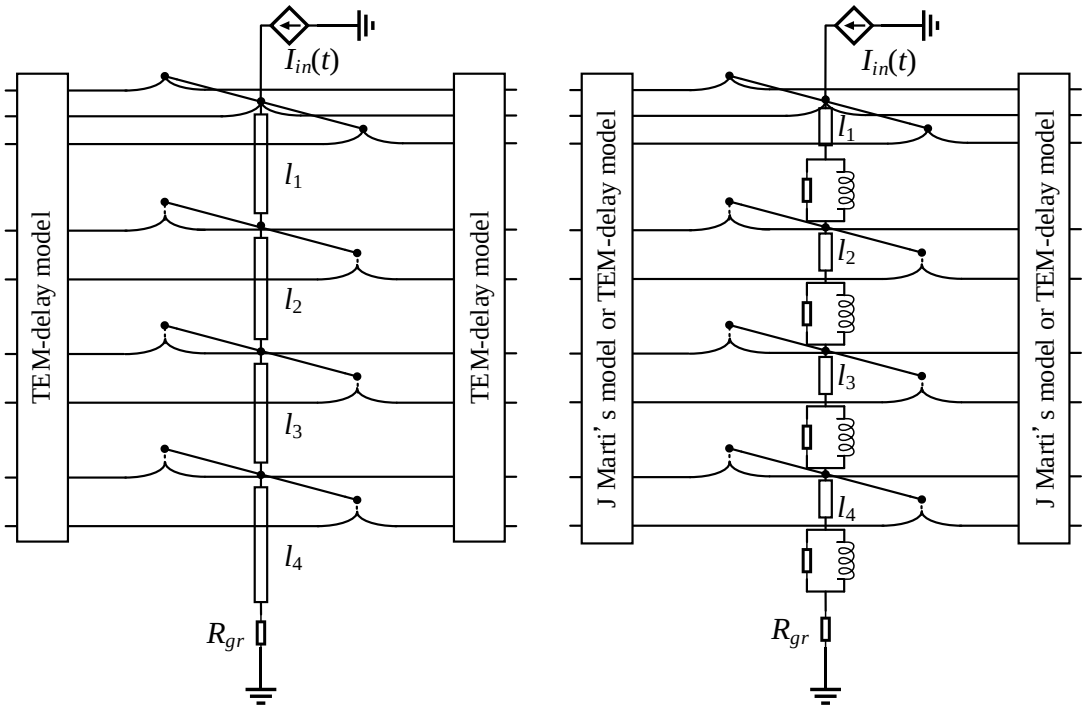

(a) TEM-delay model (b) Multistory model

Fig. 3.12 Circuit model for reproducing surge experiment performed using an actual 500-kV transmission tower performed in the past.

The multistory tower model with J. Marti's frequency-dependent line model can reproduce the peak voltages of 1-μs and 3-μs with a difference of 20% but cannot reproduce other characteristics of the measured waveforms. Fig. 3.13 (b) shows the insulator voltages calculated using this model. In the simulation results, each insulator voltage shows an initial undershoot because the upper-phase conductor voltage rises instantly due to the instant mutual coupling from the OHGWs to the phase conductor. Further, the insulator voltages attain their peaks just after the current injection in the case of the step current injection and at approximately 0.6 μs (= (89.5 m + 79.0 m) /300 m/μs) in the case of injection of 1-μs and 3-μs currents. The voltages attain their peaks in that way because the multistory tower model and the frequency-dependent transmission line model do not consider the gradually rising characteristics of the tower surge impedance and that of the self and mutual surge impedance of the transmission line. The initial deviation of the step current response from the experimental result can affect the analysis of a phenomenon accompanied by extremely steep voltage changes, such as the BFO. The measured peak voltages are reproduced with a difference of approximately 20% in the injections of 1-μs and 3-μs currents.

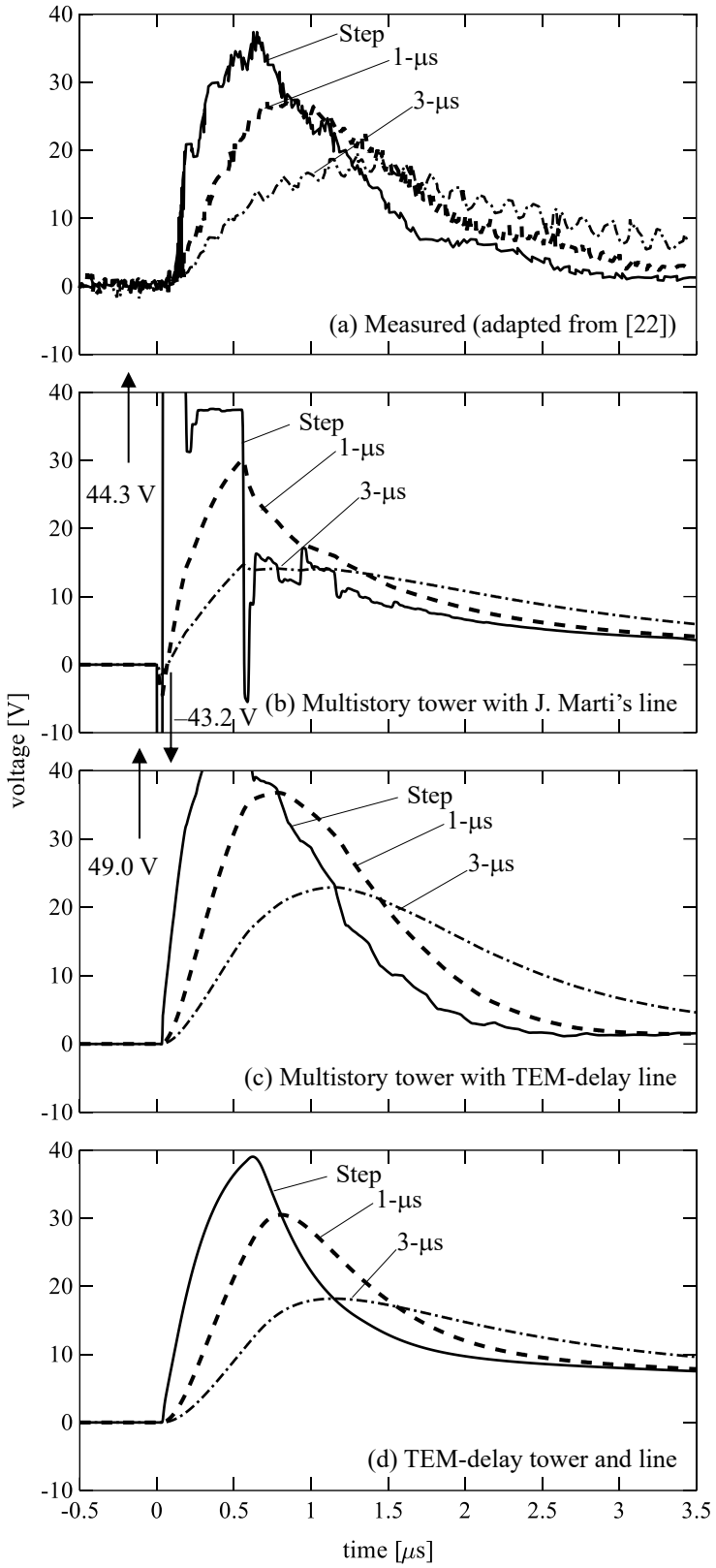

Fig. 3.13 Upper insulator voltages measured at an actual 500-kV tower and their simulation results.

The multistory tower model with the TEM-delay line model can reproduce the non-TEM characteristics of the transmission line. However, the computed insulator voltages become higher than the measured voltages. Fig. 3.13 (c) shows the insulator voltages calculated using this model. In this case, the initial undershoot of the insulator voltage is not observed because the mutual couplings between the OHGWs and the phase conductors are formed with a time delay corresponding to the line separation distances. Besides, the peak time of the insulator voltage is delayed as the rise time of the injected current increases, which is similar to the experimental results owing to the gradual rise of the OHGW self-surge impedance. However, the peak voltages derived using the three injected currents are higher than the measured voltages. The higher voltages are derived because the circuit parameters of the multistory tower model have been set to reproduce the observed insulator voltages in the experiments when the TEM-mode transmission line model, which does not represent the initial low mutual surge impedance, is considered.

The TEM-delay tower and line models can reproduce the measured insulator voltages. Fig. 3.13 (d) shows the computed voltages using these models. In this case as well, the initial undershoot of the insulator voltage is not observed because the TEM-delay line model considers the delay of the TEM-mode formation in the transmission line. Besides, the measured peak voltages and their observed times are reproduced with 10% or lower differences because the TEM-delay tower model successfully considers the non-TEM characteristics of the transmission tower.

The TEM-delay tower model without cross-arms has successfully reproduced the measured insulator voltages of the actual 500-kV transmission tower with overhead transmission lines. However, the existing models cannot reproduce them, and they can have limitations in analyzing the transient phenomenon, especially that accompanied by the extremely steep voltage changes. Note that the TEM-delay tower model with the TEM-mode transmission line model yields lower voltages due to the initially higher mutual coupling among OHGWs and phase conductors, in contrast to the case using the multistory tower with the TEM-delay line models.

3.3.2 FDTD-computed insulator voltages for several towers

The TEM-delay transmission tower and line models are validated by the FDTD-computed insulator voltages. Firstly, the 76-m high transmission tower discussed in Chapter 2 was analyzed. Then, additional three towers with a height of 86 m, 66 m, and 39.5 m were analyzed. The FDTD analysis condition for the 76-m high transmission tower was the same as that analyzed in Chapter 2, except for the current waveform. The current waveform was the step-like current having a constant rising rate with a front time of 1 μs and 2 μs. The current peak was normalized to 1 A since the present analysis does not consider nonlinear characteristics. The current waveform is usually used in an insulation design of substations and lightning performance analysis of transmission lines. The circuit analysis was performed using,

1) TEM-delay tower and line model;
2) Multistory tower model with J. Marti's frequency-dependent transmission line model.

The TEM-delay model well reproduces the 1-μs and 2-μs current responses of the 76-m high tower computed with the FDTD method. In contrast, the multistory tower model with J. Marti's frequency-dependent line model generated lower insulator voltages. Fig. 3.14 shows the transient analysis results. The figures show the injected, tower top, and grounding wire currents (I_{in}, I_T, I_{gw}), voltages of upper, middle, and lower insulators (V_U, V_M, V_L), and those of tower top and upper, middle, lower phase conductors (V_T, V_{pU}, V_{pM}, V_{pL}). The waveforms generated by both 1-μs and 2-μs currents computed by the presented TEM-delay model agree well with those by the FDTD method. The model reproduces the characteristics of the TEM-mode formation process: the more gradual rise of the voltages than that of the injected current, the gradual voltage decay after each peak, and initially low coupling between the OHGWs and phase conductors.

The multistory tower model yields the same height dependence of the voltages across insulator strings ($V_U > V_M > V_L$) as the FDTD method does, but the insulator voltages are lower than the FDTD-computed voltages. Besides, the voltages rise and decay faster. The voltages rise and decay faster because the multistory model does not consider the gradual rise of tower and line surge impedance and also does not represent the propagation characteristic of the traveling wave along the tower enough. The insufficient implementation of the propagation characteristics results in the lower insulator voltages by 2-μs current than the 1-μs current comparing with the FDTD analysis. The lower insulator voltages can also be attributed to the negative-angle current injection in the experiment, on which the multistory tower model bases. This aspect will be further discussed in Chapter 4. It should be noted that the multistory tower model better calculated the insulator voltages compared to the basic model shown in Fig. 2.6.

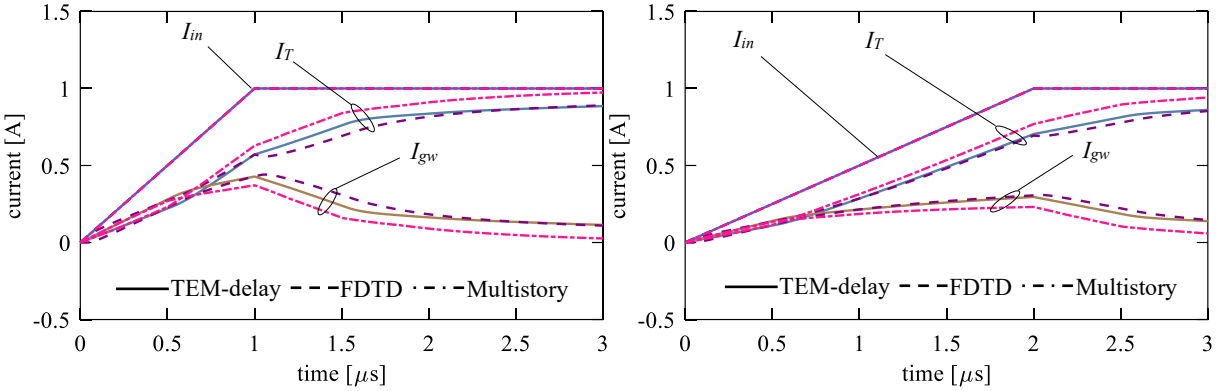

(a-1) 1-μs (a-2) 2-μs

(a) Current

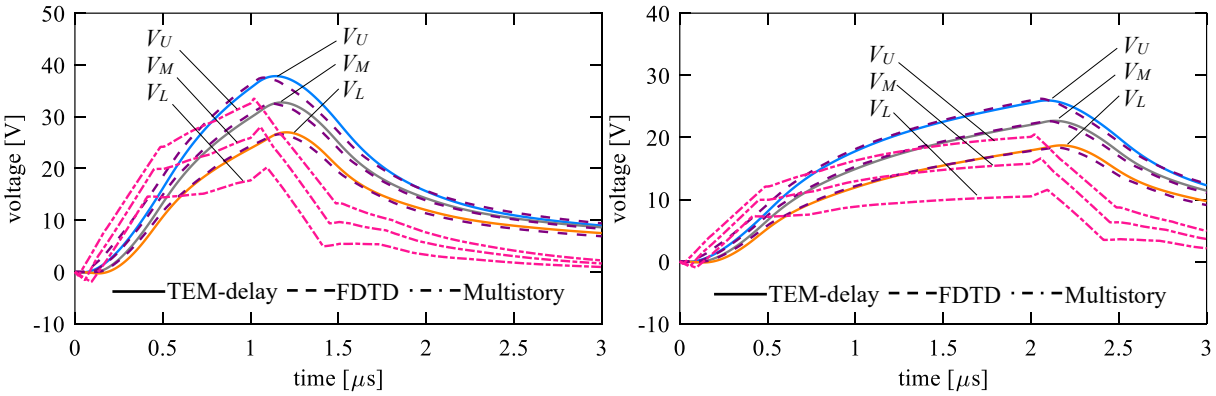

(b-1) 1-μs (b-2) 2-μs

(b) Insulator voltage

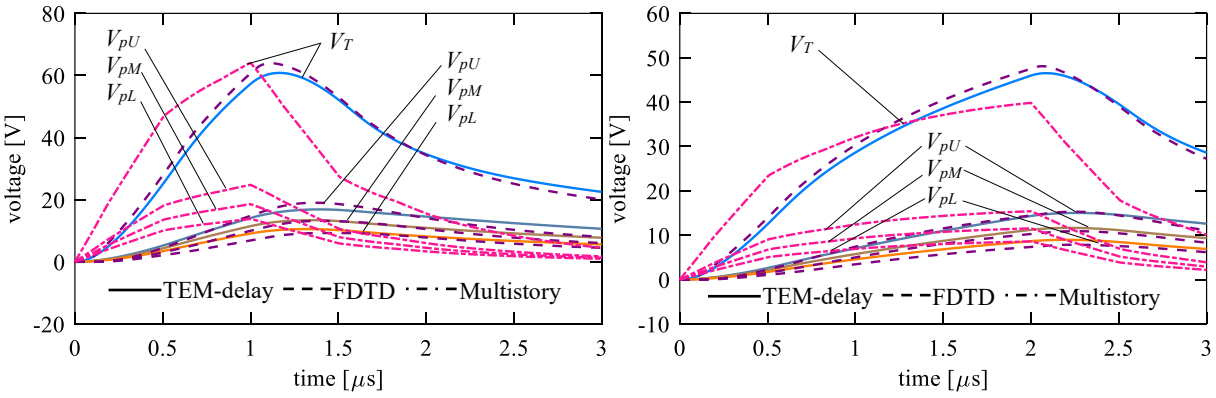

(c-1) 1-μs (c-2) 2-μs

(c) Voltage of the tower top and phase conductors

Fig. 3.14 1-μs and 2-μs ramp current responses of a 76-m high 500-kV vertical double-circuit transmission tower computed with the proposed circuit model and the FDTD method.

The other three vertical double-circuit transmission towers were studied to confirm the generality of the TEM-delay transmission tower and line models. Fig. 3.15 shows the shapes of 86-m, 66-m, and 39.5-m high transmission towers. The voltages of the insulator strings to 1-μs and 2-μs linearly rising step-like currents were computed by the same condition of the FDTD method as the 76-m high tower case for the 86-m and 66-m high towers. For the 39.5-m high tower with a single OHGW, the spatial discretization of the FDTD analysis was reduced from the 1-m side-length cubic to the 0.5-m cubic to model the smaller tower structure. The OHGW and phase conductors, with radii of 5.25 mm and 9.10 mm, were modeled by the thin wire representation method.

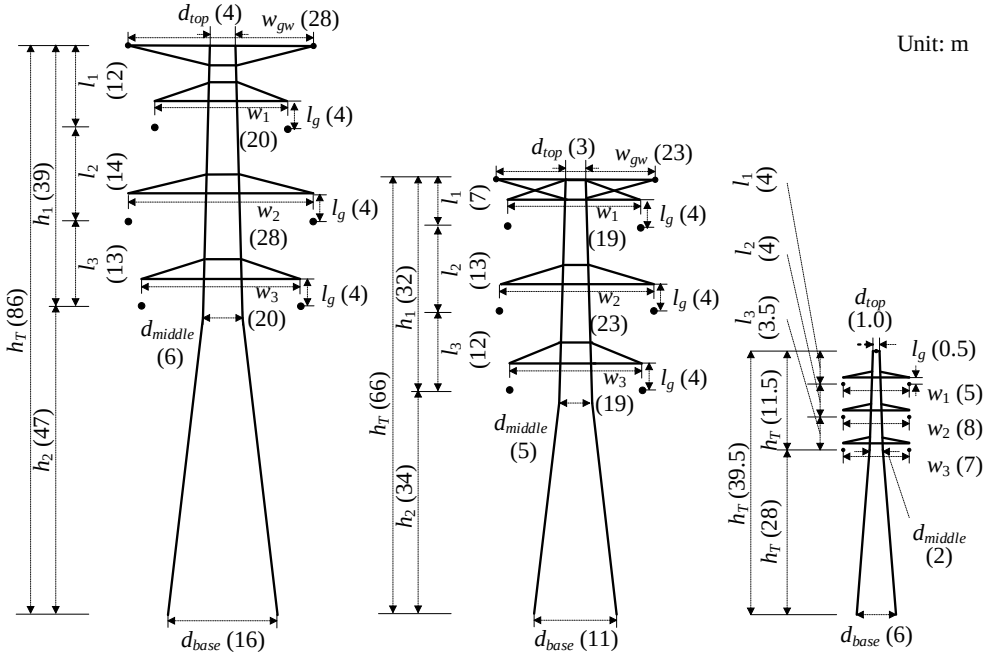

Fig. 3.15 The shape of the towers whose insulator voltages were analyzed by the FDTD method and circuit analysis by the TEM-delay model and the multistory tower model.

In the other three types of tower cases as well, The TEM-delay model well reproduces the 1-μs and 2-μs current responses computed with the FDTD method. In contrast, the multistory tower model with J. Marti's frequency-dependent line model generated lower insulator voltages. Fig. 3.16 shows the waveforms of voltages across insulator strings computed by the FDTD method and the circuit analysis using the TEM-delay and the multistory models. Higher voltages are generated across insulator strings as increasing tower height owing to their higher surge impedance and longer round-trip time. For the tower with a height of 39.5 m, the difference in peak voltages of the upper to lower insulator strings is insignificant compared to the other taller towers due to its short distance between the phases. The voltages computed by the FDTD method and the TEM-delay model are similar, including their waveforms and peaks. However, the multistory tower model yields smaller peak voltages, especially for the smaller towers. Table 3.2 summarizes peaks of the voltages across insulator strings computed by the

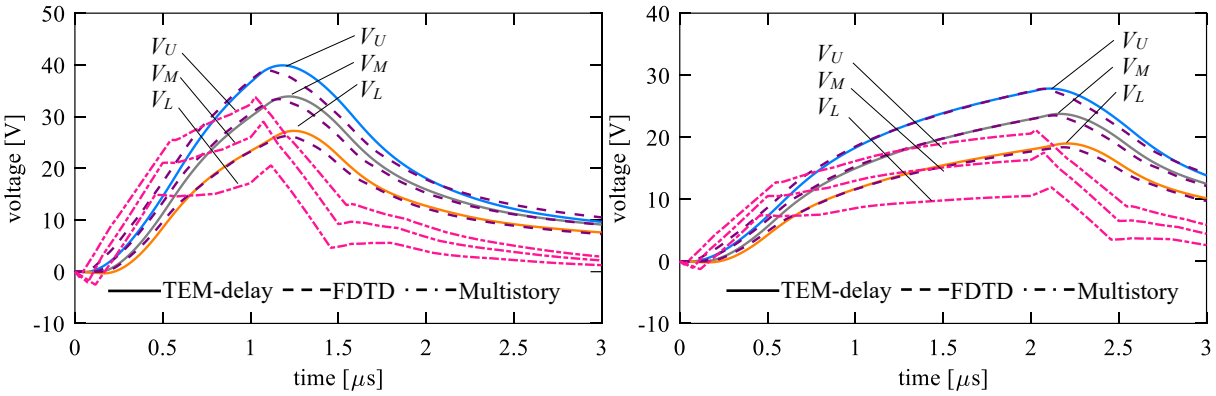

(a-1) 1-μs (a-2) 2-μs

(a) 86-m tower

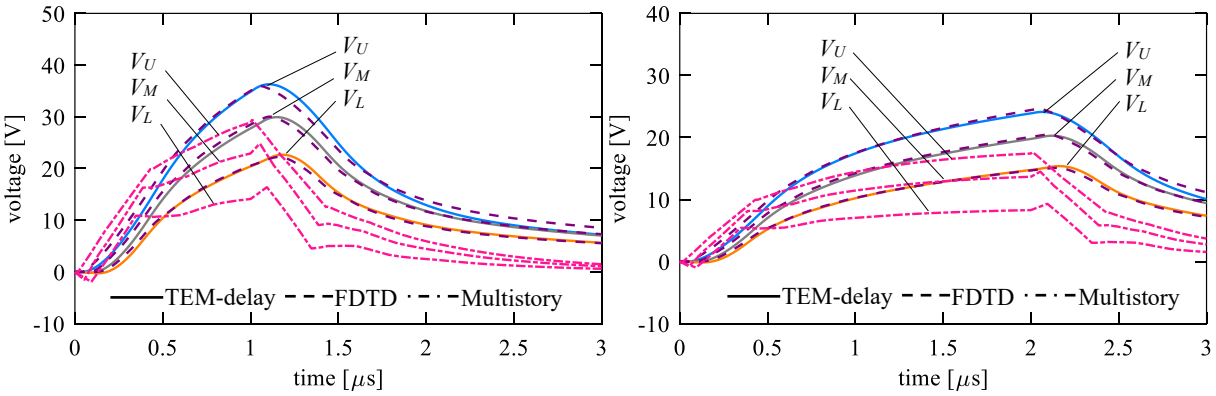

(b-1) 1-μs (b-2) 2-μs

(b) 66-m tower

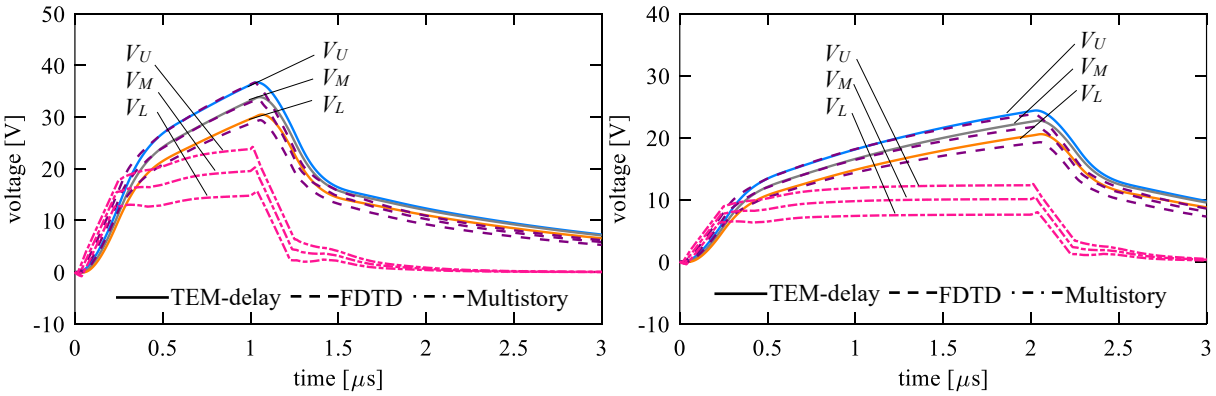

(c-1) 1-μs (c-2) 2-μs

(c) 39.5-m tower

Fig. 3.16 Voltages of insulator strings generated when lightning strikes 86-m, 66-m, or 39.5-m high vertical double-circuit transmission tower (the injection current was normalized to 1 A).

FDTD method and each circuit model as well as the differences between the results computed by the FDTD method and the circuit models. The results show the generality and applicability of the proposed circuit model to analyze vertical double-circuit transmission towers.

Table 3.2 Peaks of voltages across insulator strings computed by the multistory tower model and the proposed model, and their differences from the FDTD computation results [a].

Height	Phase	FDTD [V]	Multistory [V]	Diff., %	Proposed [V]	Diff., %
86 m	Upper	38.9,27.8	33.8, 21.2	–13, –24	39.9, 27.8	2.5, 0.2
	Middle	33.4, 23.5	29.0, 17.5	–13, –26	33.9, 23.8	1.6, 1.0
	Lower	26.2, 18.4	20.5, 11.9	–22, –35	27.2, 19.0	3.8, 3.3
76 m	Upper	37.6, 26.2	33.5, 20.5	–11, –22	37.8, 26.0	0.7,–1.0
	Middle	32.5, 22.6	28.0, 16.6	–14, –27	32.7, 22.7	0.7, 0.3
	Lower	26.6, 18.4	20.2, 11.5	–24, –37	27.0, 18.7	1.4, 2.0
66 m	Upper	35.9, 24.6	29.4, 17.6	–18, –28	36.3, 24.1	1.0,–2.1
	Middle	30.0, 20.5	24.8, 14.5	–17, –29	29.9, 20.3	–0.3,–0.9
	Lower	22.2, 15.1	16.4, 9.31	–26, –38	22.7, 15.4	2.0, 1.9
39.5 m	Upper	36.7, 23.8	24.2, 12.5	–34, –47	36.7, 24.4	0.0, 2.3
	Middle	33.4, 21.8	20.3, 10.4	–39, –52	33.8, 22.8	1.3, 4.3
	Lower	29.4, 19.3	15.6, 8.00	–47, –59	30.5, 20.6	3.7, 6.7

[a] (xx, xx) denotes results computed by the (1-μs, 2-μs) ramp current

3.3.3 FDTD-computed insulator voltages due to a lightning strike to a tip of ground wire cross-arm

The TEM-delay transmission tower model considering the cross-arms is validated by comparing the FDTD analysis results and those by the TEM-delay model. The model with cross-arms can consider the lightning-struck point and the voltage difference of the lightning-struck side and the other side. Note that the model without cross-arms can still reproduce the insulator voltages. The studied tower is the 76-m high transmission tower analyzed in Section 2.1, shown in Fig. 2.2. A lightning channel model represented by a phased-current-source array was attached to the tip of the tower top cross-arm in the FDTD analysis.

The TEM-delay model with cross-arms was employed for the analysis. Fig. 3.17 illustrates the circuit model. In the circuit analysis, a current source was connected to the tip of the tower top cross-arm. Then, the current source injected the 1-A peak step-current having 1-μs or 2-μs linearly rising wavefront. Table 3.3 summarizes the convergence value of the surge impedance of the cross-arms considered in the TEM-delay tower model. The surge impedance was determined as described in Section 3.2.1.B. For the comparison study, the analysis was also performed using the TEM-delay tower model with cross-arm without considering the mutual coupling among the cross-arms.

Table 3.3 Convergence values of cross-arms self and mutual surge impedance in ohm.

	Ground wire	Upper	Middle	Lower
Ground wire	294	159	110	79.3
Upper	159	261	144	96.6
Middle	110	144	250	132
Lower	79.3	96.6	132	228

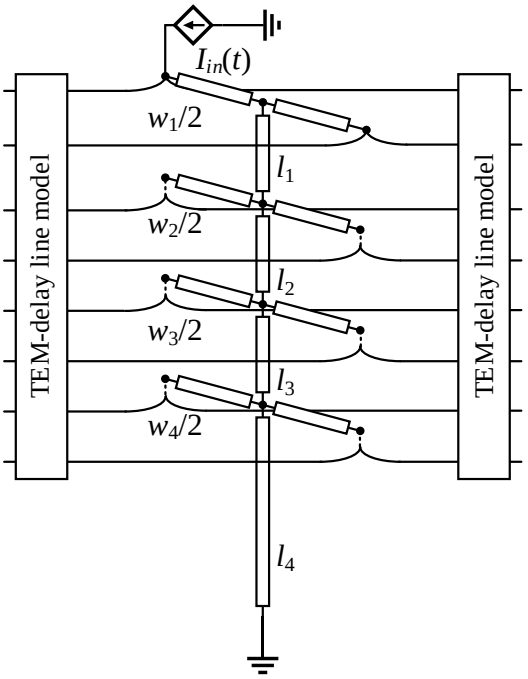

Fig. 3.17 Circuit model for analyzing lightning strike to the tip of tower top cross-arm using the TEM-delay tower model with cross-arms with and without considering the mutual couplings.

Firstly, the performance of the TEM-delay tower model with cross-arm without considering the mutual coupling among the cross-arms is discussed. The consideration of the cross-arms simply following the tower shape [32] without considering the mutual coupling among them cannot reproduce the effect of the asymmetrical lightning strike. Although the model with cross-arms without the mutual coupling cannot consider the voltage difference of the lightning-struck side and the other side, the computed insulator voltages still agree with those computed by the FDTD method. Fig. 3.18 (a) shows the FDTD-computed voltages, and Fig. 3.18 (b) shows those computed by the TEM-delay tower model with cross-arms without considering the mutual coupling among the cross-arms. Even though the current was injected into the tip of the tower top cross-arm, almost the same insulator voltages were yielded on both sides in the circuit analysis. The same voltages are derived because the voltages of the upper, middle, and lower cross-arms on both sides become essentially identical to each other in this model. In other words, a tower model with cross-arms just representing the tower shape cannot reproduce the off-center

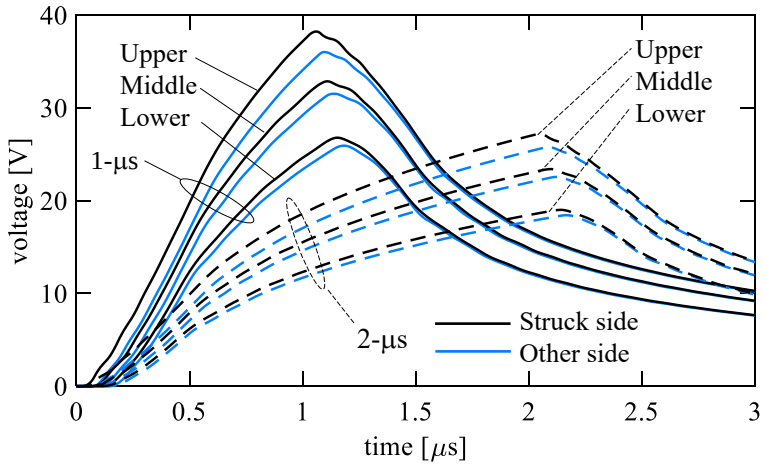

(a) FDTD-computed voltages (same as Fig. 2.7 (b))

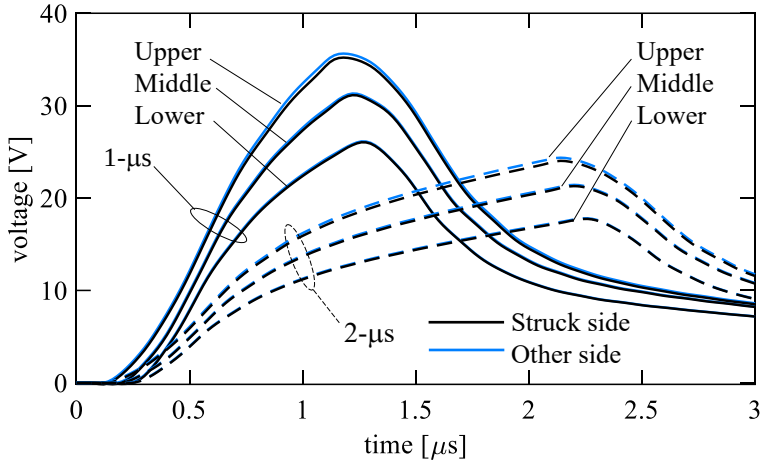

(b) Voltages computed by the TEM-delay model with cross-arms without mutual couplings

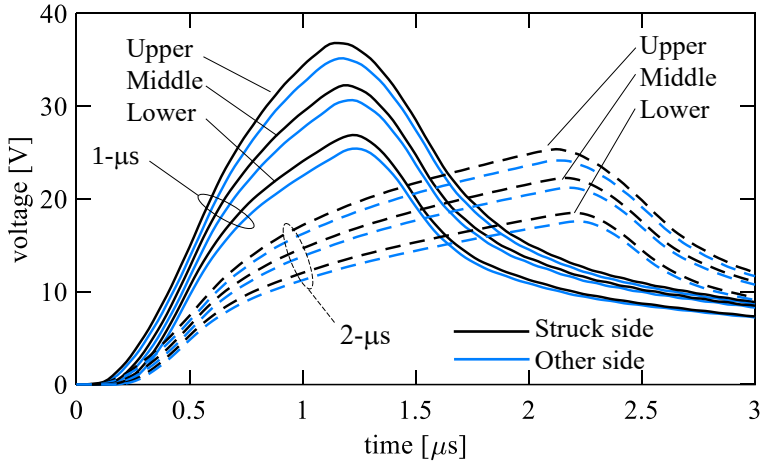

(c) Voltages computed by the TEM-delay model with cross-arms with mutual couplings

Fig. 3.18 Voltages generated by a lightning strike to the tip of ground-wire cross arm computed by the TEM-delay tower model with cross-arms (the injection current was normalized to 1 A).

lightning. Note that the slight difference in computed insulator voltages arises because the voltage rises of the lightning-struck side OHGW and phase conductors are slightly higher than those of the other side. This voltage difference in the lines is caused by the effect of the in total 23-m long tower top cross-arm. The insulator voltages, however, still agree well with the FDTD computed results. Thus, in analyzing a smaller tower, a tower with short cross-arms for ground wires, or a tower with a single OHGW, this tower model (model with cross-arms without considering mutual coupling among them) or the basic TEM-delay model (model without cross-arms) can yield sufficiently accurate insulator voltages.

The TEM-delay tower model with cross-arm reproduces the insulator voltages depending on the lightning-struck side. Fig. 3.18 (c) shows the voltages across insulator strings computed by the TEM-delay model considering the mutual coupling among the tower cross-arms. This model yields higher voltages across the insulators located on the lightning-struck side than those on the other side, as the FDTD analysis results. The difference in the voltage peaks between the circuit analysis and FDTD analysis results is less than 10%, as summarized in Table 3.4. The presented tower model can approximately consider the presence of the tower cross-arms and the difference of insulator voltages between the lightning-struck side and the other side. The TEM-delay tower model with cross-arm enables in-depth analysis of lightning surges considering lightning-struck point and BFO phases.

Table 3.4 Insulator voltages computed by the FDTD method and the proposed circuit model (the injection current was normalized to 1 A).

Rise rime	Phase	Struck side [V]		Other side [V]	
		FDTD	Proposed	FDTD	Proposed
1 μs	Upper	37.7	38.3	35.2	36.4
	Middle	32.2	33.4	30.7	31.7
	Lower	26.3	27.9	25.4	26.4
2 μs	Upper	26.9	26.7	25.3	25.3
	Middle	23.0	23.3	22.1	22.1
	Lower	18.7	19.3	18.1	18.3

3.3.4 Surge experiment on an actual UHV transmission tower

Waveforms of voltages measured at an actual 140-m high UHV transmission tower [19] were reproduced using the proposed TEM-delay tower model considering the mutual couplings among the tower cross-arms. Fig. 3.19 shows the setup of an experiment performed for the UHV transmission tower. In this experiment, a step current was injected into the center of the tower top using a PG. The PG was connected to a horizontally tensioned injection wire via a 2.5-kΩ resistor. The injection wire was a 1-mm radius copper wire, and it was terminated by a matching resistance of about 750 Ω. The voltages of the tower cross-arms and phase conductors were measured using an auxiliary potential wire. Besides, the voltages across insulator strings were measured (but only on one side).

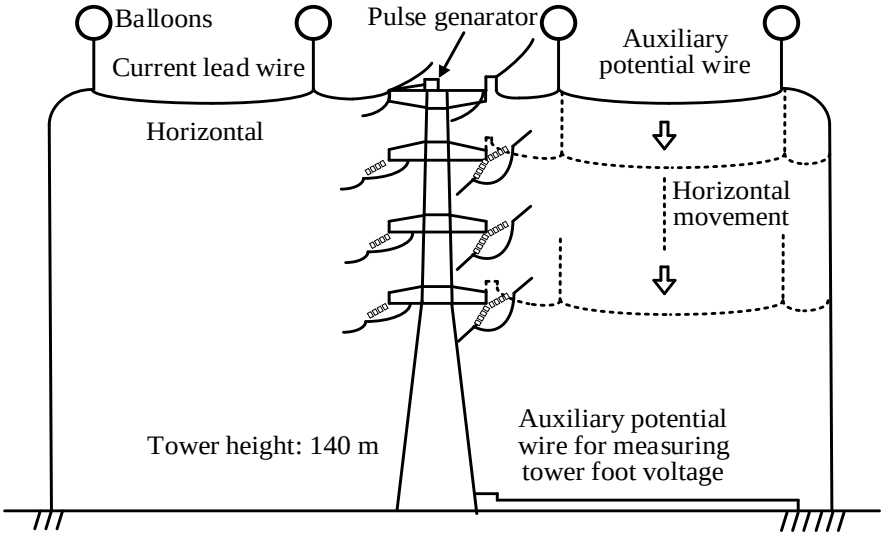

Fig. 3.19 Measurement setup for an actual UHV transmission tower.

The circuit analyses were performed using the TEM-delay tower model with cross-arms and the multistory tower model with J. Marti's frequency-dependent line model. The multistory tower model used in this analysis was the model for analyzing the UHV transmission tower proposed in [19]. In the multistory tower model for the UHV transmission tower, both the tower surge impedances, Z_{T1} and Z_{T2}, for the upper and lower parts are set to 120 Ω. In addition, the attenuation coefficient γ is set to 0.7 so that the model can well reproduce the measured peaks of insulator voltages. Note that in the original model for 500-kV transmission towers, Z_{T1} and Z_{T2} are set to 220 Ω and 150 Ω, and γ is set to 0.8. Also, note that in the TEM-delay model, the tower surge impedance was multiplied by 0.7 to consider the effect of the horizontally arranged current injection wire [20]. The DC grounding resistance was 2.0 Ω for the studied tower. The injected current waveform was the 1/70 μs triangular current with a 1-A peak, and the source circuit shown in Fig. 3.20 was employed [19].

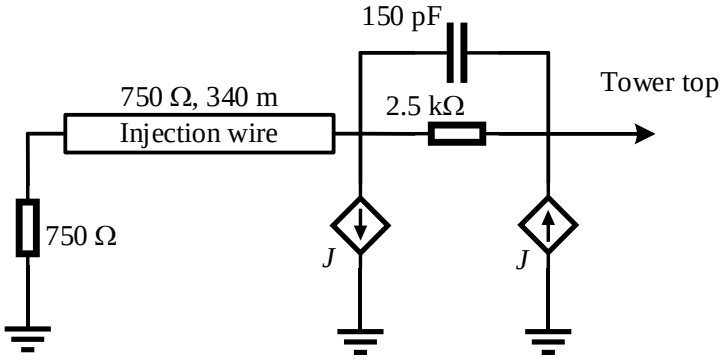

(a) Source circuit

Fig. 3.20 Circuit model for reproducing surge experiment performed at an actual UHV transmission tower in the past (this figure follows to the next page).

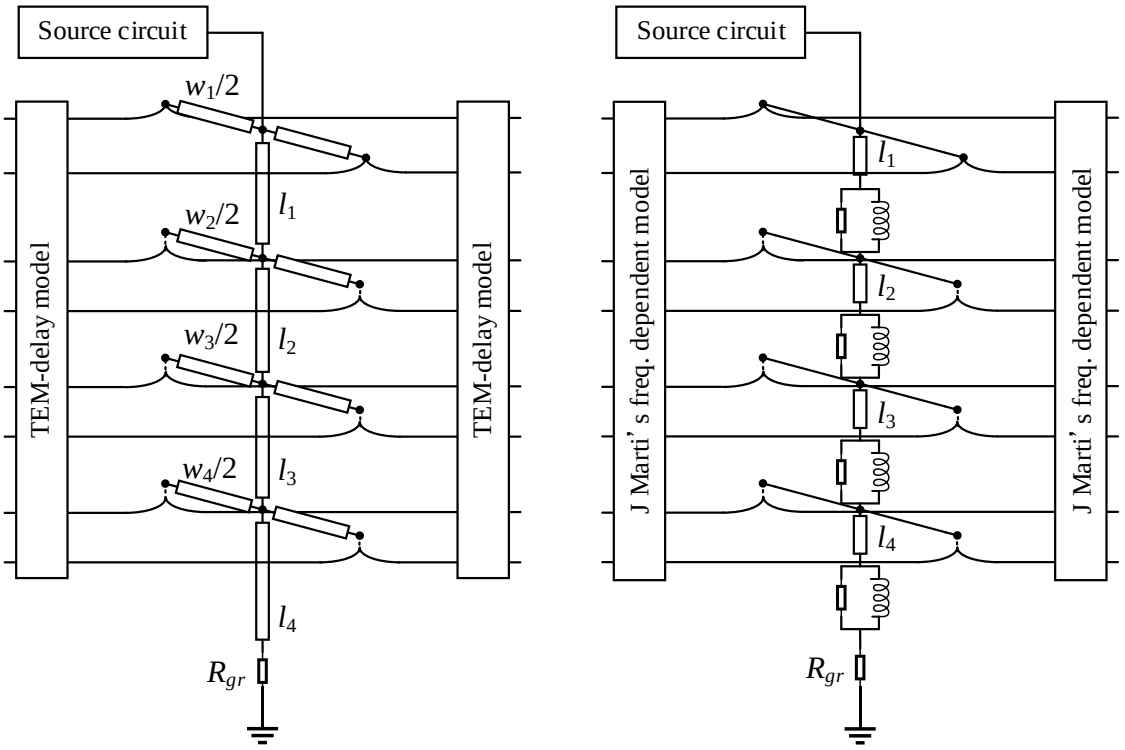

(b) TEM-delay model (c) Multistory model

Fig. 3.20 Circuit model for reproducing surge experiment performed at an actual UHV transmission tower in the past (this figure is followed from the previous page).

Both the TEM-delay tower model and the multistory tower model tuned for analyzing the UHV transmission tower reproduce the measured insulator voltage peaks. Fig. 3.21 shows the measured and simulated voltages of upper-phase cross-arm, insulator, and phase conductors. Table 3.5 summarizes the peak insulator voltages in the upper, middle, and lower phases by the experiment and simulations. As shown in the figure and the table, both the TEM-delay tower and the multistory tower models yield similar peaks of voltages in any observation point. These results show the applicability of the proposed tower model for the actual towers. Note that in the measured waveforms, the voltages decay faster after taking their peaks. For instance, the voltage of the upper-phase cross-arm crosses zero at around 2.8 μs in the measured waveform, while the simulated voltages do not cross at that time. This difference is caused by the effect of the auxiliary potential wire, as discussed in [19]. It has also been shown in [22] that the tower voltages decay faster with the horizontal current injection than those induced by the current injection from the upper angles. This characteristic will be further discussed in Chapter 4.

The TEM-delay tower model better reproduces the rising part of the voltages and does not need parameter tuning for analyzing the UHV transmission tower. The TEM-delay model yields a more similar rising part of voltage to the corresponding measured voltage since it includes the delay of the TEM-mode formation. Besides, the model does not need any trial-and-error process for determining the

model parameters since they are determined directly by the configuration of the tower. This fact shows the rationality and usefulness of the TEM-delay model.

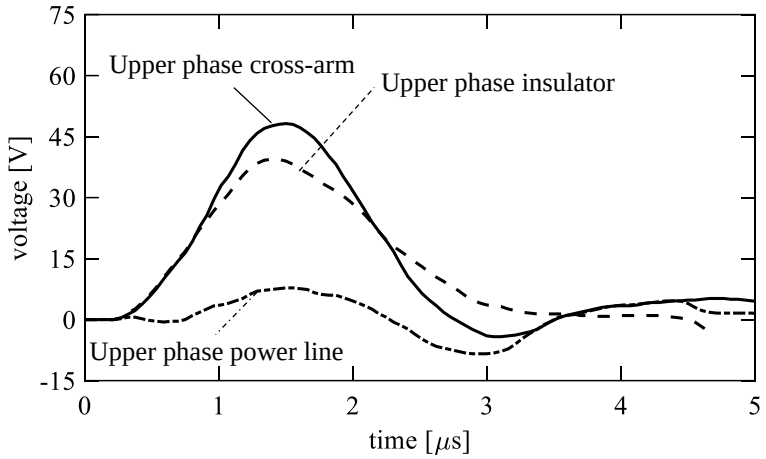

(a) Measured voltages (adapted from [19])

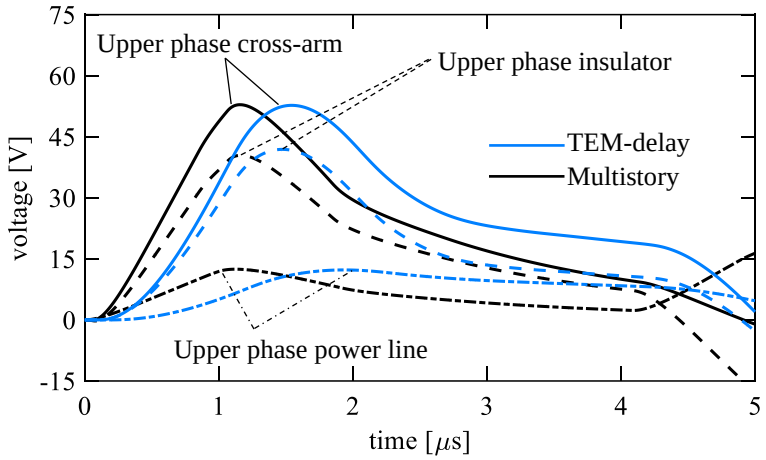

(b) Simulated voltages by the proposed TEM-delay model and the multistory tower model

Fig. 3.21 Reproduction of surge responses of an actual UHV transmission tower.

Table 3.5 Comparison of peak voltages across insulator strings induced by 1-A peak current obtained by the measurement and circuit analysis models.

Phase	Measured [19]	Proposed model	Multistory model ($Z_{T1} = Z_{T2} = 120\ \Omega$) [19]
Upper	39.2 V	41.9 V (+6.7%)	41.6 V (+6.1%)
Middle	34.9 V	38.1 V (+9.3%)	39.1 V (+12%)
Lower	30.6 V	33.5 V (+9.6%)	33.7 V (+10%)

3.4 Conclusions

In this chapter, the TEM-delay transmission tower and line models have been presented. The model can consider the non-TEM characteristics of the transmission tower and line. The gradually rising characteristics of the tower surge impedance and the self and mutual surge impedance of the transmission line are represented by the first-order delay functions. The time delay in mutual coupling among lines corresponding to their separation distances is considered in the circuit analysis through phase domain modeling. The significant attenuation of traveling waves along the tower is considered by the propagation function. The model parameters can be derived from the configuration of the tower and line without any numerical electromagnetic analysis or trial-and-error process. The extended TEM-delay tower model with cross-arms can even represent the lightning strike to the tip of the tower top cross-arm and resultant different insulator voltages depending on the side of the tower.

The presented model has been validated by the results of surge experiments reported in the past and the FDTD analysis considering the lightning strike to the center of the tower top and the tip of the tower top cross-arm. The results of surge experiments include those performed for an 89.5-m high 500-kV transmission tower with and without overhead transmission lines and for a 140-m high UHV transmission tower with overhead lines. The FDTD analysis results include 86-m, 76-m, 66-m, and 39.5-m high towers. The TEM-delay model can be applied to analyze various shapes of the tower. The validation study has also revealed that the most widely and frequently used multistory tower model with frequency-dependent transmission line model could have underestimated the insulator voltages, especially those generated by a vertical lightning channel. The performance of the transmission tower and line models should be carefully examined for analyzing lightning transients in transmission lines, such as BFOs.

References for Chapter 3

[1] A. Semlyen, and A. Dabuleanu, “Fast and accurate switching transient calculations on transmission lines with ground return using recursive convolutions,” *IEEE Trans. Power App. Syst.*, vol. PAS-94, no. 2, pp. 561–571, Mar. 1975.

[2] J. R. Marti, “Accurate modelling of frequency-dependent transmission lines in electromagnetic transient simulations,” *IEEE Trans. Power App. Syst.*, vol. PAS-101, no. 1, pp. 147–157, Jan. 1982.

[3] T. Noda, N. Nagaoka, and A. Ametani, “Phase domain modeling of frequency-dependent transmission lines by means of an ARMA model,” *IEEE Trans. Power Del.*, vol. 11, no. 1, pp. 401–411, Jan. 1996.

[4] T. Noda, N. Nagaoka, and A. Ametani, “Further improvements to a phase-domain ARMA line model in terms of convolution, steady-state initialization, and stability,” *IEEE Trans. Power Del.*, vol. 12, no. 3, pp. 1327–1334, Jul. 1997.

[5] A. Morched, B. Gustavsen, and M. Tartibi, "A universal model for accurate calculation of electromagnetic transients on overhead lines and underground cables," *IEEE Trans. Power Del.*, vol. 14, no. 3, pp. 1032–1038, Jul. 1999.

[6] T. Noda, "Application of frequency-partitioning fitting to the phase-domain frequency-dependent modeling of overhead transmission lines," *IEEE Trans. Power Del.*, vol. 30, no. 1, pp. 174–183, Feb. 2015.

[7] Can / Am EMTP user group, *Alternative Transients Program (ATP): Rule Book*. 1999.

[8] L. Dubé, and I. Bonfanti, "MODELS: A new simulation tool in the EMTP," *European Trans. Electr. Power*, vol. 2, no. 1, pp. 45–50, 1992.

[9] R. Lundholm, R. B. Finn, Jr., and W. S. Price, "Calculation of transmission line lightning voltages by field concepts," *AIEE Trans. Power App. Syst.*, vol. 77, pp. 1271–1283, Feb. 1958.

[10] C. F. Wagner, and A. R. Hileman, "A new approach to the calculation of the lightning performance of transmission lines III—a simplified method: stroke to tower," *AIEE Trans. Power App. Syst.*, vol. 79, pp. 589–603, Oct. 1960.

[11] M. A. Sargent, and M. Darveniza, "Tower surge impedance," *IEEE Trans. Power App. Syst.*, vol. PAS-88, no. 5, pp. 680–687, May 1969.

[12] H. Motoyama, and H. Matsubara, "Analytical and experimental study on surge response of transmission tower," *IEEE Trans. Power Del.*, vol. 15, no. 2, pp. 812–819, Apr. 2000.

[13] Y. Du, and Y. Ding, "Lightning surge propagation on a single conductor in free space," *IEEE Trans. Electromagn. Compat.*, vol. 59, no. 1, pp. 119–127, Feb. 2017.

[14] A. De Conti, S. Visacro, A. Soares, Jr., and M. A. O. Schroeder, "Revision, extension, and validation of Jordan's formula to calculate the surge impedance of vertical conductors," *IEEE Trans. Electromagn. Compat.*, vol. 48, no. 3, pp. 530–536, Aug. 2006.

[15] IEEE Standards Board, "IEEE guide for improving the lightning performance of transmission lines," *IEEE Std.*, no. 1243-1997, Jun. 1997 (reaffirmed in 2008).

[16] CIGRE WG 33.01 (Lightning), "Guide to procedures for estimating the lightning performance of transmission lines," *CIGRE Technical Brochure*, no. 63, Oct. 1991.

[17] M. Kawai, "Studies of the surge response on a transmission line tower," *IEEE Trans. Power App. Syst.*, vol. PAS-83, no. 1, pp. 30–34, Jan. 1964.

[18] T. Hara, and O. Yamamoto, "Modeling of a transmission tower for lightning-surge analysis," *IEE Proc.-Gener. Transm. Distrib.*, vol. 143, no. 3, pp. 283–289, May 1996.

[19] T. Yamada, A. Mochizuki, J. Sawada, E. Zaima, T. Kawamura, A. Ametani, M, Ishii, and S. Kato, "Experimental evaluation of a UHV tower model for lightning surge analysis," *IEEE Trans. Power Del.*, vol. 10, no. 1, pp. 393–402, Jan. 1995.

[20] H. Motoyama, Y. Kinoshita, K. Nonaka, and Y. Baba, "Experimental and analytical studies on lightning surge response of 500-kV transmission tower," *IEEE Trans. Power Del.*, vol. 24, no. 4, pp. 2232–2239, Oct. 2009.

[21] M. Ishii, T. Kawamura, T. Kouno, E. Ohsaki, K. Murotani, and T. Higuchi, "Multistory transmission tower model for lightning surge analysis," *IEEE Trans. Power Del.*, vol. 6, no. 3, pp. 1327–1335, Jul. 1991.

[22] H. Motoyama, Y. Kinoshita, and K. Nonaka, "Experimental study on lightning surge response of 500-kV transmission tower with overhead lines," *IEEE Trans. Power Del.*, vol. 23, no. 4, pp. 2488–2495, Oct. 2008.

[23] Y. Baba, and V. A. Rakov, "On the mechanism of attenuation of current waves propagating along a vertical perfectly conducting wire above ground: Application to lightning," *IEEE Trans. Electromagn. Compat.*, vol. 47, no. 3, pp. 521–532, Aug. 2005.

[24] N. Nagaoka, "A development of frequency-dependent tower model," *Trans. IEE of Japan*, vol. 111-B, no. 1, pp. 51–56, Jan. 1993.

[25] K. O. Geddes, "Symbolic computation of Pade approximants," *ACM Trans. Math. Software*, vol. 5, no. 2, pp. 218–233, Jun. 1979.

[26] B. Gustavsen, and A. Semlyen, "Rational approximation of frequency domain responses by vector fitting," *IEEE Trans. Power Del.*, vol. 14, no. 3, pp. 1052–1061, Jul. 1999.

[27] N. Nagaoka, and A. Ametani, "A development of a generalized frequency-domain transient program-FTP," *IEEE Trans. Power Del.*, vol. 3, no. 4, pp. 1996–2004, Oct. 1988.

[28] A. Ametani, and T. Kawamura, "A method of a lightning surge analysis recommended in Japan using EMTP," *IEEE Trans. Power Del.*, vol. 20, no. 2, pp. 867–875, Apr. 2005.

[29] J. A. Martinez-Velasco, and F. Castro-Aranda, "Modelling guidelines for overhead transmission lines in lightning studies," *in Proc. Int. CIGRE Zagreb Sym. 2007: Transient Phenomena in Large Electr. Power Syst.*, no. 0503, Zagreb, Croatia, Apr. 2007.

[30] P. Malicki, S. Papenheim, and M. Kizilcay, "Shielding failure analysis of a hybrid transmission line with AC and DC systems on the same tower," *Electr. Power Syst. Res.*, vol. 159, pp. 2–8, Jun. 2018.

[31] N. Itamoto, H. Kawamura, K. Shinjo, Y. Tanaka, and T. Noda, "Lightning fault rate calculation of transmission lines taking statistical variation of arching-horn flashovers into account," *IEEJ Trans. Power and Energy*, vol. 140, no. 2, pp. 126–133, Feb. 2020.

[32] T. Hara, and O. Yamamoto, "Modeling of a transmission tower for lightning-surge analysis," *IEE Proc.-Gener. Transm. Distrib.*, vol. 143, no. 3, pp. 283–289, May 1996.

4 Lightning Surge Analysis of a 77-kV Transmission Line

This chapter discusses BFO occurrence at a 77-kV transmission line based on the circuit analysis method. As introduced in Chapter 1, the lightning-related accidents in transmission lines can be categorized into three, SFFO, BFO, and mid-span BFO. The BFO due to lightning strike to the tower top or OHGWs accounts for the large portion in HV/EHV transmission lines with properly designed OHGWs considering shielding efficiency [1]–[4]. The multiphase BFO, which can cause severe accidents, often occurs in HV transmission lines [2]–[4]. Thus, the multiphase BFO analysis is essential in addition to the BFO rate-related aspects [5]–[7].

Field observations reported in [2] showed that the instantaneous power frequency voltages heavily affect the single and multiphase BFO phases in a 77-kV transmission system. Later in [3], it was clarified that the simplified transmission tower model can reproduce the observed effect of power frequency voltages on BFO phases. In this chapter, the effect of power frequency voltages on the BFO occurrence is further analyzed and discussed considering the multiphase BFOs and minimum lightning current causing BFOs. Moreover, the validity of the current causing BFOs is discussed and confirmed by referencing field observation and simulation results reported in the past.

The followings are the outline of this chapter. In advance of the BFO analysis, the voltage across insulator strings considering tower footing characteristics is discussed based on the FDTD analysis and circuit models. The circuit models include the TEM-delay tower and line models, the simplified tower model, and the multistory tower model. The representation methods of the FO across arcing horns and the TLSA are subsequently provided. Using the circuit models of the transmission tower and line, FO model, and TLSA model, the BFO analysis is performed. The characteristics of BFO occurrence, such as the dependence of BFO phases and minimum lightning current causing BFOs on power frequency voltages, and the effect of current waveforms, are discussed and clarified.

4.1 Insulator Voltages of Lightning-Struck 77-kV Transmission Tower Considering Tower Footing Characteristics

The insulator voltages of the lightning-struck 77-kV transmission tower were analyzed using the FDTD method and circuit analysis models. The circuit models include the TEM-delay model and existing tower and line models that have been used for practical applications. The analysis presented in this section considered the tower footing characteristics. For the basic case, perfectly conducting ground was assumed in the FDTD analysis, and a linear lumped resistor was inserted between the tower foot and the ground. Then the imperfectly conducting ground and tower foundations were introduced. Based on these analyses, this section discusses the effect of the tower footing characteristics on the insulator voltages and the performance of each circuit model.

4.1.1 FDTD analysis model

The FDTD analysis was performed considering the tower footing resistance. Fig. 4.1 shows the studied tower shape and its FDTD analysis model. The tower was a 39.5-m high vertical double-circuit transmission tower having a single OHGW typically used in Japan. The injection current was the 1/70 μs and 2/70 μs triangular current typically used in the lightning surge analysis.

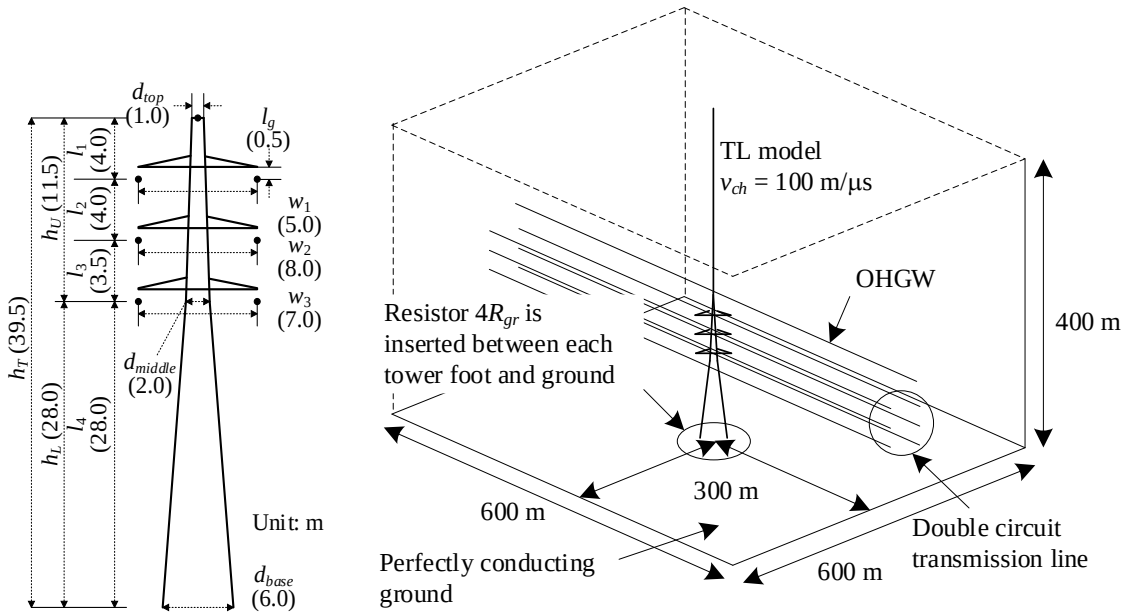

(a) Tower shape (b) FDTD analysis space

Fig. 4.1 Tower shape of the studied 77-kV transmission line and FDTD analysis space.

A Perfectly conducting ground case

The FDTD analysis space of 600 m × 600 m × 400 m was uniformly divided into cubic cells with a side length of 0.5 m. The tower structure was modeled using thin wires, including its slanted parts, represented by the staircase approximation. The radii of the OHGW and the phase conductors were 5.25 mm and 9.1 mm, respectively. They were modeled using the thin-wire representation method, which modifies the permittivity and permeability around the wires [8]. The perfectly conducting ground modeled the bottom surface. The lumped linear resistance $4R_{gr}$ was inserted between the ground and each tower foot to realize the total footing resistance of R_{gr}. The tower footing resistances of 5 Ω, 10 Ω, 20 Ω, and 50 Ω were considered. The limit of the analysis space other than the bottom surface was surrounded using Liao's second-order absorbing boundary [9]. The lightning channel was represented by a transmission line model with a current propagation speed of 100 m/μs and employed in the FDTD calculation using the phased-current-source array. The computation time step was set to 0.674 ns, which is 0.7 times the Courant stability condition, to avoid numerical instability due to the thin wire models [10]. The tip of cross-arms and phase conductors were separated 0.5 m, and insulator voltage was

defined by the electric field between them. A similar tower model was analyzed in [11]. Table 4.1 summarizes the FDTD analysis conditions.

Table 4.1 FDTD analysis condition for analyzing the 77-kV transmission tower.

Analysis space	600 m × 600 m × 400 m
Boundary condition (except for the bottom surface)	Liao's second-order absorbing boundary
Bottom surface	Perfectly conducting plane
Cell size	0.5 m × 0.5 m × 0.5 m
Time step	0.674 ns

B Imperfectly conducting ground case

The FDTD analysis conditions considering the imperfectly conducting ground and tower foundation are introduced. Fig. 4.2 shows the FDTD model in this case. The *z*-axis of analysis space was extended to 500 m, and 100-m thick imperfectly conducting ground was considered. Liao's second-order absorbing boundary was applied to all analysis space limits, including the bottom surface. The relative permittivity of the ground, ε_r, was set to 1, and soil resistivity, ρ_e, was set to 20 Ωm, 200 Ωm, and 1000 Ωm, respectively. The 3.5-m long reverse T-shape foundation was modeled by four-stage perfectly conducting objects with sizes of 0.5 m × 0.5 m × 1.5 m, 1.0 m × 1.0 m × 1.0 m, 1.5 m × 1.5 m × 0.5 m, and 2.0 m × 2.0 m × 0.5 m. The other analysis conditions, such as the tower shape and the computation time step, were the same as the perfectly conducting ground case.

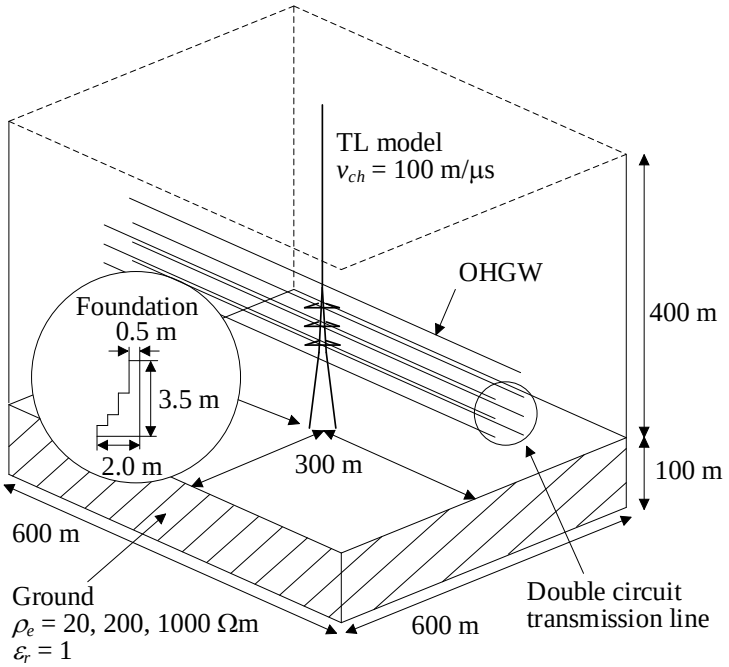

Fig. 4.2 FDTD analysis space of the 77-kV transmission line considering imperfectly conducting ground and tower foundation model.

4.1.2 Circuit analysis model

The circuit analysis was performed using four model sets, including three types of transmission tower models and two types of transmission line models. Fig. 4.3 shows the transmission tower models used in this study, and they are the following models:

(i) TEM-delay tower model + TEM-delay line model (TEM-delay)
(ii) Simplified tower model with constant surge impedance determined by Jordan's formula + frequency-dependent line model (Simplified) [3] [12] [13]
(iii) Multistory tower model with surge impedance of 124 Ω determined by Jordan's formula + frequency-dependent line model (Multistory 124/124) [1]
(iv) Multistory tower model with 220/150 Ω of surge impedance + frequency-dependent line model (Multistory 220/150) [14]

The first model, the TEM-delay model, is the model presented in this thesis. The second model, the Simplified model, was recommended in [3]. In [3], it has been shown that the multistory tower model cannot reproduce the effect of power frequency voltages on BFO phases observed in an actual 77-kV transmission line, but the Simplified model can reproduce. The effect of the power frequency voltages on BFO phases will be discussed in Section 4.3. The third model, Multistory 124/124, was used in [1], [15]–[17]. A lightning fault rate of 77-kV and 275-kV transmission lines was discussed based on this model. The fourth model is the original multistory tower model. This model has been widely used for analyzing lightning transients of vertical double-circuit transmission towers. The wave propagation speed along the tower was set to the speed of light in free space for all models.

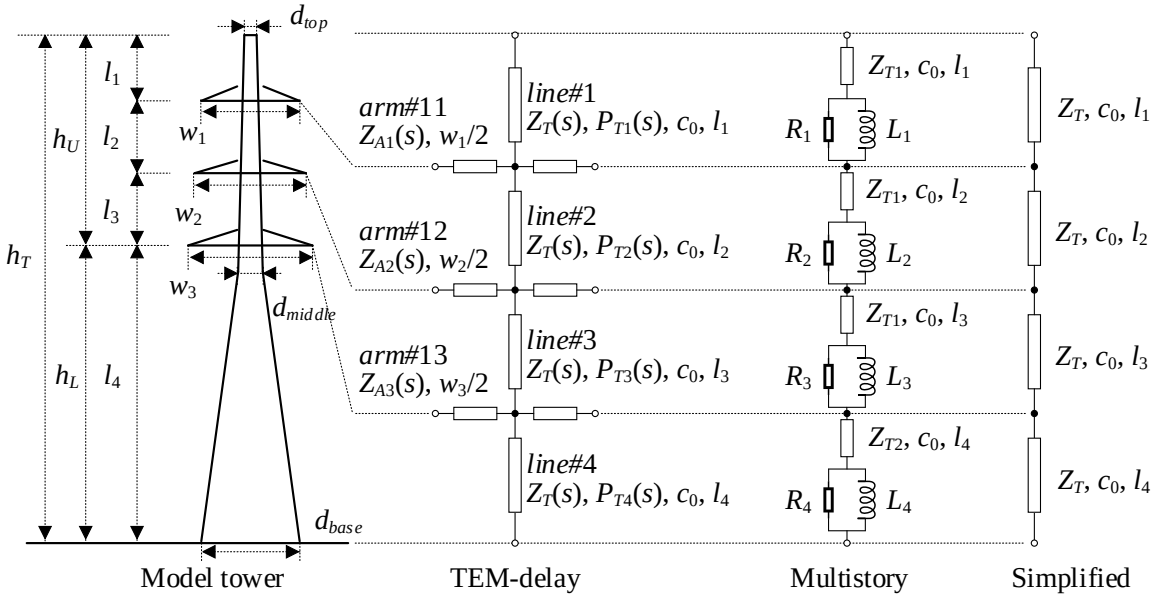

Fig. 4.3 Circuit models of a transmission tower utilized for analyzing the 77-kV transmission line.

The tower foot was modeled by a lumped linear resistor in the circuit analysis method. In the perfectly conducting ground case, lumped resistor with a resistance of 5 Ω, 10 Ω, 20 Ω, and 50 Ω was inserted between the tower foot and ground. In the imperfectly conducting ground case as well, the tower foot was modeled by the lumped resistor, but its resistance was determined differently. The resistance was determined so that the peak value of the upper phase insulator voltage generated by the 1/70 μs triangular current computed by each circuit model reproduces that computed by the FDTD analysis within the difference of 5%. The insulator voltages generated by the 2/70 μs triangular current were computed with the determined resistance in the 1/70 μs triangular current case. Note that at the end of Section 4.1.3, the formula for computing tower footing resistance will be introduced and applied to the studied reverse T-shaped tower foot.

4.1.3 Discussions on insulator voltages

A Perfectly conducting ground case

The TEM-delay model reproduces FDTD computed insulator voltages in a wide range of the tower footing resistance. However, the existing transmission tower and line models yield from 20% to 70% lower voltages than those derived by the FDTD method in this perfectly conducting ground case. Fig. 4.4 shows the voltages computed by the FDTD method and each circuit model in the 10-Ω tower footing resistance case. It appears from Fig. 4.4 that the waveform and magnitude of voltages computed using the TEM-delay model agree well with the corresponding ones computed using the FDTD method. On the other hand, the other circuit models yield relatively lower voltage peaks. Besides, the voltages computed with the Simplified model attain their first peaks around 0.26 μs, at which the traveling wave reflected at the tower base comes back to the top.

Table 4.2 summarizes the computation results by the FDTD method and those by the circuit models in all tower footing resistance cases. The table shows the FDTD-computed peak voltages by the normalized current magnitude. Also, the differences between the voltages computed by the FDTD method and each circuit model are shown in percentage. The results show that voltages computed with the TEM-delay model agree well with FDTD-computed ones in a wide range of grounding resistance. In contrast, the voltage peaks given by the other circuit models are much lower than the peaks given by the FDTD method. Note that the differences are lower for the higher grounding resistance cases since the effect of the tower characteristic on insulator voltages becomes relatively insignificant. Other Simplified models, such as that with the surge impedance of 181 Ω derived by Sargent's formula (2.17) [18] and $0.8c_0$ of surge-propagation speed [19] used in [5], [7], yield almost the same voltage peaks as those given by the Multistory 124/124 model and waveforms similar to those given by the Simplified model. The magnitude of the voltage across insulators significantly affects the occurrence of the BFO. The validity of the computed voltages will be discussed from the viewpoint of BFO occurrences in Section 4.3.

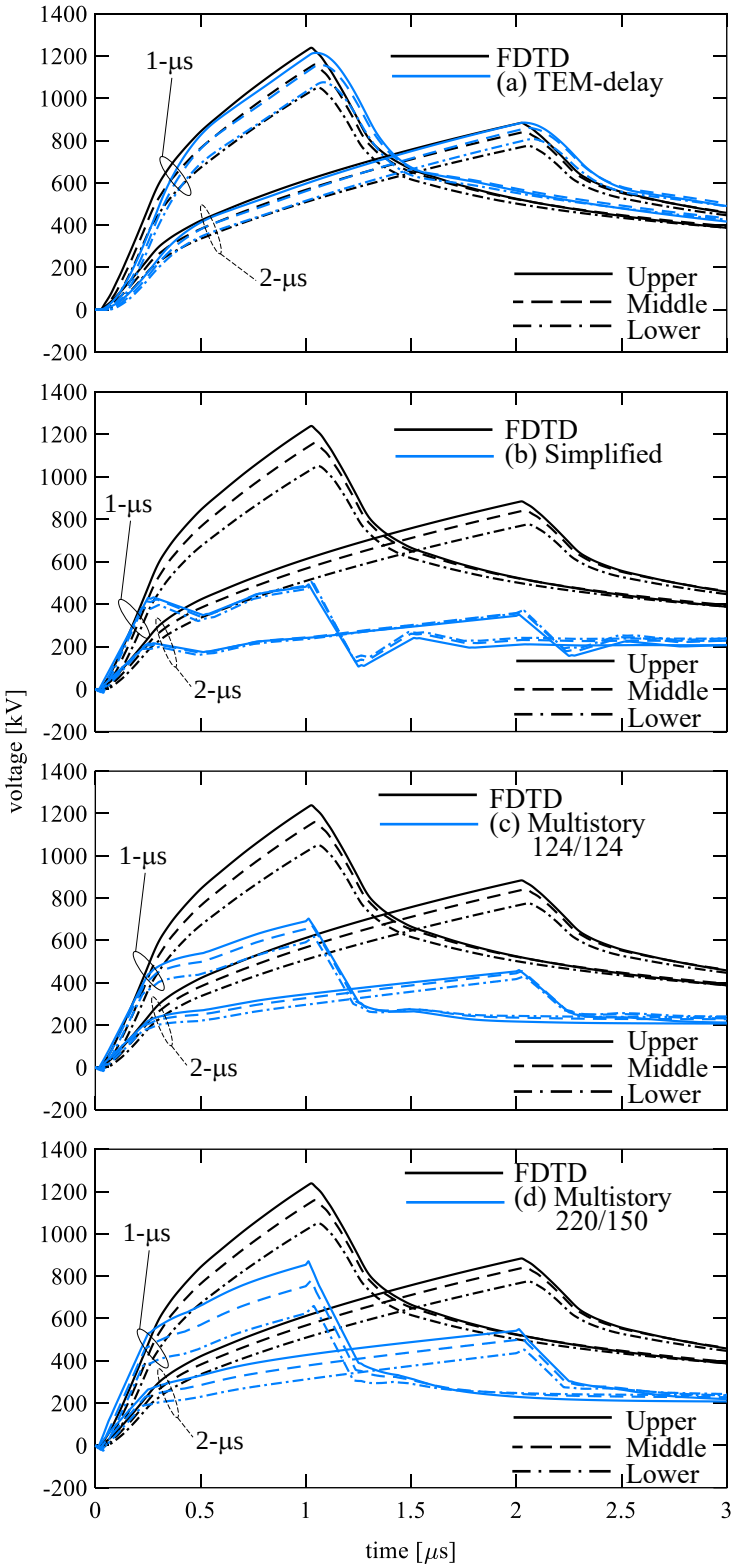

Fig. 4.4 Comparison of insulator voltages computed by the FDTD method and circuit analysis by each model in a 10-Ω tower footing resistance case generated by the 30-kA peak triangular currents.

Table 4.2 Normalized horn voltages computed by the FDTD method and differences in percentage figures between those and voltages computed by circuit analysis with each model with various tower footing resistance, R_{gr} [a].

R_{gr} [Ω]	Phase	FDTD [V/A]	TEM-delay %	Simplified %	Multistory 124/124, %	Multistory 220/150, %
5	Upper	39.0, 26.7	–3, 0	–64, –69	–48, –55	–33, –44
	Middle	36.1, 25.0	–1, 2	–62, –66	–47, –54	–37, –46
	Lower	32.3, 22.6	2, 5	–61, –63	–48, –54	–43, –51
10	Upper	41.3, 29.5	–2, 0	–60, –60	–43, –48	–30, –38
	Middle	38.7, 28.0	0, 2	–56, –56	–42, –46	–33, –39
	Lower	35.0, 25.8	2, 4	–53, –52	–41, –44	–37, –42
20	Upper	45.5, 34.7	–1, 0	–60, –50	–38, –40	–30, –32
	Middle	43.4, 33.8	1, 2	–56, –44	–35, –36	–33, –32
	Lower	40.1, 31.9	3, 4	–53, –40	–34, –35	–37, –33
50	Upper	56.1, 48.2	3, 1	–34, –30	–25, –25	–17, –20
	Middle	55.6, 48.9	4, 2	–28, –25	–22, –21	–17, –18
	Lower	53.3, 47.9	5, 3	–23, –21	–19, –18	–17, –17

[a](xx, xx) shown in each cell denotes results computed by the (1/70 μs, 2/70 μs) triangular current.

Table 4.3 summarizes the differences between the upper-phase insulator and the middle- or lower-phase insulator voltages in percentage. The FDTD-computed results show a tendency that the differences decrease with increasing tower footing resistance and current wavefront durations since the traveling wave effect of the tower becomes insignificant. The results derived by the TEM-delay model show similar characteristics to those derived by the FDTD method in all tower footing resistance cases. The voltage differences derived by other circuit models show characteristics more depending on the tower footing resistance. For instance, the results derived by the Multistory 124/124 model show differences similar to those given by the FDTD method when the grounding resistance, R_{gr}, is 5 Ω or 10 Ω. On the other hand, the results derived by the Multistory 220/150 show those for R_{gr} = 20 Ω or 50 Ω. The Simplified model does not give similar results to the FDTD-computed results in any resistance case. The voltage peaks in each phase affect the BFO phases. This aspect will also be discussed in Section 4.3.

Table 4.3 Differences in percentage between the upper-phase insulator voltage and the middle- or lower-phase horn voltages in cases of various tower footing resistance, R_{gr}.

R_{gr} [Ω]	Phase	FDTD %	TEM-delay %	Simplified %	Multistory 124/124, %	Multistory 220/150, %
5	Middle	–8, –6	–6, –4	–2, 4	–5, –3	–12, –10
	Lower	–17, –15	–13, –11	–11, 0	–17, –13	–30, –26
10	Middle	–6, –5	–5, –3	2, 5	–4, –1	–10, –7
	Lower	–15, –12	–11, –9	1, 5	–12, –6	–24, –18
20	Middle	–5, –2	–3, –1	6, 8	0, 4	–6, –1
	Lower	–12, –8	–8, –5	6, 9	–6, 0	–17, –10
50	Middle	–1, 1	0, 2	8, 9	4, 6	–1, –3
	Lower	–5, –1	–3, 1	11, 13	3, 8	–5, 2

[a] (xx, xx) shown in each cell denotes results computed by the (1/70 μs, 2/70 μs) triangular current.

The difference between the insulator voltages computed by the FDTD analysis and the circuit models is further discussed by referencing the results of a surge experiment performed at an actual tower. The difference is caused by the surge impedance and the wave attenuation characteristic of the tower, depending on the current injection angle.

The insulator voltages are affected by the current injection angle, and the change of the wave-attenuation characteristic can explain this characteristic. The surge experiment reported in [20] performed using a 500-kV transmission tower is referenced since no experiment for 77-kV transmission towers has been performed as of today. An upper-phase insulator voltage generated by three types of current injection angles was measured in the experiment. Fig. 4.5 shows the measured voltages. The "width" of the insulator voltages becomes more expansive with the larger current injection angle, as pointed out in [20]. Note that the "0 deg." indicates the horizontal current injection, and the positive angle indicates the current injection from the upper side of the tower. The downward traveling voltage generated by the current injection into the tower top increases the insulator voltage at first. Then the voltage is decreased due to the arrival of the upward traveling voltage negatively reflected from the tower foot. Since the traveling wave along the tower significantly attenuates, the insulator voltages decrease slowly, as discussed in Chapter 2. The equation (2.12) expressed the above phenomena by the traveling wave theory. Fig. 4.5 indicates that the traveling wave attenuation along the tower becomes significant and continues longer in the current injection case with a positive angle (the insulator voltage decreases most slowly in the 60-degree injection case). Note that the measured voltages cross at around 2.3 μs due to the induced voltage by the electromagnetic field from the current lead wire. The distances to the adjacent towers were longer than 500 m.

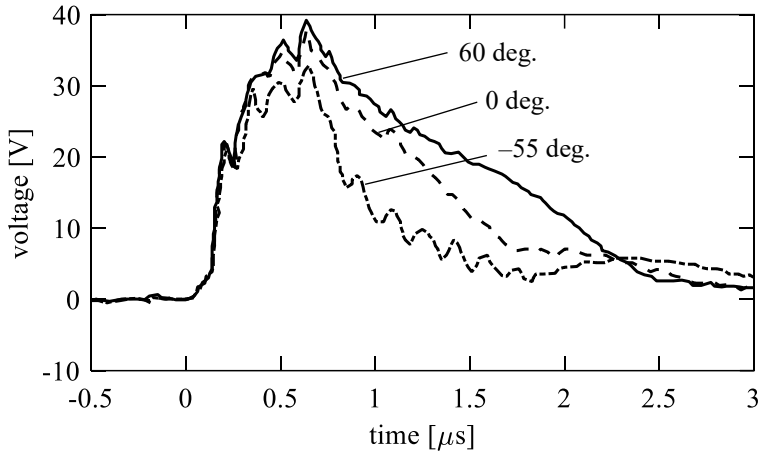

Fig. 4.5 Measured insulator voltages of a 500-kV transmission tower generated by three current injection angles (adapted from [20]).

The effect of the current injection angle on the insulator voltage was reproduced using the FDTD analysis. The 76-m high 500-kV transmission tower analyzed in Chapter 2 was used in this analysis. Fig. 4.6 shows the FDTD analysis space. In this analysis, the current injection angle was set to –55 deg., 0 deg., and 60 deg. The step-like current and the 1/70 μs triangular current were injected. Fig. 4.7 shows the upper phase insulator voltage computed by each current injection angle and waveshape. The FDTD analysis reproduces the measured characteristics of the voltage depending on the current injection angle. The further difference of voltage peaks depending on the current injection angle is derived by the slower rising current.

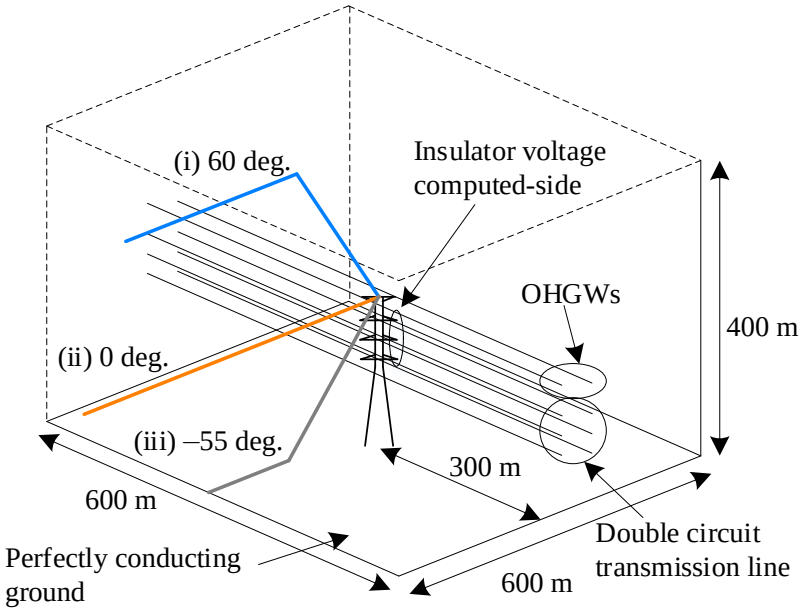

Fig. 4.6 FDTD analysis space for analyzing insulator voltages considering three current-injection angles.

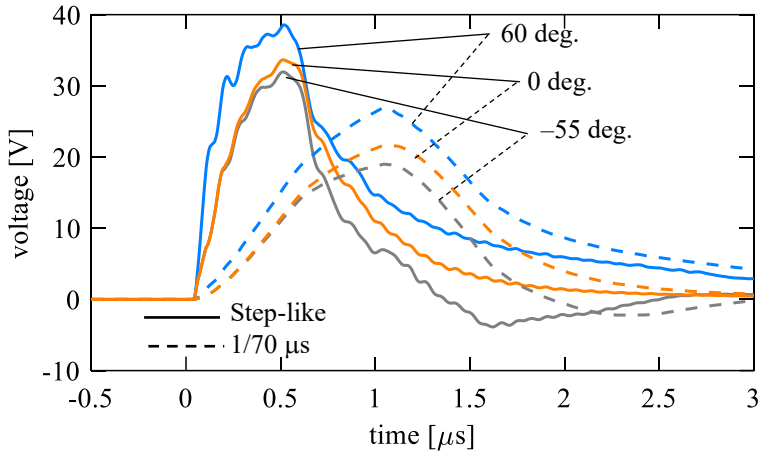

Fig. 4.7 FDTD analyzed insulator voltages by three current-injection angles.

The multistory tower model was developed based on the experiment with a current injection angle of –55 deg. The modification of the model for the UHV transmission tower was performed based on the experiment with the horizontal current injection. These experimental conditions lead to the lower tower surge impedance [20] and shorter continuous time of the wave attenuation characteristic. The time constant, $2h/c_0$, for approximately considering the attenuation, as provided in (2.21), was insufficient for analyzing surges due to the vertical or positive angle lightning channel. The lower voltages for the 77-kV transmission tower with conventional models shown in Fig. 4.4 and Table 4.2 were derived since the 77-kV transmission tower is shorter than EHV/UHV transmission tower. The typical front durations of lightning currents, 1 μs and 2 μs, and longer values, are relatively longer for the shorter 77-kV transmission tower than those for the taller EHV/UHV transmission towers. The above discussion supports the recently presented modification for the multistory tower model [21]. The model computes the tower surge impedance based on the conical approximation and sets the longer time constant around $8h/c_0$ according to the FDTD-computed reference voltages.

B Imperfectly conducting ground case

The reverse T-shaped tower foundation in the imperfectly conducting ground can be represented by a linear lumped resistance, not by the inductive grounding impedance, according to the analysis results by the FDTD method and the TEM-delay model. The TEM-delay model with lumped resistance determined by the procedure introduced in Section 4.1.2 reproduces upper to lower insulator voltages generated by both 1/70 μs and 2/70 μs triangular currents computed by the FDTD method. On the other hand, other models cannot reproduce the voltages, especially the 2/70 μs triangular current case.

Fig. 4.8 shows the insulator voltages computed by the FDTD method in the case of 200 Ωm of soil resistivity and those computed by each circuit model. The tower footing resistance for the circuit model was set to 8 Ω for the TEM-delay model, 58 Ω for the Simplified model, 46 Ω for the Multistory

124/124 model, and 35 Ω for the Multistory 220/150 model. The voltages computed by the FDTD method and TEM-delay model agree with each other in the entire waveform. A linear resistance successfully models the tower foot in the TEM-delay model case. On the other hand, the voltages computed by other models do not show agreement for wave-tail of the 1/70 μs current case and peaks of the 2/70 μs current case. The disagreements of the voltages are caused since these models insufficiently consider or do not consider the wave attenuation characteristic along the tower. An inductive grounding impedance can be derived from the voltages computed by the conventional models (gradually decreasing grounding impedance can reproduce the 2/70 μs voltage peaks). The use of inductive grounding impedance in some literature can be attributed to the insufficient implementation of the wave attenuation characteristic for the tower model, though the tower footing characteristic can be inductive or capacitive depending on the shape of the foundation and the soil characteristics. Table 4.4 summarizes insulator voltages computed by 20 Ωm, 200 Ωm, and 1000 Ωm of soil resistivity and each circuit model. The similar performance of each circuit model is derived for each soil resistivity case.

Table 4.4 Insulator voltages computed by the FDTD method with various soil resistivity, ρ_e, and differences of those by each circuit model with adjusted tower footing resistance, R_{gr}.

ρ_e [Ωm]	P.	FDTD [V/A]	R_{gr} [Ω]	TEM-delay, %	R_{gr} [Ω]	Simplified %	R_{gr} [Ω]	Multistory 124/124, %	R_{gr} [Ω]	Multistory 220/150, %
	U	36.7, 23.8		–1, 2		0, 38		–1, 23		0, 13
20	M	33.4, 21.8	2	0, 4	50	17, 61	37	10, 39	27	3, 21
	L	29.4, 19.3		2, 6		35, 86		21, 56		6, 29
	U	41.3, 29.5		–2, 0		–1, 31		0, 21		0, 11
200	M	38.7, 28.0	8	–1, 1	58	14, 49	46	10, 34	35	3, 18
	L	35.0, 25.8		0, 2		30, 68		19, 47		5, 24
	U	56.1, 48.2		1, 0		–1, 18		0, 12		0, 6
1000	M	55.6, 48.9	32	1, 0	84	11, 29	72	7, 20	60	2, 10
	L	53.3, 47.9		2, 1		21, 39		14, 27		4, 13

(xx, xx) in each cell denotes results computed by the (1/70 μs, 2/70 μs) triangular current, and (U, M, L) does (Upper, Middle, Lower) phases (P.).

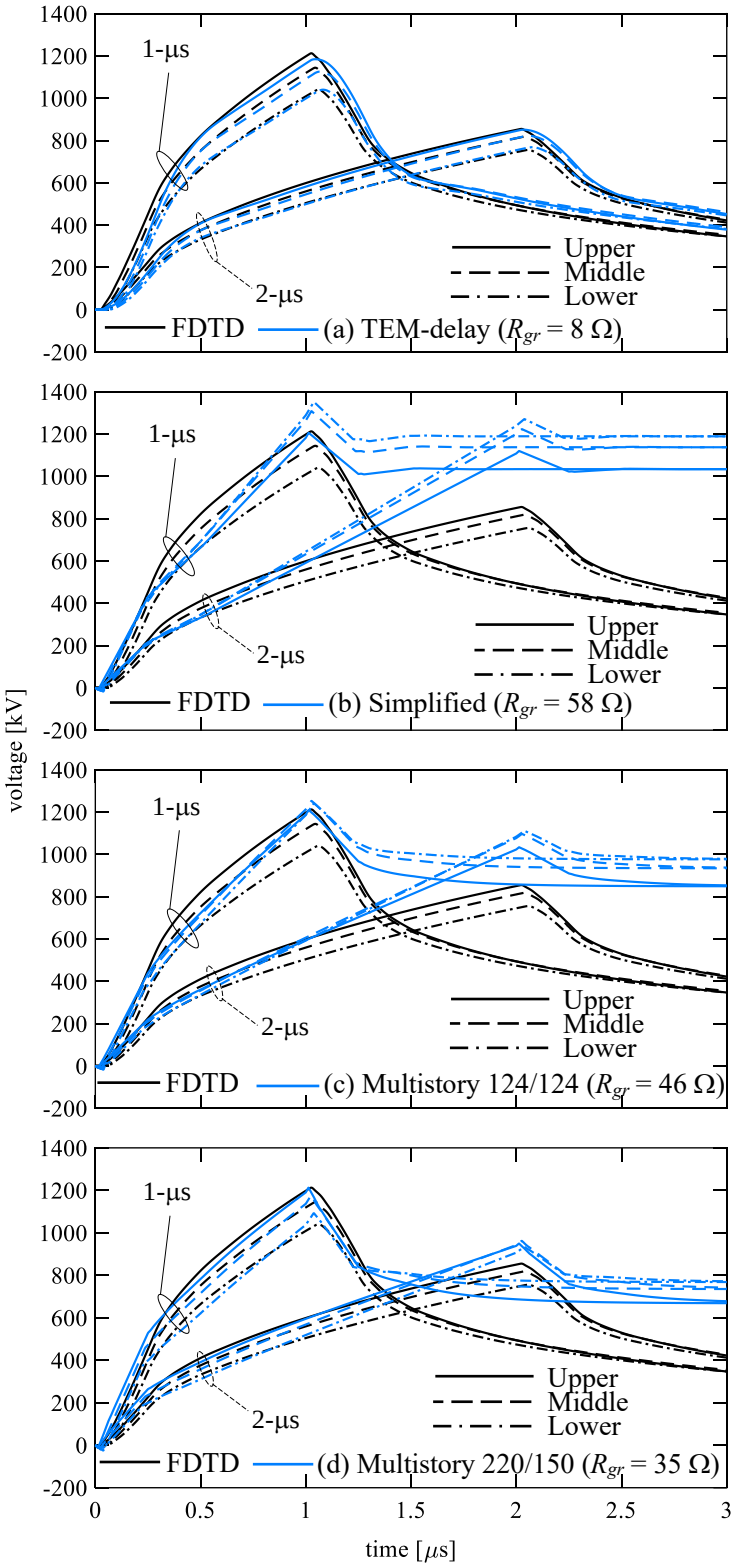

Fig. 4.8 Insulator voltages generated by 30-kA peak 1-µs and 2-µs currents computed by the FDTD method (soil resistivity of 200 Ωm) and each circuit model (adjusted tower footing resistance, R_{gr}).

The tower footing resistance derived by the TEM-delay model agrees with that computed by the theoretical formula. In [22], a formula for calculating tower footing resistance has been presented. The resistance of the one foundation of the tower, R_{gr1}, is derived by

$$R_{gr1} = K \frac{\rho_e}{2\pi l_{gr}} \left\{ \ln\left(\frac{4l_{gr}}{r_{gr}} \right) - 1 \right\}, \tag{4.1}$$

where l_{gr} and r_{gr} are the length and equivalent radius of the foundation, K is a parameter for considering the reduction of the resistance owing to the foundation bottom surface and set to 0.65 [22]. The equivalent radius r_{gr} is calculated for setting the surface area of the foundation under the ground the same as the area of the equivalent cylinder. The following equation provides the total resistance of the four foundations.

$$\begin{aligned} R_{gr} &= \frac{R_{gr1}}{4} \times \frac{1}{\eta_4}, \\ \frac{1}{\eta_4} &= 1 + \frac{l_{gr}}{l_D} \times \frac{1 + 2\sqrt{2}}{\ln\left(\frac{4l_{gr}}{r_{gr}} \right) - 1}, \end{aligned} \tag{4.2}$$

where l_D is the diagonal of the tower foot, and η_4 is a parameter for considering the reduction of the tower footing resistance due to the four-paralleled tower foundations. According to these formulae, the tower footing resistance of the studied tower can be calculated as 0.60 Ω, 6.0 Ω, and 30 Ω for 20 Ωm, 200 Ωm, and 1000 Ωm of soil resistivity. The resistances derived by the TEM-delay models, shown in Table 4.4, agree with those derived by the theoretical formula. On the other hand, the resistances derived by the other models are higher than those provided by the theoretical formula owing to the lower insulator voltages.

4.2 Models of the Flashover and Transmission Line Surge Arresters

4.2.1 Flashover model

The FO across arcing horns has to be simulated for discussing the BFO phenomena at a transmission line. Several FO models have been presented. The models include:

1) The simplest short-circuit model (the air gap part is short-circuited from the beginning of the simulation);
2) Voltage switch model;
3) Model based on a Voltage–time (*V–t*) crossover method [23];
4) Model based on a disruptive effect method [24], [25];
5) Model based on a leader progression method (LPM) [26]–[28].

The model by the LPM can consider pre-discharge current and a leader developing process, whereas other models cannot consider them. The model by the LPM developed in [28] has an advantage compared to other models by the LPM because it has been developed to reproduce the measured breakdown characteristics of 1 m to 3 m rod-rod gaps by a short-tail lightning impulse. The short-tail lightning impulse is observed in the lightning-struck transmission tower as analyzed in this thesis. Other models have been developed based on the standard lightning impulse waveform. Using the model with the LPM for the short-tail lightning impulse, a multiphase BFO at an actual 154-kV transmission line was reproduced using EMTP [29]. The same model was also used for the BFO analysis of the 77-kV transmission line based on the FDTD method by modifying the model parameters for an arcing horn with a 0.65-m long gap [11].

The FO model by the *V–t* crossover method and the LPM were used in this thesis. Firstly, the LPM for short-tail lightning impulse developed in [28] is reviewed here. The LPM consists of formulae providing the leader onset condition, the leader developing process including the definition of the pre-discharge current and the leader developing speed, and the leader stop condition. Each condition is different in each LPM model. The leader onset condition is given by the following equation [29].

$$V_{gap} \geq 500 \times D_{gap} \tag{4.3}$$

where V_{gap} [kV] is the voltage of an air gap, and D_{gap} [m] is the air gap length. The pre-discharge current, the leader developing speed, and the average leader length, is respectively provided by

$$I_L = 2Qvel_L \tag{4.4}$$

$$vel_L = \begin{cases} K_1\left(\dfrac{V_{gap}}{D_{gap}-2X_L}-E_0\right) & \left(0 \leq X_L < D_{gap}/4\right) \\ K_2\left(\dfrac{V_{gap}}{D_{gap}-2X_L}-E_0'\right)+vel_L' & \left(D_{gap}/4 \leq X_L \leq D_{gap}/2\right) \end{cases} \tag{4.5}$$

$$X_L = \int vel_L dt \tag{4.6}$$

where I_L [A] is the pre-discharge current, vel_L [m/s] is the leader developing speed, and X_L [m] is the average leader length developed from both sides of the gap, respectively. The parameters were defined based on the experiment as follows: $Q = 410$ [μC/m], $K_1 = 2.5$ [m^2/Vs], $K_2 = 0.42$ [m^2/Vs], and $E_0 = 750$ [kV/m]. The equation (4.5) calculates the leader developing speed vel_L in case the leader length is shorter than $D_{gap}/4$. The parameters vel'_L and E'_0 are leader developing speed and the average electric field $V_{gap}/(D_{gap}–2X_L)$ immediately before the leader length exceeds $D_{gap}/4$. After the leader length exceeds $D_{gap}/4$, the parameters vel'_L and E'_0 are set as constant values, and the leader developing speed is calculated until the breakdown occurs by satisfying

$$X_L > \frac{D_{gap}}{2}. \tag{4.7}$$

The leader stop condition is provided by

$$\frac{V_{gap}}{D_{gap} - 2X_L} < E_0. \tag{4.8}$$

The model parameters were modified to represent the FO in a 0.65-m long air gap used in the 77-kV transmission line. A measured breakdown characteristic of a rod-rod gap [30] was utilized for the modification [11]. The simulation was performed by a circuit with a voltage source, a 200-Ω linear resistor, and the FO model with the LPM. The voltage source outputs a triangular waveform with a wavefront duration of 1.5 μs and wave-tail duration of 40 μs, respectively [11]. Fig. 4.9 shows the measured *V–t* characteristic [30] and its simulation results by the LPM with the modified model parameter, $K_1 = 0.58$ m^2/Vs, and other parameters shown above. The FO model by the LPM with the optimized parameters can simulate both the negative and positive *V–t* characteristics with satisfactory accuracy. Note that the value of K_1 used here is different from that used in [11], $K_1 = 0.70$ m^2/Vs, though the LPM with these parameters successfully reproduced the *V–t* characteristic there. The difference can be caused since the FDTD method was employed in [11], but the circuit analysis is used here. Note that the inflection point is observed at around 1.5 μs due to the applied voltage waveform and the definition of the *V–t* curve. Although the FO voltage and time (a point of the *V–t* curve) of the wavefront FO (before 1.5 μs in the present case) is straightforwardly determined by the voltage and time observed when the FO occurs, those of the wave-tail FO (after 1.5 μs) is determined by the peak voltage, which is observed before the FO, i.e., is higher than the voltage at the FO, and the FO time.

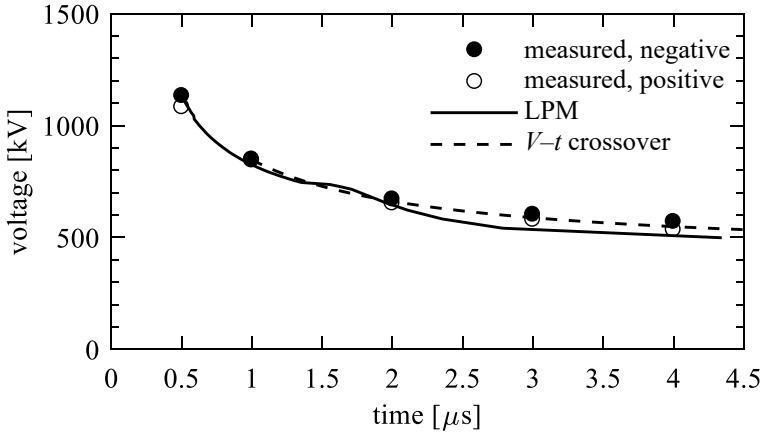

Fig. 4.9 *V–t* characteristic of FO models for the 0.65-m long air gap.

In the FO model with the *V–t* crossover method, the *V–t* characteristic of the air gap is directly compared with the simulated voltage in every simulation time step. Once the simulated voltage exceeds the *V–t* characteristic, the FO model element is short-circuited directly or via inductance with a value of

1 μH/m or some Ohms of resistance. In [23], a formula for *V–t* characteristic for air gaps by short-tail lightning impulse was proposed based on the measurement:

$$V_{FO}(t) = At^{-0.5} + B\log_{10} t, \tag{4.9}$$

where $V_{FO}(t)$ [MV/m] is the *V–t* characteristics of the model, *A* and *B* are parameters derived based on measurements. The parameters *A* and *B* were modified from 1.36 and 0.15 to 1.30 and 0.319 to reproduce the *V–t* characteristic of studying 0.65 m air gap. Fig. 4.9 showed the *V–t* characteristic of this FO model.

4.2.2 Transmission line surge arrester model

TLSAs have been installed in transmission lines due to their effectiveness in reducing lightning accidents. Externally gapped line arrester (EGLA) type TLSAs shown in Fig. 4.10 have been developed in Japan and installed. They comprise a zinc oxide (ZnO) element and a series air gap. The metal-oxide surge arrester has been developed firstly. Then that with an arcing horn has been developed with a high-performance ZnO element with the optimized energy absorption rate [17]. The latter arcing-horn type can be directly replaced with the conventional arcing horn. Both TLSAs operate in the same manner, and in this thesis, the TLSAs were modeled by series-connected nonlinear resistance representing the characteristics of the ZnO element and the FO model by the LPM representing the FO across the air gap.

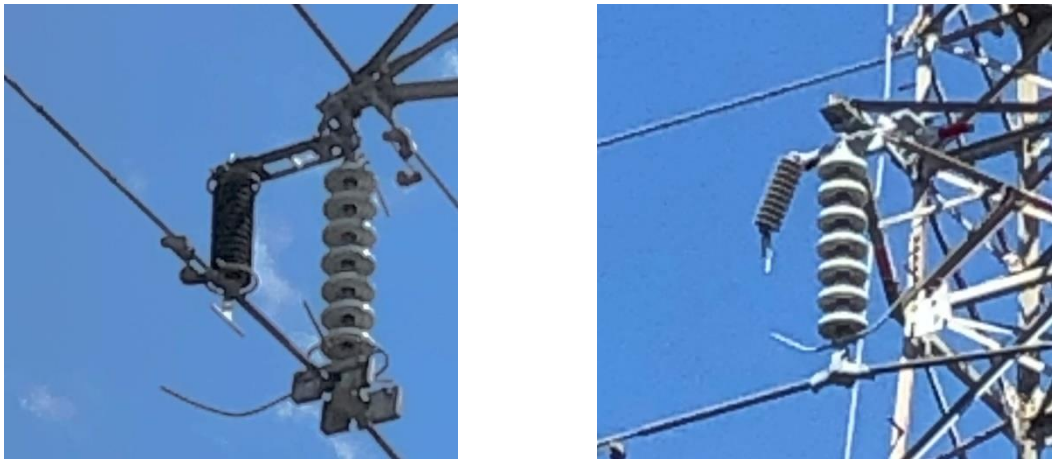

(a) Metal-oxide surge arrester (b) Arcing-horn type metal-oxide surge arrester

Fig. 4.10 Photograph of an EGLA type TLSAs
(took at Kansai Transmission and Distribution, Inc., Joyo-Shisen Line, Kyoto, Japan).

In [31], [32], it has been clarified based on measurements that the TLSAs can be modeled by series-connected nonlinear resistance and FO model. Measurements of breakdown characteristics of 66-kV TLSAs for standard and short-tail lightning impulse voltage were performed. An arcing-horn type metal-oxide surge arrester was used in the measurements. It has been revealed that the ZnO element starts operation due to the leakage current just after applying the voltage and holds its residual voltage

before the time of the FO occurrence. Thus, the ZnO element and characteristics of FO can be independently modeled. No stray capacitor to determine the voltage division between the ZnO element and air gap is required. Following the finding, in this thesis, the TLSA was modeled by a series-connected nonlinear resistance representing voltage–current (*VI*) characteristics of the ZnO element and FO model by the LPM representing the air gap. Note that the presented model does not consider other characteristics of the ZnO element, such as the hysteresis and the frequency-dependence of the *VI* characteristics. Note that in [11], the TLSA was modeled by this approach in the FDTD method, and in [33], the TLSA was modeled in circuit analysis by the series-connected nonlinear resistance representing ZnO element and FO model by the LPM based on the nonlinear resistance and inductance [34].

The parameters of LPM for the TLSA model were adjusted so that the measured characteristics of TLSA for 77-kV lines [33] can be simulated. Fig. 4.11 shows an equivalent circuit of an impulse generator for measuring the transient response of a TLSA, and Fig. 4.12 shows the *VI* characteristics of the ZnO element of TLSA for the studied 77-kV transmission line [11], [33]. The nonlinear characteristic of the ZnO element was implemented into the circuit analysis by the piecewise linear approximation and the Newton-Raphson method. The gap length was 0.35 m. A voltage was applied by the impulse generator shown in Fig. 4.11, and the transient response of the TLSA was computed.

The circuit model of the TLSA can reproduce the measured transient responses and the *V–t* characteristic of the TLSA. Fig. 4.13 shows the measured transient responses and the *V–t* characteristic of the TLSA [11], [33] and their simulation results. The pre-discharge current is generated before the FO occurrence. After the FO, the TLSA holds the residual voltage of the ZnO element. The circuit model also reproduces the measured *V–t* characteristic of the TLSA. Comparing the *V–t* characteristic of the TLSA and the arcing horn (rod-rod air gap) shown in Fig. 4.9, the TLSA operates in advance of the FO occurrence at the arcing horn. The parameters of the FO model by the LPM in determining the leader developing process are modified to $K_1 = 0.20$ m^2/Vs and $E_0 = 640$ kV/m for the TLSA model. The FO model with original parameters yielded higher FO voltages than the measured characteristics, and hence those parameters were set smaller to lower the voltages.

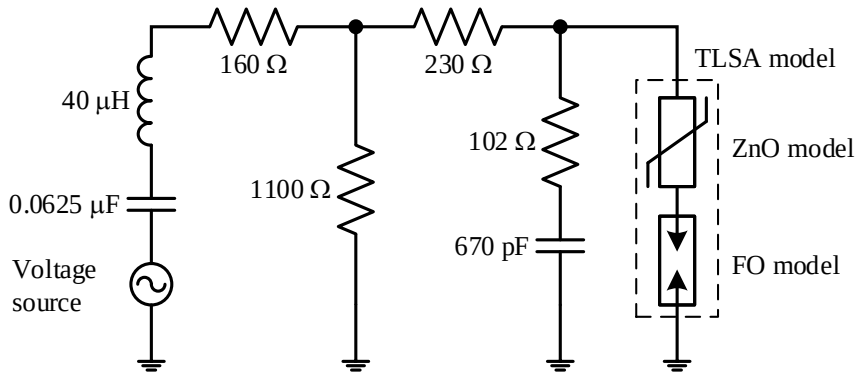

Fig. 4.11 Equivalent circuit of an impulse generator for measuring transient responses of TLSAs [11], [33].

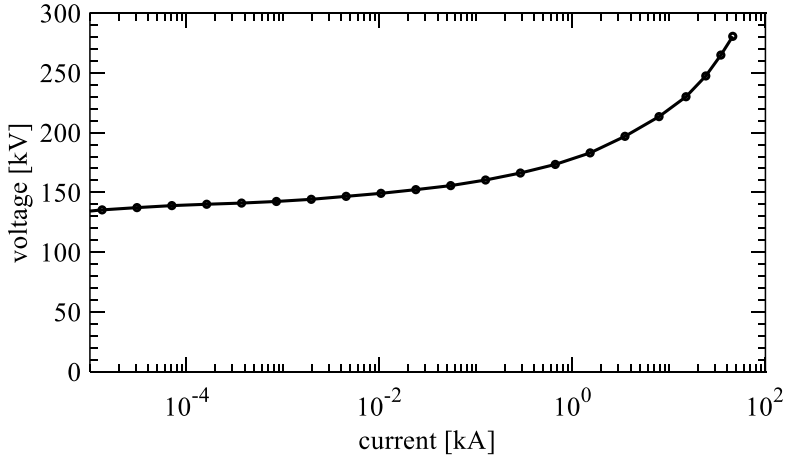

Fig. 4.12 *VI* characteristics of a ZnO element of TLSA for a 77-kV transmission line [11], [33].

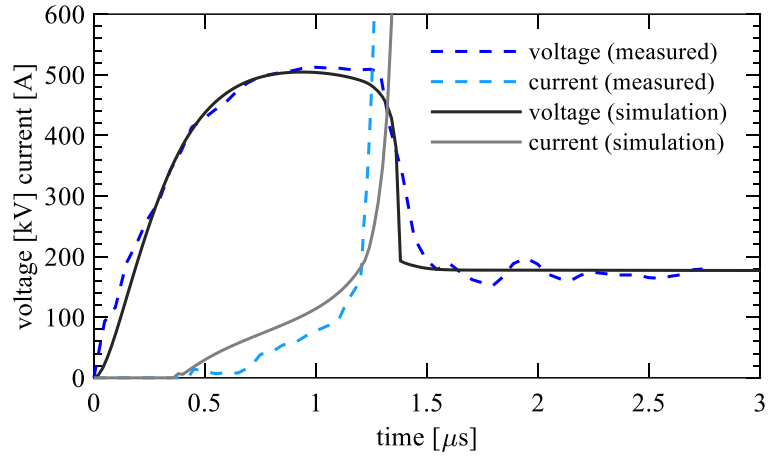

(a) Wavefront discharge

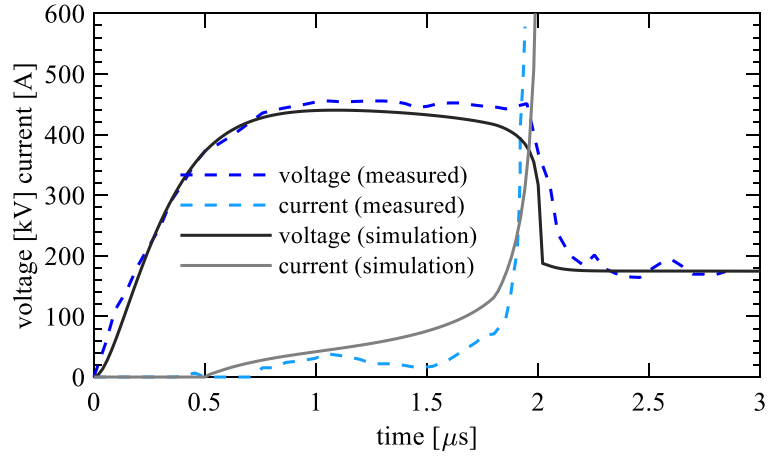

(b) Wave-tail discharge

Fig. 4.13 Transient response and *V*–*t* characteristic of a TLSA for 77-kV transmission line (the measured results are adapted from [33], this figure follows to the next page).

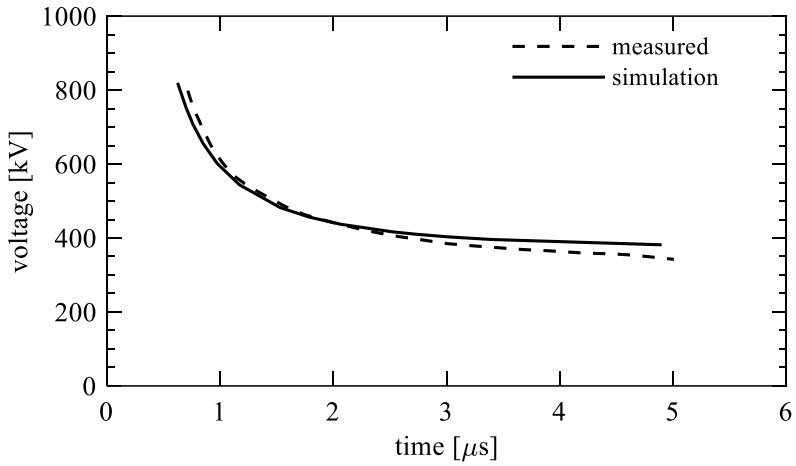

(c) *V–t* characteristic

Fig. 4.13 Transient response and *V–t* characteristic of a TLSA for 77-kV transmission line (the measured results are adapted from [33], this figure is followed from to the previous page).

4.3 Back-flashover Analysis

BFO occurrences are analyzed and discussed in this section, referencing field observation results reported in the past. The observation was performed in the summer lightning season in Japan (June to September) on a 77-kV transmission line [2], [3]. In the summer lightning season in Japan, negative downward lightning mainly occurs. Note that coastal areas of the Japan Sea experience winter lightning, which comprises a relatively large number of positive or bipolar upward lightning with excessive current and charge initiated from tall grounded objects, such as transmission towers and wind turbines. The tower and line configuration are similar to that of the 77-kV transmission tower and line analyzed in Section 4.1. The characteristics of BFO occurrence, such as the effect of power frequency voltages on BFO phases including multiphase BFOs, and minimum currents for generating BFO, are revealed. The four transmission tower and line models evaluated in Section 4.1 were used in the analysis. The performance of each model for BFO analysis is also discussed.

The BFO phases are heavily dependent on the power frequency voltage. Fig. 4.14 shows the measured BFO phases in one circuit of the line and simultaneous power frequency voltages in a total of 15 events reported in [2], [3]. It shows a noticeable tendency of the BFO phases: a large portion of the BFOs was a double-phase back-flashover (2BFO), and most of the BFOs occurred in phases with positive power frequency voltage. The latter is because the negative lightning consists of a large portion of summer lightning. The followings are the descriptions of the specific features. At around 45, 135, and 255 degrees, all three observed BFOs at each angle were 2BFO. One case of triple-phase back-flashover (3BFO) was observed at around 100 degrees, and it was probably caused by a lightning strike with a large current [2]. Two cases of single-phase back-flashover (1BFO) were observed at which the power-frequency voltage was the maximum.

In transmission systems adopting high resistance grounding, such as HV transmission systems in Japan, the voltage drop of the fault phase comparing to the healthy state becomes noticeable by line to ground fault accompanied by the line short (2BFO or more) [35]. Thus, the occurrence characteristics of multiphase BFO are as important as the lightning fault rate (occurrence probability of single-phase BFO). The BFO occurrence, including multiphase BFO, is discussed using the circuit analysis models.

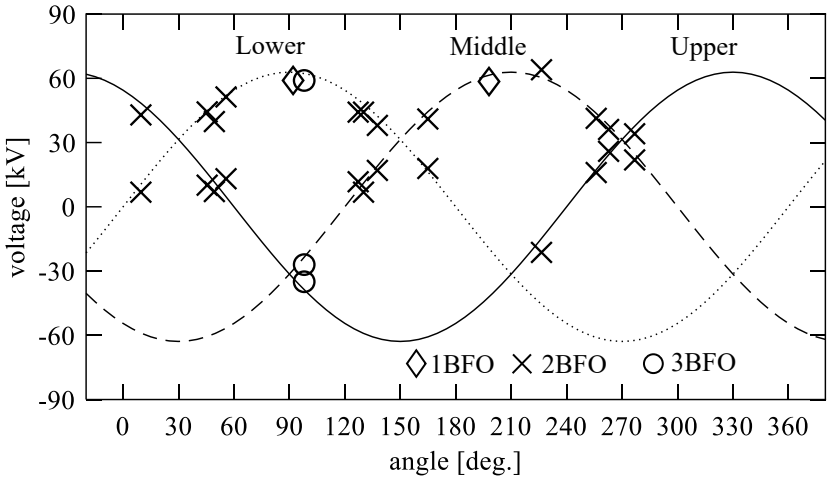

Fig. 4.14 Back-flashover phases in one circuit of the line and simultaneous power frequency voltages observed at a 77-kV transmission line in summer-lightning season (adapted from [2]).

4.3.1 Circuit analysis model for back-flashover analysis

BFO analysis was performed using four circuit models discussed in Section 4.1. The models are described again.

(i) TEM-delay tower model + TEM-delay line model (TEM-delay)
(ii) Simplified tower model with constant surge impedance determined by Jordan's formula + frequency-dependent line model (Simplified)
(iii) Multistory tower model with surge impedance of 124 Ω determined by Jordan's formula + frequency-dependent line model (Multistory 124/124)
(iv) Multistory tower model with 220/150 Ω of surge impedance + frequency-dependent line model (Multistory 220/150)

Fig. 4.15 illustrates the entire circuit analysis model, and Table 4.5 summarizes the analysis conditions. In the circuit analysis, five towers were considered, and the voltage sources for modeling the power frequency voltages were connected to left- and right-most towers via multiphase matching circuits. The span length was set to 300 m. The studied line adopts the symmetrical phase rotation. The lightning channel impedance was set to 1000 Ω [36]–[39]. The tower footing was modeled by a 10-Ω linear resistance, which is the mean value of the studied transmission line [3].

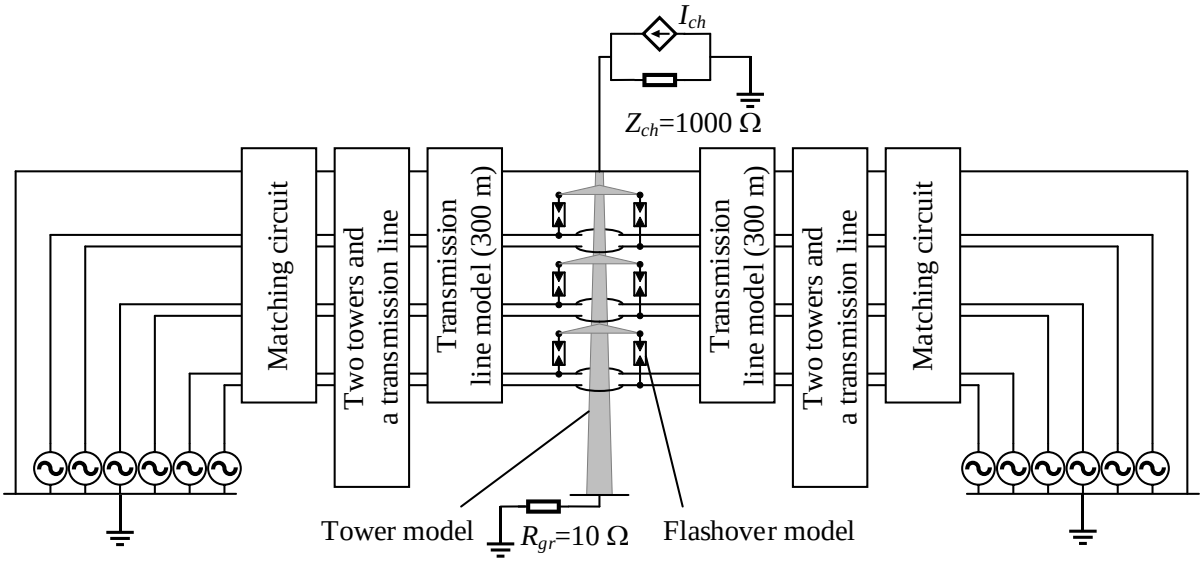

Fig. 4.15 Circuit model for back-flashover analysis of 77-kV transmission line (the presence of cross-arms are not considered explicitly in the Simplified, Multistory 124/124, and Multistory 220/150 model).

Table 4.5 Analysis conditions for a back-flashover phenomenon at a 77-kV transmission line.

Current waveform	2/70 μs triangular current or 3.83/77.5 μs double-peak current (negative polarity)
Current peak	Incremented by 1 kA
Lightning channel impedance	1000 Ω
Power frequency voltage	Incremented by 15 degrees
Phase rotation	Symmetrical rotation
Tower model	TEM-delay, Simplified, Multistory 124/124, Multistory 220/150
Line model	TEM-delay or frequency-dependent line (ρ_e = 200 Ωm)
Flashover model	LPM or *V*–*t* crossover method
Tower footing model	10-Ω linear resistor

The TLSAs were not considered since they were not installed in the studied line when the BFOs shown in Fig. 4.14 were observed. The FO model described in Section 4.2 was inserted between the tower cross-arms and phase conductors for all phases. Note that the BFO simultaneously occurs at both sides of the line in the same phase in this analysis. The co-occurrence of the BFO is caused because the phase rotation is symmetrical, and the FO model does not consider the variation of FO voltage and the concurrent FO characteristics [40], [41]. The trend of BFO occurrence can be sufficiently discussed by the present FO model, while the inclusion of these FO characteristics enables further enhancement of the validity of the circuit analysis. Note that according to [2], the BFOs, including single to triple phase BFOs in one circuit of the line, occurred in both circuits of the same phase in six cases among eight cases of observed results.

The injected current waveform was the 2/70 μs triangular current and a double-peak current waveform [42] with the negative polarity. The negative current was adopted since the negative lightning consists of a large portion of lightning in the summer lightning season in Japan. The 2/70 μs triangular current is recommended for negative first stroke with peak current less than 50 kA in a Japanese guideline for evaluating the lightning performance of transmission lines [22]. The double-peak current waveform can represent the current waveform's median characteristics observed at Mt. San Salvatore in Switzerland [43]. Table 4.6 summarizes the median parameters. The reproduced median characteristics include initial and final peak currents I_I and I_F, front time of T_{10} and T_{30} (time between I_{10} and I_{90} on the wavefront and that between I_{30} and I_{90}, where the currents I_{10}, I_{30}, and I_{90} denote 10, 30, and 90% intercept along the stroke current waveshape), time to half value T_{50}, average steepness through I_{10} and I_{90} intercepts, $S_{10/90}$, and that through I_{30} and I_{90} intercepts, $S_{30/90}$, and the maximum rate-of-rise of current along wavefront, S_m. The current is synthesized by the sum of Heidler's function [44]:

$$I_{DP}(t) = \sum_k \frac{I_{0k}}{\eta_k} \frac{\left(t/\tau_{1k}\right)^{n_k}}{1+\left(t/\tau_{1k}\right)^{n_k}} \exp\left(-t/\tau_{2k}\right), \qquad \eta_k = \exp\left\{-\left(\frac{\tau_{1k}}{\tau_{2k}}\right)\left(\frac{n_k\tau_{2k}}{\tau_{1k}}\right)^{1/n_k}\right\}. \tag{4.10}$$

Table 4.7 summarizes the model parameter of the double-peak current, I_{0k}, τ_{1k}, τ_{2k}, and n_k. Natural lightning generally has a concave shape in its wavefront part [37]. The double-peak waveform shown in Fig. 4.16 provided by (4.10) and parameters summarized in Table 4.7 can reproduce the concave characteristics.

Table 4.6 Median parameters of negative first lightning observed at Mt. San Salvatore in Switzerland [37], [43].

Front and tail time [μs]		
$t_{d10/90}$ (= $T_{10/90}$/0.8)	Equivalent linear wavefront duration of $I_F/S_{10/90}$	5.63
$t_{d30/90}$ (= $T_{30/90}$/0.6)	Equivalent linear wavefront duration of $I_F/S_{30/90}$	3.83
$t_m = I_F/S_m$	Equivalent linear wavefront duration of I_F/S_m	1.28
T_{50}	Tail time to half value	77.5
Steepness [kA/μs]		
S_m	Maximum steepness	24.3
S_{10}	Instantaneous rate-of-rise of current at I_{10}	2.6
$S_{10/90}$	Average steepness through I_{10} and I_{90} intercepts	5.0
$S_{30/90}$	Average steepness through I_{30} and I_{90} intercepts	7.2
Peak current [kA]		
I_I	Initial peak current	27.2
I_F	Final (global) peak current	31.1
I_I/I_F (no unit)	Ratio of initial and final peak current	0.9

Table 4.7 Parameters for double-peak lightning current waveform reproducing median parameters of negative first stroke observed at Mt. San Salvatore [42].

k	I_{0k} [kA]	n_k	τ_{1k} [μs]	τ_{2k} [μs]
1	2.8	2	1.2	100
2	4.8	3	3	100
3	2.9	5	4.8	25
4	4.1	7	6	60
5	16.7	36	6.6	44
6	11	2	100	600

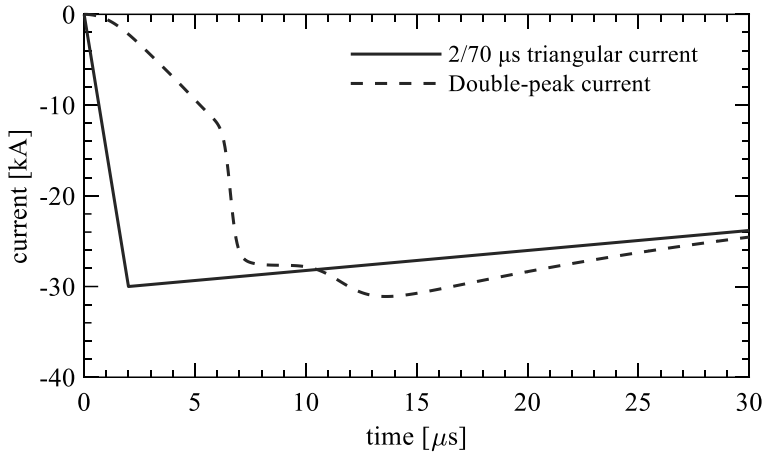

Fig. 4.16 The 2/70 μs triangular current and the 3.83/77.5 μs double-peak current for back-flashover analysis of a 77-kV transmission line.

In the BFO analysis, the phase angle of the power frequency voltage was incremented by 15 degrees. In every phase angle of the power frequency voltage, the minimum lightning current causing 1, 2, 3BFO in one side of the line (2, 4, 6BFO in both sides of the line) was calculated. Note that in this section, the 1BFO in one side of the line (2BFO in both sides of the line) is mentioned as 1(2) BFO to discuss the observed results shown in Fig. 4.14. Accordingly, the 2BFO and 3 BFO in one side of the line are mentioned as 2(4) BFO and 3(6) BFO, respectively. The minimum lightning current was derived following the flowchart shown in Fig. 4.17. The current was basically incremented by 1 kA without changing the current waveform: the analysis did not consider a correlation between the current peak magnitude and the rate of rise. Though the correlation has been identified in the observation of natural lightning currents, it is noticeable in the high current lightning, such as 100 kA or higher [45]. The correlation will be considered in the lightning surge analysis of EHV transmission lines performed in Chapter 5. Note that the current was incremented by 0.2 kA if the designated number of BFO did not occur by the 1 kA incrimination. The computation of each minimum lightning current for each number of BFO at each phase angle (3 × 24 × (number of trials for searching the current, at least two)) becomes feasible by the circuit analysis method. The circuit analysis is executable in several seconds or less,

while the FDTD analysis requires longer than several hours to derive the 3-μs transient response of a single tower shown in Section 4.1, for instance.

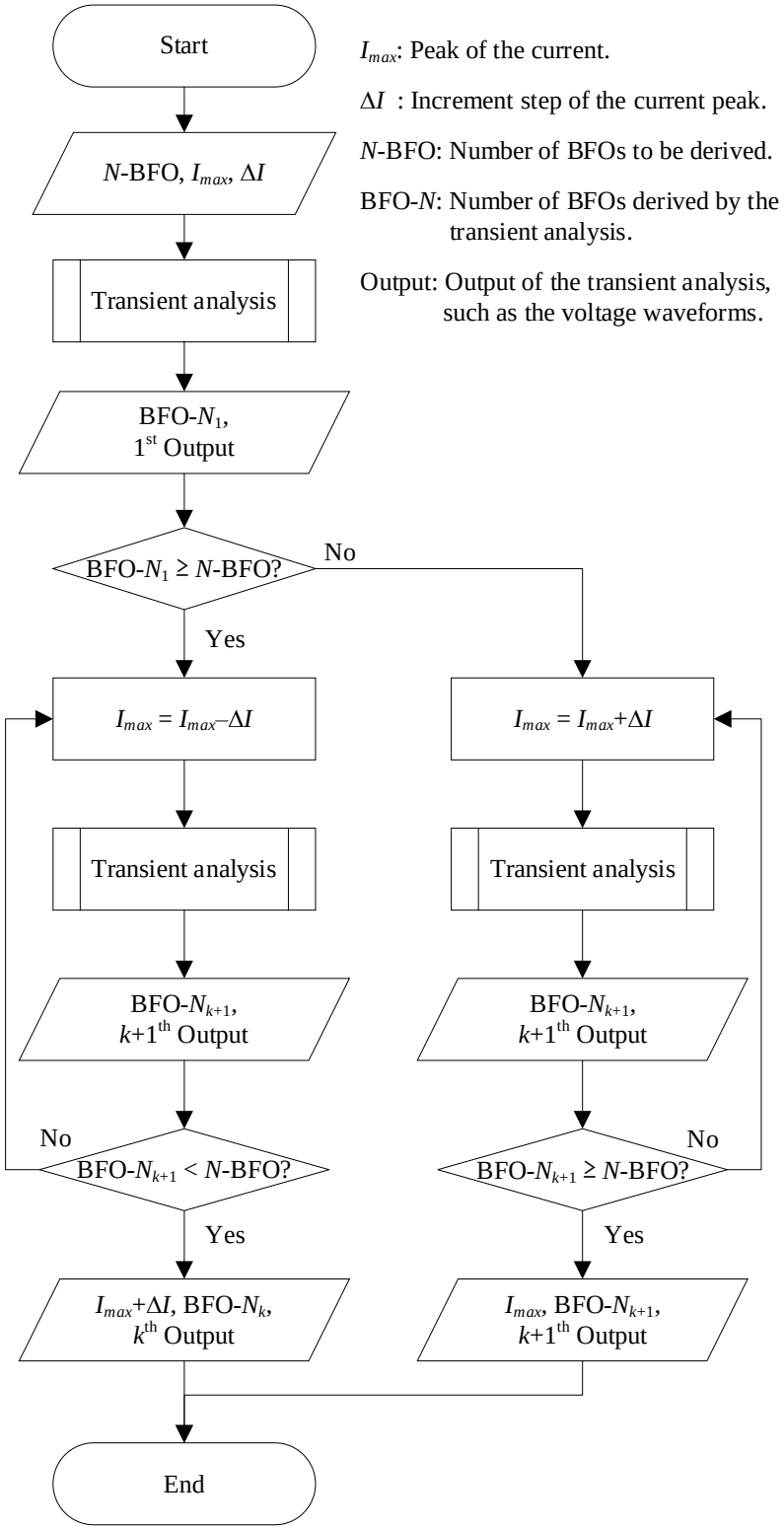

Fig. 4.17 Flowchart for deriving minimum current causing N-phase BFOs.

4.3.2 Discussions on back-flashover characteristics

A Back-flashover phases

The observed BFO phases can be reproduced by the TEM-delay model and the Simplified model, partly reproduced by the Multistory 124/124 model. However, the Multistory 220/150 model cannot reproduce the BFO phases. Regarding the BFO occurrence, the BFO at phases with positive power frequency voltages is prioritized. Fig. 4.18 shows the BFO phases derived by each circuit model. The symbols for 1(2) BFO and 2(4) BFO are shown above and below the corresponding power frequency voltages to provide better visibility. It should be noted that the BFO occurs every 15 degrees in the simulation results since the phase angle of the power frequency voltage was incremented by 15 degrees.

Regarding the 1(2) BFO, the models except for the Multistory 220/150 model reproduce two cases of the observed BFOs shown in Fig. 4.14. The observed effect of the power frequency voltages on the BFO phases was that the BFO occurs at phases with positive power frequency voltage in the negative polarity lightning strike. From this viewpoint, circuit models except for the Multistory 220/150 model can roughly reproduce the observed characteristic. The Multistory 220/150 model cannot reproduce the effect of power frequency voltages since the upper-phase insulator voltage is much higher than the lower phase voltage, as shown in Table 4.3 in the previous section. The voltage difference among the phases is caused by the different surge impedances at the tower upper and lower parts. The different surge impedance represents the different voltages depending on the phases in the EHV/UHV transmission tower cases, as shown in Fig. 3.16 for instance. In the TEM-delay model and Multistory 124/124 model, the exceptions of the BFO phases depending on the power frequency voltage are observed around 45 degrees and 135 degrees. The exception is caused because the voltages generated by the lightning current are the highest in the upper and the lowest in the lower phases in the studied tower, as shown in Fig. 4.4, Table 4.2, and Table 4.3.

Regarding the 2(4) BFO, the Simplified model reproduces all of the measured BFO cases, and the TEM-delay model reproduces all cases except for one case of 2BFO observed at around 165 degrees. This observed 2BFO of middle and lower phases at 165 degrees can be reproduced by the TEM-delay model by assuming the tower footing resistance of 16 Ω or current with a slower wavefront duration. Stochastic variation of FO voltage can also affect the BFO phases. Considering the above discussions, the TEM-delay model can still reproduce the effect of power frequency voltages on BFO phases. On the other hand, the Multistory 124/124 model and Multistory 220/150 model cannot reproduce in total four cases of 2BFOs observed at around 135 degrees and 165 degrees.

In the observed BFO phases shown in Fig. 4.14, most BFOs occurred in the phases with the positive power frequency voltage. Thus, the effect of power frequency voltages may be interpreted as “when negative lightning strikes, the BFO occurs at phases with positive power frequency voltages, but it does not occur at phases with the negative voltage.” However, the BFOs occur at phases with negative

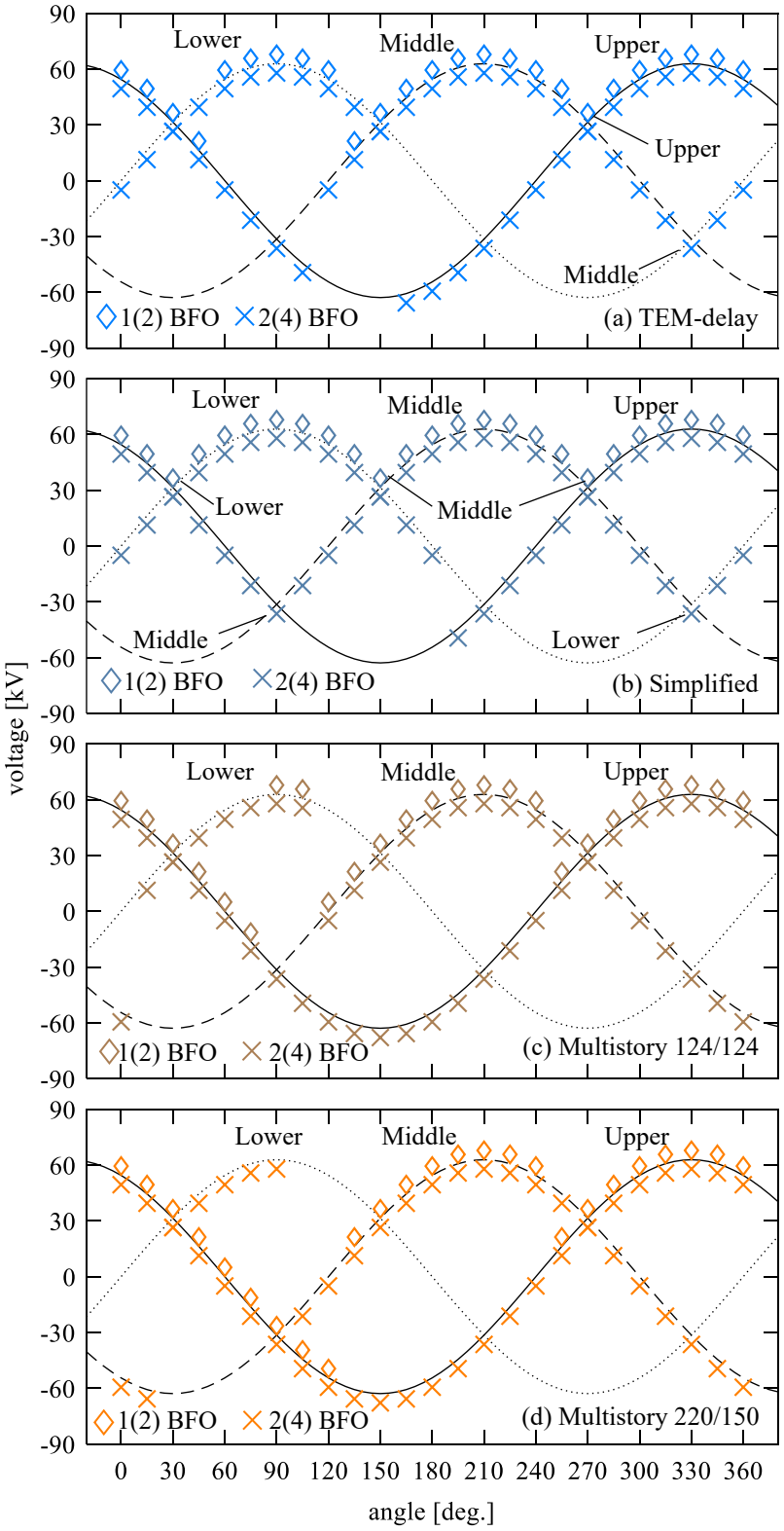

Fig. 4.18 BFO phases generated by the 2/70 μs triangular current and simultaneous power frequency voltages computed by each circuit model.

power frequency voltage, as shown in Fig. 4.18, depending on the current magnitude as introduced in the next section. The effect of the power frequency voltage can be interpreted as "the BFO occurrence at phases with positive power frequency voltages is prioritized, but it can occur at phases with the negative voltage." The effect of power frequency voltages on BFO phases can be considered by the TEM-delay and Simplified model as discussed above. The Multistory 124/124 model can roughly consider the effect, but it cannot be considered by the Multistory 220/150 model owing to the use of different surge impedance at the upper and lower part of the tower.

B Variations of critical current

The minimum lightning current causing BFOs, namely, critical current, states a variation depending on the power frequency voltages. The variation resulted in the observed characteristics of BFO described at the beginning of this section: the 2BFO in one circuit of the line consists large portion. The probability of the critical current can explain this characteristic. Among the four circuit models, the TEM-delay model well supports the characteristics, while others partly support or do not support them. Note that the validity of the critical currents will be discussed in the next section.

The critical current significantly depends on the power frequency voltages. Fig. 4.19 shows the currents derived by each circuit model. The current magnitude is quite different in each model, but a similar dependence on the power frequency voltages is derived. A general trend for the critical current can be described as follows: at a phase angle where a smaller current can cause 1(2) BFO, a larger critical current is required to cause 2(4) BFO, and vice versa. The same trend is observed in relation between the 2(4) BFO and 3(6) BFO.

The variation can be explained by the relation of power frequency voltages, insulator voltages, and the resultant leader development. This characteristic is discussed taking the 255 degrees case as an example. Fig. 4.20 shows voltages across the insulator strings and average leader lengths for 2(4) BFO derived by the TEM-delay model. At this phase angle, the difference of the critical current between the 1(2) BFO and 2(4) BFO is slight, and that of the 2(4) BFO and 3(6) BFO is significant in all circuit models. As shown in Fig. 4.20 (a), the upper- and middle-phase voltages are almost the same, and the lower phase voltage is lower than those owing to the power frequency voltages. Thus, the critical currents causing 1(2) BFO and 2(4) BFO have no significant difference (–20 kA and –22 kA for the TEM-delay model). The lower-phase insulator voltage is still low, and the development of the leader does not start at which the BFOs occur at the upper and middle phases, as shown in Fig. 4.20 (b). Hence, a much higher current (–59 kA for the TEM-delay model) is required for generating the 3(6) BFO. A similar explanation can be given for other BFOs with each power frequency angle. The relation of power frequency voltages, insulator voltages, and the resultant leader development causes the variation of the critical current depending on power frequency voltages and the number of BFO phases shown in Fig. 4.19.

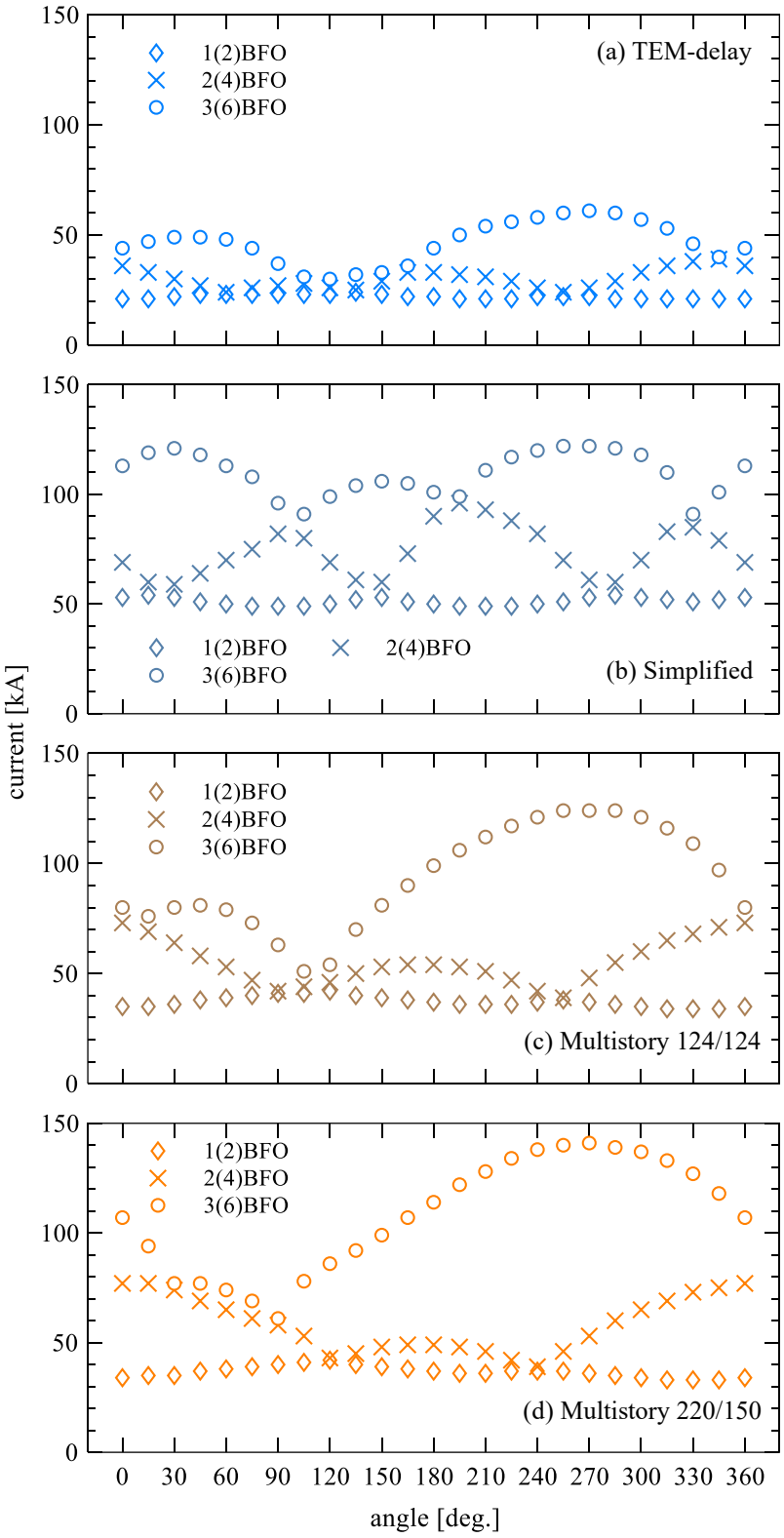

Fig. 4.19 Minimum currents causing 1(2)–3(6) phase BFOs depending on simultaneous power frequency voltage angles computed by each circuit model.

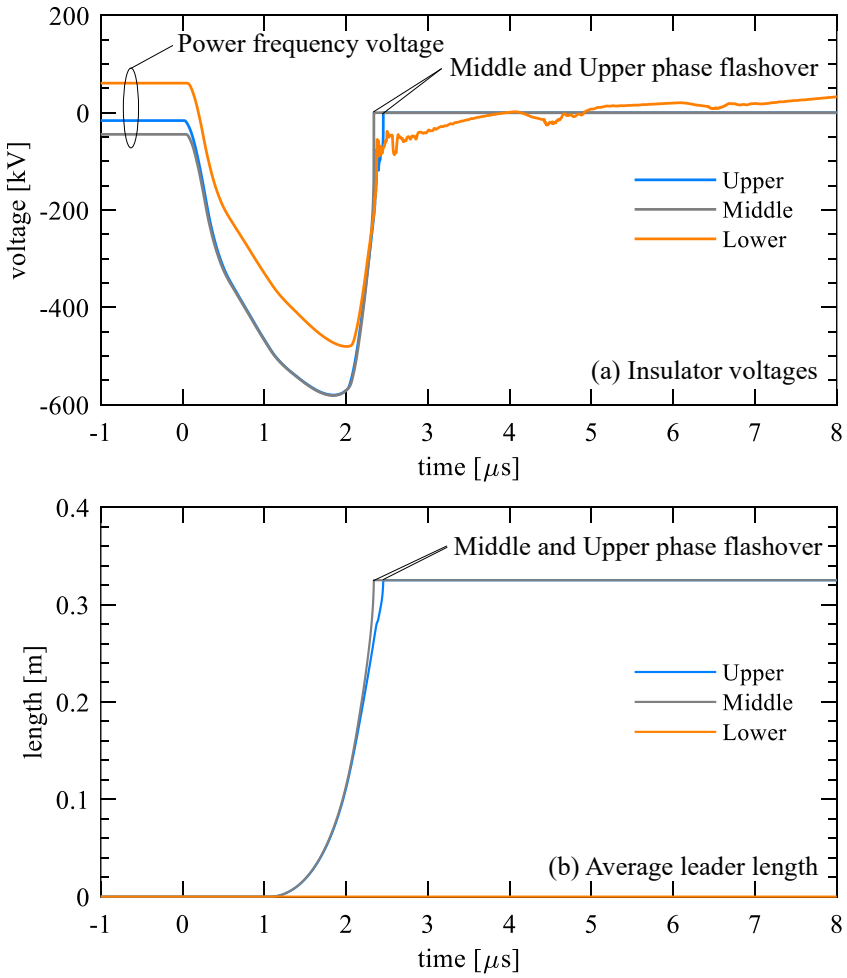

Fig. 4.20 Insulator voltages and average leader length simulated by the TEM-delay model in the case of 255 degrees of power frequency voltage angle, 2(4) BFO, and –22 kA current injection.

A different variation of critical current is derived by each model owing to the different insulator voltages generated in case FO and power frequency voltages are not considered. For example, the critical current for 3(6) BFO derived by the Simplified model has three peaks at around 30, 150, 270 degrees. At these angles, the power frequency voltages of the middle, upper, and lower phases are lowest, respectively, and thus the high current is required for causing 3(6) BFO. The critical current for 3(6) BFO derived by the other models has two peaks at around 30 and 270 degrees. The peak at around 150 degrees is diminished since the upper phase insulator voltage is the highest without the power frequency voltages as shown in Fig. 4.4 and Table 4.3 in Section 4.1.3, and thus the upper-phase insulator voltage becomes as high as the middle- and lower-phase insulator voltages in case the power frequency voltage is considered.

The probability of the critical current can explain the measured characteristics of the BFO phases, especially that derived by the TEM-delay model. Fig. 4.21 shows the probability of the critical current derived by the statistical distribution of negative first stroke current recommended in Japan [17].

$$F(I) = 1 - \frac{1}{\sqrt{2\pi}\sigma}\int_{-\infty}^{\log I} \exp\left(-\frac{\left(x - \log I_{med}\right)^2}{2\sigma^2}\right) dx, \tag{4.11}$$

where $x = \log I$, $I_{med} = 26$ kA, and $\sigma = 0.325$.

As mentioned at the beginning of Section 4.3, three BFOs were observed at each power frequency phase angle of 45, 135, and 255 degrees, and all of them were the 2BFO in one circuit of the line. This result means that the probability of the 2BFO is relatively high at these phase angles. The TEM-delay model supports this characteristic, but other models support it weakly or do not support it. The probability derived by the TEM-delay model is discussed with the observed BFO phases. As shown in Fig. 4.21, at 45, 135, and 255 degrees, the probabilities of 1(2) BFO and 2(4) BFOs are almost the same, and those of 2(4) BFO and 3(6) BFO are far different. For instance, at 255 degrees, the probabilities for 1–3(2–6) BFOs are 64%, 59%, and 14%, respectively. At 135 degrees, the probabilities derived by the TEM-delay model are 59%, 54%, and 39%. The 1BFOs in one circuit of the line were observed at around the phase angles of 90 and 195 degrees, as shown in Fig. 4.14. As shown in Fig. 4.21, the difference of the probability between 1(2) BFO and 2(4) BFO is relatively significant. For instance, at 195 degrees, the probabilities for 1(2) BFO and 2(4) BFO are 64% and 41%, respectively. A 3BFO in one circuit of the line was observed at around 105 degrees. The computed probability of 3(6) BFO is relatively high and close to that of 2(4) BFO: 44% for 3(6) BFO and 48% for 2(4) BFO. As discussed, the probabilities derived by the TEM-delay model support the observed characteristics of BFO phases.

The other three circuit models partly support or do not support the observed characteristics of BFO phases. The Simplified model reproduced all observed BFO phases. Probabilities derived by this model also support the observed phases, except for the probability derived in 255 degrees. The Multistory 124/124 and 220/150 models have reproduced 2(4) BFO phases at around 45 degrees and 255 degrees. The probability derived at 255 degrees supports the observed BFO phase, but the probability derived at around 45 degrees supports weakly, especially in the Multistory 220/150 case.

In summary, although the number of referenced BFOs is not so large and the lightning strike is a purely stochastic event, the probabilities of BFOs derived by the TEM-delay model well support the observed characteristics of BFOs as discussed above. Other models, namely the Simplified model, Multistory 124/124 model, and Multistory 220/150 model, partly support or do not support the characteristics. The variation of the critical current and resultant probability is caused by the relation of the power frequency voltage, insulator voltage, and the resultant leader development. The validity of the critical current is discussed in the next section.

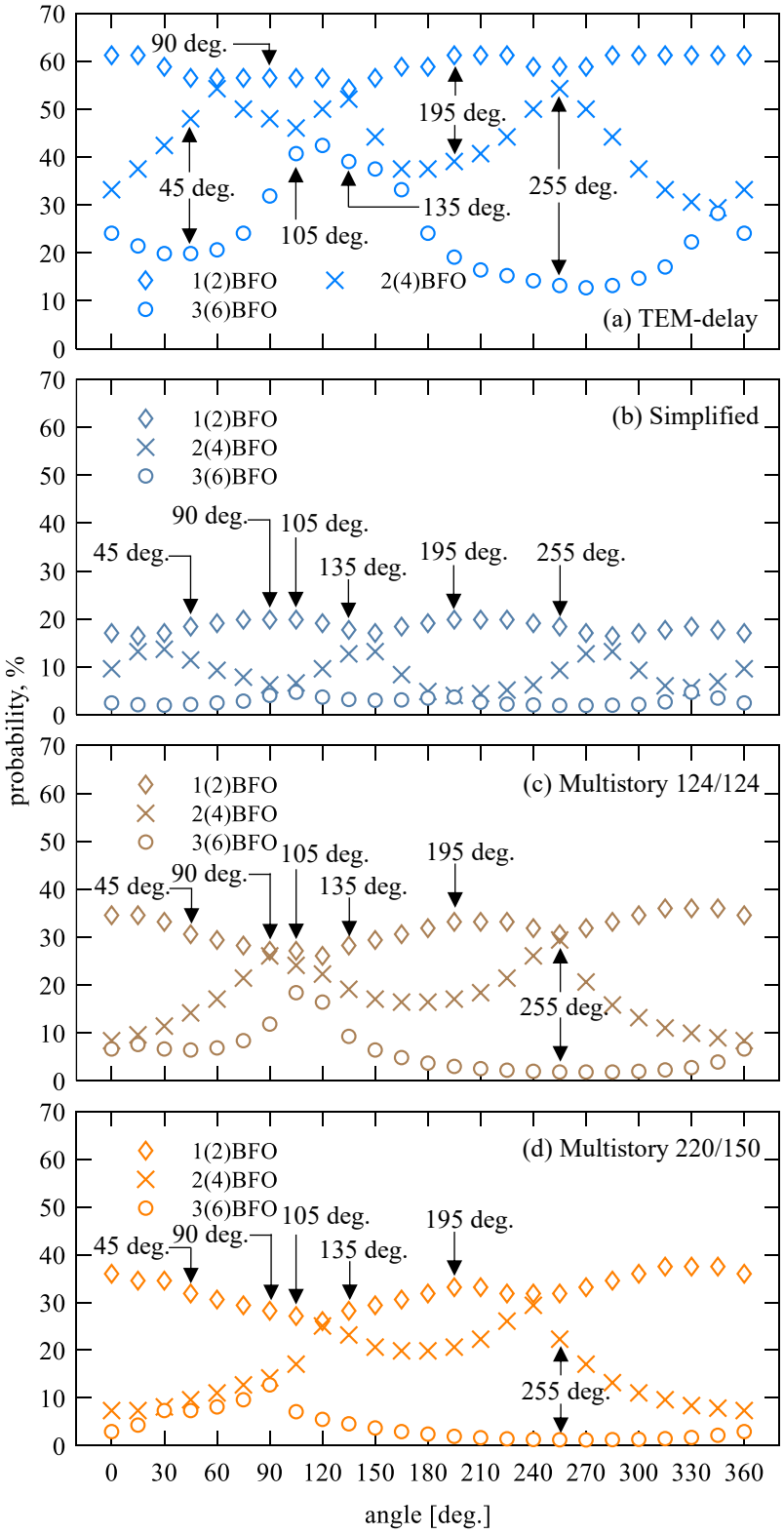

Fig. 4.21 Probabilities of minimum currents causing 1(2)–3(6) phase back-flashovers depending on simultaneous power frequency voltage angles computed by each circuit model.

C Validity of critical current

The critical currents derived by the TEM-delay model are lower than the observed currents causing BFOs reported in the past, but those derived by other models are higher than the observed ones. The critical current derived by the circuit analysis has to be lower than the observed current causing BFOs to reproduce them. In other words, the TEM-delay model can generate valid insulator voltages, while others generate smaller insulator voltages. Thus, the lightning fault rate can be underestimated by the existing transmission tower and line models. The validity is discussed based on the observed BFOs and lightning current in [2] and observed BFOs and operations of TLSAs reported in [46], which were reproduced using the FDTD method in [11]. The validity is also discussed based on the estimation of the lightning fault rate performed in [1].

Three cases of BFOs reported in [2] are introduced. The BFOs were observed, and peak currents were estimated by current sensors installed at an OHGW and tower foot. In the first case, the tower top was struck by lightning having a peak current of –30 kA when the simultaneous power frequency angle was about 270 degrees. The BFOs occurred at the upper and middle phases of one side and the middle phase of the other side of the line (case (i), 2(3) BFO, 270 degrees, –30 kA). In the second case, the mid-span of an OHGW was struck by lightning having a peak current of –56 kA when the power frequency angle was about 100 degrees. The BFOs occurred in all six phases (case (ii), 6BFO, 100 degrees, –56 kA). In the third case, also the mid-span of the OHGW was struck by lightning having a peak current of –35 kA when the power frequency angle was about 135 degrees. The BFOs occurred at the middle and lower phases on both sides of the line (case (iii), 4BFO, 135 degrees, –35 kA).

The TEM-delay model yields lower critical currents than the observed currents causing BFOs, but the other three models yield higher currents than the observed ones. Table 4.8 summarizes the three cases of the observed events mentioned above and the corresponding critical current derived by each model. The currents for cases (ii) and (iii) were calculated by considering the lightning strike to the mid-span of the OHGW in accordance with [2]. To reproduce the observed BFO phenomenon, the critical current derived by the circuit analysis has to be lower than the measured peak current. The critical currents derived by the Simplified, Multistory 124/124, and Multistory 220/150 model for each angle for each BFO are higher than the corresponding measured current peaks, respectively, though the 2/70 μs triangular current waveform is relatively severe. The existing models cannot reproduce the observed BFOs owing to the lower insulator voltages. In contrast, the critical currents derived by the TEM-delay model are lower than the reported currents in all cases, and the critical current for 3(6) BFO for cases (i) and (iii) are higher than the observed currents. Thus, the TEM-delay model can reproduce the BFOs.

Note that in some literature, lightning channel impedance less than 1000 Ω, such as 400 Ω, has been recommended or utilized [5], [16], [17]. If the lightning channel impedance less than 1000 Ω is employed, the critical current becomes even higher due to the lower current flowing into the tower. It results in further differences between the observed currents and critical currents derived by the

conventional models. The inclusion of nonlinearity of tower footing characteristics and corona discharge in OHGWs also increases the critical current magnitude because these characteristics lower the insulator voltages. These characteristics can influence the BFO occurrence in other cases, however.

Table 4.8 Observed BFO phase number and current magnitude presented in [2] and critical currents derived by each circuit model, unit in kA[a].

Case	*N*-BFO	Angle [degree]	Observed [2]	TEM-delay	Simplified	Multistory 124/124	Multistory 220/150
i	2(3) BFO	270	–30	–26	–61	–48	–53
ii	6BFO	100	–56	–50	–106	–65	–67
iii	4BFO	135	–35	–31	–72	–61	–54

[a] Case (i) is the lightning strike to the tower top, and the critical currents for 2(4) BFO are shown. The cases (ii) and (iii) are the lightning strike to the mid-span of an OHGW, and the currents for 3(6) BFO and 2(4) BFO derived by the mid-span lightning are shown.

The validity of the circuit models, including the tower and line models, FO model, and TLSA model, is further discussed by referencing the observed BFO phenomenon, including the operations of TLSAs reported in the past. The TEM-delay model reproduces the operation of TLSAs and BFO occurrence with the valid lightning current, which was used in the FDTD analysis of the same event reported in the past. However, the Multistory 124/124 model requires about twice the higher current for reproducing the observed phenomenon.

In [46], a BFO phenomenon in an actual 77-kV transmission system was observed. The tower height was about 40 m, and three TLSAs were installed in one circuit of the line. Lightning struck the tower top when the power frequency voltage was about 60 degrees. All three TLSAs operated (operation of lower phase TLSA was not observed but estimated to be operated), and BFOs occurred at the upper and lower phase of the TLSA-uninstalled line. In the same paper, the observed BFO was simulated using ATP. In the ATP analysis, the multistory tower model represented the tower, and the constant-parameter line model represented the transmission line. A current with a –35 kA peak was injected into the tower top. This model did not reproduce the observed BFO, and it was concluded that the induction current from the lightning channel should be considered to increase the insulator voltages.

Later in [11], the observed BFOs and operations of TLSAs were reproduced by the FDTD method. Besides, the analysis accurately simulated measured current waveforms at an OHGW and tower leg. A current waveform shown in Fig. 4.22 was injected into the tower top through a lightning channel model represented by a resistor-inductor loaded vertical conductor in the analysis. The equivalent impedance of the lightning channel model was ranging from 900 Ω to 1500 Ω.

The BFO phenomenon was analyzed using the circuit models and current waveform shown in Fig. 4.22. Three TLSAs were installed in one circuit, and the TEM-delay model and the Multistory 124/124 model were used. The tower footing resistance was set to 40 Ω following ref. [46].

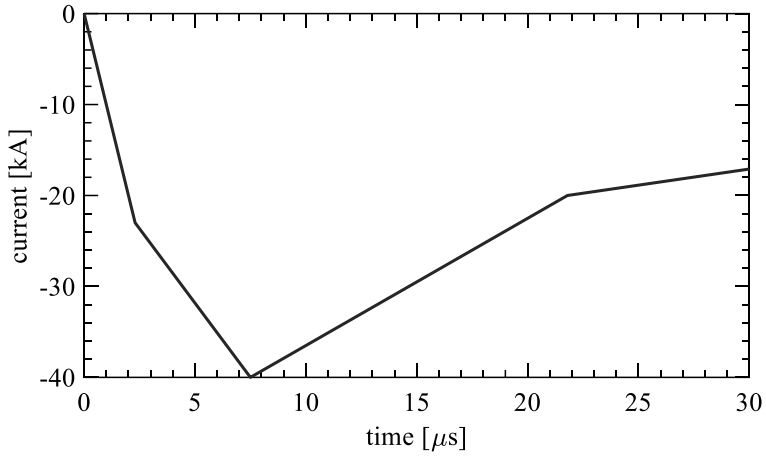

Fig. 4.22 Injection current for lightning surge analysis of the 77-kV transmission line with three TLSAs used in [11].

Fig. 4.23 shows the analyzed voltages of TLSAs (AR_U, AR_M, and AR_L) and arcing horns (AH_U, AH_M, and AH_L). The three TLSAs are operated, and BFOs occur in upper and lower phases in the simulation using the TEM-delay model, as observed in [46]. However, the simulation by the Multistory 124/124 model cannot reproduce the BFO at the upper phase and the operation of TLSA at the middle phase since the Multistory 124/124 model generates lower insulator voltages. Consequently, the induction current from the lightning channel had to be considered to increase the insulator voltages. Note that the insulator voltages are determined by the difference of the cross-arm voltages and the phase conductor voltages as provided (2.11) in Chapter 2: the induction current raises the phase conductor voltages in opposite polarity of the cross-arm voltages.

The Multistory 124/124 model requires a peak current of 70 kA in minimum to reproduce the observed results, while the TEM-delay model requires 38 kA in minimum to reproduce them. The Multistory 124/124 model requires a much higher current to reproduce the observed results due to ignorance of non-TEM characteristics, especially in the transmission line. When the BFO occurs at one phase, the voltages of other phases drop due to the mutual coupling from the BFO occurred phase. The voltage significantly drops if the model does not consider the non-TEM characteristics of transmission lines, namely the gradual rise of the mutual surge impedance with time and the time delays among lines corresponding to the separation distances. As is evident from Fig. 4.22, the voltages computed by the Multistory 124/124 model drop significantly and rise gently after the operations of TLSAs and the occurrence of the FO at the lower phase having no TLSA. These discussions stand even when the multistory tower model can reproduce the insulator voltages of lightning-struck transmission tower generated without considering the FO and power frequency voltages.

This simulation shows the validity of the TEM-delay tower and line model, the FO model, and the TLSA model. Note that induction from the lightning channel does exist, and its effect on the insulator

voltages of the lightning-struck tower is implicitly included in the TEM-delay model. Therefore, further discussion is required to analyze lightning surges intruding substations because the induction can

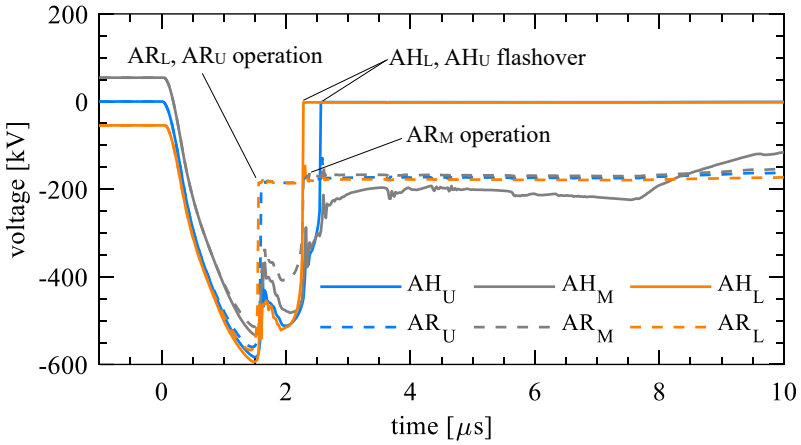

(a) TEM-delay model

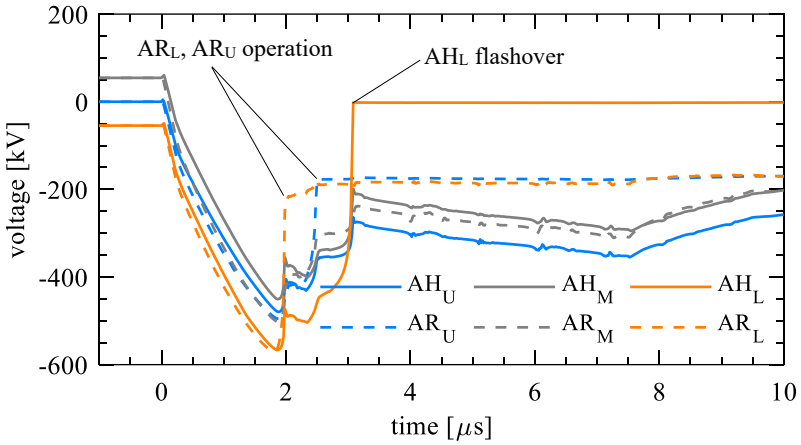

(b) Multistory model

Fig. 4.23 Arcing horn (AH_U, AH_M, and AH_L) and TLSA (AR_U, AR_M, and AR_L) voltages of a 77-kV transmission line with 40-kA peak current shown in Fig. 4.22.

significantly influence voltages at the substation entrance [47]. The induced voltage (vertical electric field) from the lightning channel and the traveling voltages along the incoming conductors generated by BFOs can have the opposite polarity.

The validity of the critical current is further discussed by referencing the estimation results of a lightning fault rate. In [1], lightning fault rates of 66- and 77-kV transmission lines were computed by the multistory tower model, whose surge impedance was computed by Jordan's formula. This model corresponds to the Multistory 124/124 model. The FO across arcing horn was modeled by the *V*–*t* crossover method, and the TLSA was modeled by the nonlinear resistance and the FO model by the *V*–*t* crossover method. The injection current was the 2/70 μs triangular current. The computed result was

compared with the experienced fault rate. Note that in computing lightning fault rates, the installation and arrangement of TLSAs and lightning activity depending on the studied period were considered by the method presented in the paper. The estimated lightning fault rate was 40% lower than the experienced one in the summer lightning season, while that was almost the same in the winter lightning season.

The deviation of the estimated and experienced fault rate in the summer lightning season can be attributed to the use of the multistory tower model because the model yields the lower insulator voltage, as discussed in this chapter, in addition to the modeling of the FO of arcing horns and TLSAs by the *V–t* crossover method pointed out in [1]. Note that the performance of the FO model by the *V–t* crossover method will be discussed in the next section. The discussions will clarify that the single-phase BFO can be sufficiently analyzed by the *V–t* crossover method, while the multiphase BFOs cannot be done. It can be interpreted that the lightning fault rate in the winter lightning season could have been successfully estimated because the current peak magnitude is higher than the summer lightning, and the lightning strike essentially causes the BFOs. The presented TEM-delay model and the FO models have the potential of precise estimation of the lightning fault rate in all seasons.

The validity of the critical current derived by the circuit analysis has been shown by referencing the observed and analyzed BFO phenomena reported in the past and the estimation results of the lightning fault rate. Every critical current derived by the TEM-delay model is lower than the measured ones, and hence the observed BFOs can be reproduced. The TEM-delay model has also reproduced the measured BFOs and operations of TLSAs. The result and discussions validate the circuit model of the tower, line, FO, and TLSA. The insulator voltages computed by the existing circuit models can be lower than the actual voltages. Further study is required for discussing lightning surges intruding substations, in which the electromagnetic induction from the lightning channel can have a significant influence.

D Impact of FO model on the BFO occurrence

The performance of the FO model by the *V–t* crossover method and the LPM is compared and evaluated. The transmission tower and line were represented by the TEM-delay models. The 2/70 μs triangular current waveform was injected. In the results, a similar critical current for single-phase BFO can be derived by the FO model by the *V–t* crossover method and the LPM since both models represent similar *V–t* characteristics. However, the occurrence of multiphase BFOs can be underestimated by the *V–t* crossover method due to the ignorance of the leader developing process. Therefore, the *V–t* crossover method can be utilized to estimate the BFO rate (occurrence of the 1BFO) if the FO model by the LPM is not available, but this method is not recommended for the multiphase BFO analysis.

BFO phases derived using the *V–t* crossover method and LPM are shown in Fig. 4.24. The results with the *V–t* crossover method roughly reproduce the observed characteristics of BFO phases depending on the power frequency voltage. Fig. 4.25 and Fig. 4.26 show the critical currents and their probabilities derived by each FO model. Regarding the 1(2) BFO, the currents derived by both models are almost the

same since both models have almost the same *V–t* characteristic, as shown in Fig. 4.9. Therefore, the occurrence probability of 1(2) BFO, a lightning fault rate in other words, can be evaluated by the *V–t*

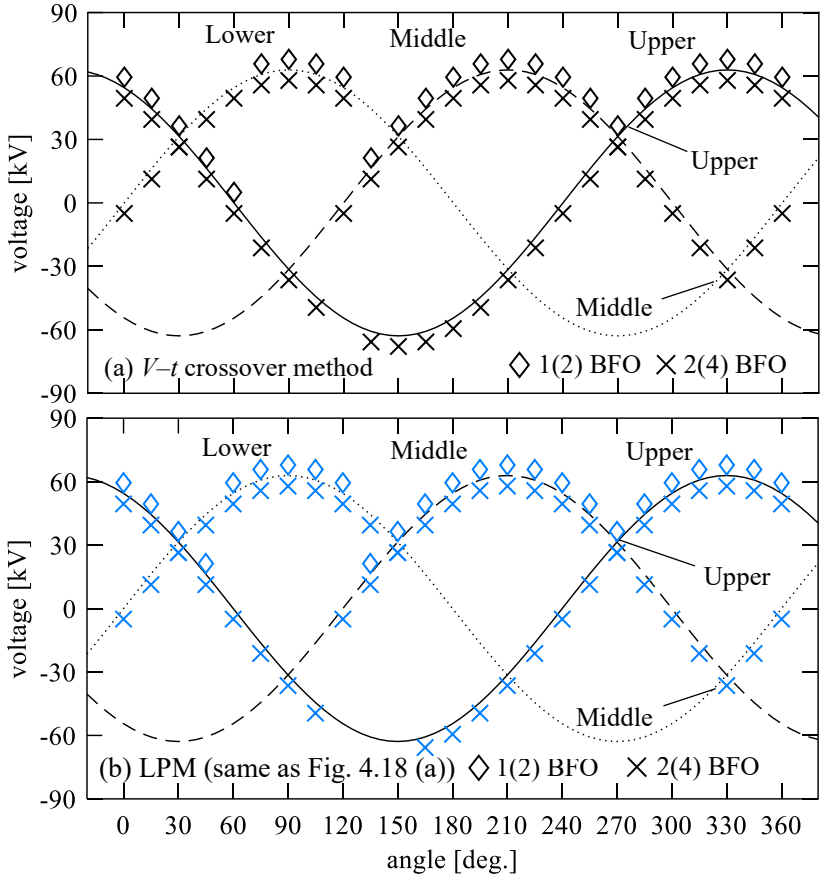

Fig. 4.24 BFO phases derived by circuit analysis using the FO model represented by the *V–t* crossover method and the LPM.

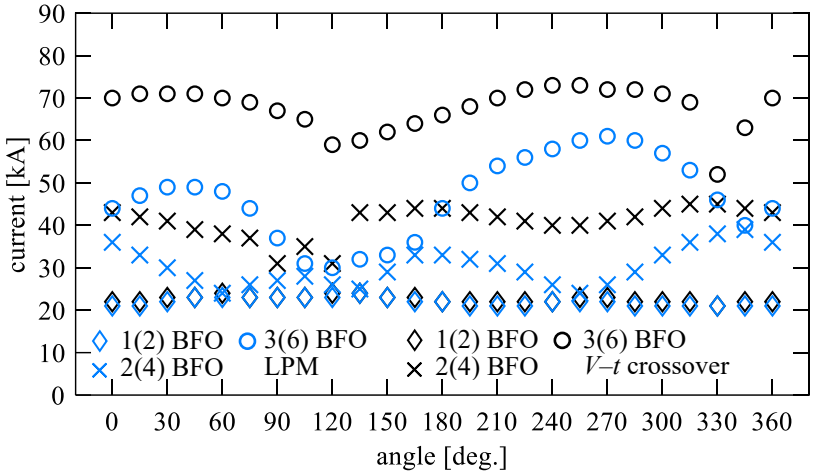

Fig. 4.25 Minimum currents causing *N*-phase BFO derived by circuit analysis using the FO model represented by the *V–t* crossover method and the LPM.

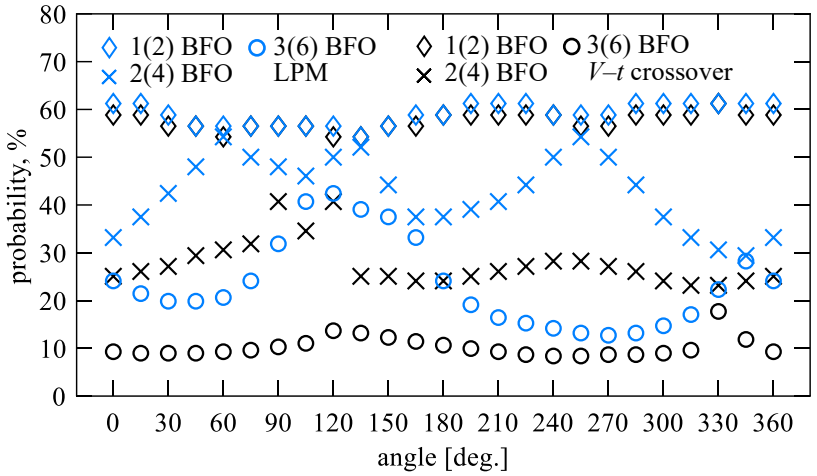

Fig. 4.26 Probability of minimum currents causing *N*-phase BFO derived by circuit analysis using the FO model represented by the *V*–*t* crossover method and the LPM.

crossover method as accurately as done by the LPM. A particular leader onset condition considering the effect of the power frequency voltages needs not to be considered as long as the triangular waveform represents the current since its wavefront rises instantly.

Different characteristics are derived by each model regarding the variation of the critical currents for 2(4) BFO and 3(6) BFO. The currents derived by the *V*–*t* crossover method have a flat variation compared to those derived by the LPM. The difference of the critical current variation can be attributed to the consideration of the leader developing process. Fig. 4.27 shows the insulator voltages derived by both FO models in 135 degrees in the 2(4) BFO case. Since the leader development is considered in the LPM, BFOs can occur continuously at the wave-tail. On the other hand, the continuous BFO in wave-tail cannot occur in the *V*–*t* crossover method due to the ignorance of the leader developing process. In this case, when the BFO occurs at one phase, insulator voltages of phases at which the BFO has not yet occurred drop significantly, and hence a higher current is required to occur the BFO in those phases, as shown in Fig. 4.27 (b). As a result, the critical currents derived by the *V*–*t* crossover method are little affected by the power frequency voltages and become much higher than those derived by the LPM.

If the *V*–*t* crossover method is used for multiphase BFO analysis, the validity of the critical currents should be carefully examined. For the reliable multiphase BFO analysis with the *V*–*t* crossover method, its *V*–*t* characteristic should be modified depending on the BFO occurrence, such as lowering the FO voltage as the BFO occurs at one phase. The same discussions can be applied to the modeling of TLSAs by the nonlinear resistance and the FO model by the *V*–*t* crossover method. Note that the critical currents for 2(4) BFO at 90–120 degrees and for 3(6) BFO at 330 degrees are much smaller than other cases with the same number of BFOs. The smaller critical currents are derived because the BFOs in different phases occur (insulator voltages cross the *V*–*t* curve) within the time delay of mutual coupling from the first BFO phase to the second BFO phase.

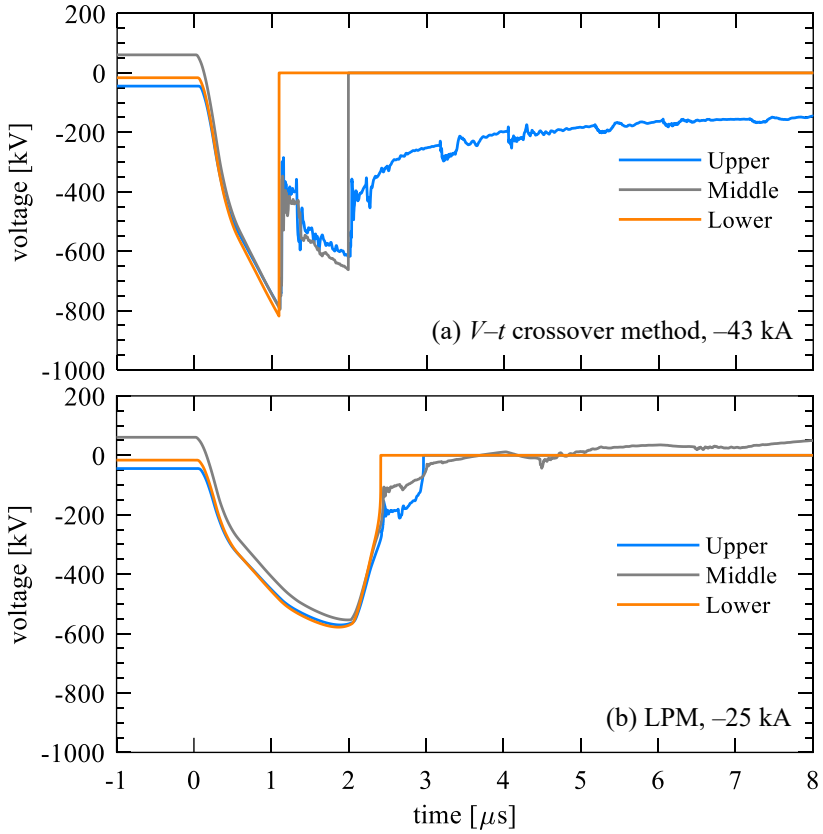

Fig. 4.27 Insulator voltages derived by circuit analysis using the FO model represented by the *V*–*t* crossover method and the LPM in 135 degrees, 2(4) BFO.

E Impact of a lightning current waveform on the BFO occurrence

The impact of a lightning current waveform on the BFO occurrence is discussed. The 2/70 μs triangular and the 3.83/77.5 μs double-peak current shown in Fig. 4.16 were used. It will be shown that both currents can yield similar BFO characteristics. The analysis was performed using the TEM-delay models.

The critical currents and their probabilities are shown in Fig. 4.28. Note that each current waveform yields the same BFO phases except for the upper and middle phase BFO in 330 degrees in the double-peak current. The critical currents derived by both waveforms have similar characteristics, but the magnitude derived by the double-peak current is about 10% higher than those derived by the triangular current. Fig. 4.29 shows the insulator voltages and injected current in the case of double-peak current injection. The steep-rising part of current after around 6 μs increases the insulator voltages, and BFO occurs subsequently. The steep-rising part is responsible for the occurrence of the BFO, and the 2/70 μs triangular current well approximates the double-peak current waveform. Note that the use of the 3.83/77.5 μs triangular current, whose wavefront is determined by the $T_{30/90}$/0.6 of the median parameter [48], requires about 10% higher critical current than that derived by the 3.83/77.5 μs double-peak current. Thus, in case the lightning current is approximated by the triangular current waveform, the rising part

shorter than $T_{30/90}/0.6$, such as the average of $T_{30/90}/0.6$ and t_m, equivalent wavefront corresponding to the maximum rate of rise introduced in Table 4.6, should be adopted (see Fig. 4.30).

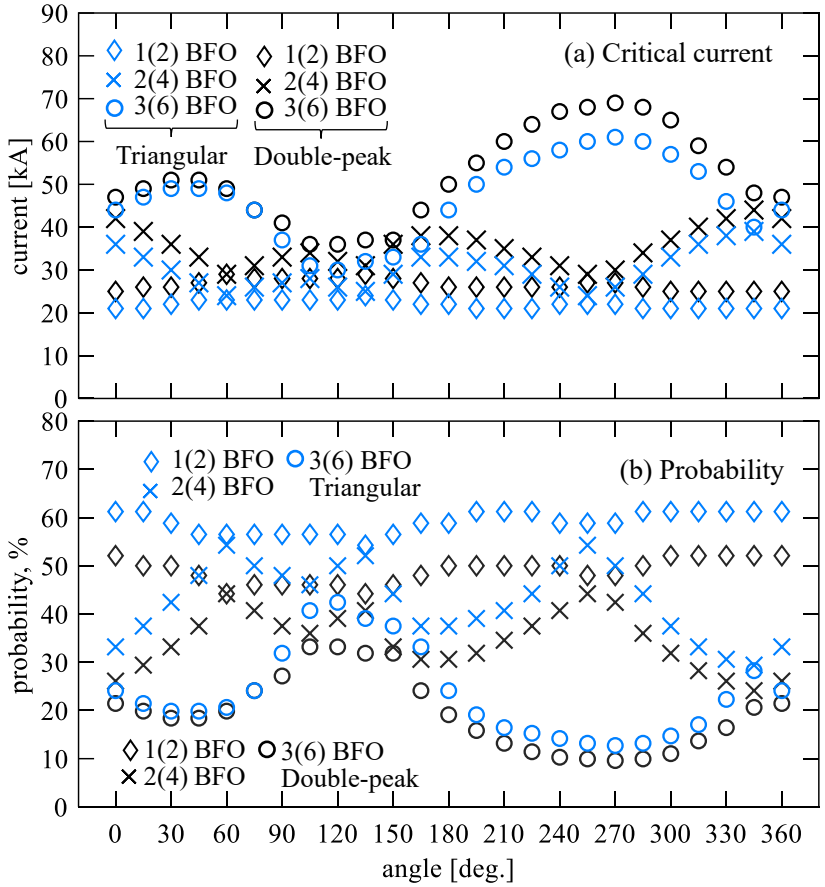

Fig. 4.28 Critical currents for *N*-phase BFOs and their probabilities derived by the TEM-delay model with the 2/70 μs triangular current and the 3.83/77.5 μs double-peak current.

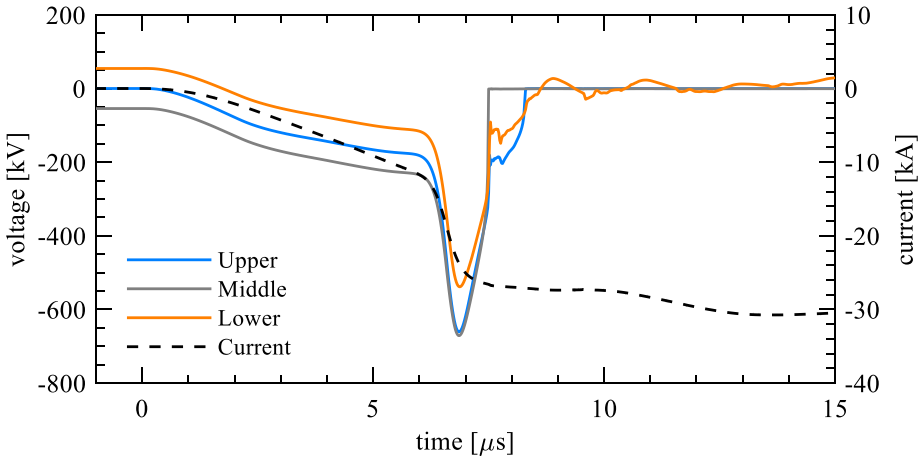

Fig. 4.29 Insulator voltages and injection current in the case of the 3.83/77.5 μs double-peak current, 255 degrees, 2(4) BFO.

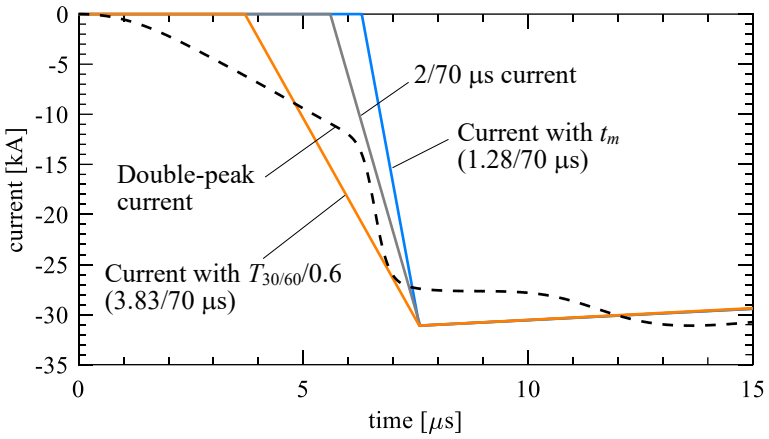

Fig. 4.30 The 3.83/70 μs double peak current and its approximation by the triangular current with three types of front durations.

4.3.3 Performance of each circuit model for the back-flashover analysis

The performance of each circuit model for BFO analysis is summarized. For BFO analysis of HV transmission lines, the TEM-delay transmission tower and line models with the FO model represented by the LPM perform the best among other existing models. The BFO characteristics derived by these models, including the BFO phases and critical currents, well support the observed results reported in the past. However, other transmission tower models and FO models have some drawbacks, and the lightning fault rate can be underestimated.

The existing tower models, including the Simplified model with constant surge impedance, the multistory tower model with surge impedance derived by Jordan's formula (Multistory 124/124), and the multistory tower model with surge impedance of 220 Ω and 150 Ω (Multistory 220/150), require higher critical current for single to multiphase BFOs. These models require higher currents since the insulator voltages are lower than the actual voltages. As a result, the lightning fault rate calculated by these models can be smaller than actual values. For example, in [1], it was reported that the multistory model with surge impedance derived by Jordan's formula provided a 40% smaller lightning fault rate than that of actually experienced one in the summer lightning season. Regarding the BFO phase, the Simplified model can reproduce the observed effect of power frequency voltages. However, the insulator voltage derived by this model is the lowest among the existing tower models, and thus the lightning fault rate can be underestimated most significantly.

The FO model by the *V*–*t* crossover method and the LPM provide a similar lightning fault rate as long as both models have similar *V*–*t* characteristics, though the LPM is suitable for analyzing multiphase BFOs. In case the FO model by the *V*–*t* crossover method is utilized to multiphase BFO analysis, a higher current is required for causing BFOs since the leader developing process is not considered. The FO model with LPM, which considers the leader developing process, is suitable for

multiphase BFO analysis. Note that the inclusion of the stochastic nature of the FO voltage and concurrent FO characteristics should be further discussed in the LPM model.

The 2/70 μs triangular current and the 3.83/77.5 μs double-peak current, representing the wavefront characteristics of the natural lightning current, provide similar critical currents. This is because the steep rising part is responsible for the BFO occurrences. In case the lightning current is simplified to the triangular current, the rising time shorter than the $T_{30/90}$/0.6 should be adopted since the steep rising part in the natural lightning current is responsible for the occurrence of the BFO.

In summary, the TEM-delay transmission tower and line model with the FO model represented by the LPM performs best for analyzing single to multiphase BFOs. Other models can underestimate the lightning fault rate or the occurrence of multiphase BFOs.

4.4 Conclusions

This chapter has evaluated the BFO characteristics of a 77-kV transmission line using circuit analysis models. The BFO phases and minimum current causing each number of BFO are significantly dependent on the power frequency voltages. The discussions on BFO phases and characteristics of minimum currents casing the BFOs have revealed that the TEM-delay tower and line model perform much better than the existing transmission tower and line models. The FO model by the LPM is suitable for analyzing multiphase BFOs, while the single-phase BFO can be sufficiently analyzed by both the *V*–*t* crossover method and the LPM.

Primarily to the BFO analysis, the insulator voltages have been further evaluated considering the tower footing characteristics by the FDTD method and circuit analysis models without the BFO phenomenon. The existing circuit models yield lower insulator voltages than those yielded by the FDTD method owing to the lower surge impedance and the lack or insufficient implementation of the wave attenuation characteristics along the tower. The experimental conditions for deriving multistory tower models could have affected these aspects. The TEM-delay model yields almost the same insulator voltages as the FDTD analysis yields, and the tower foundation can be modeled by a lumped linear resistance.

The BFO characteristics depending on the power frequency voltages have been identified by the BFO analysis especially using the TEM-delay tower and line models with the FO model by the LPM optimized for HV transmission systems. The BFO primarily occurs at phase with the positive power frequency voltage in case the negative lightning strikes, while there is a probability of the BFOs at the phases with the negative voltages. The probability of the critical current derived by the TEM-delay model supports the observed BFO phases. The BFO phenomenon accompanied by the operations of TLSAs has also been successfully reproduced by the TEM-delay model and the TLSA model with the nonlinear resistance and FO model by the LPM. Regarding the existing tower and line models, the BFO

phases can be partly reproduced by some models. However, the critical currents derived by them are higher than the observed values owing to the lower insulator voltages. In order to reproduce the BFOs, the critical current has to be lower than the observed values. Thus, the lightning fault rate can be underestimated by the conventional transmission tower and line models.

References for Chapter 4

[1] H. Kawamura, M. Kozuka, N. Itamoto, K. Shinjo, and M. Ishii, "Evaluation of relative lightning fault rate of transmission lines depending on line design and lightning activity," *IEEJ Trans. Power and Energy,* vol. 130, no. 10, pp. 895–902, Oct. 2010.

[2] T. Ueda, M. Yoda, and I. Miyachi, "Characteristics of lightning surges observed at 77 kV substations," *Trans. IEE of Japan,* vol. 116-B, no. 11, pp.1422–1428, Nov. 1996.

[3] T. Ito, T. Ueda, H. Watanabe, T. Funabashi, and A. Ametani, "Lightning flashovers on 77-kV systems: observed voltage bias effects and analysis," *IEEE Trans. Power Del.,* vol. 18, no. 2, pp. 545–550, Apr. 2003.

[4] J. He, X. Wang, Z. Yu, and R. Zeng, "Statistical analysis on lightning performance of transmission lines in several regions of China," *IEEE Trans. Power Del.,* vol. 30, no. 3, pp. 1543–1551, Jun. 2015.

[5] Z. Datsios, P. Mikropoulos, and T. Tsovilis, "Effects of lightning channel equivalent impedance on lightning performance of overhead transmission lines," *IEEE Trans. Electromagn. Compat.,* vol. 61, no. 3, pp. 623–630, June 2019.

[6] F. H. Silveira, and S. Visacro, "Lightning performance of transmission lines: impact of current waveform and front-time on backflashover occurrence," *IEEE Trans. Power Del.,* vol. 34, no. 6, pp. 2145–2151, Dec. 2019.

[7] Z. Datsios, P. Mikropoulos, and T. Tsovilis, "Closed-form expressions for the estimation of the minimum backflashover current of overhead transmission lines," *IEEE Trans. Power Del.,* vol. 36, no. 2, pp. 522–532, Apr. 2021.

[8] T. Noda, and S. Yokoyama, "Thin wire representation in finite difference time domain surge simulation," *IEEE Trans. Power Del.*, vol. 19, no. 3, pp. 840–847, Jul. 2002.

[9] Z. P. Liao, H. L. Wong, B. P. Yang, and Y. F. Yuan, "A transmitting boundary for transient wave analysis," *Scientia Sinica,* vol. A27, no. 10, pp. 1063–1076, Oct. 1984.

[10] Y. Taniguchi, Y. Baba, N. Nagaoka, and A. Ametani, "An improved thin wire representation for FDTD computations," *IEEE Trans. Antennas Propag.*, vol. 56, no. 10, pp. 3248–3252, Oct. 2008.

[11] A. Tatematsu, and T. Ueda, "FDTD-based lightning surge simulation of an HV air-insulated substation with back-flashover phenomena," *IEEE Trans. Electromagn. Compat.*, vol. 58, no. 5, pp. 1549–1560, Oct. 2016.

[12] C. A. Jordan, "Lightning computations for transmission lines with overhead ground wires, Part II," *General Electric Review*, vol. 37, no. 4, pp. 180–186, 1934.

[13] J. R. Marti, "Accurate modelling of frequency-dependent transmission lines in electromagnetic transient simulations," *IEEE Trans. Power Appar. Syst.*, vol. PAS-101, no. 1, pp. 147–157, Jan. 1982.

[14] M. Ishii, T. Kawamura, T. Kouno, E. Ohsaki, K. Murotani, and T. Higuchi, "Multistory transmission tower model for lightning surge analysis," *IEEE Trans. Power Del.*, vol. 6, no. 3, pp. 1327–1335, Jul. 1991.

[15] H. Kawamura, N. Itamoto, K. Shinjo, and M. Ishii, "Evaluation of characteristics of lightning faults on 275 kV transmission lines," *IEEJ Trans. Power and Energy*, vol. 129, no. 10, pp. 1233–1239, 2009.

[16] H. Kawamura, M. Kozuka, N. Itamoto, K. Shinjo, and M. Ishii, "Estimation of the frequency of instantaneous voltage drops dependent on arrangement of line surge arresters," *IEEJ Trans. Power and Energy,* vol. 29, no. 12, pp. 1585–1592, Dec. 2009.

[17] Subcommittee for transmission lines, study committee on lightning risk, "Application guide for transmission line surge arresters," *CRIEPI Rep.*, no. H07, 2012.

[18] M. A. Sargent, and M. Darveniza, "Tower surge impedance," *IEEE Trans. Power App. Syst.*, vol. PAS-88, no. 5, pp. 680–687, May 1969.

[19] IEEE Standards Board, "IEEE guide for improving the lightning performance of transmission lines," *IEEE Std.*, no. 1243-1997, 1997 (reaffirmed in 2008).

[20] H. Motoyama, Y. Kinoshita, and K. Nonaka, "Experimental study on lightning surge response of 500-kV transmission tower with overhead lines," *IEEE Trans. Power Del.*, vol. 23, no. 4, pp. 2488–2495, Oct. 2008.

[21] M. Saito, M. Ishii, M. Miki, and K. Tsuge, "On the evaluation of the voltage rise on transmission line tower struck by lightning using electromagnetic and circuit-based analyses," *IEEE Trans. Power Del.*, vol. 36, no. 2, pp. 627–638, Apr. 2021.

[22] Subcommittee for transmission lines, lightning protection design committee, "Guide to lightning protection design for transmission lines," *CRIEPI Rep.*, no. T72, 2003.

[23] Y. Aoshima, and K. Miyake, "Flashover characteristics of air gaps for short tail waves," *Trans. IEE of Japan*, vol. 109-B, no. 3, pp. 135–142, 1989.

[24] R. L. Witzke and T. J. Bliss, "Surge protection of cable-connected equipment," *AIEE Trans. Power App. Syst.*, vol. 69, no. 1, pp. 527–542, Jan. 1950.

[25] A. H. Hileman, *Insulation Coordination for Power Systems*. Boca Raton, FL, USA: CRC Press, 1999.

[26] A. Pigini, G. Rizzi, E. Garbagnati, A. Porrino, G. Baldo, and G. Pesavento, "Performance of large air gaps under lightning overvoltages: experimental study and analysis of accuracy predetermination methods," *IEEE Trans. Power Del.*, vol. 4, no. 2, pp. 1379–1392, Apr. 1989.

[27] T. Shindo, and T. Suzuki, "A new calculation method of breakdown voltage-time characteristics of long air gaps," *IEEE Trans. Power App. Syst.*, vol. PAS-104, no. 6, pp. 1556–1563, Jun. 1985.

[28] H. Motoyama, "Experimental study and analysis of breakdown characteristics of long air gaps with short tail lightning impulse," *IEEE Trans. Power Del.*, vol. 11, no. 2, pp. 972–979, Apr. 1996.

[29] H. Motoyama, K. Shinjo, Y. Matsumoto, and N. Itamoto, "Observation and analysis of multiphase back flashover on the Okushishiku Test Transmission Line caused by winter lightning," *IEEE Trans. Power Del*, vol. 13, no. 4, pp. 1391–1398, Oct. 1998.

[30] *Electrical Engineering Handbook*, Inst. Electr. Eng. Jpn., Tokyo, Japan, 1978.

[31] T. Miki, and M. Miki, "Flashover characteristics of arcing horn type ZnO lightning arrester (part 1) –operating characteristics with standard lightning impulse voltage and its evaluation of equivalent gap length–," *CRIEPI Rep.*, no. H11016, May 2012.

[32] T. Miki, and M. Miki, "Flashover characteristics of arcing horn with metal-oxide surge arrester (EGLA) for 66kV (part 2) –characteristics with short-tail lightning impulse voltage and its evaluation of equivalent gap length–," *CRIEPI Rep.*, no. H19009, May 2020.

[33] T. Ueda, M. Morita, A. Ametani, T. Funabashi, T. Hagiwara, and H. Watanabe, "Flashover model for arcing horns and transmission line arresters," *IEEJ Trans. Power and Energy*, vol. 112, no. 12, pp. 1085–1092, Dec. 1992.

[34] N. Nagaoka, "A flashover model using a nonlinear inductance," *Trans. IEE of Japan*, vol. 111-B, no. 5, pp. 529–534, May 1991.

[35] Electric Technology Research Association, "Voltage sag mitigation methods," *Electric Technology Research,* vol. 46, no. 3, 1990.

[36] Investigating R&D Committee on lightning parameters for insulation and protection designs of power systems, "Lightning parameters for insulation and protection designs of power systems," *IEEJ Technical Rep.*, no. 1033, Sep. 2005.

[37] CIGRE WG C4.407 (Convenor: V. A. Rakov), "Lightning parameters for engineering applications," *CIGRE Technical Brochure*, no. 549, Aug. 2013.

[38] A. Yamanaka, N. Nagaoka, Y. Baba, M. Saito, and T. Miki, "Lightning strike to a tall grounded object: part 1. circuit modeling with direction dependence," *IEEE Trans Electromagn. Compat.*, vol. 61, no. 3, pp. 727–735, Jun. 2019.

[39] M. Saito, M. Ishii, T. Miki, T. Shindo, and T. Sonehara, "Reproduction of electromagnetic field waveforms of downward lightning strokes hitting Tokyo Skytree," *IEEE Trans. Electromagn. Compat.*, vol. 61, no. 3, pp. 815–822, Jun. 2019.

[40] N. Itamoto, H. Kawamura, K. Shinjo, Y. Tanaka, and T. Noda, "Lightning fault rate calculation of transmission lines taking statistical variation of arching-horn flashovers into account," *IEEJ Trans. Power and Energy*, vol. 140, no. 2, pp. 126–133, Feb. 2020.

[41] D. Tanaka, T. Shindo, T. Miki, and M. Miki, "Probability of concurrent flashover in a parallel gap configuration," *IEEJ Trans. Power and Energy*, vol. 135, no. 11, pp. 669–674, Nov. 2015.

[42] A. D. Conti, and S. Visacro, "Analytical representation of single- and double-peaked lightning current waveforms," *IEEE Trans. Electromagn. Compat.*, vol. 49, no. 2, pp. 448–451, May 2007.

[43] K. Berger, "Parameters of lightning flashes," *ELECTRA*, vol. 41, pp. 23–37, 1975.

[44] F. Heidler, "Analytical lightning current function for LEMP-calculation," *translation from German, Proc. Int. Conf. on Lightning Protection (ICLP)*, pp. 63–66, Munich, Germany, 1985.

[45] J. Takami, and S. Okabe, "Observational results of lightning current on transmission towers," *IEEE Trans. Power Del.*, vol. 22, no. 1, pp. 547–556, Jan. 2007.

[46] T. Ueda, "Investigation of effect of transmission line arresters verified by lightning surges at substations," *Trans. IEE of Japan,* vol. 117-B, no. 10, pp. 1389–1396, Oct. 1997.

[47] J. Takami, T. Tsuboi, K. Yamamoto, S. Okabe, Y. Baba, and A. Ametani, "Lightning surge into a substation at a back-flashover and review of lightning protective level through the FDTD simulation," *IEEE Trans. Dielectr. Electr. Insul.*, vol. 21, no. 3, pp. 1044–1052, Jun. 2014.

[48] CIGRE WG 33.01 (Lightning), "Guide to procedures for estimating the lightning performance of transmission lines," *CIGRE Technical Brochure*, no. 63, 1991.

5 Performance Analysis of Transmission Line Surge Arresters

The installation of the TLSAs started around 1990. Since then, TLSAs, including metal-oxide surge arresters and those of arcing horn type, and fault current interrupting arcing horns, have been rapidly installed due to their effectiveness in reducing lightning faults [1]. The performance analysis of TLSAs is indispensable for achieving cost-effective installations.

The performance of TLSAs for reducing lightning accidents has been analyzed to determine the installation strategy. The analyzed aspects include the installation of TLSAs for every tower and every two or three towers, installation phases, the effect of tower footing resistance on the TLSAs effectiveness, and the absorbed energy of TLSAs [2]–[8], for instance. In these analyses, the power frequency voltages have been neglected or fixed in general. However, the voltages can significantly influence the BFO occurrences because the operations of the EGLA type TLSAs are initiated by the FO across the air gap. In this thesis, the effect of power frequency voltages and TLSAs operations on the BFO occurrence can be precisely analyzed because the presented models can consider the non-TEM characteristics of the lightning-struck transmission tower and line as well as the leader development in air gaps of TLSAs and arcing horns.

This chapter discusses the TLSAs effectiveness in reducing the lightning fault rate in HV and EHV transmission lines using the TEM-delay transmission tower and line models and the model of the TLSAs represented by the nonlinear resistance and the FO model by the LPM. The analysis was performed considering the power frequency voltages and the multiphase BFOs. The several arrangements of TLSAs were considered, and their effectiveness was clarified. In addition, the effect of the power frequency voltages on the BFO occurrence was analyzed.

5.1 Performance Analysis of TLSAs for HV Transmission Lines

5.1.1 Analysis conditions and cases

The BFO analysis was performed for a vertical double-circuit HV transmission line, including:

1) a TLSA uninstalled line;
2) a line with three TLSAs in one circuit of the line;
3) lines with five TLSAs (no TLSA in one of the six-phase conductors).

The second case arrangement, the installation of three TLSAs in one circuit of the line, is adopted for avoiding the double-circuit fault. The third case arrangement, the installation of five TLSAs, is adopted for further reducing lightning-related accidents. In the third case, three types of TLSA arrangement were considered: the TLSA was not installed for the upper, middle, or lower phase. The effectiveness of the

second and third case arrangements is discussed based on comparing the TLSA-uninstalled line. Note that the installation of six TLSAs best performs to decrease the lightning accidents since the occurrence of the BFO is avoided by the TLSAs. However, the absorbed energy by the lightning with excessive charge can become more significant in the installation of six TLSAs than that of five TLSAs. The installation of five TLSAs is sometimes adopted for this reason [3], [6].

The studied tower and line were the same as those studied in Chapter 4. Fig. 5.1 illustrates a circuit analysis model, and Table 5.1 summarizes circuit analysis conditions. The TEM-delay tower model with cross-arms represented the transmission tower. The different cross-arm voltages can be considered by this tower model. The TEM-delay line model represented the 300-m transmission line, the FO at the arcing horn was represented by the model by the LPM, and the TLSA was represented by the series-connected nonlinear resistance and the FO model by the LPM.

In each line with each TLSA arrangement, the following analyses were performed:

1) Calculation of the critical current causing *N*-phase BFOs without the power frequency voltages;
2) Calculation of the critical current causing *N*-phase BFOs with considering the power frequency voltages (in lines with symmetrical and asymmetrical phase rotations).

The phase angle of the power frequency voltage was incremented by 15 degrees. The comparison of the critical currents derived with and without the power frequency voltages can reduce the number of analyses. Suppose the effect of the power frequency voltages on the critical current is negligible or relatively low. In that case, the calculation of the lightning fault rate can be simply performed without the voltages. The 2/70 μs triangular current was injected and incremented by 1 kA to derive the critical current. The tower footing resistance was set to 10 Ω.

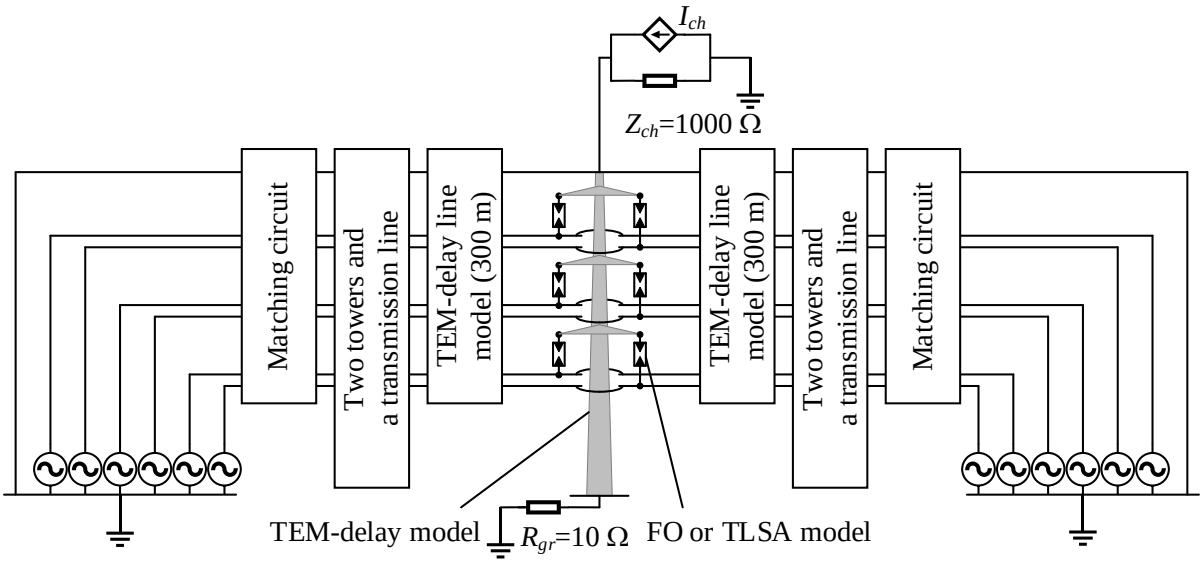

Fig. 5.1 Circuit model for BFO analysis of an HV transmission line for evaluating the performance of TLSAs using TEM-delay transmission tower and line models.

Table 5.1 Analysis cases and conditions for lightning surge analysis of an HV transmission line considering the TLSAs.

Current waveform	2/70 μs triangular current (negative polarity)
Current peak	Incremented by 1 kA
Lightning channel impedance	1000 Ω
Power frequency voltage	Incremented by 15 degrees
Phase rotation	Symmetrical and asymmetrical rotations
Tower model	TEM-delay tower model with cross-arms
Line model	TEM-delay line model
FO model	Model by the LPM
TLSA model	Series connected nonlinear resistance and FO model by the LPM
Number of TLSAs	0, 3, 5: no TLSA is installed at the upper, middle, or lower phases
Tower footing model	10-Ω linear resistor

5.1.2 Back-flashover phases and critical currents derived by each arrangement

A TLSA-uninstalled line

A similar critical current for 1BFO (lightning fault rate) and 2BFO (occurrence of the temporary voltage drop) are derived in both the symmetrical and asymmetrical phase rotation lines. Further, the power frequency voltages on 1BFO and 2BFO are negligible in the TLSA uninstalled line. The effect of the power frequency voltages on the BFO phases is similar in both phase rotations: the BFO occurrence at phases with positive power frequency voltages is prioritized, but it can occur at phases with the negative voltage, as discussed in Section 4.3.2. Note that the probability of severe accidents, including BFOs in four to six phases, can be higher in the symmetrical phase rotation line since each phase has the same power frequency voltages at both circuits.

The BFO phases are shown with the simultaneous power frequency voltages in Fig. 5.2. Note that in the symmetrical phase rotation line (Fig. 5.2 (a)), the 2BFO and 4BFO phases are shown above and below the corresponding power frequency voltages to provide better visibility. In the asymmetrical phase rotation line (Fig. 5.2 (b-1–b-5)), the BFO phases and power frequency voltages in the first and second circuits are shown above and below the corresponding voltages. A similar effect of the power frequency voltages on the BFO phases is derived in both phase rotation lines: the BFO firstly occurs in phases with the positive power frequency voltages owing to the injection of current with negative polarity; however, the BFO can occur in phases with the negative power frequency voltages. The BFO occurs in both circuits simultaneously in the symmetrical phase rotation line due to the FO model's assumption. The BFOs basically occur in each circuit at different timing in the asymmetrical phase rotation line, except for some simultaneous BFO occurring in the middle phase and other phases. The power frequency voltages are the same in both circuits at the middle phase, for instance. The consideration of the stochastic variation of the FO voltage or the concurrent FO characteristic can further

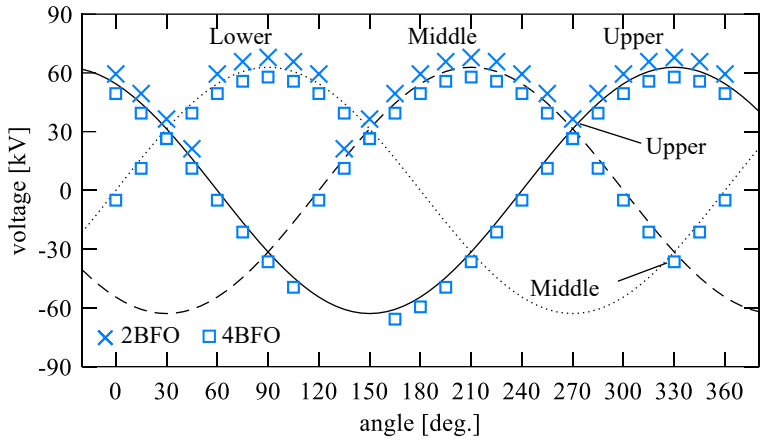

(a) Symmetrical phase rotation

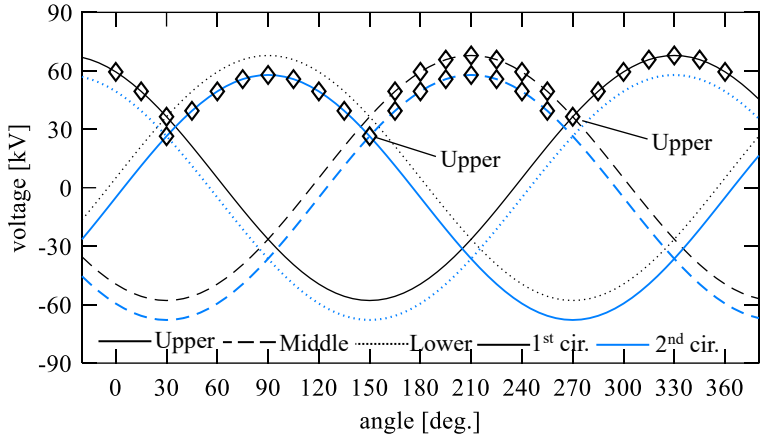

(b-1) Asymmetrical phase rotation, 1BFO

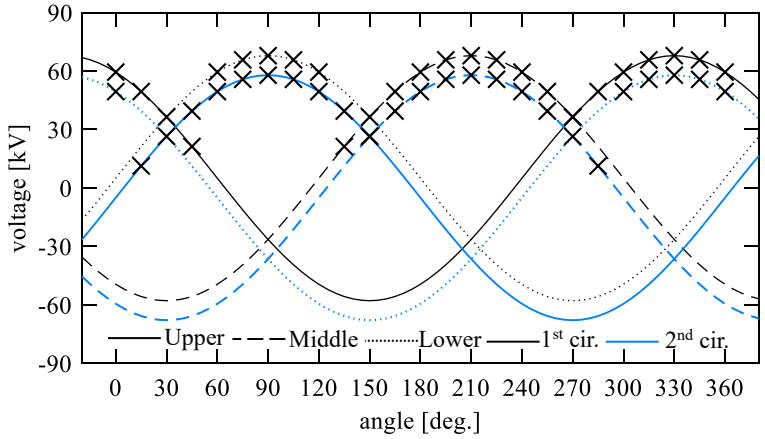

(b-2) Asymmetrical phase rotation, 2BFO

Fig. 5.2 BFO phases derived in the TLSA uninstalled HV transmission line (this figure follows to the next page).

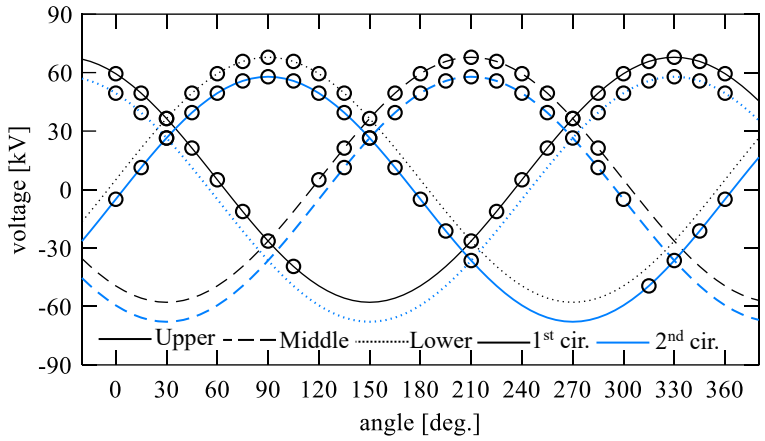

(b-3) Asymmetrical phase rotation, 3BFO

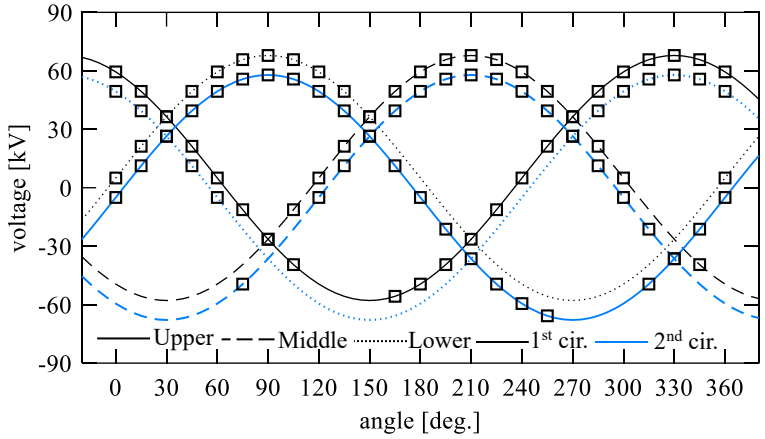

(b-4) Asymmetrical phase rotation, 4BFO

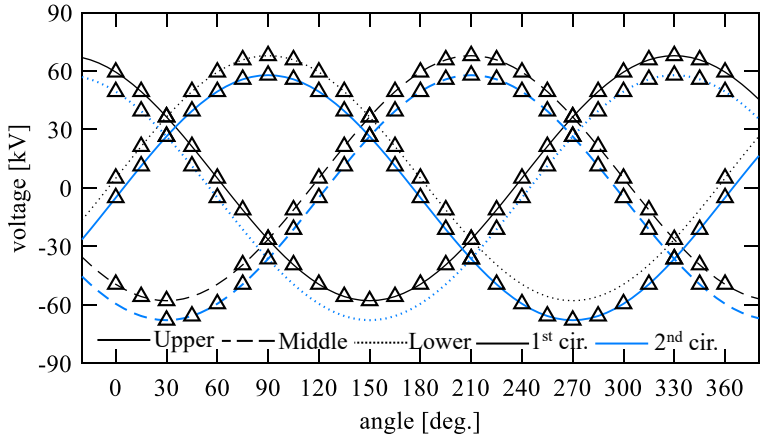

(b-5) Asymmetrical phase rotation, 5BFO

Fig. 5.2 BFO phases derived in the TLSA uninstalled l HV transmission line (this figure is followed from the previous page).

enhance the validity of the BFO analysis. Nevertheless, the present FO model by the LPM can discuss the general trend of the BFOs.

Similar critical currents are derived for 1BFO and 2BFO by both phase rotation lines, but those for the large number of BFOs are higher in the asymmetrical phase rotation line. Fig. 5.2 and Fig. 5.3 show the currents and their probabilities. The critical current for 2BFO derived in the symmetrical phase rotation line and that for 1BFO and 2BFO derived in the asymmetrical phase rotation line are similar values, ranging from 20 kA to 30 kA.

Regarding the large number of BFOs, namely, 4BFO to 6BFO, the critical current derived in the asymmetrical phase rotation line is higher than those derived in the symmetrical phase rotation line. In the asymmetrical phase rotation line, the power frequency voltages for upper and lower phases are different in both circuits of the line. Thus, the BFOs basically occur at different timing in different phases. The occurrence of BFOs drop insulator voltages of phases, where the BFO has not yet occurred, and a higher current is required for the occurrence of BFOs at those phases. However, the power frequency voltages are the same for all phases in both circuits in the symmetrical phase rotation line, and hence the simultaneous BFO occurs with a lower current. If the concurrent FO characteristic is considered, the number of BFO phases in the symmetrical phase rotation line can become rather lower.

The critical currents for 1BFO and 2BFO derived without the power frequency voltages and the mean of those derived with the voltages are similar in the TLSA uninstalled line. Table 5.2 summarizes critical currents and their probabilities derived with and without the power frequency voltage. The mean and minimum critical currents in all 24-phase angle cases, $I_{cc\text{-}mean}$ and $I_{cc\text{-}min}$, and their probabilities are shown for the simulation case with the power frequency voltage:

$$I_{cc-mean} = \frac{1}{N_{Ang}} \sum_{k} I_{cck}, \; I_{cc-min} = \min\left(I_{cck}\right). \tag{5.1}$$

Similar critical currents for 1BFO are derived with and without the power frequency voltages because the magnitude of the power frequency voltage, about 60 kV, is less than about 10% of the FO voltage of the 0.65 m air gap (higher than around 500 kV depending on the voltage waveform, see Fig. 4.9 for the *V*–*t* characteristics). The 1BFO corresponds to the lightning fault rate, and the 2BFO in HV transmission lines adopting high resistance grounding corresponds to the occurrence of the temporary voltage drop [3], [9]. If the mean probability of those events is discussed, the power frequency voltages can be neglected. As mentioned previously, the critical current for multiphase BFOs in the asymmetrical line case is higher than those derived in the symmetrical line case and the case without the power frequency voltage.

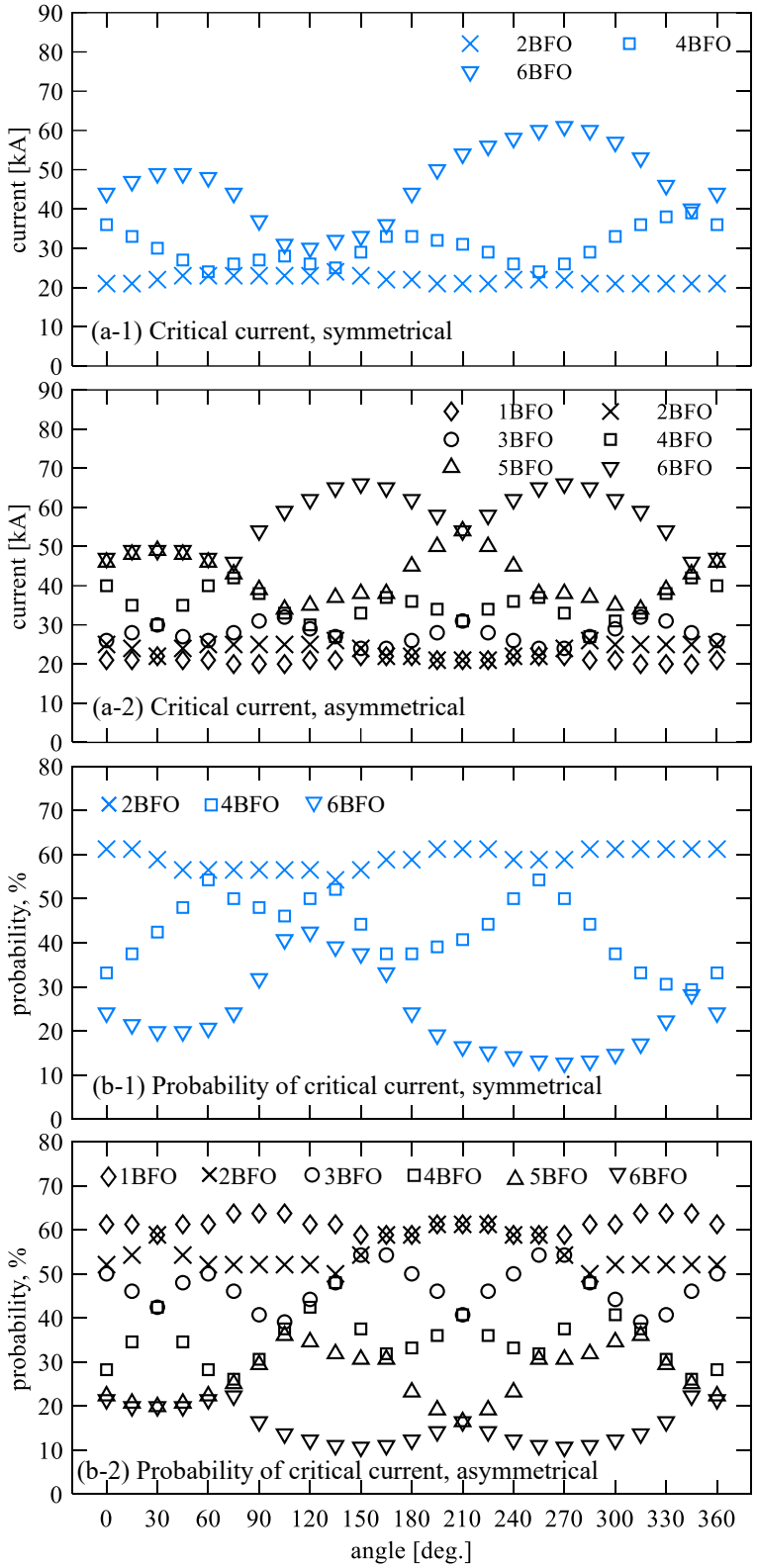

Fig. 5.3 Critical currents causing *N*-phase BFOs and their probability derived in the TLSA-uninstalled HV transmission line with symmetrical and asymmetrical phase rotations.

Table 5.2 Minimum current I_{cc} in kA causing N-phase BFOs at the TLSAs uninstalled HV transmission line and its probability [a].

Number of BFOs	[b]w/o AC	[b]with AC, symmetrical phase rotation		with AC, asymmetrical phase rotation	
		[c]mean	[c]mini	[c]mean	[c]mini
1	—	—	—	–21 (61)	–20 (64)
2	–23 (57)	–22 (59)	–21 (61)	–24 (54)	–21 (61)
3	—	—	—	–28 (46)	–24 (54)
4	–27 (48)	–29 (44)	–24 (54)	–35 (35)	–27 (48)
5	—	—	—	–42 (26)	–34 (36)
6	–39 (29)	–46 (22)	–30 (42)	–57 (15)	–46 (22)

[a] probability of the minimum current is shown in the parenthesis.
[b] for with and without AC (power frequency voltages), symmetrical phase rotation case, 1, 2, 3, BFOs are empty since BFOs occur in both circuits simultaneously due to the limitation of the FO model.
[c] "mean" provides the mean current of the 24 cases of phase angles for the power frequency voltages, and "mini" provides the minimum current among them.

B Three TLSAs installed line

Characteristics of BFO phases, the dependency of the critical current, and its probability on the power frequency voltage of the three TLSAs installed lines are similar to those in the TLSA uninstalled symmetrical rotation line. The minimum critical current derived considering the power frequency voltages is relatively smaller than those derived without considering the voltages. Thus, the power frequency voltage should be considered if the lightning fault rate is discussed based on severe conditions.

Fig. 5.4 shows the BFO phases, critical currents, and probabilities of the currents derived in the three TLSAs installed line. Note that the 1BFO and 2BFO phases are shown above and below the corresponding power frequency voltages for providing better visibility. The BFO phases are identical in both phase rotation lines, and they are similar to those derived in the TLSA uninstalled symmetrical phase rotation line (see Fig. 5.2 (a)). Further, the critical currents and their probabilities derived in both phase rotation lines are similar, and their variations are as well similar to those derived in the TLSA uninstalled symmetrical phase rotation line except for the 1BFO dependency on the power frequency voltages (see Fig. 5.3 (a-1) and (b-1)). Similar variations are derived because the BFO characteristics of the TLSA uninstalled circuit in line with three TLSAs are determined by the same power frequency voltages in the TLSA uninstalled symmetrical phase rotation case. Note that the probability of 1BFO derived in the three TLSAs installed lines is about 20% smaller than that derived in the TLSA-uninstalled line. This aspect is closely related to the TLSA effectiveness and will be summarized and discussed in Section 5.1.3.

The power frequency voltage significantly influences the magnitude of the critical current. The currents and their probabilities derived with and without considering the power frequency voltages are summarized in Table 5.3. In the three TLSAs installed line, the difference of critical currents and their

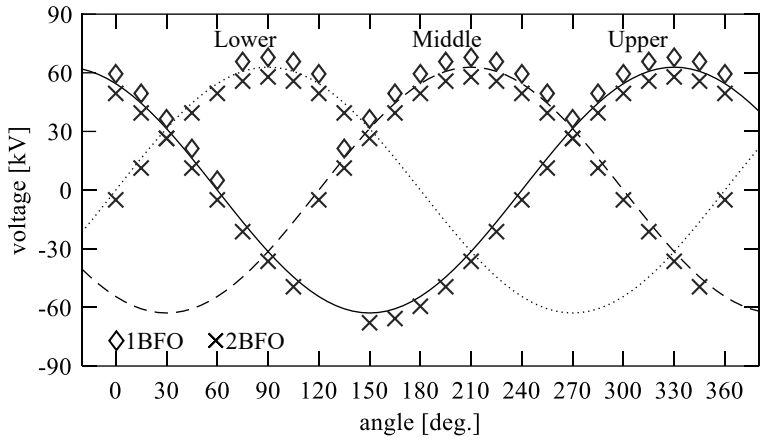

(a) BFO phases (BFO phases are identical in both phase rotation cases)

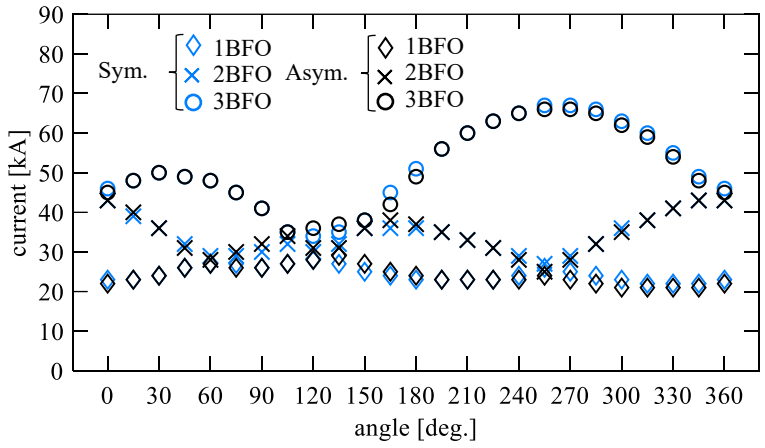

(b) Critical current

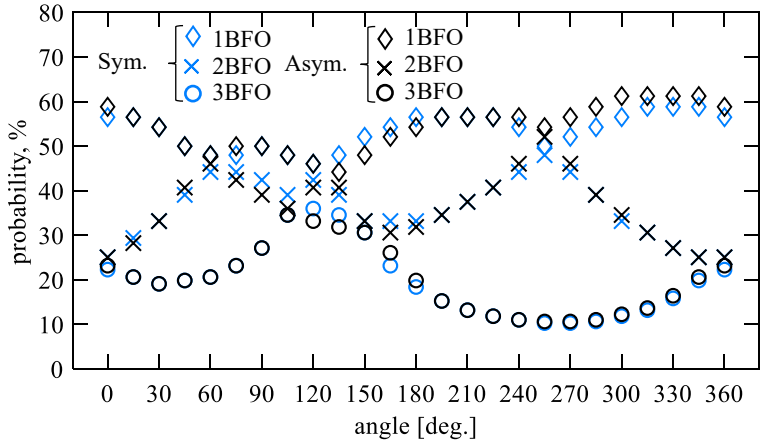

(c) Probability of critical current

Fig. 5.4 BFO phases, critical current, and probability of the critical current derived in the three TLSAs installed HV transmission line in both phase rotation cases.

probabilities derived with and without the power frequency voltages are larger even in the 1BFO case. For instance, the maximum probability for 1BFO considering the power frequency voltages is more than 10% higher than that without the voltages. The difference is attributed to the operations of TLSAs. Even in 1BFO cases, the TLSAs have been operated before the BFO occurrence of arcing horns at the phases without the TLSA (Fig. 4.9 and Fig. 4.13 provided *V*–*t* characteristics of the FO across the arcing horn and the TLSA, respectively). The FO at the air gap of the TLSA initiates its operation. Thus the 1BFO in the three TLSAs installed line can be interpreted as the multiphase BFOs, and the power frequency voltages strongly influence the occurrence of the BFOs as was in the multiphase BFOs in the TLSA uninstalled line case. The power frequency voltages should be considered in the three TLSAs installed line with both phase rotation cases if the lightning fault rate is discussed based on severe conditions.

Table 5.3 Minimum current I_{cc} in kA causing *N*-phase BFOs in the three TLSAs installed HV transmission line and its probability [a].

Number of BFOs	w/o AC	with AC, symmetrical phase rotation		with AC, asymmetrical phase rotation	
		[b]mean	[b]mini	[b]mean	[b]mini
1	–27 (48)	–24 (53)	–22 (59)	–24 (54)	–21 (61)
2	–31 (41)	–34 (36)	–27 (48)	–34 (36)	–25 (52)
3	–47 (21)	–52 (18)	–34 (36)	–51 (18)	–35 (35)

[a] probability of the minimum current is shown in the parenthesis.
[b] "mean" provides the mean current of the 24 cases of phase angles for the power frequency voltages, and "mini" provides the minimum current among them.

C Five TLSAs installed line

BFO occurs at the phase without the TLSA in the five TLSAs installed line. The minimum critical current derived considering the power frequency voltages is lower than those derived without considering the voltages. Thus, the power frequency voltage should be considered in case the lightning fault rate is discussed based on severe conditions. Regarding the TLSA arrangement, uninstallation for the lower phase is the most effective as long as the tower footing resistance is less than 40 Ω.

The critical current derived by the five TLSAs installed lines depends on the power frequency voltages and the phase without the TLSA: the uninstallation for the lower phase performs the best. Fig. 5.5 shows the currents and their probability derived in each TLSA arrangement. In the figure, legends "AH_U," "AH_M," and "AH_L" indicate the results for each case where the TLSA is not installed for the upper, middle, and lower phases, respectively. The critical current heavily depends on the power frequency voltages even for the 1BFO since this 1BFO can be interpreted as the multiphase BFOs, as discussed in the three TLSAs installed line case. The variations correspond to the variations of the power frequency voltages. For instance, for no TLSA at the lower phase case, the maximum and minimum critical current are derived around 270 degrees and 90 degrees, respectively, where the power frequency voltages for the lower phase are the minimum and the maximum. Among the three arrangements, the

highest critical current is observed if the lower phase has no TLSA. In other words, this arrangement most effectively reduces the probability of a lightning fault.

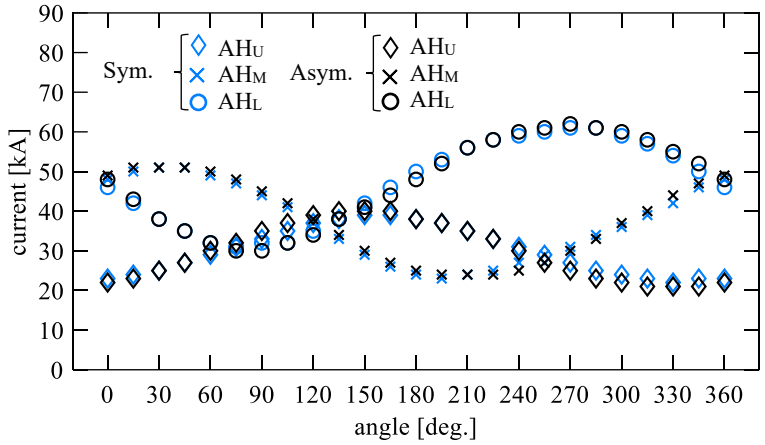

(a) Critical current

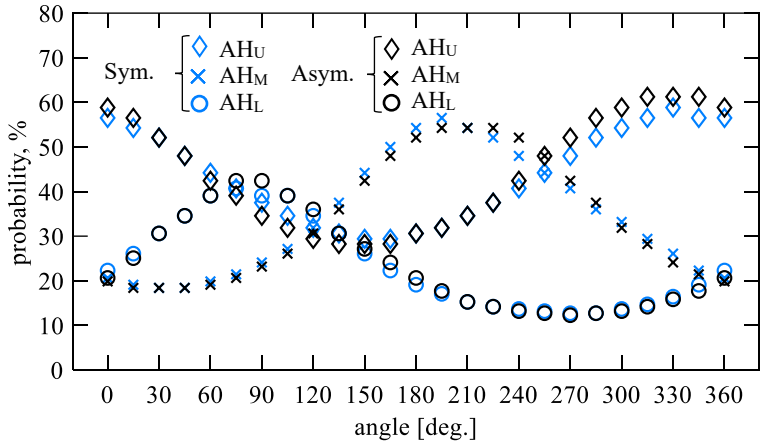

(b) Probability

Fig. 5.5 Critical current and probability of the critical current derived in the five TLSAs installed HV transmission line in both phase rotation cases (AH_U, AH_M, and AH_L provide results for cases that the TLSA is not installed for upper, middle, and lower phases, respectively).

The dependence of the critical current on the TLSA arrangement can be attributed to the insulator voltages derived without the power frequency voltages, FOs, and TLSAs. Fig. 5.6 shows the insulator voltages generated by the 1-A peak 2/70 μs and 5/70 μs triangular currents for tower footing resistance of 10 Ω and 40 Ω, respectively. In the tower footing resistance of 10 Ω cases, the lower phase voltage is the lowest among the three phases. Hence, the TLSA uninstallation for the lower phase is the most effective than the others. The voltage of each phase depends on the tower footing impedance and the wavefront duration. In the studied tower case, the TLSA uninstallation for the upper or middle phases can be more effective than that for the lower phase with a higher tower footing resistance than 40 Ω, as shown in Fig. 5.6. The TLSA uninstalled phases should be carefully determined based on the

characteristics of the insulator voltages depending on the shape of the tower and the tower footing characteristics.

In Table 5.4, the critical current derived with and without considering the power frequency voltages are summarized. As mentioned, the highest critical current is obtained if the lower phase has no TLSA, and hence this arrangement most effectively lowers the probability of the lightning fault. The maximum probability of the 1BFO derived considering the power frequency voltages is more than 20% higher than that derived without considering the voltages. The power frequency voltages should be considered in case the lightning fault rate is evaluated by the most severe conditions.

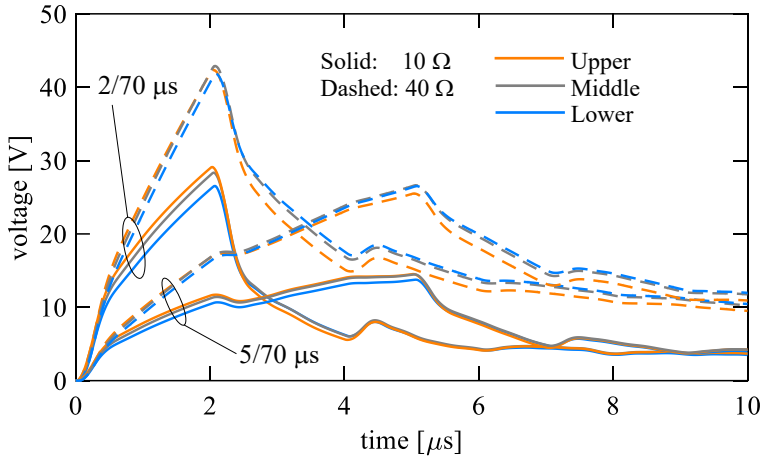

Fig. 5.6 Insulator voltages of an HV transmission tower with tower footing resistance of 10 Ω and 50 Ω generated by the 1-A peak 2/70 μs and 5/70 μs triangular currents.

Table 5.4 Minimum current I_{cc} in kA causing N-phase BFOs in the five TLSAs installed HV transmission lines and its probability [a].

TLSA uninstalled phase	w/o AC	with AC, symmetrical phase rotation		with AC, asymmetrical phase rotation	
		[b]mean	[b]mini	[b]mean	[b]mini
Upper (AH_U)	–29 (44)	–30 (42)	–22 (59)	–30 (42)	–21 (61)
Middle (AH_M)	–36 (33)	–37 (32)	–23 (57)	–37 (31)	–24 (54)
Lower (AH_L)	–48 (21)	–47 (22)	–31 (41)	–47 (21)	–30 (42)

[a] probability of the critical current is shown in the parenthesis.
[b] "mean" provides the mean current of the 24 cases of phase angles for the power frequency voltages, and "mini" provides the minimum current among them.

D Discussion on the reductions of BFO analysis cases

The following BFO analysis conditions are recommended considering the computation time and analysis outcome as discussed above.

1. TLSA uninstalled line

   The power frequency voltages can be neglected since a similar critical current for single and double-phase BFO can be derived with and without the voltages.

2. Three TLSAs and five TLSAs installed lines

   The power frequency voltages should be considered in case the lightning fault rate is evaluated by the severe condition but can be neglected if it is evaluated by the average condition.

One can determine the calculation cases depending on the acceptable lightning fault rate or the importance of the studied transmission line.

Note that the analysis with the power frequency voltage provides the critical current variations. The severe condition for lightning fault can be derived by considering the relation of FO voltage, power frequency voltage, and insulator voltages calculated without the power frequency voltages and FOs.

The followings describe severe conditions for the studied transmission line. The upper, middle, and lower phase insulator voltages are higher in this order in the studied case. In line with three TLSAs, the 1BFO occurs with the lowest critical current at around 300 degrees (see Fig. 5.4), where the upper phase voltage becomes the highest owing to the power frequency voltage. In the same line, the 2BFO occurs with the lowest critical current at around 255 degrees (also see Fig. 5.4), where the upper and middle phase voltages become the highest and almost the same at the BFO occurrence due to the power frequency voltage. In the five TLSAs installed line with the uninstallation for the lower phase, the 1BFO occurs with the lowest critical current at around 60 degrees (see Fig. 5.5). The insulator voltage of the lower phase becomes highest at this phase angle due to the power frequency voltage. The conditions can vary depending on the insulator voltage characteristics.

E Discussion on the absorbed energy

The absorbed energy to cause the arrester failure due to the negative first lightning needs not to be re-considered in the BFO by the presented model. The absorbed energy of the TLSAs in three TLSAs and five TLSAs installation cases was calculated with a 2/70 μs triangular current with a peak of 300 kA. The power frequency voltages were not considered. The maximum absorbed energy is less than about 30 kJ in both cases. Since the rated energy for arcing-horn type TLSAs is 150 kJ and that for the metal-oxide type TLSAs is 300 kJ [6], the TLSAs can deal with the energy due to the negative lightning with the excessive current. Note that the arcing-horn type fails due to direct lightning with 14 kA, for instance.

The presented models provide the precise estimation of the BFO occurrence. The BFOs definitely occur in case the TLSAs fail by the lightning with the excessive current and charge, and such phenomena can be analyzed with the conventional models. In such excessive current with high peak and long duration cases, the shape of foundations, the soil ionization, the frequency dependence of the soil parameters, and resultant tower footing characteristics can significantly influence the absorbed energy.

5.1.3 Discussions on the TLSA arrangement and effectiveness

From the viewpoint of reducing the BFO occurrence, the installation of five TLSAs is more efficient than installing three TLSAs. Table 5.5 summarizes the critical current and its probability causing 1BFO

and 2BFO depending on the TLSA installation. The table provides the critical current derived without considering the power frequency voltage. The 1BFO occurrence, in other words, the lightning fault rate, can be reduced to 84% and 37% of the TLSA uninstalled line by three and five TLSAs, respectively. In [3], it has been reported that 1BFO occurrence was reduced by about 60% by installing three TLSAs and about 30% by installing five TLSAs in an actual HV transmission line. The 2BFO, in which the voltage drop becomes noticeable in the HV transmission line, can be reduced to 71% and 0% by three and five TLSAs, respectively, compared to the TLSA uninstalled line. Considering the lightning fault rate and the occurrence of 2BFO, the installation of five TLSAs is more efficient than installing three TLSAs. However, it should be noted that the installation of three TLSAs avoids the double-circuit fault. One can determine the TLSA arrangement accomplishing the desired lightning fault rate based on the analysis conditions recommended in Section 5.1.2.D.

Table 5.5 Critical current and its probability causing 1BFO (lightning fault rate) and 2BFO (rate of temporary voltage drop) depending on the TLSA installation in the HV transmission line without the power frequency voltage [a].

Number of TLSAs	1BFO		2BFO	
	I_{cc} [kA]	$F(I_{cc})$, %	I_{cc} [kA]	$F(I_{cc})$, %
0	–23	57 (1.00)	–23	57 (1.00)
3	–27	48 (0.84)	–31	41 (0.71)
5 (AH_L)	–48	21 (0.37)	—	— (0)

[a] In parenthesis, relative probability, [probability of TLSA of each case] / [probability of TLSA-uninstalled case], is provided.

5.2 Performance Analysis of TLSAs for EHV Transmission Lines

5.2.1 Analysis conditions and cases

The BFO analysis was performed for a vertical double-circuit EHV transmission line, including:

1) a TLSA uninstalled line;
2) a line with three TLSAs in one circuit;
3) lines with two TLSAs (two types of TLSA arrangement).

Fig. 5.7 illustrates the studied 64-m high EHV transmission tower and line and the arrangement of the TLSAs. For the two TLSAs installed lines, two types of the TLSAs arrangement were considered: the installation for the upper and middle phase of the second circuit (AR_{U2M2}) and that for the upper phase of both circuits (AR_{U1U2}). The installation of three TLSAs for one circuit of the line is adopted for avoiding the double-circuit fault as done in the HV transmission line case [6]. The installation of two TLSAs is adopted in line with a multiphase auto-reclosing [6]. In the multiphase auto-reclosing, the reclosing can be performed at least two phases with different power frequency angles are in a healthy

power transmission state [10]. Note that in EHV transmission lines with direct grounding, the voltage drop of the fault phase comparing to the healthy state is noticeable even in the single-phase BFO.

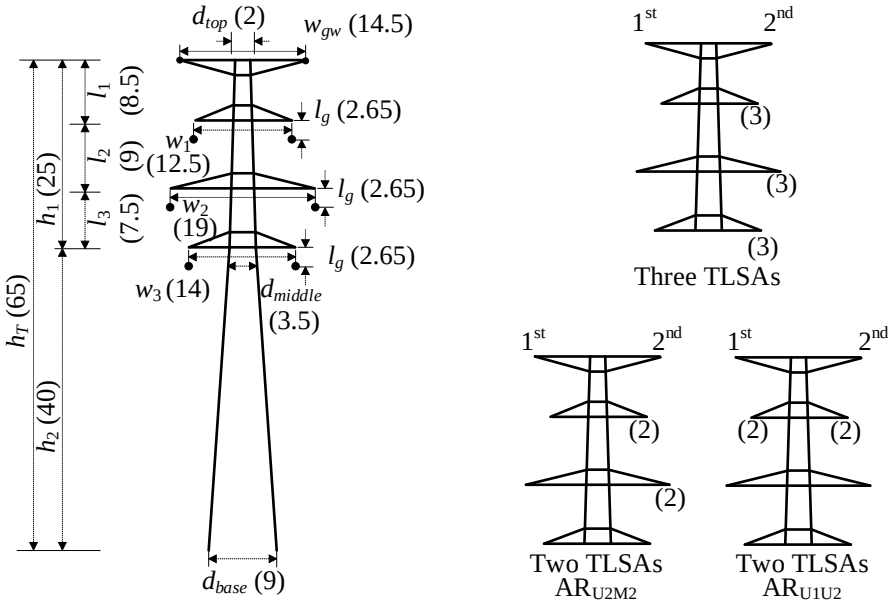

Fig. 5.7 Configuration of the studied EHV transmission tower and arrangement of the TLSAs.

Fig. 5.8 illustrates a circuit analysis model, and Table 5.6 summarizes circuit analysis conditions. The transmission tower was represented by the TEM-delay tower model with cross-arms considering the mutual coupling among the cross-arms, the TEM-delay line model represented the 400-m transmission line, the model by the LPM represented the FO at the arcing horn, and the TLSA was represented by the series-connected nonlinear resistance and FO model by the LPM. The gap length of the arcing horn was set to 2.65 m, and the FO was modeled by the LPM with the constants presented in [11], [12]. Note that the FO characteristics depending on the polarity were not considered since the leader onset condition provided by (4.3) was used. The gap length of the TLSA was set to 1.5 m. The model by the LPM also represented the FO across the gap of the TLSA. Fig. 5.9 shows the *VI* characteristics of the ZnO element. The *V*–*t* characteristics of the FO and the TLSA model were computed by an impulse generator equivalent circuit shown in Fig. 5.10, and Fig. 5.11 shows the derived characteristics. The TLSAs operate before the occurrence of BFOs at the phases without the TLSAs.

In each line with each TLSA arrangement, the following analyses were performed:

1) Calculation of the critical current causing *N*-phase BFOs without the power frequency voltages.
2) Calculation of the critical current causing *N*-phase BFOs with considering the power frequency voltages (in line with the asymmetrical phase rotation).

The phase angle of the power frequency voltage was incremented by 15 degrees. The tower foot was modeled by a 10-Ω linear resistor.

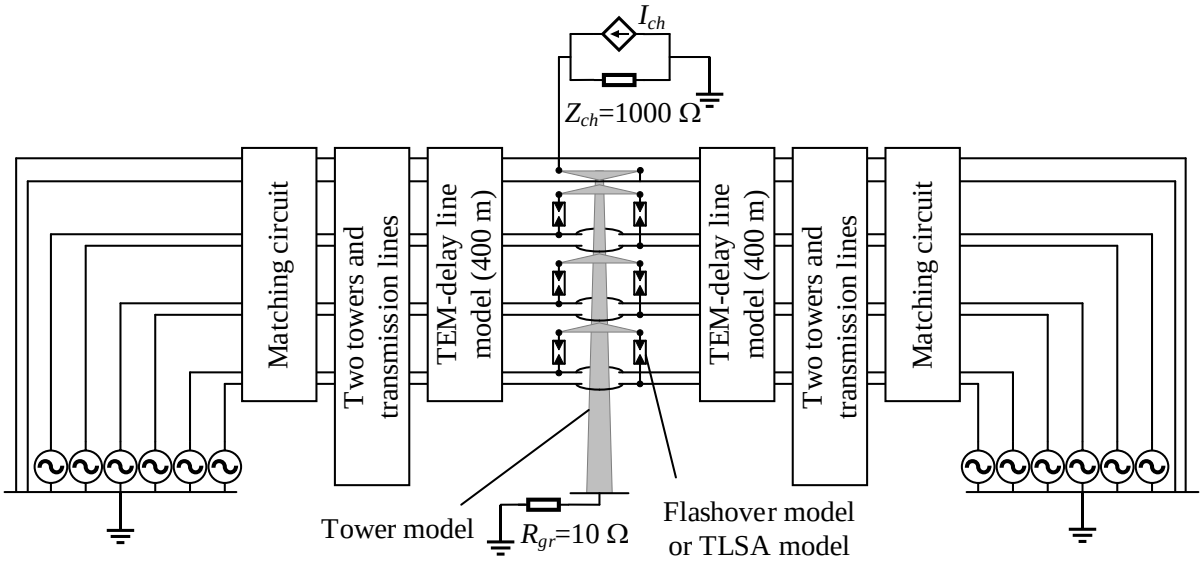

Fig. 5.8 Circuit model for BFO analysis of an EHV transmission line for evaluating the performance of TLSAs using TEM-delay transmission tower and line models.

Table 5.6 Analysis cases and conditions for lightning surge analysis of an EHV transmission line considering the TLSAs.

Current waveform	5/70 μs triangular current, waveform presented by Javor and Rancic considering the correlation of the current peak and the steepness
Current peak	Incremented by 1 kA for current lower than 150 kA and 10 kA for current higher than 150 kA
Lightning channel impedance	1000 Ω
Power frequency voltage	Incremented by 15 degrees
Phase rotation	Asymmetrical rotation
Tower model	TEM-delay tower model with cross-arms considering mutual coupling among cross-arms
Line model	TEM-delay line model
FO model	Model by the LPM
TLSA model	Series connected nonlinear resistance and FO model by the LPM
Number of TLSAs	0, 3, 2: AR_{U2M2}, AR_{U1U2}
Tower footing model	10-Ω linear resistor

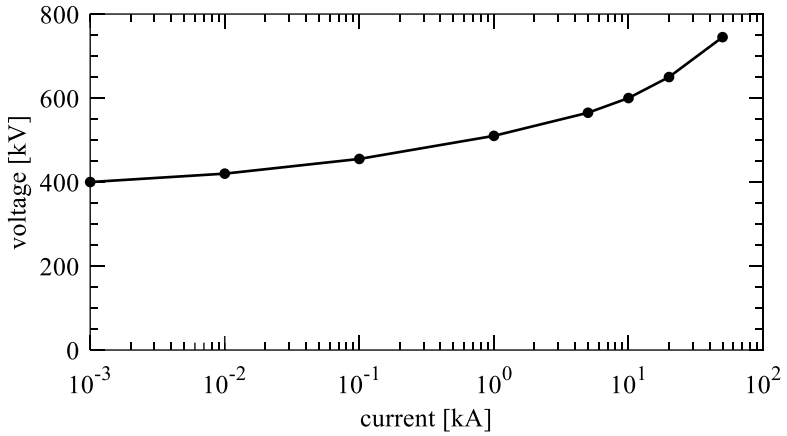

Fig. 5.9 *VI* characteristics of the ZnO element of a TLSA for the EHV transmission line [1].

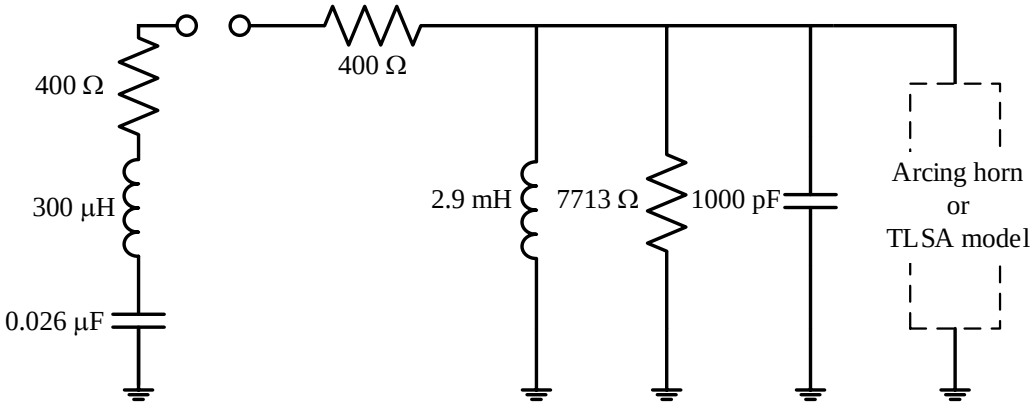

Fig. 5.10 Equivalent circuit model of an impulse generator for deriving breakdown characteristics of the arcing horn and TLSA for the EHV transmission line [11].

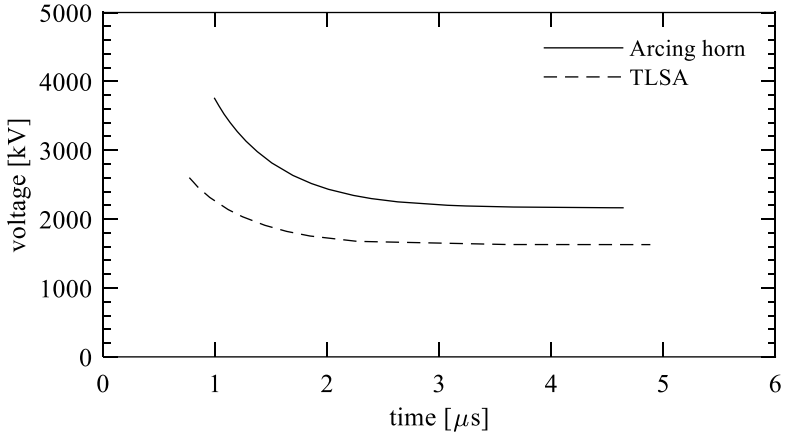

Fig. 5.11 *V–t* characteristics of the FO across the arcing horn and the TLSA of the studied EHV transmission line.

Two types of current waveforms were used for the BFO analysis: the 5/70 μs triangular current and current waveforms determined by the function and method presented by Javor and Rancic [13], considering the correlation between the peak current magnitude and the steepness [14] (mentioned as "correlated" in the abbreviated form). The 5/70 μs triangular current has been used in the lightning fault rate analysis for current higher than 50 kA in Japan [15]. The latter current waveforms were adopted to consider the correlation between the maximum rate of rise and the peak current magnitude. The correlation is noticeable in the high current region, which causes the BFOs in EHV/UHV transmission lines. In [14], a correlation formula has been presented based on the observation of lightning currents at the top of transmission towers. The following formula represents the relation between the first peak current and front duration for linearly rising waveform defined by (first peak amplitude) / (maximum rate of rise) [14]:

$$t_f = 1.31\exp\left(I_m/230\right) \tag{5.2}$$

where t_f [μs] is the front duration corresponding to the maximum rate of rise, and I_m [kA] is the current magnitude. The correlation coefficient between these parameters is 0.983. Fig. 5.12 shows the correlation.

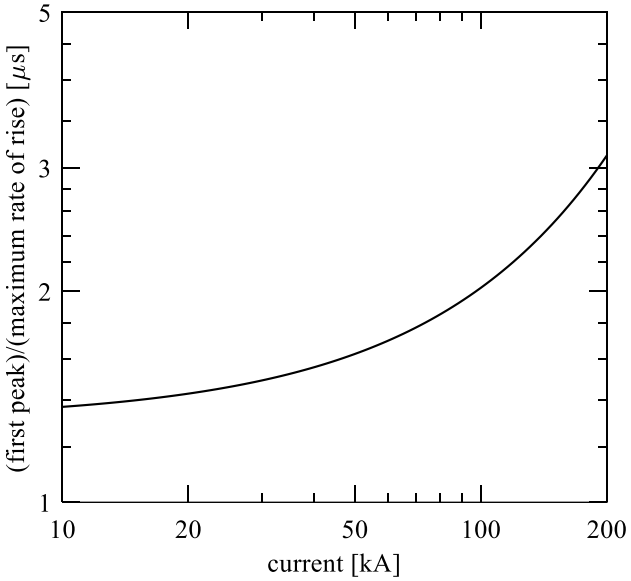

Fig. 5.12 Correlation between the peak current magnitude and front duration for linearly rising wavefront defined by (first peak amplitude) / (maximum rate of rise) [14].

The maximum rate of rise and the current peak magnitude were determined based on (5.2) and represented by the current waveform function presented in [13]. Though there are other functions for expressing the channel base current [16]–[18], this function waveform was adopted because its waveshape can be determined by the small number of the constants considering the maximum rate of rise. The following is the current waveform function.

$$i(t)=\begin{cases} I_m\left(\dfrac{t}{t_m}\right)^a \exp\left\{a\left(1-\dfrac{t}{t_m}\right)\right\} & \left(0\le\dfrac{t}{t_m}\le 1\right) \\ I_m\left(\dfrac{t}{t_m}\right)^b \exp\left\{b\left(1-\dfrac{t}{t_m}\right)\right\} & \left(1\le\dfrac{t}{t_m}\right) \end{cases} \tag{5.3}$$

Among the constants in (5.3), t_m provides the time of the peak current value, a determines the characteristics of the rising part, and b determines the characteristics of the falling part. The maximum rate of rise of the current expressed by (5.3) is calculated by:

$$\left.\frac{di}{dt}\right|_{\max} = \frac{I_m}{t_m}\sqrt{a}\exp\left(\sqrt{a}\right)\left(1-\frac{1}{\sqrt{a}}\right)^{a-1}, \text{ at } t=t_m\left(1-\frac{1}{\sqrt{a}}\right). \tag{5.4}$$

The peak current time t_m for determining the current waveshape was set to 35 μs, and the constant a was determined based on (5.4) for each current peak magnitude I_m for satisfying (5.2).

The current waveforms considering the correlation with peak magnitude ranging from –50 kA to –200 kA are shown in Fig. 5.13 as an example. As is evident from the normalized waveform shown in Fig. 5.13 (b), the current with a higher peak magnitude has slower rising characteristics. Note that the time to half value at the wave-tail was set to around 75 μs by setting b = 0.8 (time to half value at the wave-tail generally does not affect the BFO occurrence, though). Also, note that each current waveform was shifted so that each waveform had the same rising point at t = 0 μs. For the current with a magnitude higher than 200 kA, the same waveform as 200 kA was employed, not the waveform with the rising part determined by (5.2), considering the application limit of the correlation equation. Table 5.7 summarizes the current peak magnitude, constant a, equivalent wavefront duration t_f, and the maximum rate of rise S_m. The current magnitude for deriving critical current was incremented by 1 kA for current lower than 150 kA and 10 kA for that higher than 150 kA. If this current incrimination did not yield the designated number of BFOs, the current was incremented by the lower step.

Table 5.7 Peak current I_m, constant, equivalent wavefront t_f, and maximum rate of rise S_m of current waveforms determined by the function and method presented by Javor and Rancic [13] considering the correlation of the peak magnitude and the steepness [14].

I_m [kA]	a	t_f [μs]	S_m [kA/μs]
50	1208	1.63	30.7
75	967.9	1.82	41.3
100	774.7	2.02	49.4
125	619.7	2.26	54.4
150	495.4	2.51	59.6
175	395.7	2.80	62.4
200	315.7	3.12	64.0

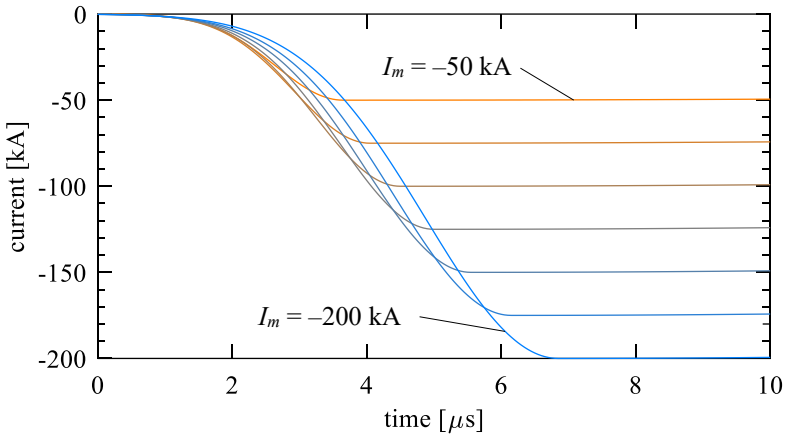

(a) Original waveforms

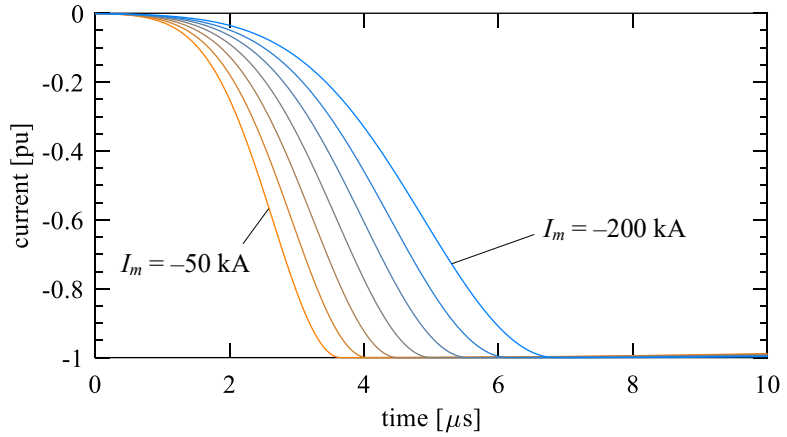

(b) Normalized waveforms for comparing wavefront characteristics

Fig. 5.13 Current waveforms determined by the function and method presented by Javor and Rancic [13] considering the correlation of the peak magnitude and the steepness [14].

5.2.2 Back-flashover phases and critical currents derived by each arrangement

A TLSAs uninstalled line

In the TLSAs uninstalled EHV transmission line, BFO phases and critical current show a similar dependency on the power frequency voltages derived in the TLSAs uninstalled HV transmission line. Also, the same effect of the power frequency voltages on the BFO phase as in the HV transmission line case is derived: the BFO occurrence at phases with positive power frequency voltages is prioritized. However, a much higher critical current is required to cause BFOs in the EHV transmission line case owing to its longer air gap. The power frequency voltage has a relatively small influence on the occurrence of 1BFO.

The BFO phases derived by the 5/70 μs triangular current are shown in Fig. 5.14. Similar BFO phases are derived by the current waveform determined by the function and the method presented in [13], considering the correlation between the peak magnitude and the steepness. Note that the voltages

of the first and second circuits are shown above and below the corresponding voltages to provide better visibility. The BFO occurs at phases with positive power frequency voltages since the negative current is injected. The effect of the power frequency voltage on the BFO phases is the same in the HV and EHV transmission lines. Note that in the EHV transmission line case, the BFO occurs at the lightning-struck side (the first circuit in the present analysis case) due to the difference of insulator voltages depending on the strike side.

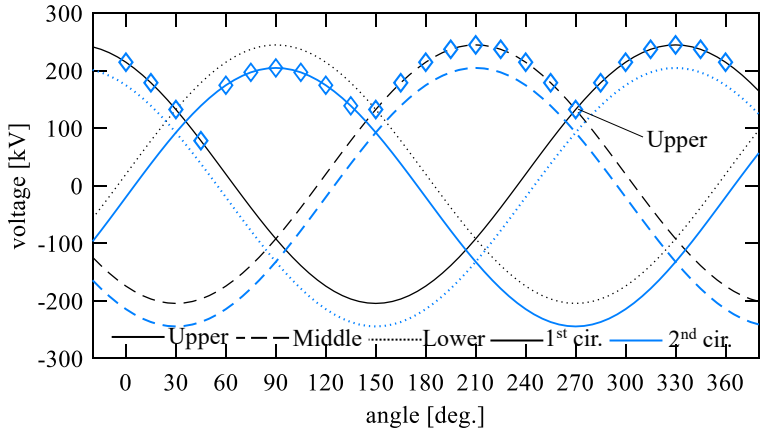

(a) 1BFO

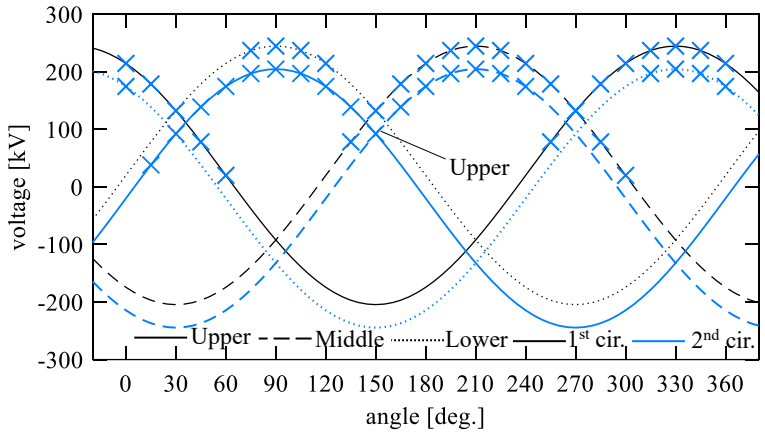

(b) 2BFO

Fig. 5.14 BFO phases derived in the TLSA-uninstalled EHV transmission line derived by the 5/70 μs triangular current (this figure follows to the next page).

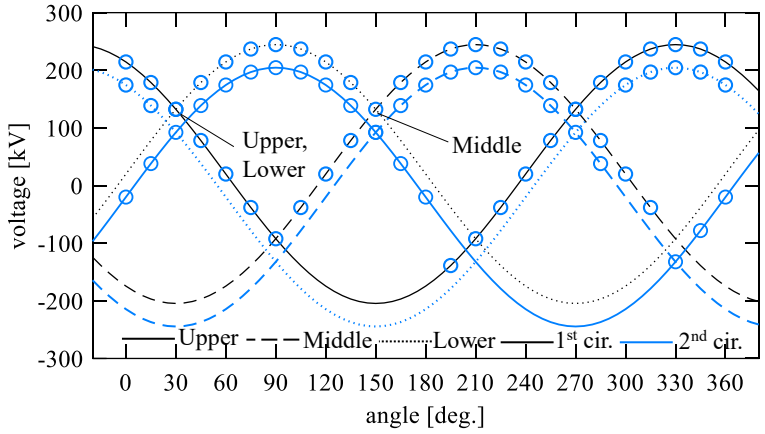

(c) 3BFO

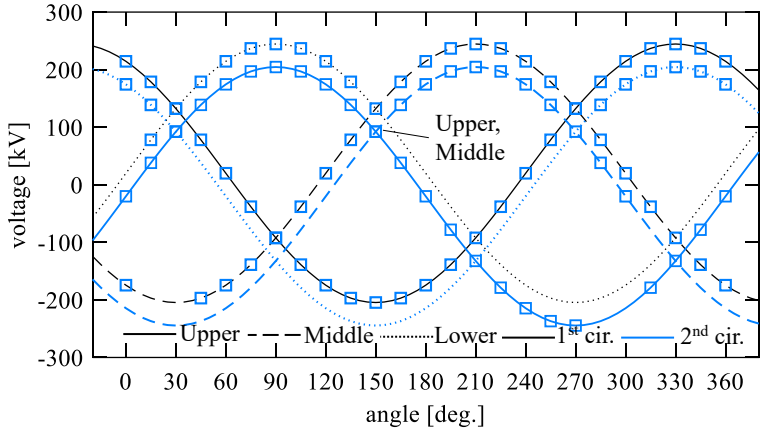

(d) 4BFO

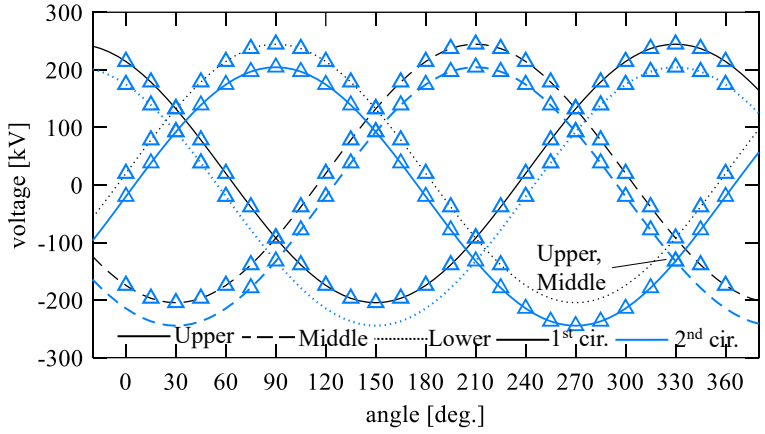

(e) 5BFO

Fig. 5.14 BFO phases derived in the TLSA-uninstalled EHV transmission line derived by the 5/70 μs triangular current (this figure is followed from the previous page).

The critical current derived by the 5/70 μs triangular current is much higher than that derived by the current determined based on the Javor and Rancic function considering the correlation between the peak magnitude and the rate of rise. Fig. 5.15 shows the critical currents and their probabilities. The probability is derived by the log-normal distribution presented in [14], a median peak current of 29 kA and dispersion of 0.28, and the distribution was applied to the whole current magnitude. The much higher current for the 5/70 μs triangular current is derived owing to the slower wavefront and the lower rate of rise. For instance, the current rate of rise of 150-kA peak 5/70 μs triangular current is 30 kA/μs while that of the correlated current is 60 kA/μs, according to (5.2). The selection of current waveforms and the validity of the critical current should be discussed based on the comparison between the simulation and observation. The ratio between the critical current for 1BFO and multiphase BFOs is more prominent in the current with the correlation than the 5/70 μs triangular current because the wavefront becomes longer in the higher current magnitude. For instance, the ratio in average between critical currents for 1BFO and 6BFO in the 5/70 μs triangular current is 2.9, while that in the correlated current is 4.6. The variation of critical current depending on the power frequency voltage is similar in both current waveforms. The highest probability of lightning fault (1BFO) is derived around 330 degrees. Around this phase angle, the upper phase insulator voltage of the first circuit (lightning struck side) becomes maximum due to the power frequency voltage.

Table 5.8 summarizes the critical current derived with and without considering the power frequency voltages by both current waveforms. A similar critical current, and thus the similar lightning fault rate, can be derived with and without considering the power frequency voltages. The same discussions on the FO voltage and the maximum value of the power frequency voltage in the HV transmission line case can be applied here. The power frequency voltage is negligible if the lightning fault rate is not discussed in severe conditions. The effect of the power frequency voltage is significant in the multiphase BFO cases in the EHV transmission line case as well.

Table 5.8 Minimum current I_{cc} in kA causing N-phase BFOs at the TLSAs uninstalled EHV transmission line and its probability [a].

Num. of BFOs	w/o AC 5/70 μs	w/o AC Correlated	with AC, 5/70 μs		with AC, Correlated	
			[b] mean	[b] min	[b] mean	[b] min
1	–152 (0.51)	–98 (2.94)	–158 (0.43)	–150 (0.54)	–90 (3.88)	–85 (4.77)
2	–170 (0.30)	–111 (1.87)	–184 (0.21)	–170 (0.30)	–111 (1.85)	–95 (3.29)
3	–180 (0.23)	–115 (1.63)	–212 (0.10)	–180 (0.23)	–133 (0.91)	–110 (1.93)
4	–260 (0.03)	–180 (0.23)	–271 (0.03)	–220 (0.08)	–183 (0.21)	–123 (1.25)
5	–340 (0.01)	–260 (0.03)	–351 (0.01)	–260 (0.03)	–270 (0.03)	–170 (0.30)
6	–430 (0.00)	–350 (0.01)	–492 (0.00)	–390 (0.00)	–410 (0.00)	–300 (0.01)

[a] probability of the minimum current is shown in the parenthesis.
[b] "mean" provides the mean current of the 24 cases of phase angles for the power frequency voltages, and "mini" provides the minimum current among them.

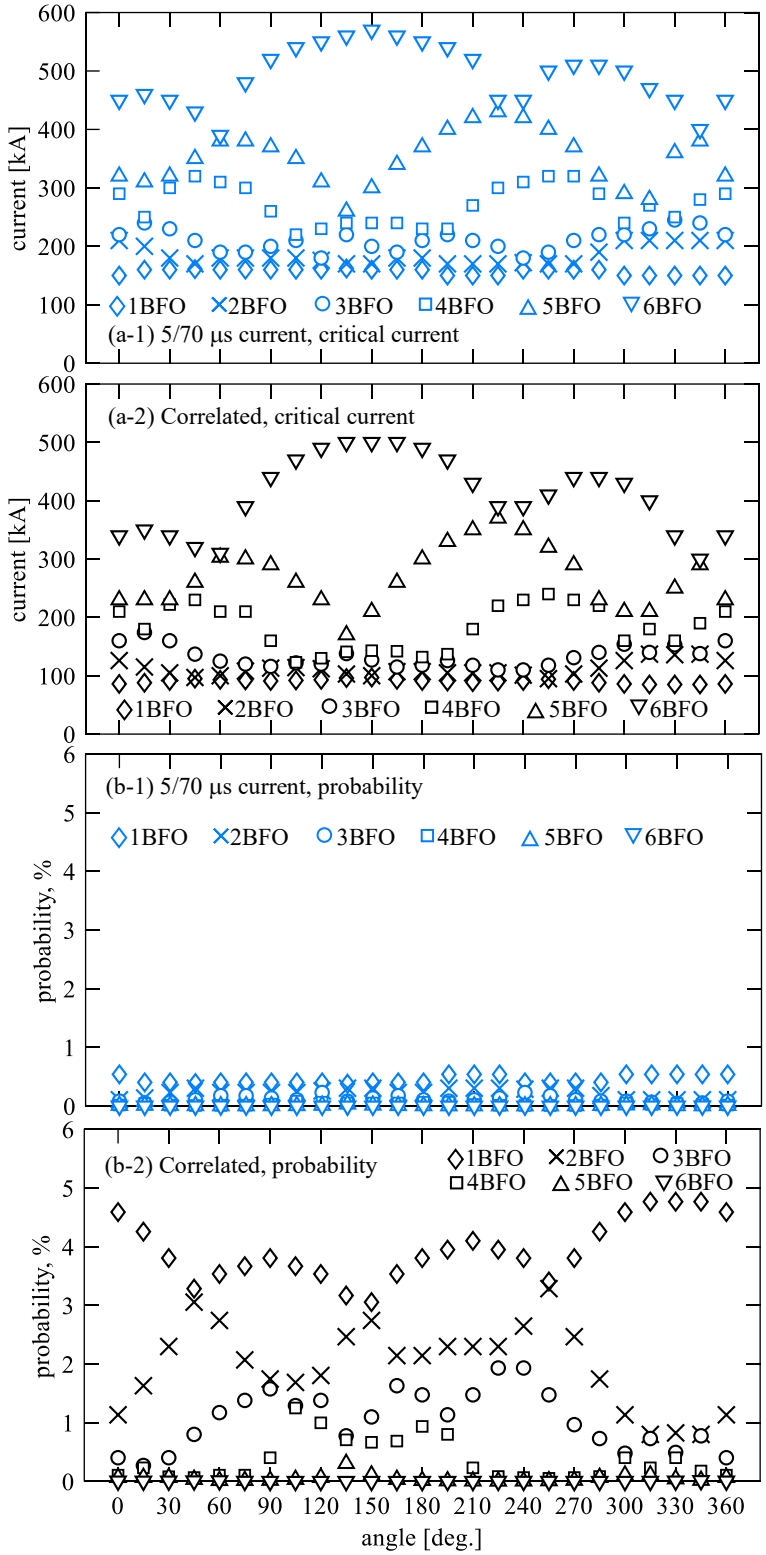

Fig. 5.15 Critical currents causing *N*-phase BFOs and their probability derived in the TLSA-uninstalled EHV transmission line with the asymmetrical phase rotation.

The occurrence of BFOs with a quite high current can be negligible. In [19], it has been shown that the theoretical maximum lightning current is about 300 kA in temperate regions and 450 kA–500 kA in the tropics. Thus, the BFO generated by the current higher than these extreme values is negligible. The maximum current reported in [14] was 130 kA, where 120 cases of negative first lightning were observed at the top of transmission towers in Japan. Therefore, lightning with a peak current higher than about 130 kA is quite rare in the negative lightning in Japan. A much higher current has been observed in winter lightning regions and caused a lightning fault of transmission lines [20], [21]. Even in these regions, the maximum current observed as of today is 340 kA [22] (the higher current has been estimated by lightning location systems (LLSs), though). This discussion on the maximum current should also be applied to the critical current derived in the TLSAs installed line cases discussed in the next section.

B Three TLSAs installed line

In the three TLSAs installed EHV transmission line, characteristics of BFO phases, the dependency of the critical current, and its probability on the power frequency voltage are similar to those in the TLSA uninstalled HV transmission line with the symmetrical rotation, which was discussed in Section 5.1.2.A. The minimum value of the critical currents derived considering the power frequency voltages is much lower than those derived without considering the voltages. Thus, the power frequency voltage should be considered if the lightning fault rate is discussed based on severe conditions.

The critical current and its probability derived by both currents are shown in Fig. 5.16, and the BFO phase derived by the 5/70 μs triangular current is shown in Fig. 5.17. Note that the 1BFO and 2BFO phases are shown above and below the corresponding power frequency voltages to prove better visibility. Similar BFO phases are derived by both current waveforms. The BFO phases are similar to those derived in the TLSA uninstalled HV transmission line with the symmetrical phase rotation (see Fig. 5.2 (a)). Further, the variations of the critical current and its probabilities are similar to those derived in the TLSA uninstalled HV transmission line with the symmetrical phase rotation as well, except for the 1BFO dependence on voltages (see Fig. 5.3 (a-1) and (b-1)). Similar variations are derived because the BFO characteristics of the TLSA uninstalled circuit are determined by the same power frequency voltages in those cases. Note that the probability of 1BFO derived in the three TLSAs installed lines is about 30% smaller than that derived in the TLSA uninstalled line due to TLSA operations. This aspect will be summarized and discussed in Section 5.2.3.

Table 5.9 summarizes the critical currents and their probabilities derived with and without considering the power frequency voltages. In the three TLSAs installed line, the difference of critical currents and their probabilities derived with and without considering the power frequency voltages is significant. The significant difference is derived since the BFOs in the TLSAs installed line are interpreted as the multiphase BFOs, as discussed in the HV transmission line cases. If the lightning fault rate is discussed based on severe conditions, the power frequency voltages should be considered.

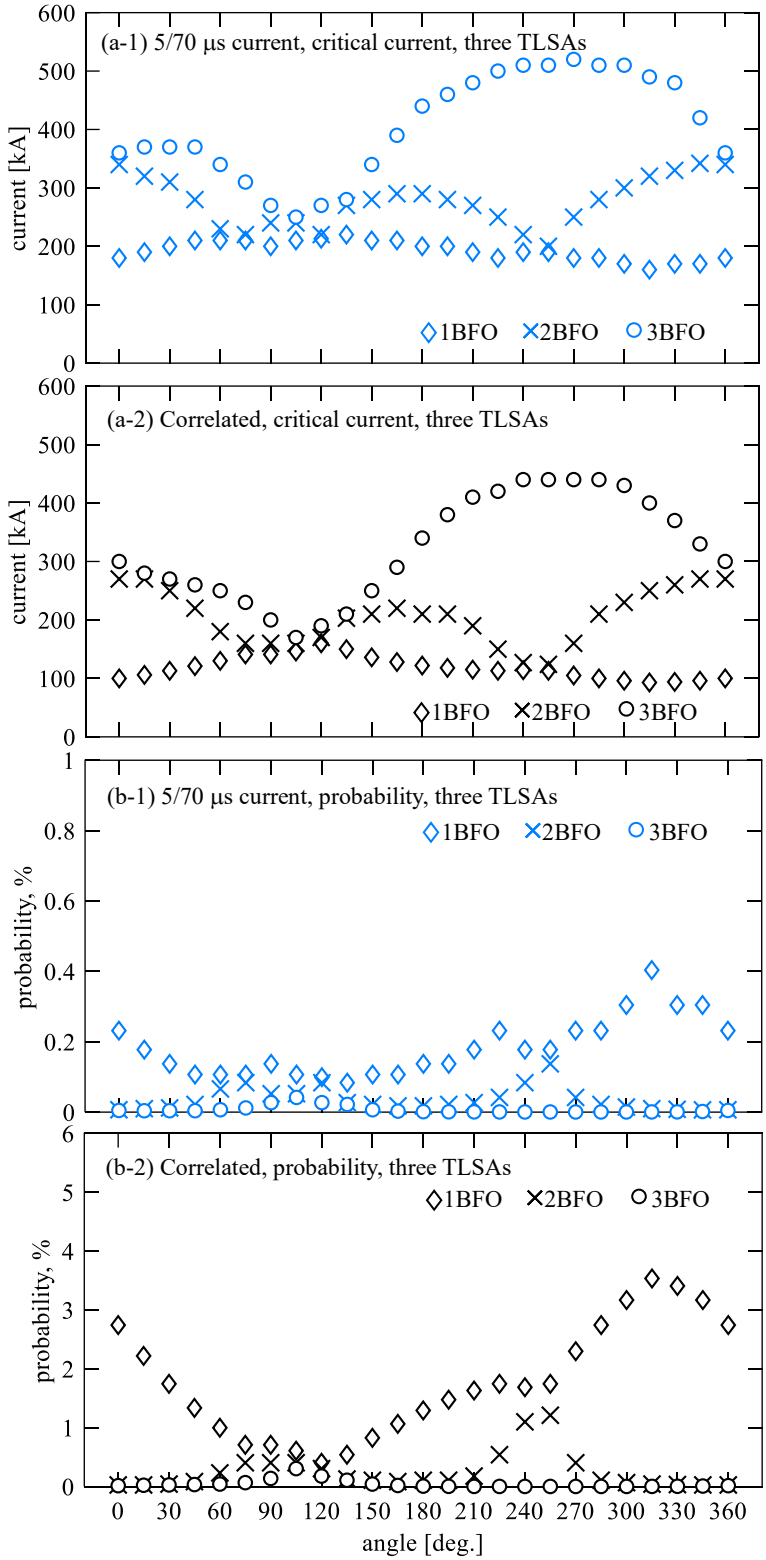

Fig. 5.16 Critical current and its probability derived in the three TLSAs installed EHV transmission line.

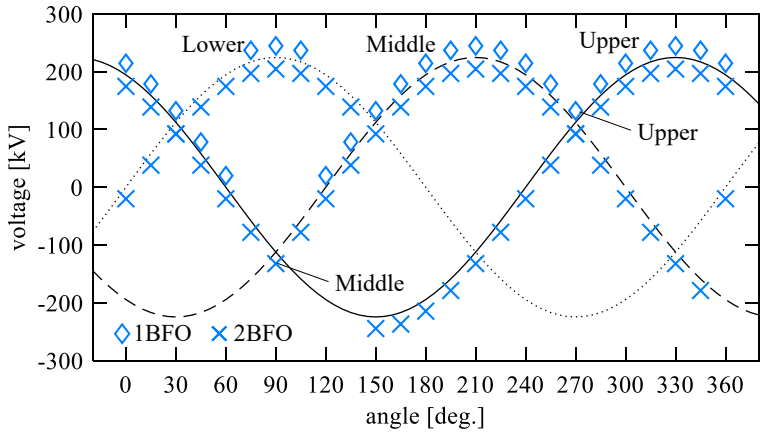

Fig. 5.17 BFO phases derived in the three TLSAs installed EHV transmission line by the 5/70 μs triangular current.

Table 5.9 Minimum current I_{cc} in kA causing N-phase BFOs in the three TLSAs installed EHV transmission line and its probability [a].

Num. of BFOs	w/o AC 5/70 μs	w/o AC Correlated	with AC, 5/70 μs		with AC, Correlated	
			[b] mean	[b] min	[b] mean	[b] min
1	–220 (0.08)	–127 (1.10)	–194 (0.16)	–160 (0.40)	–119 (1.44)	–93 (3.53)
2	–260 (0.03)	–180 (0.23)	–274 (0.02)	–200 (0.14)	–203 (0.13)	–124 (1.21)
3	–440 (0.00)	–350 (0.01)	–406 (0.00)	–250 (0.04)	–322 (0.01)	–170 (0.30)

[a] probability of the minimum current is shown in the parenthesis.
[b] "mean" provides the mean current of the 24 cases of phase angles for the power frequency voltages, and "mini" provides the minimum current among them.

C Two TLSAs installed line

In the two TLSAs installed lines, two types of TLSAs arrangements, installations for the upper and middle phases of one circuit of the line (AR_{U2M2}) and that for upper phases in both circuits (AR_{U1U2}), were analyzed as introduced in Section 5.2.1. The latter arrangement performs better in the studied case because the highest voltage is induced at the upper phase if the FO, TLSAs, and power frequency voltages are not considered. The power frequency voltage has a significant influence on the critical current in these cases as well.

The BFO phases derived by the 5/70 μs triangular current in each TLSA arrangement are shown in Fig. 5.18 and Fig. 5.19. Note that voltages of the first and second circuits are shown above and below the corresponding voltage to provide better visibility. Also, note that the power frequency voltages of the TLSAs installed phases are omitted from the figure. Basically, the BFOs occur at phases with the positive power frequency voltage in both TLSAs arrangements. Fig. 5.20 and Fig. 5.21 show the critical current and its probability derived in each TLSA arrangement by both current waveforms. A higher critical current is required in line with TLSAs installed for the upper phase of both circuits (AR_{U1U2}). This arrangement performs better since the upper phase insulator voltage is the highest if the FO, TLSAs,

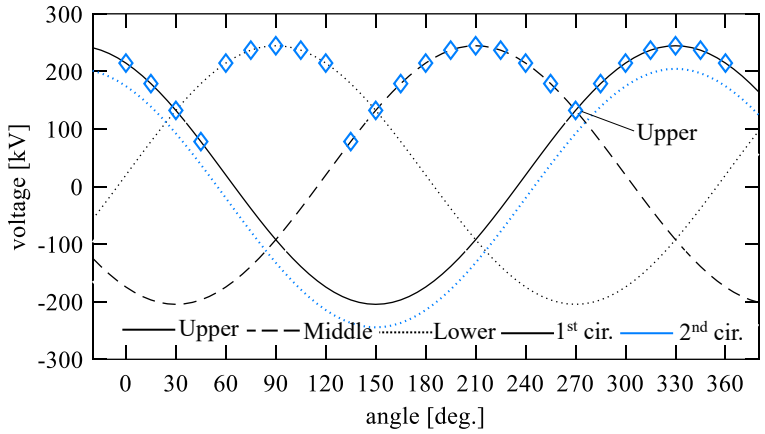

(a) 1BFO

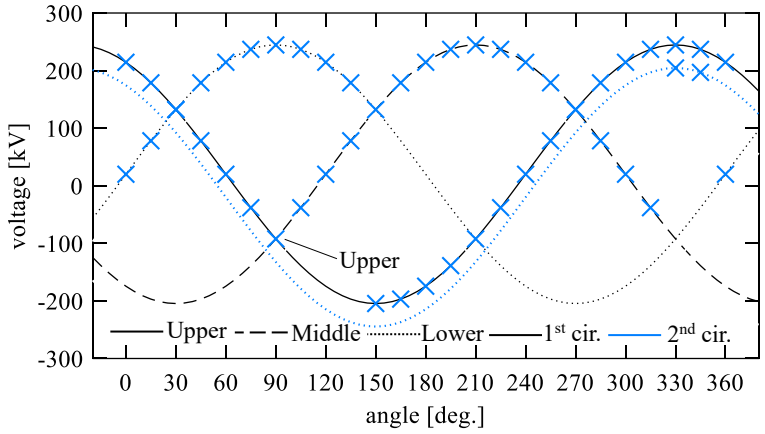

(b) 2BFO

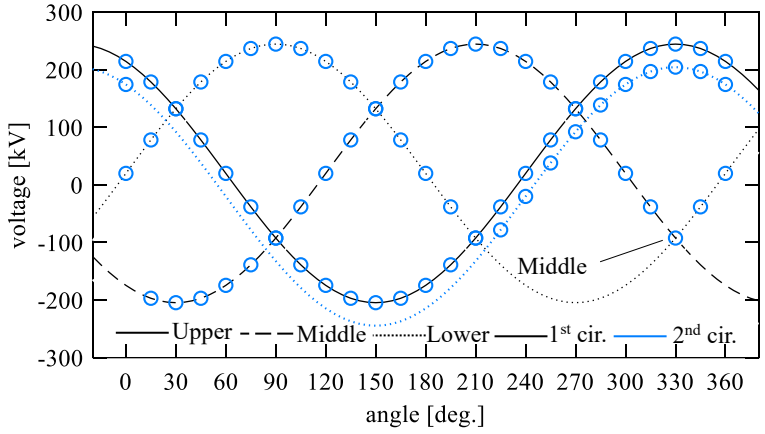

(c) 3BFO

Fig. 5.18 BFO phases derived in the EHV transmission line with two TLSAs installed for the upper and middle phases of one circuit (AR_{U2M2}) by the 5/70 μs triangular current.

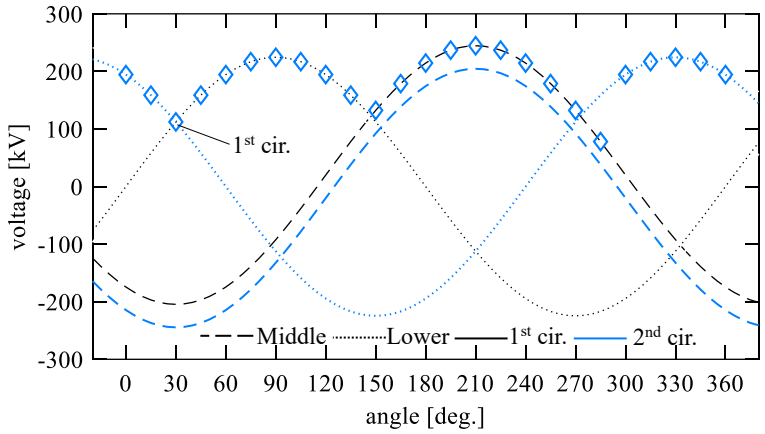

(a) 1BFO

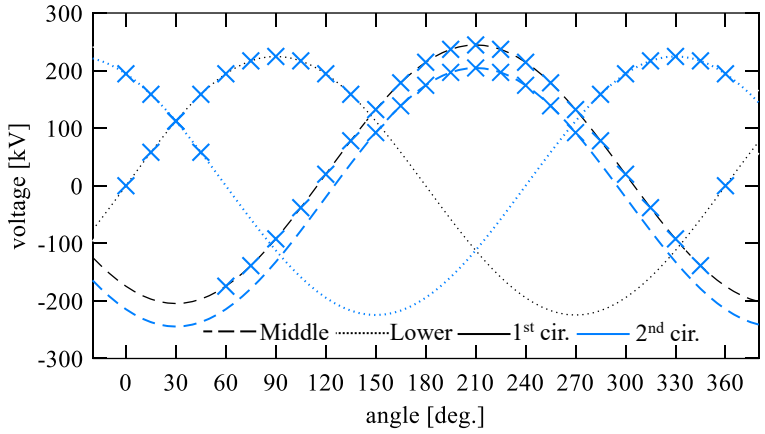

(b) 2BFO

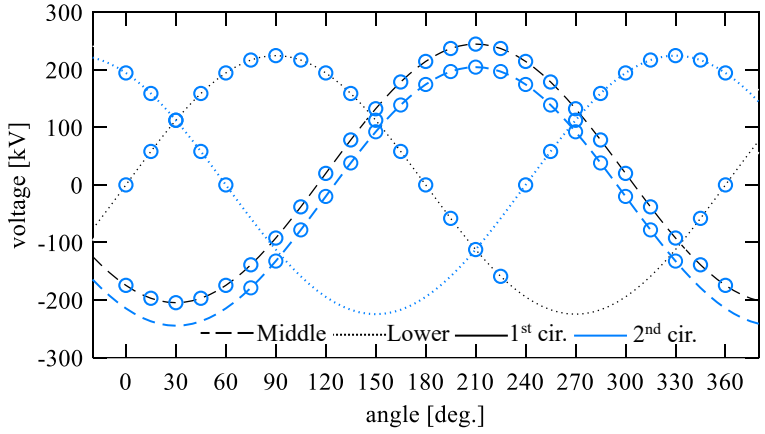

(c) 3BFO

Fig. 5.19 BFO phases derived in the EHV transmission line with two TLSAs installed for the upper phase of both circuits (AR_{U1U2}) by the 5/70 μs triangular current.

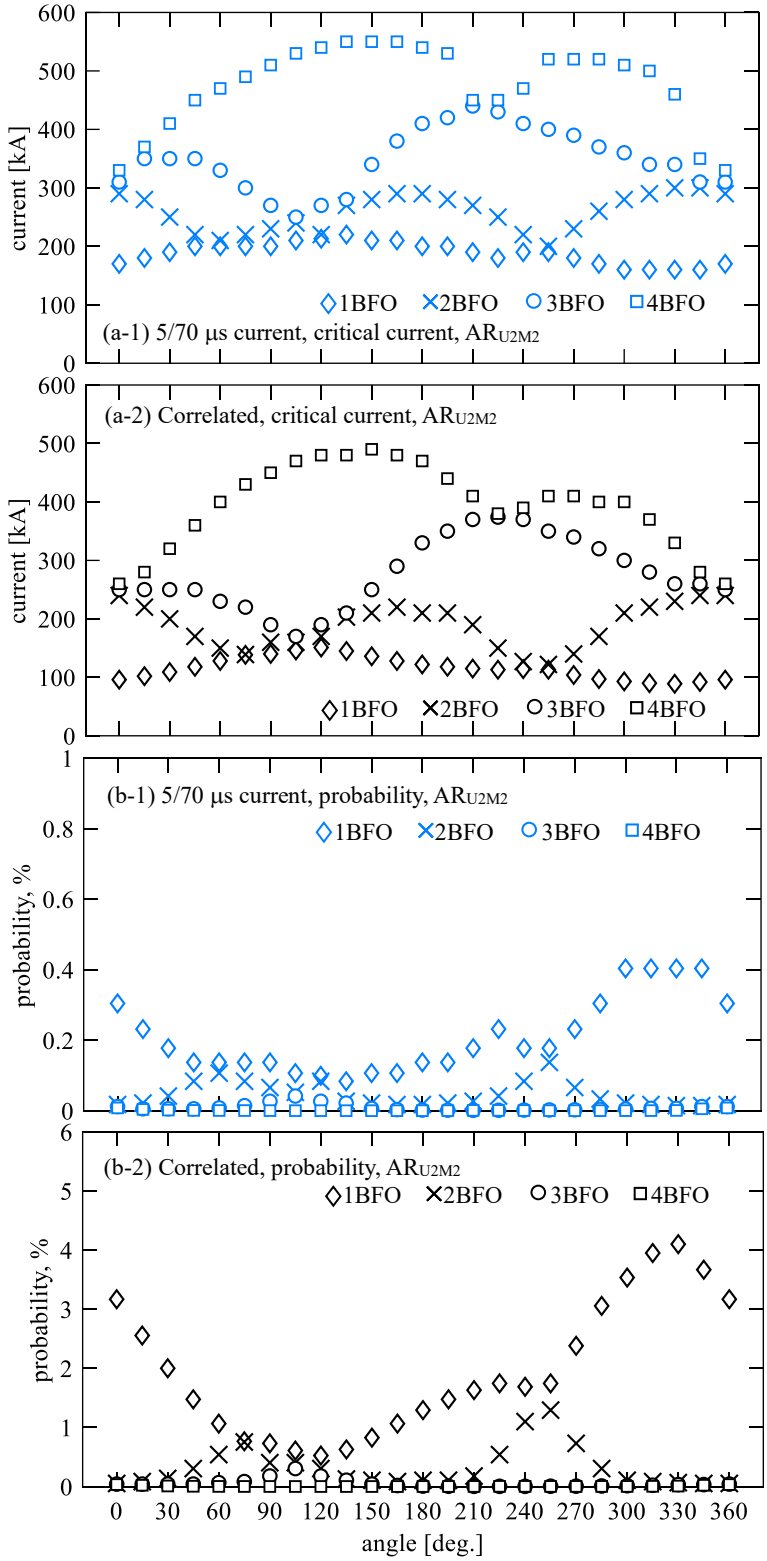

Fig. 5.20 Critical current and probability of the critical current derived in the two TLSAs installed EHV transmission line

(AR_{U2M2}, a line with TLSAs installed for the upper and lower phases of the second circuit).

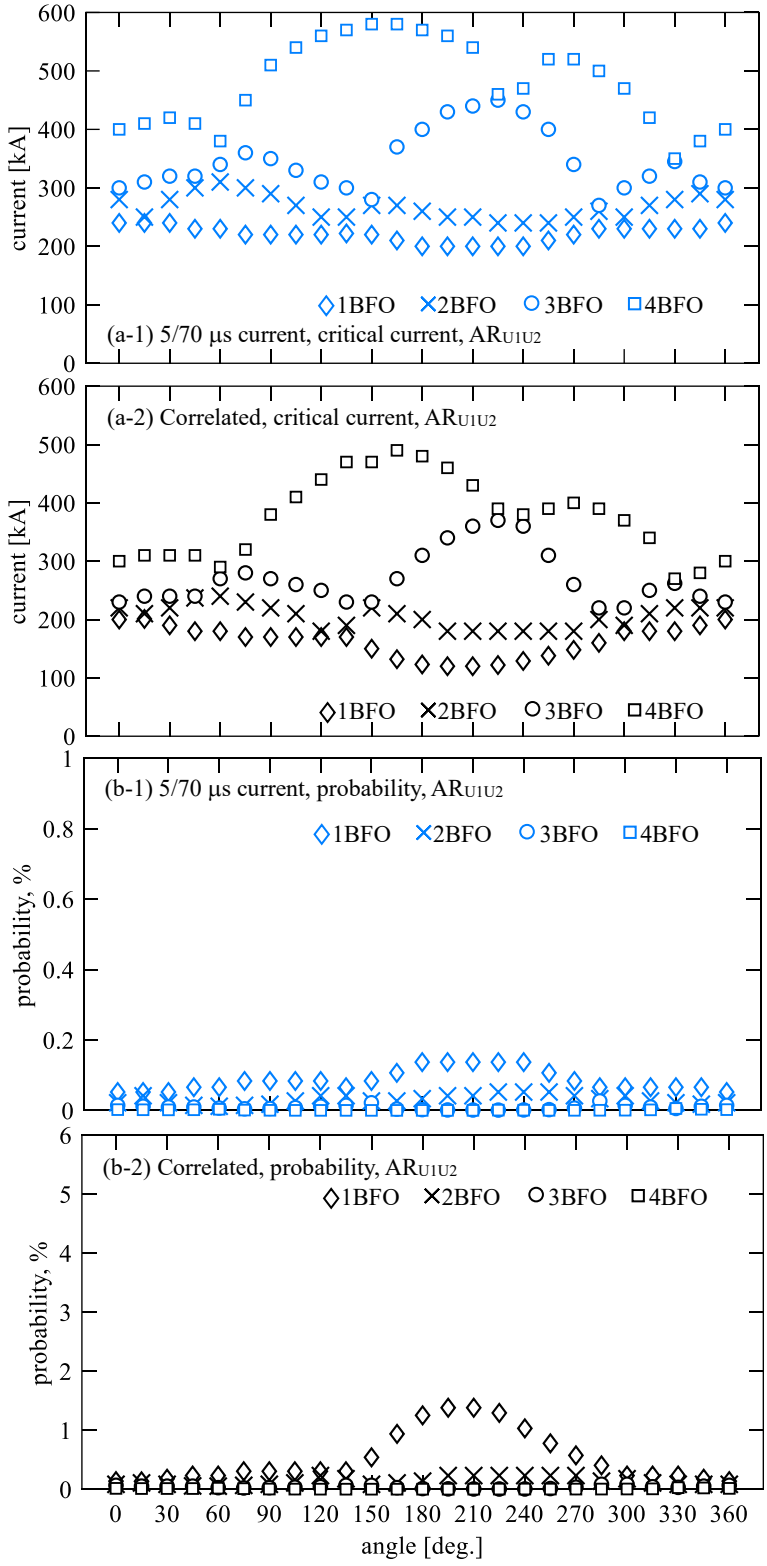

Fig. 5.21 Critical current and probability of the critical current derived in the two TLSAs installed EHV transmission line

(AR_{U1U2}, a line with TLSAs installed for the upper phase of both circuits).

and power frequency voltages are not considered. Note that the double-circuit fault may be avoided efficiently in the installation of TLSAs for the upper and middle phase (AR_{U2M2}) since two phases in one circuit are protected by the TLSAs. The highest probability is derived around 300 degrees in the upper and middle phase installation case (AR_{U2M2}) because the TLSA-uninstalled upper phase voltage in the first circuit becomes the highest due to the power frequency voltage. In the installation for the upper phase of both circuits (AR_{U1U2}), the highest probability is derived around 210 degrees since the TLSA-uninstalled middle phase voltage becomes the highest due to the power frequency voltage.

Table 5.10 summarizes the critical currents and their probabilities derived with and without considering the power frequency voltages in each arrangement by each current waveform. As mentioned, installing TLSAs for the upper phase of both circuits performs better than that for the upper and middle phase of one circuit for suppressing 1BFO. The power frequency voltage significantly influences the critical current magnitude in these two TLSAs installation cases as well since BFOs in the TLSAs installed line can be interpreted as the multiphase BFOs, as discussed in the HV line cases. If the lightning fault rate is discussed based on severe conditions, the power frequency voltages should be considered.

Table 5.10 Minimum current I_{cc} in kA causing N-phase BFOs in the two TLSAs installed EHV transmission lines and its probability [a].

(a) TLSAs installation for the upper and middle phases of the second circuit (AR_{U2M2})

Num. of BFOs	w/o AC 5/70 μs	w/o AC Correlated	with AC, 5/70 μs		with AC, Correlated	
			[b] mean	[b] min	[b] mean	[b] min
1	–220 (0.08)	–127 (1.10)	–190 (0.18)	–160 (0.40)	–117 (1.55)	–89 (4.10)
2	–250 (0.04)	–170 (0.30)	–257 (0.04)	–200 (0.14)	–186 (0.20)	–122 (1.29)
3	–390 (0.00)	–300 (0.01)	–350 (0.01)	–250 (0.04)	–278 (0.02)	–170 (0.30)
4	–480 (0.00)	–400 (0.00)	–482 (0.00)	–330 (0.01)	–400 (0.00)	–260 (0.03)

(b) TLSAs installation for the upper of both circuits (AR_{U1U2})

Num. of BFOs	w/o AC 5/70 μs	w/o AC Correlated	with AC, 5/70 μs		with AC, Correlated	
			[b] mean	[b] min	[b] mean	[b] min
1	–240 (0.05)	–180 (0.23)	–221 (0.08)	–200 (0.14)	–162 (0.38)	–120 (1.38)
2	–280 (0.02)	–223 (0.08)	–267 (0.03)	–240 (0.05)	–205 (0.12)	–180 (0.23)
3	–290 (0.02)	–230 (0.07)	–347 (0.01)	–270 (0.03)	–272 (0.03)	–220 (0.08)
4	–380 (0.00)	–290 (0.02)	–482 (0.00)	–350 (0.01)	–378 (0.00)	–270 (0.03)

[a] probability of the minimum current is shown in the parenthesis.
[b] "mean" provides the mean current of the 24 cases of phase angles for the power frequency voltages, and "mini" provides the minimum current among them.

Fig. 5.22 shows the insulator voltages of an EHV transmission line with tower footing resistance R_{gr} of 10 Ω and 30 Ω generated by the 1-A peak 2/70 μs and 5/70 μs triangular current. In the 30-Ω tower footing resistance case, the upper phase insulator voltage is the lowest among the voltages

generated by the 5/70 μs current. For transmission lines with lower tower footing resistance such as 10 Ω, the TLSA installation for the upper phases in both circuits is the most efficient. However, the TLSA installation for the middle or lower phase can be more efficient for the transmission lines with a relatively higher tower footing resistance, such as 30 Ω. The TLSAs installation phases should be carefully determined considering the shape of the transmission tower, the tower footing resistance, and the resultant height dependence of the insulator voltages. Note that depending on the shape of the tower foot and the soil characteristic, the tower footing impedance can also affect the insulator voltages.

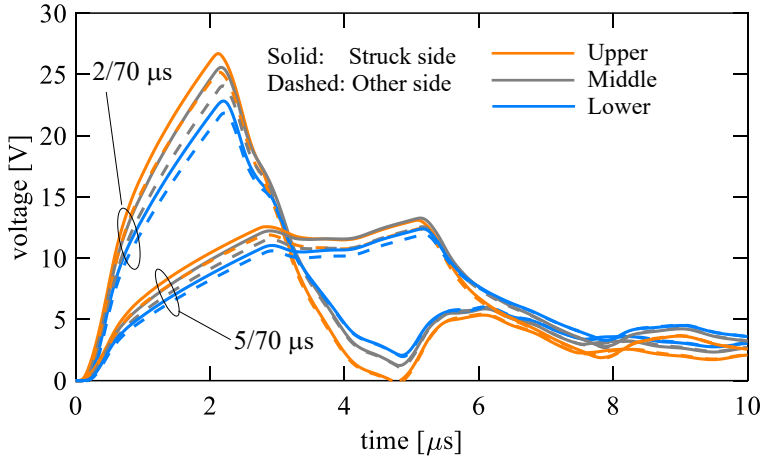

(a) R_{gr} = 10 Ω

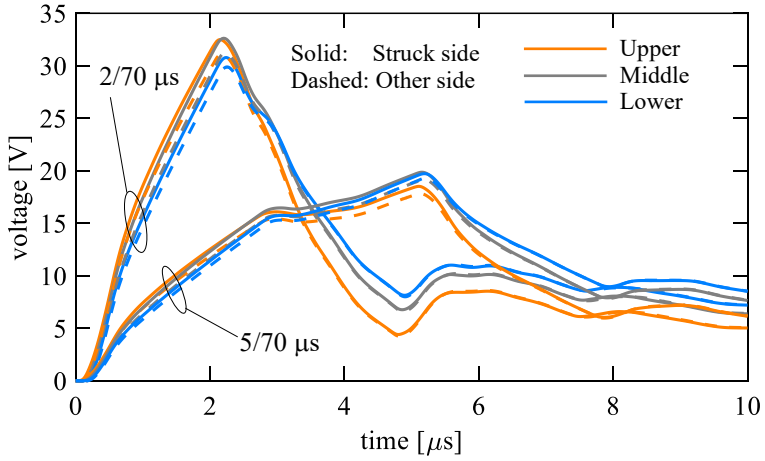

(b) R_{gr} = 30 Ω

Fig. 5.22 Insulator voltages of an EHV transmission tower with tower footing resistance R_{gr} of 10 Ω and 30 Ω generated by the 1-A peak 2/70 μs and 5/70 μs triangular currents.

5.2.3 Discussions on the TLSA arrangement and effectiveness

An installation of two TLSAs for the upper phase in both circuits of the line performs best to reduce the occurrence of the lightning fault. Table 5.11 summarizes the critical current and its probability causing

1BFO depending on the TLSA installation. The table provides the mean critical current derived with considering the power frequency voltage. The 1BFO occurrence, namely, the lightning fault rate and the temporary voltage drop in EHV lines with the direct grounding, can be reduced to about 40%, 40%, and 15% of the TLSA uninstalled line by installing three TLSAs for one circuit, installing two TLSAs for the upper and middle phases in one circuit, and installing two TLSAs for the upper phase of both circuits, respectively. The reduction of the 1BFO occurrence in line installing two TLSAs for the upper and middle phase of one circuit derived here is consistent with that experienced in an actual EHV transmission line, as reported in [3]. Considering the lightning fault rate, the installation of two TLSAs in the upper phase of both circuits performs best in the lines with the multiphase auto-reclosing. However, the double-circuit fault may be avoided efficiently in the TLSAs installation for the upper and middle phases of one circuit. The installation of three TLSAs performs almost the same as that of the two TLSAs installed line. However, note that the installation of three TLSAs can avoid the single-circuit fault in any line with any grounding system. One can determine the TLSA arrangement accomplishing the desired lightning fault rate based on the analysis discussed in this section.

Table 5.11 Critical current and probability causing 1BFO (the lightning fault rate and the rate of the temporary voltage drop) depending on the TLSA installation in the EHV transmission line (mean current and probability derived by the case considering the power frequency voltage) [a].

Number of TLSAs	1BFO, 5/70 μs		1BFO, Correlated	
	I_{cc} [kA]	$F(I_{cc})$, %	I_{cc} [kA]	$F(I_{cc})$, %
0	–158	0.43 (1.00)	–90	3.88 (1.00)
3	–194	0.16 (0.37)	–119	1.44 (0.37)
2 (AR_{U2M2})	–190	0.18 (0.42)	–117	1.55 (0.40)
2 (AR_{U1U2})	–221	0.08 (0.19)	–162	0.38 (0.10)

[a] In parenthesis, relative probability between the TLSAs uninstalled case and the installed case, [probability of TLSA of each case] / [probability of TLSA-uninstalled case], is provided.

Note that similar effectiveness of the TLSAs was derived by the installation of three TLSAs in one circuit of the line and the two TLSAs for upper and middle phases of the one circuit of the line. This result can be attributed to the BFO phases in both TLSA arrangements. Fig. 5.18 showed the BFO phases derived in the two-TLSA installed case. The 1BFO occurred all in the phases located on the first circuit, where no TLSA is installed, and these BFO phases are similar to those of the three TLSAs installed case (see Fig. 5.17, the BFO phases in 60 deg. and 120 deg. are different, and the others are identical). The lower phase arcing horn in the second circuit, where the TLSAs are installed at the upper and middle phases, does not experience the BFO until the 2BFO occurs in this arrangement. In other words, the probability of the lower-phase TLSA operation in the three TLSAs installed line is low, and the probability of the BFO at the phases (especially upper) of the TLSA uninstalled circuit is high. Thus,

the similar effectiveness of the TLSAs was derived by the installation of three TLSAs in one circuit of the line and the two TLSAs for the upper and middle phases of the one circuit of the line.

The validity of the critical current magnitude should be discussed based on the comparison between the observation of the BFOs and simulation. In [3], the lightning fault rate computed using the multistory tower model was compared by the experienced fault rate. The 2/70 μs triangular current, which is relatively severe in discussing BFOs in an EHV transmission, was used in the analysis. In the analysis results, the lightning fault rate experienced in the summer lightning season was estimated within a 10% difference, while that in the winter lightning season was estimated about 30% lower. The insulator voltages computed by the multistory tower model are lower than those computed by the FDTD method and the presented TEM-delay model, as shown in Chapter 3. The successfully estimated lightning fault rate in the summer lightning season can be attributed to the use of the severe lightning current waveform and the multistory tower model, which yields lower voltages. The lower estimated lightning fault rate in the winter lightning season can be attributed to the modeling of the FO using the *V*–*t* crossover method for the arcing horn and TLSAs, as pointed out in [3]. It can be considered that the effect of the FO modeling on the lightning fault rate becomes noticeable in the winter lightning season since the probability of lightning with a high current is higher than that in summer lightning. The use of the presented tower and line models, FO and TLSAs model with the LPM, and realistic current waveform have the potential to provide a better estimation of the lightning fault rate. A comparison between the simulated and experienced lightning fault rates for EHV transmission lines should be performed.

5.3 Conclusions

BFO analyses for HV and EHV transmission lines have been carried out to discuss the effectiveness of the TLSA installations to reduce the BFO occurrences. Installations of three TLSAs for one circuit of the line and five TLSAs have been analyzed in the HV transmission line, while the installations of two and three TLSAs have been analyzed in the EHV transmission line.

In the HV transmission line, the installation of five TLSAs except for the lower phase performs best as long as the tower footing resistance is lower than around 40 Ω for the studied tower case. This arrangement performs best since the lower phase insulator voltage becomes the lowest among the phases. Each three and five TLSAs installations reduces the lightning fault rate by around 20% and 60%, respectively, and occurrence of temporary voltage drop around 30% and 100% compared to the TLSAs uninstalled line, respectively. Note that both TLSAs installation can avoid the double-circuit fault. The power frequency voltages can be negligible in discussing the BFO rate in the TLSAs uninstalled line, owing to the relation between the maximum value of the power frequency voltage and the FO voltage. However, the power frequency voltage significantly influences the BFO rate in the TLSAs installed line since the TLSAs operate in advance of the BFOs at the phases without the TLSAs.

In the EHV transmission line, the installation of two TLSAs for the upper phase in both circuits performs best as long as the tower footing resistance is lower than around 30 Ω for the studied tower case since the upper phase insulator voltage becomes the highest among the phases. The installation of three TLSAs can avoid the double-circuit fault in any line with any grounding and reclosing systems. The installation of two TLSAs for the upper and middle phases of one circuit and the upper phases of both circuits can maintain the reclosing condition in lines with multiphase auto-reclosing. The installation of three TLSAs reduces the BFO occurrence by around 60%, that of two TLSAs for the upper and middle line of one circuit also reduces by around 60%, and that of two TLSAs for the upper phase of both circuits reduces by 85% compared to the TLSAs uninstalled lines, respectively. In the EHV transmission line case as well, the power frequency voltages can be negligible in discussing the BFO rate in the TLSAs uninstalled line, but they have a more significant influence on that in the TLSAs installed lines.

The performance of the TLSAs for HV and EHV transmission lines has been clarified in this chapter by the many times transient analyses with nonlinear calculation considering various conditions. It has been achieved by fully taking advantage of the numerical circuit analysis approach. The presented methodology can be utilized for any voltage class of the transmission lines. Thus, one can apply the methodology to design new transmission lines and to evaluate the reduction of lightning fault rates by installing TLSAs for those under operation. Furthermore, the reduction of the analysis cases based on the careful discussions can lead to the possibility of using the numerical electromagnetic analysis method, such as the FDTD method, for evaluating the specific case, not only reducing the analysis case and time in using the circuit analysis.

References for Chapter 5

[1] Investigating Research Committee on Evaluation and Application for Surge Arresters, IEEJ, “Technical trend on evaluation and application for surge arresters,” *IEEJ Technical Rep.,* no. 1444, Nov. 2018.

[2] K. Munukutla, V. Vittal, G. T. Heydt, D. Chipman, and B. Keel, “A practical evaluation of surge arrester placement for transmission line lightning protection,” *IEEE Trans. Power Del.*, vol. 25, no. 3, pp. 1742–1748, Jul. 2010.

[3] H. Kawamura, M. Kozuka, N. Itamoto, K. Shinjo, and M. Ishii, “Evaluation of relative lightning fault rate of transmission lines depending on line design and lightning activity,” *IEEJ Trans. Power and Energy*, vol. 130, no. 10, pp. 895–902, Oct. 2010.

[4] CIGRE WG C4.301 (Convener: A. Xemard), “Use of surge arresters for lightning protection for transmission lines,” CIGRE Technical Brochure, no. 440, Dec. 2010.

[5] T. H. Pham, S. A. Boggs, H. Suzuki, and T. Imai, "Effect of externally gapped line arrester placement on insulation coordination of a twin-circuit 220 kV line," *IEEE Trans. Power Del.*, vol. 27, no. 4, pp. 1991–1997, Oct. 2012.

[6] Subcommittee for transmission lines, study committee on lightning risk, "Application guide for transmission line surge arresters," *CRIEPI Rep.*, no. H07, 2012.

[7] C. Cardoso, J. Mendes, N. Filipe, A. Leiria, D. Duarte, L. Perro, and M. M. Fernandes, "Guidelines for transmission lines lightning performance improvement using a statistical approach," *in Proc. 2016 33rd Inter. Conf. on Lightning Protection (ICLP)*, pp. 1–6, Estoril, Portugal, Sep. 2016.

[8] S. Visacro, F. H. Silveira, B. Pereira, and R. M. Gomes, "Constraints on the use of surge arresters for improving the backflashover rate of transmission lines," *Electr. Power Syst. Res.*, vol. 180, pp. 106064-1–106064-7, Mar. 2020.

[9] Electric Technology Research Association, "Voltage sag mitigation methods," *Electric Technology Research,* vol. 46, no. 3, 1990.

[10] H. Takani, Y. Sonobe, T. Kagami, F. Kawano, P. Beaumont, G. P. Baber, and G. T. Main, "The application and advantages of multi-phase autoreclosing," *in Proc. 10th IET Int. Conf. on Developments in Power System Protection (DPSP 2010)*, Managing the Change, pp. 1–5, Manchester, UK, Mar. 2010.

[11] H. Motoyama, "Experimental study and analysis of breakdown characteristics of long air gaps with short tail lightning impulse," *IEEE Trans. Power Del.*, vol. 11, no. 2, pp. 972–979, Apr. 1996.

[12] H. Motoyama, K. Shinjo, Y. Matsumoto, and N. Itamoto, "Observation and analysis of multiphase back flashover on the Okushishiku Test Transmission Line caused by winter lightning," *IEEE Trans. Power Del.*, vol. 13, no. 4, pp. 1391–1398, Oct. 1998.

[13] V. Javor, and P. D. Rancic, "A channel-base current function for lightning return-stroke modeling," *IEEE Trans. Electromagn. Compat.*, vol. 53, no. 1, pp. 245–249, Feb. 2011.

[14] J. Takami, and S. Okabe, "Observational results of lightning current on transmission towers," *IEEE Trans. Power Del.*, vol. 22, no. 1, pp. 547–556, Jan. 2007.

[15] Subcommittee for transmission lines, lightning protection design committee, "Guide to lightning protection design for transmission lines," *CRIEPI Rep.*, no. T72, 2003.

[16] F. Heidler, "Analytical lightning current function for LEMP-calculation," *translation from German, Proc. Int. Conf. on Lightning Protection (ICLP)*, pp. 63–66, Munich, Germany, 1985.

[17] A. Andreotti, and L. Verolino, "A new channel-base current function for lightning studies," *IEEE Trans. Electromagn. Compat.*, vol. 57, no. 6, pp. 1539–1546, Dec. 2015.

[18] D. Mestriner, M. Brignone, R. Procopio, A. Piantini, and F. Rachidi, "A new channel-base lightning current formula with analytically adjustable parameters," *IEEE Trans. Electromagn. Compat*, vol. 63, no. 2, pp. 542–549, Apr. 2021.

[19] V. Cooray, and V. Rakov, "On the upper and lower limits of peak current of first return strokes in negative lightning flashes," *Atmospheric Research*, vol. 117, pp. 12–17, Nov. 2012.

[20] M. Ishii, M. Saito, F. Fujii, M. Matsui, and N. Itamoto, "High-current lightning discharges in winter," *IEEJ Trans. Power and Energy*, vol. 128, no. 1, pp. 291–297, Jan. 2008.

[21] M. Ishii and M. Saito, "Lightning electric field characteristics associated with transmission-line faults in winter," *IEEE Trans. Electromagn. Compat.*, vol. 51, no. 3, pp. 459–465, Aug. 2009.

[22] A. Smorgonskii, M. Rubinstein, and F. Rachidi, "Extreme values of lightning parameters," *in Proc. 2018 Int. Lightning Detection Conf. (ILDC)*, Fort Lauderdale, FL, USA, Mar. 2018.

6 Conclusions

This thesis has proposed transmission tower and line models for lightning surge analysis of overhead transmission lines by means of circuit analysis. The non-TEM characteristics of the lightning-struck transmission tower and line have been revealed, taking advantage of three-dimensional numerical electromagnetic field analysis. The proposed tower and line model can represent the non-TEM characteristics in the circuit analysis, enabling faster simulation with smaller memories than the numerical electromagnetic analysis. BFO analyses of transmission lines have been carried out by the proposed model, assuming various conditions taking advantage of the circuit analysis method. In the analyses, the optimized FO and TLSA models have been employed as well. The characteristics of BFO occurrence and TLSA operation have been discussed.

Chapter 1

Chapter 1 has provided an overview of lightning-related accidents in transmission lines, namely the shielding failure and subsequent SFFO, BFO, and mid-span BFO. Then general features of the lightning surge analysis method have been discussed. The SFFO and BFO mainly initiate lightning-related accidents in power systems. An accurate analysis of the lightning overvoltage can accomplish to prepare cost-effective countermeasures. The transmission tower and line characteristics are essential for discussing BFO characteristics since they preliminary determine the voltage of insulator strings.

For analyzing lightning surges in transmission systems, theoretical, experimental, and numerical approaches have been utilized. The numerical approaches, which have been validated from the theoretical and experimental viewpoint, can become a powerful tool for evaluating the lightning performance of transmission systems. The thesis has adopted numerical electromagnetic field analysis for revealing characteristics of a lightning-struck transmission tower and line taking its advantage: directly solving Maxwell's equations. Based on the analysis, new circuit models that can consider the revealed characteristics have been proposed, and practical lightning surge analyses have been carried out taking its advantage: executable with small computational resources.

Chapter 2

In Chapter 2, non-TEM characteristics of the lightning-struck tower and line have been discussed using the FDTD method and the most basic TEM-mode circuit analysis model. Comparisons of the analyzed results and discussions on them with referencing the experimental results reported in the past have revealed the non-TEM characteristics of the lightning-struck tower and line: 1) the gradual rise of the tower surge impedance with time, 2) the gradual rise of the self and mutual surge impedance of the transmission line with time and the time delays of mutual coupling among lines corresponding to their separation distances, and 3) the significant wave attenuation characteristics along the tower. Also,

suppose the lightning strikes the tip of the tower top cross-arm. In that case, the insulator voltages generated at the lightning-struck side can be higher than those at the other side due to the electromagnetic shielding by the tower and farther distances. The numerical circuit analysis model of the transmission tower and lines, which can consider the above characteristics, can enhance the validity and usefulness of the circuit analysis method.

Existing transmission tower and line models have also been overviewed. The models include a simplified model with constant surge impedances, a multistory tower model, a multi-section distributed line model, tower models based on the numerical electromagnetic field analysis, frequency-dependent models, and non-uniform line models. Some of the models, such as the model based on the numerical electromagnetic field analysis, frequency-dependent model, and non-uniform model, can partly consider the non-TEM characteristics of the lightning-struck transmission tower and line. However, they have rarely been employed for practical lightning surge analysis due to their relatively sophisticated modeling process. As a result, the multistory tower model, which cannot consider the non-TEM characteristics but is relatively accurate and simple compared to other models, has long and widely been employed for practical lightning surge analysis. Although the multistory tower model has been utilized for analysis and many findings have been accomplished, its accuracy and applicability to other towers than the original 500-kV tower should be re-evaluated. In this view, new transmission tower and line models, which can consider the non-TEM characteristics, and whose model parameters can be directly determined from the shape of the tower and line, have been presented in the thesis. Besides, lightning surge analysis has been carried out with the proposed model and the multistory tower model.

Chapter 3

The TEM-delay transmission tower and line models have been presented and validated in Chapter 3. The proposed TEM-delay model represents the non-TEM characteristics by 1) tower and line surge impedances provided by first-order delay functions, 2) phase-domain modeling of transmission line considering time delay in mutual coupling corresponding to the separation distances among the line, and 3) propagation function considering the significant attenuation characteristic of traveling waves along the tower. The model parameters can be derived from the configuration of the tower and line. No trial-and-error process or electromagnetic field analysis is required for determining the model parameters.

The proposed model has been validated by comparing measured and simulated tower surge responses and insulator voltages. Regarding the tower surge response, measured responses of the 500-kV tower reported in the past have been reproduced by the TEM-delay tower model. Regarding the insulator voltages, measured voltages of 500-kV and UHV transmission towers reported in the past, and simulated voltages by the FDTD method of HV/EHV transmission towers, have been reproduced by the TEM-delay tower and line models. The TEM-delay tower model considering tower cross-arms can even analyze the lightning strike to a tip of tower top cross-arm and resultant insulator voltages. The validity

and applicability of the proposed TEM-delay model have been shown. Besides, it has been shown that the existing tower models could have been underestimated the insulator voltages.

Chapter 4

In Chapter 4, insulator voltages of lightning-struck HV transmission towers have been evaluated considering tower footing characteristics. Then the FO and TLSA models for BFO analysis have been presented. Based on these models, the BFO characteristics of the HV transmission line have been clarified.

Regarding the insulator voltage, the TEM-delay tower model can reproduce the insulator voltages of the HV transmission line in various tower footing resistance cases. In contrast, the existing models provide lower insulator voltages due to the low tower surge impedances and lack or insufficient implementation of propagation characteristics of traveling waves. The characteristics of the existing models are caused by the experimental setups for developing the multistory tower model. The reverse T-shape tower foot can be modeled by a linear resistor for soil resistivity ranging from 20 Ωm to 1000 Ωm, the typical value in Japan.

The FO model of the arcing horn includes the model by the LPM and *V–t* crossover method. The TLSA comprises the series-connected non-linear resistor representing *VI* characteristic of ZnO element and FO model by the LPM representing the air gap. The measured *V–t* characteristics of the arcing horn and TLSA reported in the past have been reproduced precisely by adjusting the constants of the LPM and *V–t* crossover method.

The BFO characteristics of the HV transmission line have been clarified. Suppose the negative lightning strikes the transmission tower or OHGWs. In that case, the BFO primarily occurs at phases with positive power frequency voltages since the insulator voltages become higher (the voltage rise of the tower cross-arm and the phase conductors have the opposite polarity). This characteristic does not mean that the BFO does not occur at phases with positive power frequency voltage in the negative lightning case. The minimum currents causing *N*-phase BFOs, critical current, are significantly dependent on the power frequency voltages. The BFO phases and critical currents derived by the proposed TEM-delay model well support the observed results reported in the past, but the existing model cannot support both or one of them. The TEM-delay model also reproduced TLSA operation and 2BFOs observed in the past. Regarding the FO model, the LPM is suitable for single and multiphase BFO analysis, but the *V–t* crossover method is only applicable to single-phase BFO analysis. Consideration of the leader developing process is attributed to this difference. Regarding the current waveform, the 2/70 μs triangular current and double-peak current representing median values of natural lightning provide similar BFO phase and critical current since the steep-rising part is responsible for the BFO occurrence.

Chapter 5

In Chapter 5, BFO analyses for HV and EHV transmission lines have been carried out to discuss the effectiveness of the TLSA installations to reduce the BFO occurrences. The specific reduction rate of the lightning fault and the threshold of tower footing resistance can variate depending on the conditions, such as the configuration of the tower and lines. However, the modeling process and methodology of the BFO analysis can be applied to any transmission line.

The installation of three TLSAs for one circuit of the line and that of five TLSAs have been analyzed in the HV transmission line. The installation of five TLSAs except for the lower phase performs best as long as the tower footing resistance is lower than around 40 Ω since the lower insulator voltage is the lowest among the phases in this condition for the studied line. The installation of three and five TLSAs reduces the lightning fault rate by around 20% and 60%, respectively, compared to the TLSAs uninstalled line. These installations reduce the occurrence of temporary voltage drop around 30% and 100%, respectively, also compared to the TLSAs uninstalled line. Note that both TLSAs installation can avoid the double-circuit fault. The power frequency voltages can be negligible in discussing the BFO rate in the TLSAs uninstalled line since the maximum power frequency voltage is less than about 10% of the FO voltage. However, they have a relatively significant influence on that in the TLSAs installed line since the operations of TLSAs initiate the BFOs at the phases without the TLSAs.

In the EHV transmission line, the installation of three TLSAs in one circuit of the line, two TLSAs for the upper and middle phases of one circuit, and that for the upper phase of both circuits have been analyzed. Among three types of TLSAs arrangements, the installation of two TLSAs for the upper phase in both circuits performs best as long as the tower footing resistance is lower than around 30 Ω for the studied tower case since the upper insulator voltage becomes the highest among the phases. The installation of three TLSAs can avoid the double-circuit fault in any line with any grounding and reclosing systems. The installation of two TLSAs for the upper and middle phase of one circuit and the upper phase of both circuits can maintain the reclosing condition in lines with the multiphase auto-reclosing. The installation of three TLSAs reduces the BFO occurrence by around 60%, that of two TLSAs for the upper and middle line of one circuit also reduces by around 60%, and that of two TLSAs for the upper phase of both circuits reduces by 85% compared to the TLSAs uninstalled lines, respectively. In the EHV transmission line case as well, the power frequency voltages can be negligible in discussing the BFO rate in the TLSAs uninstalled line, but they significantly influence that in the TLSAs installed lines.

The proposed tower and line models have been validated and applied to practical lightning surge analysis in this thesis. The proposed models can be widely utilized for lightning surge analysis if they are implemented in the EMT-simulators as standard models. In this view, more and more practical analyses should be performed by the proposed models, and their validity should be discussed in detail.

The presented methodology for evaluating the BFO occurrence with various line arrangements can be applied to any voltage class transmission line. The development of software for calculating the lightning fault rate of transmission lines can help engineers in utilities. From the viewpoint of the insulation design, the proposed models should be extended for analyzing lightning surges intruding substations. The modeling of interaction among the lightning channel, transmission tower, inclined entrance conductors, and gantry becomes more critical in those analyses.

Appendix

A1 Fundamentals of the FDTD Analysis

This appendix section describes the basic formulation of the FDTD method [1] and the computational resources required for the analysis. As discussed in Chapter 1 and Chapter 2, the FDTD method allows us to analyze the characteristics of a lightning-struck transmission tower and line in detail, though it requires massive computational resources comparing to other analysis techniques such as the numerical circuit analysis. Here the FDTD method in the three-dimensional Cartesian coordinate system is discussed.

The FDTD method solves Maxwell's equations by using spatial and time discretization. The electric and magnetic field components, E_x, E_y, E_z, H_x, H_y, and H_z, are placed as shown in Fig. A 1 and they are updated as described below. Ampere's low is provided by:

$$\nabla \times \boldsymbol{H}^{n-1/2} = \varepsilon \frac{\partial \boldsymbol{E}^{n-1/2}}{\partial t} + \boldsymbol{J}^{n-1/2} = \varepsilon \frac{\partial \boldsymbol{E}^{n-1/2}}{\partial t} + \sigma \boldsymbol{E}^{n-1/2} \tag{A 1}$$

where $\boldsymbol{H}$ and $\boldsymbol{E}$ are the magnetic- and electric-field vectors, $\boldsymbol{J}$ is the conduction-current-density vector, σ is the electric conductivity, and n–1/2 is the present time step number. By applying the central finite difference to the time derivative term of (A 1), the following can be derived:

$$\varepsilon \frac{\partial \boldsymbol{E}^{n-1/2}}{\partial t} + \sigma \boldsymbol{E}^{n-1/2} \approx \varepsilon \frac{\boldsymbol{E}^{n} - \boldsymbol{E}^{n-1}}{\Delta t} + \sigma \frac{\boldsymbol{E}^{n} + \boldsymbol{E}^{n-1}}{2} \approx \nabla \times \boldsymbol{H}^{n-1/2} \tag{A 2}$$

where Δt is the time step, and $\boldsymbol{E}^{n-1/2}$ is approximated by its average value. The update equation for the electric field at the step n can be derived by rearranging (A 2), and it is given by the one time-step previous electric field $\boldsymbol{E}^{n-1}$ and half time-step previous magnetic field rotation $\nabla \times \boldsymbol{H}^{n-1/2}$ as:

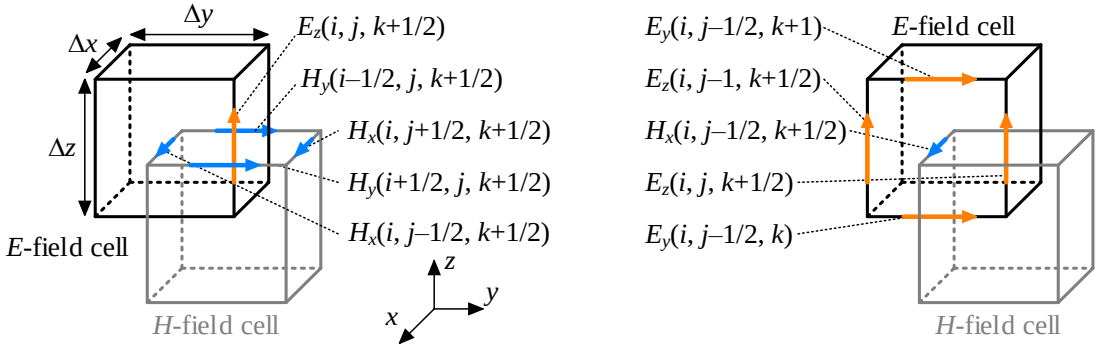

Fig. A 1 Electric- and magnetic-field placement of the FDTD method in the three-dimensional Cartesian coordinate system.

$$\boldsymbol{E}^n = \frac{1-\sigma\Delta t/2\varepsilon}{1+\sigma\Delta t/2\varepsilon}\boldsymbol{E}^{n-1} + \frac{\Delta t/\varepsilon}{1+\sigma\Delta t/2\varepsilon}\nabla\times\boldsymbol{H}^{n-1/2} \tag{A 3}$$

The updating equation for the z-direction electric field E_z^n at the point $(i, j, k+1/2)$ can be expressed by:

$$\begin{aligned} E_z^n\left(i,j,k+\frac{1}{2}\right) &= \frac{1-\left(\sigma\left(i,j,k+1/2\right)\Delta t\right)/\left(2\varepsilon\left(i,j,k+1/2\right)\right)}{1+\left(\sigma\left(i,j,k+1/2\right)\Delta t\right)/\left(2\varepsilon\left(i,j,k+1/2\right)\right)}E_z^{n-1}\left(i,j,k+\frac{1}{2}\right) \\ &\quad + \frac{\Delta t/\left(2\varepsilon\left(i,j,k+1/2\right)\right)}{1+\left(\sigma\left(i,j,k+1/2\right)\Delta t\right)/\left(2\varepsilon\left(i,j,k+1/2\right)\right)} \\ &\quad \times\left\{\frac{\partial H_y^{n-1/2}\left(i,j,k+1/2\right)}{\partial x} - \frac{\partial H_x^{n-1/2}\left(i,j,k+1/2\right)}{\partial y}\right\} \\ &\approx \frac{1-\left(\sigma\left(i,j,k+1/2\right)\Delta t\right)/\left(2\varepsilon\left(i,j,k+1/2\right)\right)}{1+\left(\sigma\left(i,j,k+1/2\right)\Delta t\right)/\left(2\varepsilon\left(i,j,k+1/2\right)\right)}E_z^{n-1}\left(i,j,k+\frac{1}{2}\right) \\ &\quad + \frac{\Delta t/\left(2\varepsilon\left(i,j,k+1/2\right)\right)}{1+\left(\sigma\left(i,j,k+1/2\right)\Delta t\right)/\left(2\varepsilon\left(i,j,k+1/2\right)\right)}\frac{1}{\Delta x\Delta y} \\ &\quad \times\begin{Bmatrix} H_y^{n-1/2}\left(i+1/2,j,k+1/2\right)\Delta y - H_y^{n-1/2}\left(i-1/2,j,k+1/2\right)\Delta y \\ -H_y^{n-1/2}\left(i,j+1/2,k+1/2\right)\Delta x + H_x^{n-1/2}\left(i,j-1/2,k+1/2\right)\Delta x \end{Bmatrix} \end{aligned} \tag{A 4}$$

where the spatial derivative terms for the magnetic field are approximated by their central finite differences. The updating equations for the *x*- and *y*-direction electric fields E_x^n and E_y^n can be derived in the same manner.

The derivation of the updating equations for the magnetic field is started from Faraday's low:

$$\nabla\times\boldsymbol{E}^n = -\mu\frac{\partial\boldsymbol{H}^n}{\partial t} \tag{A 5}$$

where n is the present time step number and μ is the permeability. In this case as well, the central time difference is applied to the time-derivative term, and the following equation is derived:

$$\mu\frac{\partial\boldsymbol{H}^n}{\partial t} \approx \mu\frac{\boldsymbol{H}^{n+1/2}-\boldsymbol{H}^{n-1/2}}{\Delta t} \approx -\nabla\times\boldsymbol{E}^n \tag{A 6}$$

The update equation for the magnetic field at the step n+1/2 can be derived by rearranging (A 6), and it is given by the one time-step previous magnetic field $\boldsymbol{H}^{n-1/2}$ and half time-step previous electric-field rotation $\nabla\times\boldsymbol{E}^n$ as:

$$\boldsymbol{H}^{n+1/2} = \boldsymbol{H}^{n-1/2} - \frac{\Delta t}{\mu}\nabla\times\boldsymbol{E}^n \tag{A 7}$$

The updating equation for the *x*-direction magnetic field $H_x^{n+1/2}$ at the point $(i, j-1/2, k+1/2)$ can be expressed as:

$$
\begin{aligned}
H_x^{n+1/2}\left(i, j-\frac{1}{2}, k+\frac{1}{2}\right) &= H_x^{n-1/2}\left(i, j-\frac{1}{2}, k+\frac{1}{2}\right)+\frac{\Delta t}{\mu\left(i, j-1/2, k+1/2\right)} \\
&\times\left\{-\frac{\partial E_z^n\left(i, j-1/2, k+1/2\right)}{\partial y}+\frac{\partial E_y^n\left(i, j-1/2, k+1/2\right)}{\partial z}\right\} \\
&\approx H_x^{n-1/2}\left(i, j-\frac{1}{2}, k+\frac{1}{2}\right)+\frac{\Delta t}{\mu\left(i, j-1/2, k+1/2\right)}\frac{1}{\Delta y \Delta z} \\
&\times\left\{\begin{matrix}-E_z^n\left(i, j, k+1/2\right)\Delta z & +E_z^n\left(i, j-1, k+1/2\right)\Delta z \\ +E_y^n\left(i, j-1/2, k+1\right)\Delta y & -E_z^n\left(i, j-1/2, k\right)\Delta y\end{matrix}\right\}
\end{aligned}
\tag{A 8}
$$

where the spatial derivative terms for the electric field are approximated by their central finite differences. The updating equations for the *x*- and *y*-direction magnetic fields $H_x^{n+1/2}$ and $H_y^{n+1/2}$ can be derived in the same manner.

The excitations, such as the voltage and current sources, are modeled by forcing the electric and magnetic fields. The lumped elements, such as the resistor, inductor, and capacitor, are modeled by modifying electric- and magnetic-field updating equations considering characteristics of each element [2]. In order to analyze the unbounded space, absorbing boundary conditions, such as Liao's conditions [3] and perfectly matched layers [4], are utilized. Other specific modeling methods, such as the representation of thin wires, lossy conductors, coaxial cables, nonlinear elements, and others, have been developed and used for lightning surge analysis (e.g., [5] and references therein).

Regarding the computation resources, the FDTD analysis of the 76-m high transmission tower performed in Chapter 2 requires about 10 GB of memory. It took about 6 hours to derive 3-μs long transient response by Intel Core i7-6700K, 4.00 GHz (RAM 64 GB) environment. The number of cells of this analysis was 600 × 600 × 400 = 14.4 million cells. Note that the use of nonuniform cells reduces the computation memory. Furthermore, parallel computation by multi-core computing and/or by multi-node computing can reduce the computation time [6], though not simple programming is required.

References

[1] K. S. Yee, "Numerical solution of initial boundary value problems involving Maxwell's equations in isotropic media," *IEEE Trans. Antennas Propag.*, vol. 14, no. 3, pp. 302–307, May 1966.

[2] T. Uno, *Finite difference time domain method for electromagnetic field and antennas*, Corona Publishing Co., Ltd., Tokyo, Japan, 1998.

[3] Z. P. Liao, H. L. Wong, B. P. Yang, and Y. F. Yuan, "A transmitting boundary for transient wave analysis," *Scientia Sinica,* vol. A27, no. 10, pp. 1063–1076, Oct. 1984.

[4] J. P. Berenger, "A perfectly matched layer for the absorption of electromagnetic waves," *J. of Comp. Phys.*, vol. 114, no. 2, pp. 185–200, Oct. 1994.

[5] CIGRE WG C4.37 (Convenor: Y. Baba), "Electromagnetic computation methods for lightning surge studies with emphasis on the FDTD method," *CIGRE Technical Brochure*, no. 785, Dec. 2019.

[6] e.g., A. Tatematsu, "Acceleration of an FDTD-based surge simulation program (VSTL REV) and its application to lightning surge analysis of a reinforced concrete building," *CRIEPI Rep.*, no. H13009, 2014.

A2 Fundamentals of the Numerical Circuit Analysis

This appendix section describes the basics of the numerical circuit analysis method. The numerical circuit analysis used in this thesis was the nodal-analysis-based circuit analysis method. Distributed parameter line theory was included to analyze the transmission towers and lines.

In the numerical circuit analysis, the circuit formulation is carried out based on the nodal analysis technique. The original version of EMTP has adapted the basic nodal analysis method [1], whereas the modified ones have been developed and adapted in the other programs [2]–[4]. The Tableau method [5] has been adapted in XTAP [6].

The time-domain response is derived by applying a numerical integration technique to the differential equation of each circuit element. The trapezoidal rule is the representative technique since it is simply implemented but provides an accurate solution. Note that the numerical oscillation emerges in some cases, and thus specific methods such as the critical damping adjustment using the backward Euler method [7], [8], and two-stage diagonally implicit Runge-Kutta method [9] have been developed. Upon applying the trapezoidal rule, each circuit element is represented by the resistance and current source parallel circuit. For instance, the inductance voltage v_L and current i_L has the following relation:

$$v_L(t) = L\frac{di_L(t)}{dt} \tag{A 9}$$

where L is the inductance. The following can be derived by applying the trapezoidal rule to (A 9):

$$\begin{aligned} i_L(t) &= \frac{\Delta t}{2L}v_L(t) + \left\{\frac{\Delta t}{2L}v_L(t-\Delta t) + i_L(t-\Delta t)\right\} \\ &= \frac{v_L(t)}{R_L} + J_L(t) \end{aligned} \tag{A 10}$$

where Δt is the computation time step. The second term of the right-hand side of (A 10) becomes the history term $J_L(t)$. Therefore, the inductance can be modeled by the parallel circuit of resistance and current source, as shown in Fig. A 2.

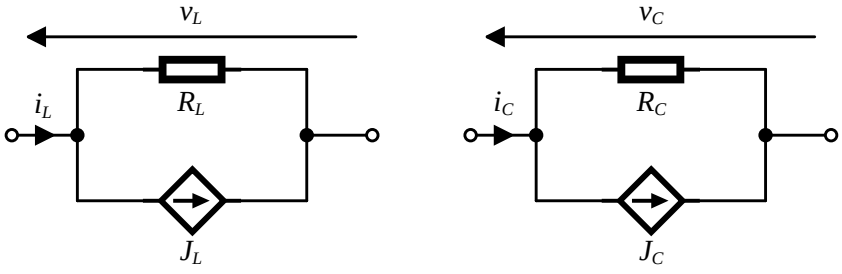

(a) Inductance (b) Capacitance

Fig. A 2 Representation of the inductance and capacitance in the numerical circuit analysis.

In the same manner, capacitance can also be represented by the resistance and current source parallel circuit:

$$\begin{aligned} i_C(t) &= \frac{2C}{\Delta t} v_C(t) - \left\{ \frac{2C}{\Delta t} v_C(t-\Delta t) + i_C(t-\Delta t) \right\} \\ &= \frac{v_C(t)}{R_C} + J_C(t) \end{aligned} \tag{A 11}$$

Distributed lines are also represented by the parallel circuit of the resistance and the current source [1]. The voltage and current of the line at point x can be written by the forward and backward traveling waves F_f and F_b as:

$$\begin{aligned} v(x,t) + Z_0 i(x,t) &= 2F_f(t - x/vel) \\ v(x,t) - Z_0 i(x,t) &= 2F_b(t + x/vel) \end{aligned} \tag{A 12}$$

where Z_0 is the characteristic impedance, and *vel* is the propagation speed of the traveling wave. These equations can be written at nodes s and r as:

$$\begin{aligned} v_s(t-\tau) + Z_0 i_s(t-\tau) &= v_r(t) + Z_0 i_r(t) \\ v_s(t) + Z_0 i_s(t) &= v_r(t-\tau) + Z_0 i_r(t-\tau) \end{aligned} \tag{A 13}$$

where τ is the one-way propagation time of the line, derived by dividing line length with the propagation speed. As shown in (A 13), the sending-end voltage and current influence the receiving-end voltage and current, and vice versa. Finally, the following relation can be derived for representing the distributed line in the numerical circuit analysis, as shown in Fig. A 3:

$$\begin{aligned} i_s(t) &= \frac{v_s(t)}{Z_0} - \frac{v_r(t-\tau)}{Z_0} - i_r(t-\tau) = \frac{v_s(t)}{Z_0} + J_s(t) \\ i_r(t) &= \frac{v_r(t)}{Z_0} - \frac{v_s(t-\tau)}{Z_0} - i_s(t-\tau) = \frac{v_r(t)}{Z_0} + J_r(t) \end{aligned} \tag{A 14}$$

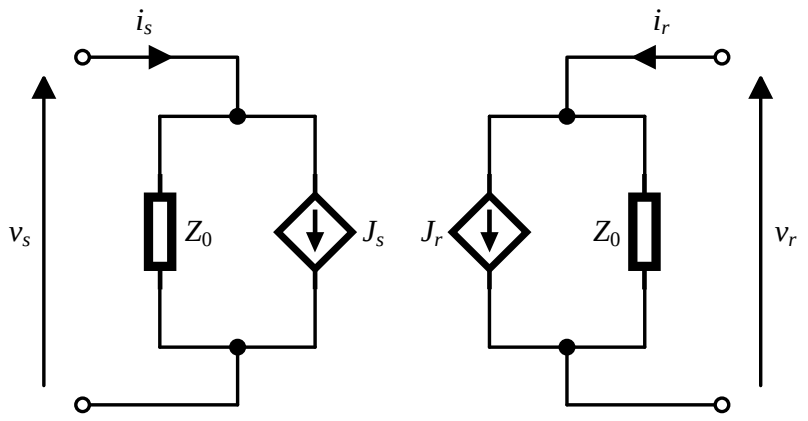

Fig. A 3 Representation of the distributed parameter line in the numerical circuit analysis.

Note that the characteristic impedance Z_0 has been set constant value or frequency-dependent value derived based on the TEM-mode assumption.

The node conductance matrix $\boldsymbol{G}$ is readily derived for the circuit to be studied by applying the above formulation to each circuit element:

$$[\boldsymbol{G}](\boldsymbol{v}) = (\boldsymbol{J}) \tag{A 15}$$

where $\boldsymbol{v}$ is the unknown voltage vector and $\boldsymbol{J}$ is the current vector composed of the independent current sources and the history terms. For instance, the transient analysis of the 76-m high transmission tower performed in Chapter 2 requires 23 nodes. The node conductance matrix becomes 22 × 22 matrix, and the 3-μs long transient response is calculated in 0.094 s. Note that the representation of other models such as the switches, control circuits, and nonlinear elements have been developed and used in the transient analysis [10].

References

[1] H. Dommel, "Digital computer solution of electromagnetic transients in single-and multiphase networks," *IEEE Trans. Power App. Syst.*, vol. 88, no. 4, pp. 388–399, Apr. 1969.

[2] C.-W. Ho, A. Ruehli, and P. Brennan, "The modified nodal approach to network analysis," *IEEE Trans. Circuits Syst.*, vol. 22, no. 6, pp. 504–509, Jun. 1975.

[3] J. Mahseredjian, and F. Alvarado, "Creating an electromagnetic transients program in MATLAB: MatEMTP," *IEEE Trans. Power Del.*, vol. 12, no. 1, pp. 380–388, Jan. 1997.

[4] J. Mahseredjian, S. Dennetière, L. Dubé, B. Khodabakhchian, and L. Gérin-Lajoie, "On a new approach for the simulation of transients in power systems," *Electr. Power Syst. Res.*, vol. 77, no. 11, pp. 1514–1520, Sep. 2007.

[5] G. Hachtel, R. Brayton, and F. Gustavson, "The sparse tableau approach to network analysis and design," *IEEE Trans. Circuit Theory*, vol. 18, no. 1, pp. 101–113, 1971.

[6] T. Noda, T. Miki, N. Gibo, and K. Takenaka, "Development of an electromagnetic transient analysis program for power systems (Part 1) –Fundamental design–," *CRIEPI Rep.*, no. H06002, 2007.

[7] J. R. Marti and J. Lin, "Suppression of numerical oscillations in the EMTP power systems," *IEEE Trans. on Power Syst.*, vol. 4, no. 2, pp. 739–747, May 1989.

[8] J. Lin and J. R. Marti, "Implementation of the CDA procedure in the EMTP," *IEEE Trans. on Power Syst.*, vol. 5, no. 2, pp. 394–402, May 1990.

[9] T. Noda, K. Takenaka, and T. Inoue, "Numerical integration by the 2-stage diagonally implicit Runge-Kutta method for electromagnetic transient simulations," *IEEE Trans. Power Del.*, vol. 24, no. 1, pp. 390–399, Jan. 2009.

[10] e.g., J. A. Martinez-Velasco, *Transient analysis of power systems: a practical approach*, Wiley-IEEE Press, Hoboken, N.J., USA, 2020.

A3 Papers Presented by the Author

Journal Papers

1. A. Yamanaka, N. Nagaoka, and Y. Baba, “Lightning surge analysis of HV transmission line: bias AC-voltage effect on multiphase back-flashover,” *IEEE Transactions on Power Delivery*, (in press, early access article is available doi.org/10.1109/TPWRD.2020.3045170)

2. A. Yamanaka, N. Nagaoka, and Y. Baba, “Circuit model of an overhead transmission line considering the TEM-mode formation delay,” *IEEJ Transactions on Electrical and Electronic Engineering,* vol. 16, no. 6, pp. 888–895, Jul. 2021.

3. A. Yamanaka, N. Nagaoka, and Y. Baba, “Equivalent circuit model of a transmission tower considering a lightning struck point and cross-arms,” *Electric Power Systems Research,* vol. 196, pp. 107253-1–107253-7, Jul. 2021.

4. A. Yamanaka, N. Nagaoka, Y. Baba, H. Motoyama, and T. Ueda, “Lightning surge response of a transmission tower with overhead lines analyzed by TEM-delay model,” *IEEJ Transactions on Power and Energy,* vol. 141, no. 2, pp. 145–153, Feb. 2021. (in Japanese)
山中章文，長岡直人，馬場吉弘，本山英器，植田俊明：「TEM-delay モデルによる鉄塔ー送電線系雷サージ応答の検証」，電気学会論文誌 B，vol. 141，no. 2，pp. 145–153 (2021-2)

5. A. Yamanaka, N. Nagaoka, and Y. Baba, “Circuit model of vertical double-circuit transmission tower and line for lightning surge analysis considering TEM-mode formation,” *IEEE Transactions on Power Delivery*, vol. 35, no. 5, pp. 2471–2480, Oct. 2020.

6. A. Yamanaka, S. Inoue, N. Nagaoka, and H. Morita, “Equivalent circuit synthesis for grounding impedance of foundation based on FDTD analysis,” *Transaction of Institute of Electrical Installation Engineers of Japan*, vol. 39, no. 8, pp. 50–56, Oct. 2019. (in Japanese)
山中章文，井上翔太，長岡直人，森田祐志：「FDTD 解析に基づく構造体基礎接地インピーダンス等価回路」，電気設備学会論文誌，vol. 39，no. 8，pp. 50–56 (2019-10)

7. A. Yamanaka, N. Nagaoka, Y. Baba, M. Saito, and T. Miki, “Lightning strike to a tall grounded object: Part2—LEMP calculation with a channel approximation,” *IEEE Transactions on Electromagnetic Compatibility*, vol. 61, no. 3, pp. 736–744, Jun. 2019.

8. A. Yamanaka, N. Nagaoka, Y. Baba, M. Saito, and T. Miki, “Lightning strike to a tall grounded object: part1. circuit modeling with direction dependence,” *IEEE Transactions on Electromagnetic Compatibility*, vol. 61, no. 3, pp. 727–735, Jun. 2019.

9. A. Yamanaka, N. Nagaoka, Y. Baba, and M. Saito, “Effect of earth surface on lightning electromagnetic pulse propagation,” *CIGRE Science & Engineering Journal*, vol. 14, pp. 111–117, Jun. 2019.

10. A. Yamanaka, A. Hori, H. Murakami, and N. Nagaoka, “A vertical conductor circuit model including up- and down-ward traveling waves,” *Electric Power Systems Research*, vol. 162, pp. 50–56, Sep. 2018.

International Conferences

1. A. Yamanaka, N. Nagaoka, and Y. Baba, “Lightning surge analysis of HV transmission line: bias AC-voltage effect on multiphase back-flashover,” *Proc. 21st International Conference on Environment and Electrical Engineering*, Bari, Italy, Sep. 2021 (presentation of the accepted paper for *IEEE Transactions on Power Delivery*).

2. A. Yamanaka, N. Nagaoka, and Y. Baba, “Equivalent circuit model of a transmission tower considering a lightning struck point and cross-arms,” *in Proc. 14th International Conference on Power Systems Transients (IPST) 2021*, Belo Horizonte, Brazil, Jun. 2021.

3. K. Kutsuna, A. Yamanaka, and N. Nagaoka, “Estimation of lightning channel impedance using current waveforms observed at a tall structure,” *Proc. the 14th International Symposium on EMC and Transients in Infrastructures and the 16th International Student Session (ISET/ISS)*, no. SS-3-1, Kyoto, Japan, Dec. 2020.

4. A. Yamanaka, N. Nagaoka, and Y. Baba, “Circuit model of vertical double-circuit transmission tower and line for lightning surge analysis considering TEM mode formation,” *in Proc. 20th International Conference on Environment and Electrical Engineering*, Madrid, Spain, Jun. 2020 (presentation of the accepted paper for *IEEE Transactions on Power Delivery*).

5. A. Yamanaka, N. Nagaoka, Y. Baba, and M. Saito, “Effect of earth surface on lightning electromagnetic pulse propagation,” *in Proc. CIGRE-IEC 2019 Conference on EHV and UHV (AC & DC)*, Hakodate, Japan, Apr. 2019.

6. A. Yamanaka, N. Nagaoka, and Y. Baba, “Determination method of short-circuit current for lightning hitting a tall grounded object,” *in Proc. The 5th International Symposium on Lightning Protection and High Voltage Engineering (ISLH)*, pp. 43–48, Bangkok, Thailand, Mar. 2019.

7. A. Yamanaka, N. Nagaoka, and H. Morita, “Effect of inductive grounding impedance on lightning transients in wind farm,” *Proc. 34th International Conference on Lightning Protection (ICLP) 2018*, Rzeszow, Poland, Sep. 2018.

8. A. Yamanaka, and N. Nagaoka, “Circuit model of a vertical conductor including a lightning channel,” *in Proc. the 11th International Symposium on EMC and Transients in Infrastructures and the 13th International Student Session (ISET/ISS)*, no. ISS-15, Kyoto, Japan, Dec. 2017.

9. A. Yamanaka, A. Hori, H. Murakami, and N. Nagaoka, “A vertical conductor circuit model including up- and down-ward traveling waves,” *in Proc. International Conference on Power Systems Transients (IPST) 2017,* no. 17IPST089, Seoul, Korea, Jun. 2017.

Domestic Conferences and Research Meetings

1. A. Yamanaka, N. Nagaoka, and Y. Baba, “Lightning surge analysis on HV transmission system: performance analysis of flashover models,” *The papers of Technical Meeting on High Volt*age Engineering, IEEJ, no. HV-21-048, Jan. 2021. (in Japanese)
山中章文，長岡直人，馬場吉弘：「フラッシオーバモデルに着目した高圧送電線の雷サージ解析」，電気学会高電圧研資，No.HV-21-048 (2021-1)

2. A. Yamanaka, N. Nagaoka, Y. Baba, H. Motoyama, and T. Ueda, “Lightning surge response of a transmission tower with overhead lines analyzed by TEM-delay model,” *2020 IEEJ Power and Energy Society Annual Meeting*, no. 52, Sep. 2020. (in Japanese)
山中章文，長岡直人，馬場吉弘，本山英器，植田俊明：「TEM-delay モデルによる鉄塔－送電線系雷サージ応答の検討」，2020 年電気学会 B 部門大会，no. 52 (2020-9)

3. K. Kutsuna, A. Yamanaka, Y. Baba, and N. Nagaoka, “Estimation of lightning open-circuit-voltages using current waveforms observed at a tall structure,” *2020 IEEJ Power and Energy Society Annual Meeting*, no. 312, Sep. 2020. (in Japanese)
忽那幸希，山中章文，馬場吉弘，長岡直人：「高構造物雷撃電流観測波形による開放雷電圧波形の推定」，2020 年電気学会 B 部門大会 no. 312 (2020-9)

4. A. Yamanaka, N. Nagaoka, and Y. Baba, “Numerical electromagnetic and circuit analysis of lightning surge on a 66 or 77 kV transmission tower,” *Proc. Annual Meeting of IEEJ*, no. 7-078, Mar. 2019. (in Japanese)
山中章文，長岡直人，馬場吉弘：「66･77 kV 鉄塔雷サージの数値電磁界・回路解析」，令和 2 年電気学会全国大会，no. 7-078 (2020-3)

5. K. Fuchikami, A. Yamanaka, N. Nagaoka, and Y. Baba, “FDTD analysis of the potential of a grounding electrode considering frequency dependence of soil,” *The papers of Technical Meeting on High Voltage Engineering*, IEEJ, no, HV-20-029, Jan. 2020. (in Japanese)
渕上恭平，山中章文，馬場吉弘，長岡直人：「土壌周波数依存性を考慮した接地電極電位の FDTD 解析」，電気学会高電圧研究会，no. HV-20-029 (2020-1)

6. T. Shimizukawa, A. Yamanaka, K. Yamazaki, K. Yamamoto, Y. Baba, and N. Nagaoka, “Fault detection of down-conductor using double wire by resonant frequency,” *The papers of Technical Meeting on High Voltage Engineering*, IEEJ, no. HV-20-013, Jan. 2020. (in Japanese)
清水川拓巳，山中章文，山崎健一，山本和男，馬場吉弘，長岡直人：「2 導体からなるダウンコンダクタによる共振周波数を用いた断線検出法」，電気学会高電圧研究会，no. HV-20-013 (2020-1)

7. A. Yamanaka, N. Nagaoka, and Y. Baba, “Circuit model of an overhead transmission line considering the TEM-mode formation delay,” *The papers of Joint Technical Meeting on Electrical Discharges, Plasma and Pulsed Power / Switching and Protecting Engineering / High Voltage Engineering*, IEEJ, no. EPP-19-110, SP-19-032, HV-19-095, Dec. 2019. (in Japanese)
山中章文，長岡直人，馬場吉弘：「TEM モード形成遅れを考慮した架空送電線の回路解析モデル」，電気学会放電・プラズマ・パルスパワー / 開閉保護 / 高電圧合同研資，no. EPP-19-110, SP-19-032, HV-19-095 (2019-12)

8. K. Fuchikami, A. Yamanaka, Y. Baba, and N. Nagaoka, “Measurement of frequency characteristic of soil conductivity and relative permittivity using coaxial electrode,” *The papers of Joint Technical Meeting on Frontier Technology and Engineering and High Voltage Engineering*, IEEJ, no. FTE18-034, HV-18-082, May 2018. (in Japanese)
渕上恭平，山中章文，馬場吉弘，長岡直人：「同軸型電極を用いた土壌導電率・比誘電率の周波数特性測定法」，電気学会新エネルギー環境・高電圧合同研資，no. FTE18-034, HV-18-082 (2018-5)

9. T. Shimizukawa, A. Yamanaka, Y. Baba, N. Nagaoka, and K. Yamazaki, “Fault detection of down-conductors by current injection using a Rogowski coil,” *The papers of Joint Technical Meeting on Frontier Technology and Engineering and High Voltage Engineering*, IEEJ, no. FTE18-031, HV-18-078, May 2018. (in Japanese)
清水川拓巳，山中章文，馬場吉弘，長岡直人，山崎健一：「ロゴスキーコイルを用いた電流注入によるダウンコンダクタ断線検出法」，電気学会新エネルギー環境・高電圧合同研資，no. FTE18-031, HV-18-078 (2018-5)

10. A. Yamanaka, N. Nagaoka, Y. Baba, and H. Morita, “Wave propagation characteristics of a vertical conductor on imperfectly conducting earth analyzed with FDTD,” *Proc. Annual Meeting of IEEJ*, No.7-075, Mar. 2018. (in Japanese)
山中章文，長岡直人，馬場吉弘，森田祐志：「FDTD 解析に基づく不完全大地上垂直導体波形伝搬特性」，平成 30 年電気学会全国大会，no.7-075 (2018-3)

11. A. Yamanaka, N. Nagaoka, and Y. Baba, “A direction-dependent circuit model of a vertical conductor considering the presence of a return stroke channel,” *The papers of Technical Meeting on High Voltage Engineering*, IEEJ, no. HV-18-27, Jan. 2018. (in Japanese)
山中章文，長岡直人，馬場吉弘「帰還雷撃を考慮した伝搬方向依存垂直導体回路解析モデル」，電気学会高電圧研資，no. HV-18-27 (2018-1)

12. A. Hori, A. Yamanaka, H. Tanaka, and N. Nagaoka, “On a numerical analysis model of rails for lightning surge,” *Proc. Annual Meeting of IEEJ*, No.5-165, Mar. 2017. (in Japanese)
堀晃徳，山中章文，田中弘毅，長岡直人：「鉄道用レールの雷サージ伝搬特性を表現し得る数値解析モデルの検討」，平成 29 年電気学会全国大会，No.5-165 (2017-3)

Talks

1. Lecture: “Lightning surge analysis of vertical objects in combination of numerical electromagnetic analysis and EMTP-circuit analysis method,” *Workshop at Annual meeting of the Japanese EMTP committee*, Doshisha University Imadegawa Campus, Kyoto, Sep. 2019. (in Japanese)
講演：「電磁界解析法と EMTP 回路解析法を融合した垂直構造物雷サージ解析」，日本 EMTP 委員会ワークショップ，同志社大学今出川キャンパス (2019-9)

Thesis

- 山中章文：「進行波の伝搬方向依存性を考慮した垂直導体回路解析モデル」，卒業論文，同志社大学 (2017-2)
- A. Yamanaka, “Lightning strike to a tall grounded object considering direction- and frequency-dependent characteristics,” MSc Thesis, Doshisha University, Jan. 2019.

Acknowledgment

I would like to express deep and sincere appreciation to Prof. Naoto Nagaoka and Prof. Yoshihiro Baba of Doshisha University for their invaluable guidance, advice, and support regarding the research activities and others since I entered the Power System Analysis Laboratory in April 2016. They opened my eyes to lightning transient studies. I admire their high scientific standards and hard works. This five years activity with professors became the most exciting period in my life. Thanks to professors, the present thesis has been completed even under challenging situations due to the worldwide Covid-19 Pandemic.

I am also grateful to Visiting Professors of Doshisha University, Dr. Hiroshi Morita of Kinden Corporation, and Dr. Kenichi Yamazaki of Central Research Institute of Electric Power Industry (CRIEPI) for their comments and discussions on various topics. Dr. Hideki Motoyama of CRIEPI is deeply appreciated for his valuable comments on the transient characteristics of the lightning-struck towers, and Prof. Toshiaki Ueda of Daido University is deeply appreciated for his valuable comments on the lightning fault in HV transmission systems.

Further, I appreciate the old and current members of the Power System Analysis Laboratory of Doshisha University for casual discussions and daily support. Dr. Hiroki Tanaka, Dr. Minella Bezha, Akinori Hori, Shota Inoue, Hiroyuki Murakami, Yukiyoshi Yamada, Kyohei Fuchikami, Takumi Shimizukawa, Hiroaki Okabe, and Koki Kutsuna should be specially thanked. I also would like to express gratitude to Ko Oue, who has been sharing much time since we entered Doshisha University and still pursuing each dream with sharing a sense of values as a prospective researcher. The Japan Society for the Promotion of Science is thanked for the financial support by the research fellowship program.

Finally, I would like to thank my parents, grandparents, and the “growing” family for their preserving support all through my activities at Doshisha University.

Akifumi Yamanaka